

Probing Intermediate-mass Black Holes Using Tidal Disruption Events

Zheng Cao

Probing Intermediate-mass Black Holes Using Tidal Disruption Events

Zheng Cao

Radboud Dissertation Series

ISSN: 2950-2772 (Online); 2950-2780 (Print)

Published by RADBOUD UNIVERSITY PRESS Postbus 9100, 6500 HA Nijmegen, The Netherlands www.radbouduniversitypress.nl

Design: Zheng Cao Cover: Zheng Cao

Printing: DPN Rikken/Pumbo

ISBN: 9789465151045

DOI: 10.54195/9789465151045

Free download at: https://doi.org/10.54195/9789465151045

© 2025 Zheng Cao

RADBOUD UNIVERSITY PRESS

This is an Open Access book published under the terms of Creative Commons Attribution-Noncommercial-NoDerivatives International license (CC BY-NC-ND 4.0). This license allows reusers to copy and distribute the material in any medium or format in unadapted form only, for noncommercial purposes only, and only so long as attribution is given to the creator, see http://creativecommons.org/licenses/by-nc-nd/4.0/.

Probing Intermediate-mass Black Holes Using Tidal Disruption Events

Proefschrift

ter verkrijging van de graad van doctor aan de Radboud Universiteit Nijmegen op gezag van de rector magnificus prof. dr. J.M. Sanders, volgens besluit van het college voor promoties in het openbaar te verdedigen op maandag 7 juli 2025 om 16.30 uur precies

door

Zheng Cao

geboren op 1 februari 1995 te Sichuan, China PROMOTOREN: Prof. dr. P.G. Jonker

Prof. dr. A.J. Levan

Manuscriptcommissie: Prof. dr. W.D. van Suijlekom (voorzitter)

Prof. dr. G.A. Nelemans

Dr. E.G. Körding
Prof. dr. E.M. Rossi *Universiteit Leiden*Prof. dr. K. Maguire

Trinity College Dublin, Ierland

Probing Intermediate-mass Black Holes Using Tidal Disruption Events

Dissertation

to obtain the degree of doctor
from Radboud University Nijmegen
on the authority of the Rector Magnificus prof. dr. J.M. Sanders,
according to the decision of the Doctorate Board
to be defended in public
on Monday, July 7, 2025, at 4.30 pm

by

Zheng Cao

born on 1 February, 1995 in Sichuan, China Supervisors: Prof. dr. P.G. Jonker

Prof. dr. A.J. Levan

Manuscript committee: Prof. dr. W.D. van Suijlekom (chair)

Prof. dr. G.A. Nelemans

Dr. E.G. Körding Prof. dr. E.M. Rossi *Leiden University* Prof. dr. K. Maguire

Trinity College Dublin, Ireland

Contents

1	Intr	oduction	1
	1.1	Black holes in context	1
		1.1.1 Black holes across different mass scales	1
		1.1.2 Intermediate–mass black hole	2
		1.1.3 Accretion disc	3
		1.1.4 Measuring the black hole mass and spin	5
	1.2	Tidal disruption event	9
		1.2.1 TDE as multi-wavelength source	9
		1.2.2 Constraining IMBHs using TDEs	1
		1.2.3 Constructing the disc spectrum	1
	1.3	This thesis	2
2	The	rapidly spinning IMBH J150052	5
	2.1	Introduction	5
	2.2	Data and data reduction	3
	2.3	Results)
		2.3.1 Modelling using simple phenomenological models)
		2.3.2 Slim disc modelling	1
		2.3.3 Slim disc+thermal Comptonisation	3
	2.4	Discussion	5
		2.4.1 Implications of IMBH mass and spin	5
		2.4.2 Origin of the Comptonisation component)
		2.4.3 Transition from super– to sub–Eddington accretion	1
		2.4.4 Constraining ultralight boson masses	1
	2.5	Conclusions	3
	2.6	Appendix	5
3	A va	rying accretion rate in IMBH J1231 43	3
	3.1	Introduction	1

ii Contents

	3.2	Observations and data reduction	5
		3.2.1 XMM-Newton observations	5
		3.2.2 <i>Swift</i> observations	5
		3.2.3 <i>Chandra</i> observation	7
		3.2.4 Fit methods	7
	3.3	Results	8
		3.3.1 Low black hole mass and high spin from slim disc modelling 48	8
		3.3.2 An unusual short-term variability pattern for a QPE	2
		3.3.3 Short–term variability from a changing disc mass accretion rate? 54	4
	3.4	Discussion	4
	3.5	Conclusions	7
	3.6	Appendix	9
		3.6.1 Phenomenological characterisation of J1231 by blackbody models 59	9
		3.6.2 Generating the time–resolved spectra for X2 and X3 59	
		3.6.3 Slim disc fit to S1 and C1 data	
4	AT2	020ocn: a possible disc alignment process 6.	3
	4.1	Introduction	4
	4.2	Data and data reduction	5
		4.2.1 <i>NICER</i>	5
		4.2.2 XMM-Newton	5
		4.2.3 <i>Swift</i>	7
	4.3	Results)
		4.3.1 Long-term light curve of AT2020ocn)
		4.3.2 Long-term spectral evolution of AT2020ocn)
		4.3.3 Spectral analysis of X-ray data	2
		4.3.4 Analysis of UV data using MOSFiT	8
	4.4	Discussion	1
	4.5	Conclusions	9
	4.6	Supplementary materials	1
_	~**		_
5		a-disk modeling reveals an IMBH in the LFBOT AT2018cow 109	
	5.1	Introduction	
	5.2	Methods and data reduction	
		5.2.1 <i>NuSTAR</i> observations	
		5.2.2 XMM-Newton observations	
		5.2.3 <i>Swift</i> observations	
	5.3	Extending slim disk model slimdz to lower M_{\bullet}	
	5.4	Results	
	5.5	Discussion	
	5.6	Conclusions 12')

5.7		Tables	. 124
Summa		Tables	133
Samenv	vatting		137
Bibliog	raphy		141
Researc	ch Data	Management	157
About t	the auth	or	159
Acknow	vledgme	ents	161





Introduction

1.1 BLACK HOLES IN CONTEXT

1.1.1 Black holes across different mass scales

Black holes are a direct prediction of the general theory of relativity (GR). While by definition no light can escape from the event horizon, black holes help shape the Universe, through their extreme gravity and through various feedback processes related to accretion of gas. We can thus infer the existence of black holes by observing how surrounding stars and gas are affected by them. Astrophysical black holes can be broadly grouped into three categories, based on the black hole mass M_{\bullet} : stellar-mass black holes with mass $3M_{\odot} \leq M_{\bullet} \leq 100M_{\odot}$, intermediate-mass black holes (IMBHs) with mass $100M_{\odot} \leq M_{\bullet} \leq 10^6M_{\odot}$, and supermassive black holes (SMBHs) with mass $M_{\bullet} \gtrsim 10^6M_{\odot}$. The mass unit M_{\odot} is the solar mass. Here I briefly describe stellar-mass black holes and SMBHs, and in Section 1.1.2 I will describe IMBHs in more detail, as this thesis is mainly focused on studies of IMBHs.

Stellar–mass black holes are commonly discovered in the X–ray bands or through gravitational wave detections. They reside in binary systems in our Galaxy (e.g., Bolton 1972; Remillard & McClintock 2006; Fender & Belloni 2012). They are thought to be the end products of high–mass stars (see, e.g., Mapelli 2020 for a review). In some cases, a black hole in a binary starts to accrete material from its stellar companion, through Roche–lobe overflow (RLOF; Savonije 1978). Such black hole accreting systems are often referred to as black hole X–ray binaries (BH–XRBs).

During so called BH–XRB outbursts, their X–ray appearance changes between different spectral states, which sometimes can be traced well on a hardness–intensity diagram (e.g., Fender & Belloni 2012). In general, the spectral states are hard states (at high or low mass accretion rate) when the X–ray spectrum is described well by a power–law thought to originate in a corona, and soft states (often at a high mass accretion rate) when the disc spectrum is more prominent in the X–rays. While a vast amount of work has been done on studying BH–XRBs, the spectral states related to different accretion rate levels are most relevant for the study of IMBHs in this thesis.

SMBHs occupy the high-mass end of the black hole population. Most massive galaxies have an SMBH at the centre (e.g., Kormendy & Richstone 1995; Richstone et al. 1998). Our

own Galaxy is no exception (e.g., Eckart et al. 2002; Akiyama et al. 2022). Active galactic nuclei (AGN) are multi-wavelength sources that are powered by an actively accreting SMBH. Observations reveal that the black hole mass in an AGN correlates with the stellar mass of the galactic central bulge, as well as with the velocity dispersion σ of the stars orbiting in the bulge (e.g., Kormendy & Richstone 1995; Merritt & Ferrarese 2001; Gültekin et al. 2009; Zhuang & Ho 2023). These empirical relations indicate that the evolution of the host galaxy and that of the central SMBH are correlated. Unlike the stellar-mass black holes, the formation of SMBHs is one of the main questions to be answered in modern astrophysics (e.g., Volonteri 2010).

1.1.2 Intermediate-mass black hole

IMBH is the least studied class of black holes, compared to stellar–mass black holes and SMBHs. The reason is that, observationally, few IMBHs are found among the actively–accreting black hole systems such as AGNs and BH–XRBs. It remains unclear where IMBHs exist, what is their mass distribution, what mechanism(s) produce them, and most importantly, what roles they play in forming SMBHs. Finding more IMBHs and studying their host environments will be crucial to solve these puzzles.

Searches for IMBHs have been carried out. For example, people search for IMBHs at centres of low-mass galaxies (stellar mass between 10^9 — $10^{10}~M_{\odot}$; e.g., Barth et al. 2008; Moran et al. 2014; Baldassare et al. 2015), which could be IMBH hosts as suggested from extrapolating the scaling relations for SMBHs to lower BH masses. Some studies focus on ultra-luminous X-ray sources (ULXs), which could be IMBHs accreting at high mass accretion rates (e.g., Straub et al. 2014; Mezcua et al. 2018)). IMBH searches are also performed in dense stellar clusters, as runaway collisions in such clusters is one of the candidate mechanisms for producing IMBHs (e.g., Noyola et al. 2010; Wu et al. 2024). One of the strongest evidence for the existence of an IMBH comes from the centre of ω Centauri, the most massive globular cluster of our Galaxy, by analysing the proper motion of the seven central stars which are moving faster than the escape velocity of the cluster (Häberle et al. 2024). Gravitational wave data has also proven that the mergers from stellar–mass black holes can produce IMBHs $\gtrsim 100~M_{\odot}$ (e.g., Abbott et al. 2020). However, many other reported IMBH detections often involve more indirect methods to assess the IMBH mass and those carry significant systematic uncertainties in many cases (see, e.g., Lützgendorf et al. 2015; Brightman et al. 2016; Tremou et al. 2018; Earnshaw et al. 2019; Nguyen et al. 2019).

Despite the elusiveness of IMBHs, their existence might be common in the Universe. Both computer simulations and X-ray surveys of nearby galaxies support a black hole occupation fraction of $\gtrsim 20\%$ among low-mass galaxies (e.g., Miller et al. 2015; She et al. 2017; Ricarte & Natarajan 2018; Bellovary et al. 2019; Rizzuto et al. 2021), where the central black hole is likely to be an IMBH. Meanwhile, mergers of IMBHs are expected to be the prime sources for future space-based gravitational wave detectors such as the *Laser Interferometer Space Antenna (LISA)* (e.g., Amaro-Seoane et al. 2015). The existence of a population of IMBHs can help to

solve the puzzle of SMBH formation. While multiple scenarios have been proposed to explain the formation and evolution of an SMBH (see, e.g., Volonteri et al. 2021 for a review), virtually all require a less–massive seed black hole ($\lesssim 10^6~M_{\odot}$) to form before it grows to an SMBH, making an IMBH population indispensable.

Three major channels have been proposed to produce IMBHs (see, e.g., Greene et al. 2020 for a review). In the first channel, IMBHs are expected to be remnants of the first generation of stars (Pop III stars). Pop III stars in the early Universe are expected to be quite massive and of low metallicity (e.g., Bromm & Larson 2004; Karlsson et al. 2013). They are likely to produce IMBHs $\sim 100~M_{\odot}$ at the end of their lives (e.g., Madau & Rees 2001; Ryu et al. 2016). In the second channel, IMBHs $\sim 10^3-10^4~M_{\odot}$ are produced in dense stellar environments through runaway collisions (e.g., Begelman & Rees 1978; Zwart & McMillan 2002; Stone et al. 2017). In the third channel, IMBHs are expected to be produced through direct collapse of primordial gas clouds in the early Universe (e.g., Bromm & Loeb 2003; Begelman et al. 2006; Luo et al. 2020). In such cases, gas clouds collapse into IMBHs as massive as $\sim 10^4-10^5~M_{\odot}$, skipping stellar evolution phases (except perhaps undergoing a short–lived, quasi–stellar phase; e.g., Reisswig et al. 2013; Inayoshi et al. 2014). Recent observations of the high–redshift ($\gtrsim 6$) Universe find that SMBHs $\geq 10^7~M_{\odot}$ are formed within the first few hundred million years after the Big Bang (e.g., Natarajan et al. 2023; Bogdán et al. 2024; Eilers et al. 2024), which also indicates that IMBHs may exist already in the early Universe to become the seed black holes for SMBHs.

Regardless of their formation channel, IMBHs in the current Universe can be more massive than their birth mass due to subsequent accretion episodes or black hole mergers. Currently, it is not certain if one production channel prevails over the others in producing IMBHs, or if one or more channels are dominant at different cosmic times. Studying IMBHs and their host environment at different redshifts will help us to understand these puzzles about the production of IMBHs.

1.1.3 ACCRETION DISC

Often matter that falls towards a black hole carries angular momentum. The matter needs to transfer some of its angular momentum in order to reach the event horizon. Such an accretion process usually takes the form of an accretion disc, where angular momentum of the in–falling disc matter is transported outwards by viscous torques in the disc (e.g., Shakura & Sunyaev 1973). Here I briefly review some of the textbook accretion disc theories that are most relevant to this thesis.

One of the first and most–studied descriptions of the radial structure of an accretion disc is that of a geometrically–thin, optically–thick, and steady–state disc (Shakura & Sunyaev 1973, 1976). A disc becomes geometrically thin when the disc height H(R) (i.e., the disc vertical thickness at a given radius R) always satisfies H(R)/R << 1. The scale of the accretion disc is typically described in units of the gravitational radius R_g of the central black hole, which is the

characteristic length scale of a black hole system:

$$R_g = \frac{GM_{\bullet}}{c^2},\tag{1.1}$$

where G is Newton's gravitational constant and c is the light speed. The outer disc radius can vary between $\sim 10^2$ to 10^4 R_g . It is usually set by the physical condition of specific systems, e.g., a fraction of the orbital separation of the binary in the case of BH–XRBs, or the in–falling matter subject to Toomre instability at large distance in the case of AGNs.

The radius of the inner disc is important for the generation of high–energy (i.e., X–ray) emission, since most of the high–energy photons are emitted from the hottest, innermost disc region. In GR, the innermost–stable–circular–orbit (ISCO) is measured in R_g and is a function of the black hole spin. Under GR, closer than the ISCO radius, there are no stable circular orbits for a test particle, hence the name. Therefore, $R_{\rm ISCO}$ poses a theoretical limit on how close to the black hole the inner edge of the thin accretion disc can be. For a standard Shakura–Sunyaev thin disc (Shakura & Sunyaev 1973, 1976), inside the inner edge of the disc, matter plunges into the black hole quickly in the form of a hot, optically–thin flow and does not contribute much to the electromagnetic emissions. It can also happen that the standard thin accretion disc is truncated before reaching $R_{\rm ISCO}$ and the emission inside this truncation radius is dominated by such a hot flow (e.g., Dubus et al. 2001). For a non-spinning black hole the ISCO radius is $6R_g$ and for an extreme prograde spinning black hole the ISCO radius could reach R_g and then it coincides with the event horizon (see, e.g., Frank et al. 2002, for the calculation of the ISCO radius as a function of black hole spin).

The Eddington luminosity $L_{\rm Edd}$ is defined as:

$$L_{\rm Edd} = \frac{4\pi G M_{\bullet} m_p c}{\sigma_T} \approx 1.26 \times 10^{38} \left(\frac{M_{\bullet}}{M_{\odot}}\right) \, {\rm erg/s} \,, \tag{1.2}$$

where m_p is the mass of a proton, and σ_T is the Thompson scattering cross–section for electrons. $L_{\rm Edd}$ is derived by equating the outward force exerted by radiation pressure to the gravitational force onto hydrogen atoms (in–falling spherically) by the accreting black hole. Radiation is produced in the accretion process by converting potential energy into radiation. Therefore, $L_{\rm Edd}$ sets an idealised upper limit on the luminosity that an spherical accreting system can reach if the accretion process is stable.

In the study of accretion discs, it is useful to also consider the Eddington mass accretion rate $\dot{M}_{\rm Edd}$. It is the equivalent of the Eddington luminosity limit expressed in the disc mass accretion rate $\dot{M} = dm/dt$. Here $\dot{M}_{\rm Edd}$ is defined as:

$$\dot{M}_{\rm Edd} = 1.37 \times 10^{24} \left(\frac{0.1}{\eta}\right) \left(\frac{M_{\bullet}}{10^6 M_{\odot}}\right) \text{ g/s.}$$
 [1.3]

Here, η is the radiative efficiency of the black hole accretion system $0 < \eta < 0.43$, such that the energy radiated from the accretion L_{acc} is:

$$L_{\rm acc} = \eta \dot{M} c^2 \ . \tag{1.4}$$

The actual value of η depends on the details of each accretion system as well as the black hole spin, and it can reach up to ≈ 0.43 (e.g., Davis & Laor 2011).

As most black hole accretion systems are found to be in a disc-like geometry instead of a spherical accretion, a large fraction of the radiation can escape the system and stop interacting with the in-falling matter, allowing more matter to be accreted and a higher-than $L_{\rm Edd}$ to be reached. Therefore, it is not surprising that astrophysical sources can be more luminous than the theoretical limit of $L_{\rm Edd}$ while the accretion process is not impeded by the strong radiation pressure force.

Emerging observational evidence shows that indeed some black hole accretion systems can reach or even exceed $L_{\rm Edd}$. Such systems include some of the most luminous AGNs where SMBHs are accreting at high–Eddington ($\gtrsim 0.1 L_{\rm Edd}$) or super–Eddington levels (> $L_{\rm Edd}$; e.g., Warner et al. 2004; Collin & Kawaguchi 2004). Some of the tidal disruption events (TDE; see Section 1.2), where stars are tidally disrupted by black holes, are observed to be super–Eddington for timescales of weeks to years initially, before they gradually decay to sub–Eddington levels due to a depletion of in–falling matter (e.g., Lin et al. 2017b). ULXs (e.g., Gladstone et al. 2009; Motta et al. 2012; Sutton et al. 2013) have also been proposed to be BH–XRBs accreting at high–Eddington ($\gtrsim 0.1 L_{\rm Edd}$) or super–Eddington levels (> $L_{\rm Edd}$).

In the high–Eddington or super–Eddington regime (e.g., $\dot{M} \gtrsim 0.1 \dot{M}_{\rm Edd}$), the standard thin disc model no longer adequately describes the accretion disc. In the thin disc model, the thermal equilibrium at a given radius is determined by the local balance between viscous heating and radiative cooling, ignoring other energy transport mechanism such as advection. As advection becomes increasingly important when \dot{M} increases (e.g., Shakura & Sunyaev 1973), a slim disc model has been developed to describe such advection–dominated discs. These discs are both geometrically and optically thick (e.g., Abramowicz et al. 1988).

Here I will highlight a few major differences between the thin and the slim disc models (see, e.g., Abramowicz & Fragile 2013, for a more thorough review of these different disc models). First, as the name already implies, a slim disc is no longer geometrically thin. In a slim disc, the large \dot{M} leads to enhanced radiation pressure and thermal pressure inside the disc, resulting in an inflated disc. Second, the inner disc radius in the slim disc model extends further down from the ISCO to the event horizon. Instead of matter free–falling inside the ISCO the slim disc maintains a disc structure inside the ISCO, because the disc is dominated by radiation pressure and so is supported by the advective transport of heat from the disc outside ISCO. Meanwhile, the thin disc is dominated by viscous pressure, which vanishes inside the ISCO. Third, the radiation efficiency η becomes dependent on \dot{M} in a slim disc. A part of the heat generated by viscosity is trapped in the flow inwards and advected into the black hole. The higher the \dot{M} , the lower the fraction of energy that is dissipated in the form of electro–magnetic radiation. Instead, the dissipated energy is advected inwards, thereby reducing η . In summary, when \dot{M} is close to the Eddington limit or even super–Eddington, advection becomes very important, significantly impacting the disc.

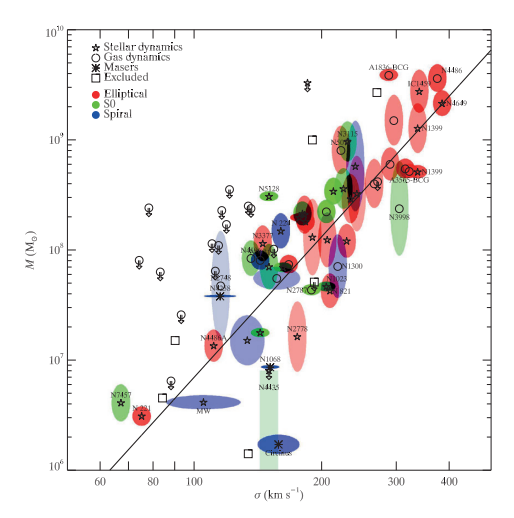


FIGURE 1.1: The correlation between the mass of the supermassive black hole in an AGN and the stellar velocity dispersion σ , measured in various sources. This empirical M_{\bullet} – σ relation is often used to infer the masses of newly found SMBHs. Figure taken from Gültekin et al. (2009).

1.1.4 Measuring the black hole mass and spin

The black hole mass M_{\bullet} is the primary property of a black hole. There are several methods to determine the M_{\bullet} , including dynamical measurements through tracking the orbits of surrounding stars or gas clouds (this method is generally limited to BH-XRBs and nearby SMBHs; e.g., Ghez et al. 2008; Genzel et al. 2010; Walsh et al. 2013; Casares & Jonker 2014). In a few cases the black hole mass can be determined through imaging of the size of the black hole shadow. So far this has been possible for the Galactic centre SMBH Sgr A★ and the M 87 SMBH using the Event Horizon Telescope data; e.g., Akiyama et al. 2019, 2022). In addition, the black holes mass can be derived from the gravitational wave signal and its evolution as a function of time, in the gravitational wave detection of binary BH merger events (e.g., Abbott et al. 2016a). Moreover, several M_{\bullet} measurement methods focus on SMBHs in AGNs, such as the M_{\bullet} -bulge mass relation and the M_{\bullet} - σ relation (e.g., Kormendy & Richstone 1995; Häring & Rix 2004; Gültekin et al. 2009). These methods rely on empirical relations between the M_{\bullet} of the central black hole and signatures from the environment (e.g., stellar population in the bulge), carrying large intrinsic scatters (e.g., Fig. 1.1). Other methods to measure the black hole mass include reverberation mapping (e.g., Blandford & McKee 1982; Peterson et al. 2004), and gravitational micro-lensing (e.g., Mediavilla et al. 2018).

It is also possible to constrain the M_{\bullet} by analysing the accretion disc spectrum. For instance, the effective temperature of a Shakura–Sunyaev thin disc $T_{\rm eff}$ at a disc ring with radius R, is related

to M_{\bullet} such that:

$$T_{\text{eff}}^{4} = \frac{3GM_{\bullet}\dot{M}f_{\text{col}}^{4}}{8\pi\sigma_{\text{SB}}R^{3}} \left[1 - \left(\frac{R_{\text{in}}}{R}\right)^{1/2} \right] .$$
 [1.5]

Here, $\sigma_{\rm SB}$ is the Stefan–Boltzmann constant, $R_{\rm in}$ is the inner edge of the disc ($\geq R_{\rm ISCO}$), and $f_{\rm col}$ is a colour correction factor characterising the scattering processes in the disc's atmosphere (typically ≈ 1.7 ; e.g., Ross et al. 1992; Shimura & Takahara 1995). A thin disc spectrum can then be seen as a combination of black–body emission from different annuli. Therefore, we are able to constrain the M_{\bullet} by fitting a model disc spectrum to the observational data. This method has been used to measure the M_{\bullet} in many black hole accretion systems (e.g., Wandel & Petrosian 1988; Laor 1990; Li et al. 2005; Ghisellini et al. 2010; Calderone et al. 2013; Campitiello et al. 2020). In the case of a slim disc, the presence of strong advection alters the energy dissipation process at each disc annulus and this changes several terms in the $T_{\rm eff}$ equation (e.g., Sądowski et al. 2011; Straub et al. 2011), but essentially the method of measuring the M_{\bullet} stays the same.

Compared to M_{\bullet} , the second property defining a black hole, its spin a_{\bullet} is more difficult to constrain, as GR predicts that a_{\bullet} only affects higher–order terms of the space–time geometry than M_{\bullet} . The a_{\bullet} will change the geodesics of a test particle significantly only when it gets very close to the black hole. Hence, only emission generated in or strongly dependent on the vicinity of the black hole (e.g., the accretion disc and perhaps the base of the jet) are sensitive to the a_{\bullet} value. The a_{\bullet} measurement methods include, for example, disc continuum fitting (e.g., Li et al. 2005; McClintock et al. 2006), disc reflection spectroscopy (e.g., Fabian et al. 1989; Miller et al. 2009), quasi–periodic oscillation modelling (e.g., Abramowicz & Kluźniak 2001), spin–jet power correlations (e.g., Daly 2011; Narayan & McClintock 2012), and gravitational wave detection of binary black hole mergers (e.g., Abbott et al. 2023).

Similar to the M_{\bullet} measurement, the continuum fitting method of the accretion disc is commonly used to constrain a_{\bullet} in many black hole accretion systems (e.g., Shafee et al. 2005; Liu et al. 2008; Steiner et al. 2014; McClintock et al. 2015; Zhao et al. 2021). Most of the observational constraints use the thin disc model. For a thin disc, the ISCO radius is a monotonically decreasing function of a_{\bullet} (Fig. 1.2). Through this, the hard X-ray spectrum part of a thin disc spectrum is sensitive to a_{\bullet} , assuming the disc is not truncated by other processes than the ISCO. The reflection spectroscopy method is also employed regularly. The accretion disc reflects emission generated above it, such as from a corona above the disc, or the base of a jet, creating a reflection spectrum. This reflection spectrum is sensitive to the location of the $R_{\rm in}$ and thus the a_{\bullet} . Clearly, both methods rely on the $R_{\rm ISCO}$ dependency of the a_{\bullet} . In the super-Eddington regime, though the $R_{\rm in}$ can be smaller than $R_{\rm ISCO}$, the disc spectrum remains sensitive to the a_{\bullet} value, as the hard spectral tail of the disc spectrum is still dominated by the innermost disc region where the impact of the a_{\bullet} is significant (e.g., Fig. 1.3; Wen et al. 2020).

Some stellar–mass black holes and most SMBHs with a mass $< 3 \times 10^7 M_{\odot}$ are found to be rapidly spinning ($a_{\bullet} > 0.9$; e.g., Reynolds 2021). A selection bias towards high spins is expected in observations of black holes: given the same \dot{M} , the higher the a_{\bullet} , the more luminous the

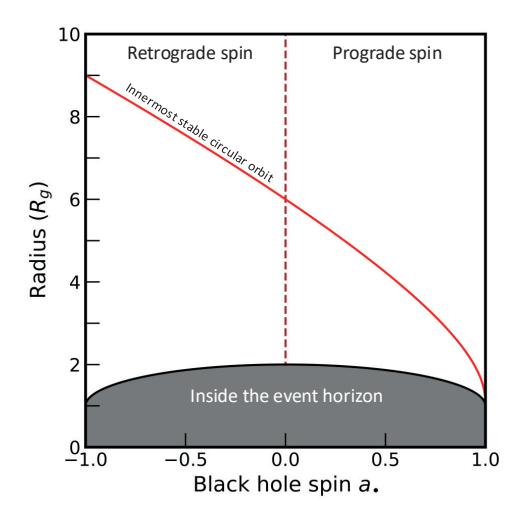


FIGURE 1.2: The evolution of two characteristic radii as a function of the Kerr black hole spin. The radius of the innermost–stable circular orbit (red) is monotonically decreasing with respect to the spin (positive value for prograde black hole spin and negative value for retrograde spin, as seen by the disc). Figure adapted from Reynolds (2021).

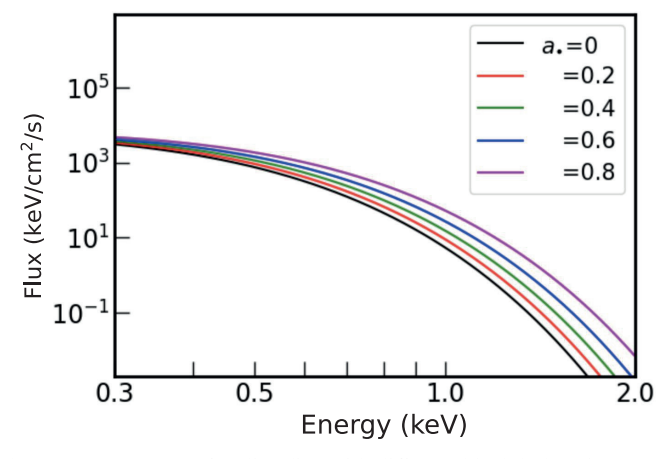


FIGURE 1.3: The X-ray spectrum of a slim disc with different black hole spin a_{\bullet} . The disc spectrum is calculated following the presented method in Wen et al. (2020, 2022), assuming $M_{\bullet}=1\times 10^6~M_{\odot}$, disc inclination $\theta=45^{\circ}$, and $\dot{M}=10~\dot{M}_{\rm Edd}$. The hard spectral tail of the disc spectrum is dominated by the innermost disc region where the impact of the a_{\bullet} is significant.

accretion disc with a larger fraction of the spectrum emitted in X–rays instead of UV bands (while the extinction of the UV light from the interstellar medium is very strong). The spin measurements often require high–quality X–ray data, implying that the black holes should be sufficiently bright to have a_{\bullet} constrained. Therefore, we should expect the rapidly–spinning black holes to be over represented in any flux limited sample.

Despite the observational bias towards black holes with high spin values, the spin measurement still provides a way to probe the evolution history of individual black holes. In particular, if a black hole gains its last *e*—fold mass via a single, large, accretion episode after its birth, then it may be spun-up by the angular momentum of the accreted material. Otherwise, if the mass growth of the IMBH is through several accretion episodes where the gas cloud feeding the accretion process comes from different directions, i.e., carrying randomly oriented angular momentum, the black hole is expected to be significantly spun—down by accretion episodes. Similarly, for IMBHs growing through mergers with other black holes and through the accretion of gas supplied by tidally disrupted stars (which come from an isotropically distributed population of stars and stellar orbits) the expected IMBH spin is low (e.g., Hughes & Blandford 2003; Volonteri et al. 2007; King et al. 2008; Metzger & Stone 2016).

1.2 TIDAL DISRUPTION EVENT

1.2.1 TDE AS MULTI-WAVELENGTH SOURCE

A tidal disruption event (TDE) refers to the process where a star is tidally disrupted by tidal forces when it gets too close to a black hole. A schematic representation of a TDE is shown in Fig. 1.4. To an accuracy of a factor ≈ 2 , a star with a mass m_* and radius r_* can be fully disrupted if the pericentre of its stellar orbit falls within the tidal radius R_T (Hills 1975):

$$R_{\rm T} = r_* \left(\frac{M_{\bullet}}{m_*}\right)^{1/3} \tag{1.6}$$

A partial TDE can happen if the pericentre is slightly larger than $R_{\rm T}$, then only outer layers of the star are stripped away by the tidal force. After a full TDE, about half of the stellar debris is initially gravitationally bound to the black hole (Rees 1988). Eventually, the fall–back of the bound debris accretes onto the black hole, often at super–Eddington mass accretion rates initially (e.g., Wen et al. 2020). The accretion disc formed after a TDE is expected to have a characteristic outer radius of $\approx 2R_{\rm T}$ which is $\sim 10^2~R_g$ (e.g., Rees 1988; Ulmer 1999). This is much smaller than that of typical AGN discs ($\gtrsim 10^3~R_g$). The circularisation of the debris streams to form such a TDE disc is complex, but it is likely that energy and angular momentum dissipation in shocks and outflows at several specific locations in the streams is important (see e.g., Bonnerot & Stone 2021, for a review on the disc formation process in TDE). In those cases where the equatorial plane of the black hole spin and the orbital plane of the star prior to the disruption are misaligned, nodal precession of the debris streams might significantly delay the circularisation process and subsequently the formation of a circularised disc (e.g., Hayasaki et al. 2016).

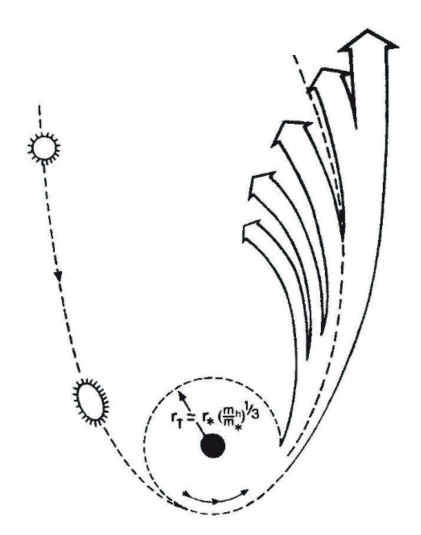


FIGURE 1.4: Schematic representation of a tidal disruption event. A star is tidally disrupted by a black hole. About half of the stellar debris will be gravitationally bound to the black hole. The fall–back of debris triggers the subsequent black hole accretion process. Figure adapted from Rees (1988).

A TDE can lead to electromagnetic signals across various energy bands, from radio (e.g., Alexander et al. 2020), to optical and UV (e.g., van Velzen et al. 2020), to X–rays and γ –rays (e.g., Saxton et al. 2020; Murase et al. 2020). Usually TDEs are discovered in optical/UV or X–ray bands, through one of the numerous wide–field transient surveys such as *XMM-Newton* slew surveys (e.g., Esquej et al. 2007), *Zwicky Transient Facility* (ZTF; Bellm et al. 2018) , and *All–Sky Automated Survey for Supernovae* (ASASSN; Kochanek et al. 2017). Typically, the optical/UV lightcurves of a TDE show a fast rise and a slow decay over the first few hundred days (e.g., van Velzen et al. 2020). On longer timescales, often an optical/UV plateau is detected (e.g., Brown et al. 2017). While the late–time optical/UV emission at the plateau phase is consistent with originating from the disc (e.g., Van Velzen et al. 2019; Mummery & Balbus 2020; Wen et al. 2023), the origin of the early–time optical/UV emission is a topic of active debate (e.g., see Roth et al. 2020 for a review). Possible explanations include shock–powered emission during the circularisation of debris streams (e.g., Piran et al. 2015; Andalman et al. 2022; Steinberg & Stone 2024), or a "reprocessing layer" that re–emits the inner disc's X–ray emission in the optical/UV band (e.g., Loeb & Ulmer 1997; Metzger & Stone 2016; Dai et al. 2018; Bonnerot & Lu 2020).

There is consensus that TDE X-ray emission likely originates from the inner disc region. However, it is not always the case that optical/UV-selected TDEs will have X-ray signals detected, and vice versa for X-ray selected TDEs. It is possible that, as the disc formation after the circularisation of debris streams can be delayed with respect to the disruption, the X-ray emission of a TDE is produced or becomes detectable only in late-time observations. Indeed, some

optical/UV-selected TDEs only have late-time X-ray detections, consistent with this explanation (e.g., Jonker et al. 2020; Hayasaki & Jonker 2021). Another factor affecting the multi-wavelength detectability of a TDE could be the inclination angle. Large inclination angles between our line-of-sight and the black hole spin angular momentum vector can lead to significant obscuration of the inner X-rays by the outflows or the outer disc (e.g., Dai et al. 2018; Wen et al. 2020).

1.2.2 Constraining IMBHs using TDEs

The TDE-triggered black hole accretion processes provide an unique opportunity to measure the mass and the spin of a black hole that is otherwise quiescent and un-detectable, through for instance spectral analysis of the disc's X-ray emission (Section 1.1.4). IMBH-TDE detections will provide valuable insights into the question of where IMBHs could be located in our Universe (e.g., in off-nuclear stellar clusters; e.g., Lin et al. 2018; Wen et al. 2021).

As the black hole radius scales with $R_g \propto M_{\bullet}$ and $R_T \propto M_{\bullet}^{1/3}$, for a non–spinning black hole above a critical mass (in its Newtonian limit, known as the Hills mass):

$$M_{\text{Hills}} \approx 1.1 \times 10^8 M_{\odot} \left(\frac{r_*}{R_{\odot}}\right)^{3/2} \left(\frac{m_*}{M_{\odot}}\right)^{-1/2} ,$$
 [1.7]

the tidal radius $R_{\rm T}$ becomes inside the event horizon, meaning that the star will enter the black hole before it can be tidally disrupted. Therefore, by its nature TDE emission can only be used to probe $\lesssim 10^8 M_{\odot}$ black holes (for a solar star disrupted by a non–spinning black hole).

TDEs are powerful tools to search for IMBHs. First, as a direct result from the argument of the Hills mass, IMBHs can disrupt a larger variety of stars when compared to SMBHs. Stars less massive than the Sun often cross over the event horizon before being disrupted in the case of a SMBH, while they can be disrupted by an IMBH outside the event horizon.

Second, the dynamics of dense stellar environments predict that IMBHs should contribute significantly to the total TDE rate (though the actual rate depends heavily on the not–well known mass distribution of the IMBH population, which significantly impacts the occupation fraction of black holes in low–mass galaxies; e.g., Metzger & Stone 2016; Stone et al. 2020). This is primarily because for lower–mass galactic nuclei with an IMBH, the stellar density is higher than that for the nuclei with a central SMBH in larger galaxies, and the density profile is a steeper function of distance to the centre. Therefore, the steady–state TDE rate is higher due to the shorter 2–body relaxation time in the case of low–mass galaxies with a central IMBH.

Third, for a given matter supply \dot{M} from the stellar debris, the disc temperature is higher and therefore emits more in the X–ray band when the M_{\bullet} is smaller. Therefore, the selection bias in any X–ray flux limited TDE samples of observations will also favour less–massive black holes.

1.2.3 Constructing the disc spectrum

To measure the mass and the spin of a black hole in a TDE, the primary method used in this thesis is modelling the X–ray spectra of the accretion disc. Early works of modelling of the disc spectrum

focuses on a Shakura–Sunyaev, thin disc (e.g., Li et al. 2005; Brenneman & Reynolds 2006). In general, to construct a disc spectrum, the first step is calculating the disc profile under pre–defined conditions (e.g., assuming certain values for M_{\bullet} , a_{\bullet} , and \dot{M}), deriving the disc spectrum as seen by a local observer. The second step is to take into account the relativistic effects (e.g., light–bending and Doppler shifts) modifying the disc spectrum before we observe the spectrum on Earth, often utilising photon ray–tracing techniques (e.g., Psaltis & Johannsen 2011).

As the accretion in TDEs is often found to be close to or even super–Eddington (e.g., Saxton et al. 2012; Gezari et al. 2012; Holoien et al. 2016; Lin et al. 2022b), a slim disc spectral model is needed to describe the disc spectrum. Some studies explored the spectral shape of a slim disc (e.g., Straub et al. 2011; Kubota & Done 2019). Improving on those pioneering works, the state–of–art slim disc model, *slimdz* (Wen et al. 2020, 2022), includes the loss of angular momentum due to radiation at each disc annulus. This adjustment alters the predicted effective temperature of the inner disk region, especially for high–spin discs (Wen et al. 2021). The latest estimate of the disc spectral hardening effect (Davis & El-Abd 2019) is also employed by *slimdz*. By comparing the observed disc spectrum with a library of disc spectra calculated with various mass and spin values, we are able to infer constraints on the mass and the spin of the black hole in a TDE within a certain confidence level.

1.3 This thesis

IMBHs play an important role in the formation and evolution history of SMBHs, while few are detected. To constrain the IMBH population, more IMBHs need to be identified. Meanwhile, X-ray detected TDEs provides a unique opportunity to measure both the mass and the spin of IMBHs, as well as to study the black hole accretion process in the super–Eddington regime. This thesis focuses on finding more IMBHs and measuring their mass and spin, by analysing the X–ray spectra of IMBH candidates during the accretion process triggered by TDEs or TDE candidates.

In Chapter 2, *The rapidly spinning intermediate–mass black hole 3XMM J150052.0+015452*, multi–epoch *XMM-Newton* and *Chandra* X-ray spectra obtained after 2008 during the decade–long decay of a TDE are analysed. Based on fitting the slim disc model to the observed spectra, the mass and the spin measurements of the black hole 3XMM J150052.0+015452 are derived. We confirm it as an IMBH, refine its mass measurement, and find a rapid, near extremal, spin. A black hole corona is found to be present before 2014 when the disc mass accretion rate is at super–Eddington levels, while later spectra show no sign of the corona when the accretion rate is around the Eddington limit. Our analysis demonstrates the importance of early–time X–ray observations in understanding the TDE accretion, as well as in constraining the black hole mass and spin. We further discuss the impact of the mass and the spin measurement of 3XMM J150052.0+015452 on its inferred formation and evolution.

Chapter 3, *The intermediate–mass black hole 2XMM J123103.2+110648: a varying disc accretion rate during possible X–ray quasi–periodic eruptions?*, presents the X–ray spectral analysis of the candidate TDE 2XMM J123103.2+110648. We analyse the X–ray spectra obtained

1.3 This thesis

through observations of *XMM-Newton*, *Swift*, and *Chandra*. The black hole is constrained to be a rapidly–spinning black hole. Furthermore, previous studies have proposed that the X–ray short–term variability present during two of the *XMM-Newton* observations are related to quasi–periodic eruptions (QPEs). QPEs are found in multiple AGN and TDE sources, showing "hard–rise–soft–decay" flares of unknown origin (in some models linked to extreme mass ratio inspirals, or EMRIs; e.g., Linial & Metzger 2023a; Arcodia et al. 2021). Our results show that the short–term variability are consistent with the explanation of a slim disc, where the mass accretion rate varies. While several proposed QPE mechanisms are able to generate this accretion rate variation, we find that during the short–term variability each flare does not follow the "hard–rise–soft–decay" mode, suggesting the source is atypical for the QPE explanation.

Chapter 4, *Tidal disruption event AT2020ocn: early–time X–ray flares caused by a possible disc alignment process*, presents the spectral analysis of high–cadence *NICER* observations, together with multiple *XMM-Newton* observations of TDE AT2020ocn. We constrain the black hole to be an IMBH, while the data quality does not allow the spin to be constrained. We find that the early–time X–ray flares of AT2020ocn can be explained by the disc alignment process. This process happens when the plane of the stellar orbit prior to the disruption is not equal to the black hole equatorial plane. The simultaneous UV monitoring finds no flares correlated with the X–rays, providing further evidence that the early–time UV emission has an origin unrelated to the accretion disc.

In Chapter 5, Slim—disc modelling reveals an accreting intermediate—mass black hole in the luminous fast blue optical transient AT2018cow, we find that the X-ray spectral data is consistent with an accreting IMBH powering the most luminous class of the fast blue optical transients (LFBOTs). The origin of LFBOTs is still unknown, with a TDE as one of the candidate mechanisms. Here, we present X-ray spectral analysis of AT2018cow — the LFBOT archetype — using NuSTAR, Swift, and XMM-Newton data. The X-ray spectra can be explained by the presence of a slim accretion disc around an IMBH, a possible outcome from several scenarios proposed to explain the LFBOTs, including the TDE scenario. Our work provides evidence for an accreting IMBH as the central engine in AT2018cow, and, by extension, in LFBOT sources similar to AT2018cow.

THE RAPIDLY SPINNING INTERMEDIATE—MASS BLACK HOLE 3XMM J150052.0+015452

Z. Cao, P.G. Jonker, S. Wen, N.C. Stone, A.I. Zabludoff Monthly Notices of the Royal Astronomical Society, Volume 519, Issue 2, February 2023

Abstract

A star tidally disrupted by a black hole can form an accretion disc with a super-Eddington mass accretion rate; the X-ray emission produced by the inner disc provides constraints on the black hole mass M_{\bullet} and dimensionless spin parameter a_{\bullet} . Previous studies have suggested that the M_{\bullet} responsible for the tidal disruption event 3XMM J150052.0+015452 (hereafter J150052) is $\sim 10^5 M_{\odot}$, in the intermediate black hole (IMBH) regime. Fitting multi-epoch XMM-Newton and Chandra X-ray spectra obtained after 2008 during the source's decade-long decay, with our latest slim accretion disc model gives $M_{\bullet} = 2.0^{+1.0}_{-0.3} \times 10^5 M_{\odot}$ (at 68% confidence) and $a_{\bullet} > 0.97$ (a 84.1% confidence lower limit). The spectra obtained between 2008-2014 are significantly harder than those after 2014, an evolution that can be well explained by including the effects of inverse-Comptonisation by a corona on the early-time spectra. The corona is present when the source accretion rate is super–Eddington, while there is no evidence for its effect in data obtained after 2014, when the mass accretion rate is around the Eddington-limit. Based on our spectral study, we infer that the corona is optically thick and warm ($kT_e = 2.3^{+2.7}_{-0.8}$ keV). Our mass and spin measurements of J150052 confirm it as an IMBH and point to a rapid, near extremal, spin. These M_{\bullet} and a_{\bullet} values rule out both vector bosons and axions of masses $\sim 10^{-16} \text{ eV}.$

2.1 Introduction

A star approaching a black hole (BH) can be broken apart by tidal forces, leading to a tidal disruption event (TDE; e.g., Hills 1975; Rees 1988). The stellar debris from the disrupted star

can be subsequently accreted by the BH through an accretion disc. The electromagnetic flares associated with TDEs induced by supermassive black holes (SMBH; $\gtrsim 10^6~M_\odot$) are mainly observed in the optical/UV and X-ray energy bands (e.g., Bade et al. 1996; Komossa et al. 2004; Gezari et al. 2006; van Velzen et al. 2011; Saxton et al. 2014; van Velzen et al. 2020; Saxton et al. 2020). The TDE X-ray spectrum is often dominated by soft X-ray thermal emission (Ulmer 1999; Lodato & Rossi 2011). Therefore, it has been proposed that the X-ray data of TDEs can be used to constrain the mass and the spin of their host BHs due to the high sensitivity of the disc emission to these two BH properties (e.g., Wen et al. 2020).

Studying TDEs provides a unique opportunity to find intermediate—mass black holes (IMBHs; $10^2 \le M_{\bullet} \le 10^6~M_{\odot}$) and to constrain their properties, because the volumetric rate of TDEs is predicted to be dominated by IMBHs, should they exist in dense stellar environments (Wang & Merritt 2004; Stone & Metzger 2016). IMBHs are believed to be important stepping-stones in the growth of SMBHs (e.g., Volonteri 2010; Banados et al. 2018). Thus, searching for IMBHs can help constrain the masses of SMBH seeds (e.g., Kormendy & Ho 2013; Shankar et al. 2016; Pacucci et al. 2018). It is also expected that IMBH mergers will be a prime source of gravitational radiation for the upcoming gravitational wave detector in space (*Laser Interferometer Space Antenna* or LISA; e.g., Amaro-Seoane et al. 2015). However, it is still unclear how IMBHs form and evolve (see Inayoshi et al. 2020, for a recent review). Furthermore, direct measurements of their masses and spins (e.g., Wen et al. 2021) are lacking (see, e.g., Greene et al. 2020 for a review on searching for IMBHs).

To constrain BH properties with TDEs, we need to model the TDE disc emission. The mass accretion rate of a TDE can vary by orders of magnitude on humanly accessible timescales, from sometimes highly super–Eddington to significantly sub–Eddington (Evans & Kochanek 1989). In near/super–Eddington phases, the inward advection of disc energy can no longer be neglected, and radiation pressure on the accretion flow makes fluid orbits non-Keplerian (Abramowicz et al. 1988). As a result, a standard "thin" disc model (e.g., Shakura & Sunyaev 1973) is not adequate to describe such a TDE disc, and a "slim" disc model has to be used. Details of the slim disc solution can be found in Abramowicz et al. (1988) and Sądowski (2009). We have now developed such models for application to TDEs, including those associated with IMBHs (Wen et al. 2020, 2021, 2022).

Modelling TDE disc emission not only constrains the BH mass, but also the spin. In fact, TDE modelling is currently the only way to probe the spins of IMBHs (Wen et al. 2020, 2021). The BH spin distribution reveals how they have grown (e.g., Berti & Volonteri 2008), and, for individual IMBHs, how they may have formed (e.g., Inayoshi et al. 2020). In the near future, time domain surveys from the VRO (Bricman & Gomboc 2020), eROSITA (Khabibullin et al. 2014; Jonker et al. 2020), Einstein Probe (Yuan et al. 2018), and ULTRASAT (Sagiv et al. 2014) will together find thousands of TDEs. The resulting large TDE samples, when their follow-up X-ray observations are analysed through slim disc modelling, will produce constraints on the distributions of IMBH mass and spin for the first time, providing a unique opportunity to probe the formation and evolution theory of the IMBH population.

2.1 Introduction 17

Table 2.1: *XMM-Newton* and *Chandra* observations of J150052 analysed in this work. The exposure time is the time remaining after filtering for epochs of enhanced background count rates. The average count rates of the source+background spectra are given in the energy ranges 0.3–10.0 keV (*XMM-Newton*) and 0.3–7.0 keV (*Chandra*). We also list in the last column the source counts estimated by subtracting the estimated number of background counts in the source extraction region. We treat observations C2–C8 as a single-epoch observation, and its estimated total source count is 6905.

Satellite	ObsID (Label)	Date	Exposure (ks)	Count rate (cts/s)	Est. Source counts (cts)
XMM-Newton	0554680201 (X1)	2009-02-11	39	$(4.1 \pm 0.1) \times 10^{-2}$	1305
	0554680301 (X2)	2009-02-17	35	$(4.0 \pm 0.1) \times 10^{-2}$	1146
	0804370301 (X3)	2017-07-21	14	$(3.5 \pm 0.2) \times 10^{-2}$	417
	0804370401 (X4)	2017-08-09	5.4	$(3.4 \pm 0.3) \times 10^{-2}$	146
	0804370501 (X5)	2018-01-20	4.5	$(3.7 \pm 0.3) \times 10^{-2}$	145
	0844040101 (X6)	2020-02-21	20	$(2.8 \pm 0.1) \times 10^{-2}$	467
Chandra	9517 (C1)	2008-06-05	99	$(1.37 \pm 0.04) \times 10^{-2}$	1223
	12951 (C2)	2011-03-28	74	$(1.47 \pm 0.06) \times 10^{-2}$	
	13246 (C3)	2011-03-30	45	$(1.47 \pm 0.08) \times 10^{-2}$	
	13247 (C4)	2011-03-31	36	$(1.62 \pm 0.09) \times 10^{-2}$	
	12952 (C5)	2011-04-05	143	$(1.52 \pm 0.04) \times 10^{-2}$	C2-C8: 6905
	12953 (C6)	2011-04-07	32	$(1.67 \pm 0.09) \times 10^{-2}$	
	13253 (C7)	2011-04-08	118	$(1.49 \pm 0.05) \times 10^{-2}$	
	13255 (C8)	2011-04-10	43	$(1.50 \pm 0.08) \times 10^{-2}$	
	17019 (C9)	2015-02-23	37	$(0.51 \pm 0.04) \times 10^{-2}$	185

By constraining both the mass and the spin of IMBHs, we can also test for the existence of ultralight bosons, such as axions (or axion-like particles) and vector bosons. Scalar axions have long been considered a possible solution to the strong CP problem (Peccei & Quinn 1977). More recently, axion-like particles have received attention as a natural consequence of string theory (Arvanitaki et al. 2010). Both scalar and vector ultralight bosons are of astrophysical interest as particle dark matter candidates (Dine & Fischler 1983; Preskill et al. 1983; Nelson & Scholtz 2011; Arias et al. 2012; Graham et al. 2016). A rapidly–spinning BH can interact with ultralight bosons, causing a superradiant scattering instability that spins down the BH (Bardeen et al. 1972; Press & Teukolsky 1972; see also Brito et al. 2020 for a recent review). Efficient spindown only occurs when bosons of the appropriate mass exist, such that their Compton wavelength is close to the size of the event horizon. Without a close match, the timescale for establishing the instability grows exponentially. Therefore, we can use the mass and spin measurements of a rapidly–spinning BH to rule out roughly one order–of–magnitude in ultralight particle mass (e.g., Cardoso et al. 2018).

Furthermore, TDEs are good laboratories for studying accretion theories in the super–Eddington regime. The X–ray spectrum of sources accreting in the so-called ultra-luminous state can sometimes be well-described by two black-bodies (e.g., Pinto et al. 2017, 2021), similar to some TDEs (e.g., Kara et al. 2018). For example, it has been proposed that ultra–luminous X–ray sources (ULXs) host stellar–mass compact objects (neutron stars or BHs) accreting at super–Eddington rates (e.g., King et al. 2001; Roberts 2007; Feng & Kaaret 2009; Gladstone et al. 2009; Kaaret et al. 2017). Perhaps these ULXs are BH X–ray binaries (XRBs) accreting in an ultra–luminous state (e.g., Gladstone et al. 2009; Motta et al. 2012; Sutton et al. 2013). Modelling

TDE X-ray emission tests whether similarities in spectral shape and evolution between TDEs and other super-Eddington accretors like ULXs could arise from common physical circumstances, e.g., a super-Eddington slim disc.

The X-ray source 3XMM J150052.0+015452 (J150052) was detected by *XMM-Newton* and *Chandra* in observations of the foreground galaxy group NGC 5813 (redshift z=0.0064; Paturel et al. 2002) in 2005. It has a well–constrained X-ray position coincident with the center of the galaxy SDSS J150052.07+015453.8 (redshift z=0.14542; Lin et al. 2017b). Follow–up *XMM-Newton* and *Chandra* observations started in 2008, and together the observations span more than a decade. All the observational evidence presented in Lin et al. (2017b, 2022a) suggests that J150052 is a slowly-decaying TDE. This decade–long decay distinguishes J150052 from many other faster–decaying TDEs (e.g., Van Velzen et al. 2021). The long duration can be attributed to slow circularisation of the fall back material, as well as a long super–Eddington phase for a less–massive BH (< $10^6 M_{\odot}$; Lin et al. 2022a). Both the BH–bulge scaling relation (Graham & Scott 2013) and spectral analysis using a model for a thin accretion disc+corona (Lin et al. 2022a) determine the mass of the BH J150052 to be ~ $10^5 M_{\odot}$.

Here we analyze the X-ray spectra and light curve obtained over J150052's decade—long decay, considering the slim disc model for the accretion disc (Wen et al. 2020, 2021). We include all the archived *XMM-Newton* and *Chandra* X-ray data obtained since 2008. In Section 2, we describe the selected data and our data reduction. In Section 3, we present the results from our model fits, including the constraints on black hole mass and spin. In Section 4 we discuss the implications of our results for IMBH formation scenarios, the origin of the Comptonisation component, the evolution of that component, and the mass of ultralight bosons. In Section 5, we end with our conclusions.

2.2 Data and data reduction

We use *XMM-Newton* and *Chandra* observations of J150052 in this work. Some basic properties of those observations are listed in Table 2.1. Note that we do not include observations obtained before 2006, as at those epochs the mass accretion rate in J150052 was too low for our slim disc model to apply. The labels indicating the observations differ therefore from those used in Lin et al. (2017b).

For the *XMM-Newton* data reduction, we use HEASOFT (version 6.28) and SAS (version 18.0.0) with the calibration files renewed on January 5th, 2021 (CCF release: XMM-CCF-REL-380). We use the SAS command epproc to process the Science 0 data from *XMM-Newton*/EPIC-pn. We employ the standard filtering criteria¹ for EPIC-pn data, where we require that the 10-12 keV detection rate of pattern 0 events is < 0.4 counts s⁻¹. This way the data are cleared from periods with an enhanced background count rate. We use a circular source region of 20'' radius centred on the source for the spectral counts extraction. The background count spectra are extracted from

¹https://www.cosmos.esa.int/web/xmm-newton/sas-thread-epic-filterbackground

apertures close to the source on the same EPIC-pn detector and free from other bright sources. We use a rectangular region of $134'' \times 45''$ to extract the background in observations X1 and X2 due to the source location being close to the edge of the EPIC-pn detector, while a circular region of 50" radius is used for the background extraction in X3–X6. We check for the presence of photon pile-up using the SAS command epatplot and conclude the pile-up is not important in any of our *XMM-Newton* observations.

During some of the *XMM-Newton* observations, one of the two MOS detectors was turned off. Therefore, for consistency, we do not use the MOS data. We also do not use the RGS data, because the signal–to–noise ratio in the RGS detectors is too low.

For the *Chandra* data reduction, we use CIAO (version 4.12). We employ the CIAO commands chandra_repro and specextract for *Chandra*/ACIS data filtering and spectral extraction, respectively. J150052 has a large off-axis angle for the first eight *Chandra* observations. Following Lin et al. (2017b) we take the deterioration of the point spread function with off-axis angle into account: we set the radius of the circle used for the source extraction region to 16."7 for C1, 13."4 for C2–C8, and 1."6 for C9 (during the observation labelled C9 the source is observed on-axis). The background spectra are extracted from apertures close to the source, on the same *Chandra*/ACIS chip, and free from other bright sources. We use rectangular apertures with length >100" and width ~ 70 " as the background regions in C1–C8, and a circular region of 50" radius in C9. Because observations C2 to C8 are obtained close in time and the source spectra did not change significantly on such short time scales, we combine the spectra from C2 to C8 using the CIAO command combine_spectra. We subsequently treat the C2–C8 observations as a single epoch observation, similar to the approach of Lin et al. (2017b).

In this paper, we focus on the energy bands 0.3–10 keV for *XMM-Newton*/EPIC-pn and 0.3–7.0 keV for *Chandral* ACIS. We require each source+background and the background spectral energy bins to have a minimum of one photon per bin. For each epoch, we first fit the background spectrum with a phenomenological model. When we fit the source+background spectrum, we add the best-fit background model to the fit-function describing the source+background, fixing the background model parameters to their best-fit values determined from the fit to the background-only spectra. The best-fit background model varies from epoch to epoch and between instruments; it consists of between 1–3 power-laws and 3–6 Gaussian components (with a full–width half–maximum or FWHM of $\sigma=0.001$ keV, less than the spectral resolution in both *XMM-Newton*/EPIC-pn and *Chandral* ACIS instruments) that accounts for the background continuum and background fluorescence lines (e.g., Markevitch et al. 2003; Katayama et al. 2004).

Throughout this paper, we carry out the spectral analyses using the XSPEC package (Arnaud 1996; version 12.11.1), applying Poisson statistics (Cash 1979; C-STAT in XSPEC). Unless otherwise specified, we quote all the parameter errors at the 1σ (68%) confidence level, assuming Δ C-stat=1.0 and Δ C-stat=2.3 for single– and two–parameter error estimations (Wen et al. 2021), respectively. All the spectra we present here and in the Appendix are re-binned for plotting purposes only. All models in this paper include Galactic absorption of column density $N_{H,G} = 4.4 \times 10^{20} \text{cm}^{-2}$ (Kalberla et al. 2005) using the model TBabs (Wilms et al. 2000). We

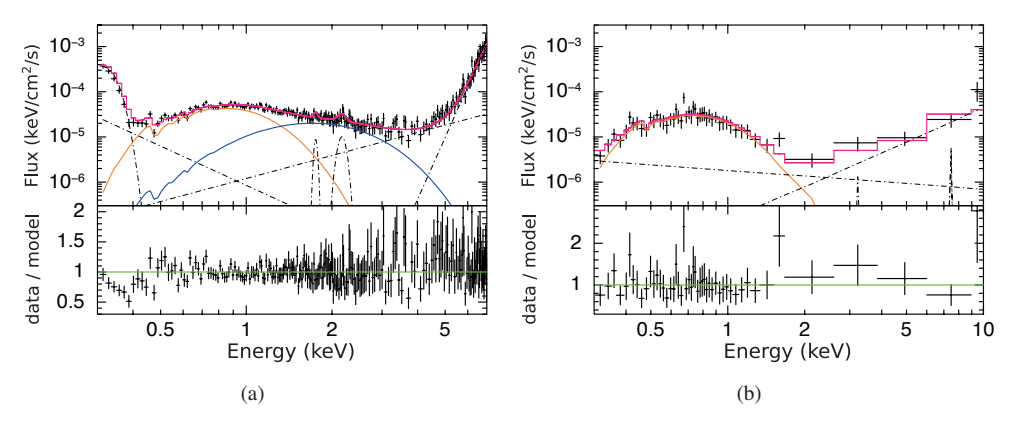


FIGURE 2.1: **a)** The source+background spectrum from combining the C2–C8 observations (as one epoch), de-convolved from the detector response curve (i.e., the unfolded spectrum), and the data/model ratio. Here the source fit function consists of two BBs. The red line is the total source+background continuum, the orange and the blue lines stand for the two best-fitting BB models, and the dot-dash lines are the background model components. The parameters of the background model have been kept fixed during the fits (see Section 2.2); **b)** Unfolded source+background spectrum observed at Epoch X3 and the data/model ratio for a source model fit function comprised of one BB. The format follows that of Fig. 2.1(a), except that here only one BB model in orange is present. J150052 shows two-BB-like, hardened spectra at early epochs (C1, X1, X2, C2–C8), compared to spectra at late epochs (C9, X3, X4, X5, X6).

also consider the absorption intrinsic to the X-ray source and its host galaxy at redshift z=0.14542 (using the model zTBabs), leaving the zTBabs column density $N_{H,i}$ to be a free parameter. With the energies command in XSPEC, we take a logarithmic energy array of 1000 steps from 0.1 to 1000.0 keV for model calculations in place of response energy arrays, to correctly calculate the Comptonisation model when needed (see Section 2.3.3). Residuals of each of our joint fits are shown in Figures in the Appendix.

2.3 RESULTS

2.3.1 Modelling using simple phenomenological models

We first use phenomenological models to fit the individual spectra. Here the goal is to describe the data with a few parameters, as well as to capture any changes in the parameter values between epochs. First, we use a black body (BB) to model the spectra (zbbody with redshift z=0.14542). We find a best–fit with a total C-stat/d.o.f (degrees–of–freedom) = 2269/2162, fitting nine epochs together while letting all parameters vary freely. However, visual inspection of the fit and the residuals shows that the best-fit single BB model does not describe the spectra well around 2 keV in several epochs (Fig. 2.A(a)).

2.3 Results 21

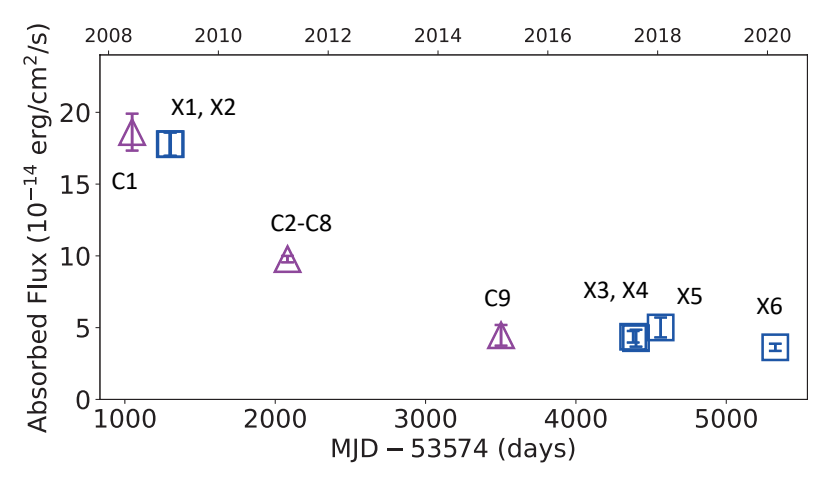


FIGURE 2.2: Long–term lightcurve of J150052 starting from 2008. The x-axis is in days since J150052's first detection on modified Julian date (MJD) 53574, with the corresponding calendar year denoted at the top of the figure. The y-axis denotes the observed flux (0.3–10 keV), including both the effects of intrinsic and Galactic absorption calculated using our two–BB fit. Blue squares are used for *XMM-Newton* observations and purple triangles for *Chandra* observations. J150052 has experienced a decade–long decay since its first detection on MJD 53574.

Instead, a fit function comprised of two BBs describes the data well (C-stat/d.o.f. = 2003/2154, Fig. 2.A(b)). The best-fit parameter values are given in Table 2.2. We then use the Akaike information criteria (AIC; Akaike 1974) to investigate the significance of adding a second BB model. From the one–BB model to the two–BB model, Δ AIC = 250 (with Δ AIC>5 and >10 considered a strong and very strong improvement, respectively, over the simpler model). Therefore, we conclude that adding a second BB improves the goodness of the fits significantly. We find that the source spectra of X1, X2, C1, and C2–C8, which we refer to as the "early epochs," can be well-described by two BBs, with an average temperature of 0.19 ± 0.01 keV and 0.48 ± 0.03 keV (e.g., Fig. 2.1(a)). On the other hand, the spectra obtained at epochs C9, X3, X4, X5, and X6, a.k.a. the "late epochs," are consistent with a single BB model with a lower average temperature of 0.15 ± 0.01 keV (e.g., Fig. 2.1(b)).

We find that $N_{H,i}$ and the BB normalisations, A_{zbbody_1} and A_{zbbody_2} , are consistent with being constant within their 3σ uncertainties: the best-fitted overall values are $0.14 \times 10^{22} \text{cm}^{-2}$, $3.83 \times 10^{-6} [10^{37} (1+z)^{-2} \text{erg/s/kpc}^2]$, and $7.2 \times 10^{-7} [10^{37} (1+z)^{-2} \text{erg/s/kpc}^2]$, respectively. Fig. 2.2 shows the observed flux of J150052 as a function of time. The observed flux values are attenuated by the effect of the intrinsic and the Galactic absorption based on our two–BB fit.

2.3.2 SLIM DISC MODELLING

Based on our spectral analyses using simple phenomenological models, we conclude that the shape of the continuum is changing throughout the decay of J150052 (from a two-BB shape to

Table 2.2: Best-fit parameters using the fit function TBabs*zTBabs*(zbbody+zbbody) to describe the source spectra. From top to bottom, epochs are listed in time sequence. The second zbbody model component is not necessary to obtain a good fit in C9, X3, X4, X5, X6. Therefore, it is omitted from the fit-function at these epochs.

Model Component		zTBabs	zbbodyl			C-stat/d.o.f	
Free parameter		$N_{H,i}$	kT	A_{zbbody_1}	kT	A_{zbbody_2}	
Unit		$10^{22}~{\rm cm}^{-2}$	keV	$10^{37}(1+z)^{-2}$ erg/s/kpc ²	keV	$10^{37}(1+z)^{-2}$ erg/s/kpc ²	
Early Epoch	C1	< 0.16	$0.21^{+0.03}_{-0.02}$	$5^{+2}_{-1} \times 10^{-6}$	0.47+0.09	$8^{+4}_{-3} \times 10^{-7}$	179/205
	X1	0.17+0.08	0.19 ± 0.03	$7^{+4}_{-2} \times 10^{-6}$	$0.41^{+0.14}_{-0.09}$	$10^{+10}_{-5}\times10^{-7}$	335/396
	X2	0.18+0.06 -0.05	0.18 ± 0.02	$8^{+3}_{-2} \times 10^{-6}$	$0.56^{+0.11}_{-0.09}$	$7\pm2\times10^{-7}$	401/392
	C2-C8	0.14 ± 0.04	0.19 ± 0.01	$30^{+7}_{-5} \times 10^{-7}$	0.48 ± 0.03	$7\pm1\times10^{-7}$	384/417
Late Epoch	C9	$0.14^{+0.09}_{-0.08}$	$0.14^{+0.02}_{-0.01}$	$3^{+3}_{-1} \times 10^{-6}$	-	-	85/63
	X3	0.11+0.07	$0.16^{+0.02}_{-0.01}$	$23^{+14}_{-7} \times 10^{-7}$	-	-	193/223
	X4	0.3+0.2	0.12 ± 0.02	$8^{+29}_{-5} \times 10^{-6}$	-	-	80/121
	X5	< 0.19	$0.17^{+0.02}_{-0.03}$	$19^{+22}_{-6} \times 10^{-7}$	-	-	106/115
	X6	0.15 ± 0.07	0.14 ± 0.01	$3^{+2}_{-1} \times 10^{-6}$	-	-	240/222

a single-BB shape). This behaviour might potentially be explained by the spectra at the early epochs being affected by additional spectral hardening from electron scattering and a temperature gradient in the disc atmosphere (Shimura & Takahara 1993, 1995). To constrain the TDE accretion disc parameters, as well as the mass and the spin of the black hole, we use the slim disc model (Wen et al. 2020, updated by Wen et al. 2021) to simultaneously fit the spectra at all epochs.

The slim disk model considers the stationary, relativistic "slim disc" accretion disc solutions and ray-traces the disc photons self-consistently to the observer's frame. The free parameters for the slim disc are the BH mass M_{\bullet} , the BH dimensionless spin a_{\bullet} , the disc accretion rate \dot{m} , the inclination θ , and the spectral hardening factor f_c (Shimura & Takahara 1993, 1995), which parameterises the spectral hardening due to electron scattering and temperature gradient in the disc atmosphere. The disc accretion rate \dot{m} is in units of the Eddington-limited accretion rate $\dot{m}_{\rm Edd}$. In the model we define $\dot{m}_{\rm Edd} = 1.37 \times 10^{21} \text{ kg s}^{-1} \times M_{\bullet}/10^6 M_{\odot}$ (Wen et al. 2020). Note that the actual \dot{M} in kg s⁻¹ units is not identical to the \dot{m} , and needs to be calculated after the BH mass is constrained. The model implements the astrophysical spin limit of a Kerr BH a_{\bullet} <0.998 (Thorne 1974). The f_c is expected to be >2, but saturates at ~ 2.4 , for near/super-Eddington accretion discs (Davis et al. 2006; Davis & El-Abd 2019). During the (simultaneous) fitting of the X-ray spectra, we let \dot{m} vary between epochs, while the value of M_{\bullet} , a_{\bullet} , and θ are free to vary but are required to have the same value at each epoch. Similarly f_c is treated as a single free parameter for all early epochs, while we keep it fixed to 2.2 for the late epochs. We make this latter choice because the late spectra are softer and have fewer counts, preventing us from constraining the spectral hardening effects that mainly impact the hard spectral tail (> 1.0 keV). As for $\{M_{\bullet}, a_{\bullet}\}$, we follow the approach of Wen et al. (2021) and search the $\{M_{\bullet}, a_{\bullet}\}$ parameter space by performing a joint fit and minimizing the C-stat at each $\{M_{\bullet}, a_{\bullet}\}\$ grid point. As a result, 2.3 Results 23

we fix $\{M_{\bullet}, a_{\bullet}\}$ to different values during each of the joint fits.

By jointly fitting the J150052 spectra at early and late times with the slim disc model, we obtain a minimum C-stat/d.o.f = 2183/2169 with M_{\bullet} = 1.5 × 10⁵ M_{\odot} and a_{\bullet} = 0.998 (Fig. 2.B). However, the slim disc model does not fit the early epochs above 2 keV well, as was also the case for the phenomenological models. Furthermore, the physical tension in this joint-fit is that f_c becomes larger than 4.0 during all the early epochs, instead of saturating around 2.4 as expected in the super-Eddington regime (Davis et al. 2006). We then test the slim disc model with f_c fixed to 2.4 during the early epochs while keeping it fixed to 2.2 at late times. We find a new minimum C-stat/d.o.f = 3980/2170 at M_{\bullet} = 0.5 × 10⁵ M_{\odot} and a_{\bullet} = 0.998. This fit is worse than the previous fit because now more hard photons above 2 keV are left un–fitted. Fig. 2.C shows the residual of this joint-fit. In both joint fits, the slim disc model describes the late epochs well but it has difficulties in describing the hard spectrum observed at early epochs, especially around and above 2 keV. This discrepancy is more prominent when we fixed f_c value to 2.4, as when f_c is allowed to float freely the slim disc fit tries to describe the high energy photons in the spectra by increasing the disc spectral hardening, thereby increasing the value of f_c (Shimura & Takahara 1995).

2.3.3 SLIM DISC+THERMAL COMPTONISATION

From our joint-fits with the slim disc model, we find that the early epochs of the J150052 spectra tend to be harder than a typical slim disc spectrum, which can not be solely explained by the disc spectral hardening factor f_c . Interestingly, this deviation from a slim disc spectrum becomes negligible at later epochs. We explore here if inverse–Comptonisation of the soft (slim disc) photons can help explain the spectral data above 2 keV.

As a starting point, we investigate the effect of Comptonization on the slim disc photons assuming a thermal distribution of energetic electrons. These electrons can originate in a disc wind, or if present, the base of a jet. We use the convolution model thcomp (Zdziarski et al. 2020) to self-consistently determine the up–scattered spectra from thermally-distributed electrons. The thcomp model parameterises the up–scattered spectra through the Thomson optical depth τ and the electron temperature kT_e parameters.

We fit the spectra of all epochs together and the inverse–Comptonisation component to the fit-function is only used to describe the spectra of the early epochs, as the late-epoch spectra can be well-described using a fit-function comprised of only the slim disc model (Fig. 2.C). The spectral hardening f_c in slim disc is free–to–vary between 1.0 and 2.4 during the early epochs. Following section 2.3.2, we fixed the f_c to a value of 2.2 at the late epochs. Based on the stand–alone, depreciated, Comptonisation nthComp model for thin disc accretion (Zdziarski et al. 1996; Życki et al. 1999), Lin et al. (2022a) infer the optical depth τ in the corona could be varying between early epochs. Therefore, here for the early epochs we fix the kT_e to be the same but let τ be free–to–vary between the early epochs. Finally, we fix the covering fraction of thcomp to unity during the early epochs, so that all seed photons are going through the Comptonising cloud.

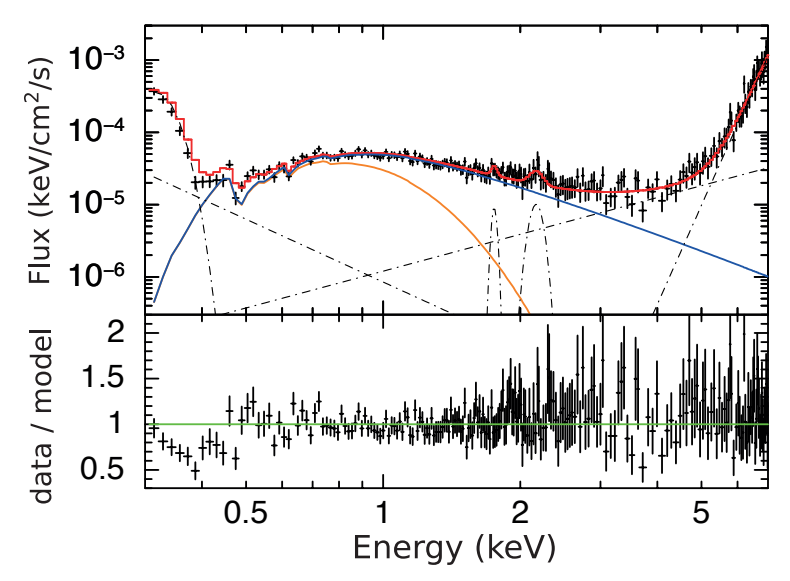


FIGURE 2.3: Unfolded source+background spectrum observed at Epoch C2–C8 with data/model residuals (the data points correspond to those shown in magenta in Fig. 2.D but here they are shown with a slightly different re-binning). The observed source+background spectrum is shown together with the best-fit slim disc model convolved with a thermal electron Comptonisation model. The format follows Fig. 2.1(a), except that here the orange line shows the slim disc continuum before Comptonisation and the blue line shows the total source continuum spectrum with the effect of scenario–dependent Comptonisation included. The slim disc+thermal Comptonisation model can describe the observed early epoch spectra of J150052 well.

We find a best fit at $M_{\bullet} = 2 \times 10^5 \, \mathrm{M_{\odot}}$ and $a_{\bullet} = 0.998$ for the thermal Comptonisation scenario. We find a total C-stat/d.o.f. = 2024/2164. Fig 2.4 shows the Δ C-stat contour in $\{M_{\bullet}, a_{\bullet}\}$ space. From the contour, we can constrain the mass of the BH in J150052 to be $2.0^{+1.0}_{-0.3} \times 10^5 \, \mathrm{M_{\odot}}$; the lower limit to the BH spin is constrained to be > 0.97 at the 1- σ 84.1% single–sided confidence level. The residuals and the parameter values of the best-fit are summarised in Fig. 2.D and Table 2.3.

Compared to the slim-disc-alone case when f_c is allowed to have a value larger than 2.4 (section 2.3.2), Δ AIC is 149 for the thermal Comptonisation scenario. In Fig. 2.3, we show the best-fit spectrum of C2–C8 (combined and treated as a single epoch), de-convolved from the detector response curve (i.e., the unfolded spectrum), illustrating the impact of the thermal Comptonisation on the disc continuum. From the residuals of this best-fit (Fig. 2.D) we can see that a slim disc+thermal Comptonisation model can describe the observed spectra during all J150052 early epochs well. The source intrinsic absorption $N_{H,i}$ is consistent with being constant in time (from C1 to X6) within 3σ errors. The best-fit overall value is $(0.28 \pm 0.01) \times 10^{22} \text{cm}^{-2}$, in agreement with the previous estimate of $N_{H,i} = (0.26 \pm 0.06) \times 10^{22} \text{cm}^{-2}$ based on the thin disc

2.4 Discussion 25

assumption (Lin et al. 2022a). Furthermore, compared to the test case when we tie all τ values, letting τ free–to–vary between early epochs improves the fit significantly (C-stat/d.o.f. from 2047/2167 to 2024/2164, Δ AIC= 17). While the uncertainties on the best-fit value for τ is such that no significant trend or changes in its value can be discerned (Table 2.3), the errors can be reduced if we perform the joint–fit with $N_{H,i}$ fixed to the best–fit value of $0.28 \times 10^{22} \text{cm}^{-2}$ and kT_e fixed to 2.3 keV. We will discuss the potential change of τ between epochs as well as the physical origin of the Comptonisation process in the next section.

Meanwhile, \dot{m} is estimated to decrease by roughly an order of magnitude over the period the spectra were obtained. In this scenario, the spectral hardening f_c at early epochs is constrained to be > 2.36, below the upper limit of 2.4. Compared to the slim-disc-only scenario (section 2.3.2), the best-fit f_c obtained at early epochs is more in line with theoretical expectations.

We also investigate if the $\{M_{\bullet}, a_{\bullet}\}$ constraints are sensitive to the value of $f_c = 2.2$ we used for the late-epoch spectral fits. Freeing the late-time f_c (but fixing it to be constant over the late epochs) results in a best-fit with a slightly higher $M_{\bullet} = 2.7 \times 10^5 M_{\odot}$ (Fig. 2.E), while the spin value is still consistent with the maximal spin. The late-time f_c is constrained to be > 2.27 (1σ error), at the best-fitted $\{M_{\bullet}, a_{\bullet}\}$ grid-point. However, by varying the late-time f_c , the constrained 1σ error range is not changed essentially for either M_{\bullet} or a_{\bullet} , and Δ AIC= 0 (C-stat/d.o.f. = 2023/2163). Therefore, we conclude that our choice of $f_c = 2.2$ for the late-epoch spectra did not influence the constraints on either M_{\bullet} or a_{\bullet} significantly.

2.4 Discussion

2.4.1 IMPLICATIONS OF IMBH MASS AND SPIN

Fitting the XMM-Newton and Chandra X-ray spectra using a slim disc model supplemented by a thermal Comptonisation model to account for the presence of a second, harder spectral component at observing epochs between 2008–2014, we constrain the mass and spin of the BH in J150052 to be $M_{\bullet} = 2.0^{+1.0}_{-0.3} \times 10^5 M_{\odot}$ and $a_{\bullet} > 0.97$. The mass uncertainties are given at the 68% confidence level (1σ single parameter), and the limit on the spin is at the 84.1% confidence level (single–sided 1σ single parameter). By modelling all the late–epoch spectra with a physical model for thin disc+corona accretion optxagnf (assuming the inclination $\theta = 60^{\circ}$; Done et al. 2012), Lin et al. (2022a) estimate the mass of J150052 to be a few $\times 10^5 M_{\odot}$. Our measurements are consistent with this previous mass estimate, though our best–fit does not include a powerlaw component (as the non–thermal Comptonisation in the corona considered by optxagnf) for the late–epoch spectra. Furthermore, Lin et al. (2022a) find the estimated mass and spin are degenerate and the BH mass would be $\approx 7.6 \times 10^5 M_{\odot}$ if $a_{\bullet} = 0.998$, but we find a smaller BH mass and here we do not see the mass–spin degeneracy (Fig. 2.4).

To directly compare our results to the estimates from the thin disc+corona scenario, we try to jointly fit only the spectra at late epochs with the slim disc model. Through this fit, we also test if our mass and spin constraints are driven mainly by the late–time data. We find that using only the

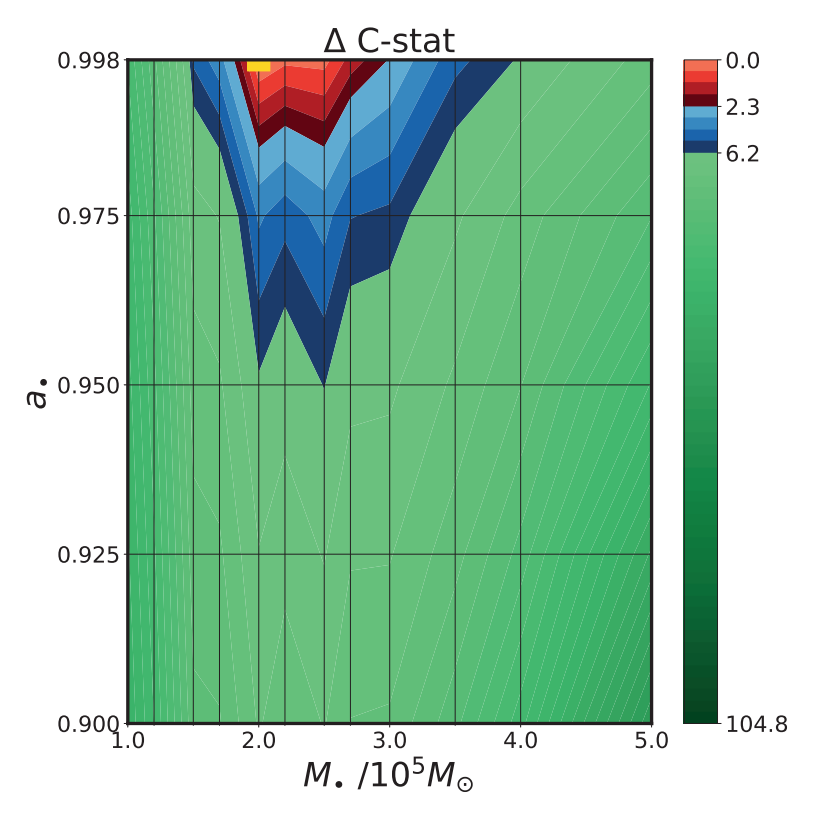


FIGURE 2.4: Constraints on M_{\bullet} and a_{\bullet} from the slim disc+thermal Comptonisation model-fit to all the observed X-ray spectra. We calculate the ΔC -stat across a model grid in the $\{M_{\bullet}, a_{\bullet}\}$ plane (grid points are indicated by vertices of the black lines) and then fill in the colour contours by linear interpolation. The best-fit point with the lowest C-stat is marked by a yellow square. Areas within 1σ and 2σ are filled by red and blue colours, respectively. M_{\bullet} and a_{\bullet} are constrained to be $2.0^{+1.0}_{-0.3} \times 10^5 \ {\rm M}_{\odot}$ and > 0.97, respectively.

2.4 Discussion 27

Table 2.3: Best-fit parameters for the fit function comprised of the slim disc model convolved by a thermal Comptonisation model. The fit function for the source model as used in XSPEC is given below, followed by the best-fit $\{M_{\bullet}, a_{\bullet}\}$, the constraint on the source inclination, the C-stat/d.o.f. from the joint-fit to all the spectra, and other epoch-dependent parameter values. Values fixed during the fit are given in between brackets. The accretion rate \dot{m} is in the unit of the Eddington-limited accretion rate $\dot{m}_{\rm Edd} = 1.37 \times 10^{21} \text{ kg s}^{-1} (M_{\bullet}/10^6 M_{\odot})$. Note that the actual \dot{M} in kg s⁻¹ units is not identical to the \dot{m} , and needs to be calculated (see section 2.3.2). The f_c is the spectral hardening parameter. For the thermal Comptonisation model, the Thomson optical depth τ parameter and the electron temperature kT_e are given, while the covering fraction of theomp is fixed to unity during the early epoch spectra.

TBabs*zTBabs*thcomp*slimdisc $M_{\bullet} = 2 \times 10^5 \text{ M}_{\odot}, a_{\bullet} = 0.998: \theta < 19^{\circ}$ C-stat/d.o.f. = 2024/2164

	Time since MJD 53574	Epoch	zTBabs	thcomp		slimdisc		C-stat/data bins
	Days	(in time sequence)	$N_{H,i} (10^{22} cm^{-2})$	τ	kT_e (keV)	$\dot{m} \; (\dot{m}_{\rm Edd})$	f_c	
Early Epoch	1048	C1	0.25+0.05	4 ± 2	2.3+2.7	8 ⁺²⁸ ₋₄	> 2.36	180/210
	1299	X1	0.31+0.01	4 ± 2	=C1	> 27	=C1	339/401
	1305	X2	$0.30^{+0.01}_{-0.03}$	4 ± 2	=C1	> 7.8	=C1	412/397
	2080	C2-C8	0.23+0.02	5 ± 2	=C1	1.0 ± 0.1	=C1	386/422
Late Epoch	3502	C9	$0.24^{+0.03}_{-0.03}$	-	-	$1.6^{+0.3}_{-0.2}$	(2.2)	85/66
	4381	X3	$0.27^{+0.02}_{-0.02}$	-	-	$1.9^{+0.4}_{-0.3}$	=C9	194/226
	4400	X4	$0.24^{+0.03}_{-0.03}$	-	-	$1.5^{+0.5}_{-0.3}$	=C9	80/124
	4564	X5	$0.28^{+0.04}_{-0.04}$	-	-	$2.6^{+1.5}_{-0.7}$	=C9	108/118
	5326	X6	$0.24^{+0.02}_{-0.02}$	-	-	$1.2^{+0.2}_{-0.1}$	=C9	241/225

data from late epochs will not change the best-fit $\{M_{\bullet}, a_{\bullet}\}$ values, and they are insensitive to the inclination given the data quality (θ is constrained to be < 66°). Meanwhile, the 1 σ uncertainty regions for the BH mass and spin increase. We find there is a mass-spin degeneracy similar to that found by Lin et al. (2022a) through their thin disc modelling (a higher mass corresponds to a higher spin; Fig. 2.F). We conclude that, while modelling late-time TDE spectra alone can constrain the mass and the spin well, we need the consistent modelling of both early- and late-epoch spectra to break the mass-spin degeneracy and minimise uncertainties. This conclusion is in line with the results of Wen et al. (2022): they find the mass-spin degeneracy of the slim disc solution can be broken when one or more epochs of data obtained when the accretion rate is well above the Eddington-limit are included in the fit.

Despite recovering the mass–spin degeneracy, our joint–fit of only the late–epoch spectra (Fig. 2.F) still suggests a BH mass lower than $7.6 \times 10^5~M_{\odot}$. To check this, we simulate the X-ray spectrum using the best–fit slim disc model from fitting only the late–epoch spectra. For a thin disc² to fit the simulated spectrum, we find either the spin needs to decrease (~ 0.6) or the mass needs to increase ($\sim 8 \times 10^5~M_{\odot}$). This degeneracy appears to be similar to that found by Lin

²In practice, an optxagnf model with the corona switched off ($r_{cor} = 0$ in optxagnf).

et al. (2022a) when they fit late–epoch spectra using optxagnf that has an additional powerlaw component. Meanwhile, we find the thermal disc emission in optxagnf from Lin et al. (2022a) is similar to our best–fit slim disc model (Fig. 2.G). Thus, we conclude the difference in the mass constraints is mainly due to the degeneracy between the thin– and the slim– disc model, while whether the high–energy end of the spectra is modelled by the powerlaw or not has little impact on the disc constraints. As another test, we can fit the data with the slim disc model while forcing the $N_{H,i} = 0.26 \times 10^{22} \text{cm}^{-2}$, $M_{\bullet} = 8 \times 10^5 M_{\odot}$, $\theta = 60^{\circ}$, and $a_{\bullet} = 0.998$ (similar to the best–fit optxagnf disc parameters in Lin et al. 2022a). We find the slim disc of such settings fails to fit the spectra (Fig. 2.G), and when adding a powerlaw the best–fit is still significantly worse (C-stat/d.o.f. = 761/748) than the one in Fig. 2.F. Our tests show the difference between a thin disc and a slim disc can not be neglect when estimating the BH mass from TDE spectra at Eddington accretion rates.

The slim disc model that we use to constrain the BH mass and spin assumes a relativistic, stationary slim disc accretion disc (Abramowicz et al. 1988; Sądowski 2009; Sądowski et al. 2011). An important assumption in our modelling is that the accretion disc should be aligned with the spinning BH equatorial plane. The angular momentum vector of the orbit of the star that has been disrupted is likely to be inclined with respect to the black hole spin vector, possibly resulting in a tilted accretion disc after the disruption.

The time it takes for a tilted disc to be aligned into the equatorial plane is likely much faster than 10^2 days, for a $M_{\bullet} \sim 10^5 \ M_{\odot}$ and a very high spin value due to a combination of the Bardeen-Petterson effect (Stone & Loeb 2012) and internal torques (which is the dominant mechanism in the case of a fast–spinning BH; Franchini et al. 2016). Because J150052 was first detected in 2006, three years before the observational epoch we labelled as C1, the disc responsible for the X-ray emission is likely to have both circularized (Lin et al. 2017b) and aligned itself with the BH equatorial plane by epoch C1. Thus our assumption about a slim disk aligned with the BH spin is reasonable.

The only other spin measurement of an IMBH candidate is for the TDE 3XMM J215022.4-055108 (J2150), where people also find a high spin of $a_{\bullet} \gtrsim 0.7$ (e.g., Wen et al. 2021). It is not surprising to find IMBH candidates in X-ray selected TDEs. Theory predicts that the rate of TDEs will be dominated by the smallest BH mass range with a high occupation fraction in a dense stellar environment (Wang & Merritt 2004; Stone & Metzger 2016) and that, conversely, it will be suppressed for BH masses $M_{\bullet} \gtrsim 10^{7.5} M_{\odot}$ (e.g., Kesden 2012; Stone & Metzger 2016). Because smaller BH masses and higher spin parameters produce brighter soft X-ray emission, (flux-limited) X-ray selected TDE samples will be biased towards this parameter combination (Jonker et al. 2020; Mummery 2021).

The mass and spin measurements of J150052 (and J2150) can shed light on how IMBHs form. Furthermore, an IMBH is likely a key phase in the growth of SMBHs. So far, three major classes of theories for the formation of an IMBH have been proposed: runaway collisions of main–sequence stars, which subsequently collapse due to a general relativistic instability (producing IMBH seeds of $M_{\bullet} \sim 10^3 - 10^4 M_{\odot}$; e.g., Zwart & McMillan 2002); the growth of a seed stellar–mass BH

2.4 Discussion 29

 $(M_{\bullet} < 10^2 \ M_{\odot})$ through the accretion of gas (e.g., Madau & Rees 2001; Greif et al. 2011); and the direct collapse of pristine gas clouds in the early Universe (e.g., Loeb & Rasio 1994; Bromm & Loeb 2003; Lodato & Natarajan 2006). Theoretical arguments suggest that only the direct collapse channel is able to produce a BH of $M_{\bullet} \sim 10^5 \ M_{\odot}$ at its birth (Inayoshi et al. 2020), but the resulting spin is highly uncertain. We note that if the collapsing cloud goes through a supermassive stellar (SMS) phase before collapsing into a BH, a fast–spinning SMS is found from simulations. The collapse of this SMS might result in a BH with a high $(a_{\bullet} \sim 0.9)$ or even extremal $(a_{\bullet} > 0.99)$ spin (e.g., Reisswig et al. 2013; Inayoshi et al. 2014).

Besides the possibility that J150052 formed at $\sim 10^5~M_\odot$ with a high spin, the BH could have started at much lower mass. In that case, it must have gained its last e-fold in mass through a subsequent accretion episode, with the final IMBH spin depending heavily on how the accretion took place. If this accretion proceeds through so–called chaotic accretion episodes, where the angular momentum vectors of the infalling gas clouds are oriented randomly with respect to the BH spin vector, then the IMBH is likely to be spun–down (e.g., Shibata & Shapiro 2002; King et al. 2008) and not end up with J150052's fast spin. The spin–down effect also applies to the accretion from preceding TDEs of stars on random/isotropic orbits (Metzger & Stone 2016). Therefore, our measurements imply that, if J150052 formed at a much lower mass, the seed BH grew to its current mass in accretion episodes where the angular momentum vector of the accreted material was aligned with that of the BH spin.

2.4.2 Origin of the Comptonisation component

Our analysis using phenomenological models implies that the spectral continuum of J150052 at early epochs can be well approximated by two BB models of different temperatures. Interestingly, several other systems likely to be accreting at a super-Eddington rate have a similar spectral shape (e.g., Pinto et al. 2017, 2021 for ULXs; Kara et al. 2018 for a TDE). In this paper, we find that the early–epoch spectra of J150052 can not be well-fit by only the slim disc model. Instead, when the slim disc emission is subsequently altered by the effects of inverse-Comptonisation, the spectra at early epochs can be fitted well.

We compare our spectral fit results with those derived for ULXs to investigate if a similar corona can help explain the similarity in the spectral shape and its evolution among super–Eddington accreting sources. To explain the observed spectral shape in ULXs, it is assumed that, in super–Eddington accreting BH-XRB systems, a "warm" ($kT_e \sim 1 \text{ keV}$), optically thick ($\tau \gtrsim 10$) region of high–energy electrons with a thermal distribution causes inverse Compton scattering of the thermal photons from the disc (e.g., Magdziarz et al. 1998; Gladstone et al. 2009; Done et al. 2012). This region, i.e., the corona, could be supplied by the disc atmosphere (e.g., Kubota & Done 2019), and it differs from that of a typical, hot ($kT_e \sim 100 \text{ keV}$), optically thin ($\tau <<1$) corona that is usually invoked to be responsible for the power-law continuum in XRBs at low-hard states (e.g., Belloni 2010) and in AGNs. Our results on J150052 for the thermal Comptonisation scenario show that the corona is similar to a ULX "warm" corona, and our constraint on the

 kT_e is consistent with that derived from using the nthcomp model ($kT_e = 1.0^{+2.5}_{-0.3}$ keV; Lin et al. 2022a). The current uncertainties in the constraints of τ (Table 2.3) are largely due to the degeneracies between model parameters. When we re-fit all the spectra jointly with $N_{H,i}$ fixed to the best-fit value of $0.28 \times 10^{22} \text{cm}^{-2}$ and also kT_e fixed to 2.3 keV, the goodness-of-fit is C-stat/d.o.f. = 2047/2174 while $\Delta AIC = -3$ compared to the fit presented in Table 2.3; the τ is better constrained at each epoch: 4.4 ± 0.2 (C1), 4.6 ± 0.2 (X1), 4.4 ± 0.2 (X2), and 4.9 ± 0.1 (C2–C8). The optical depth increases at C2–C8, which is in agreement with found from the results in Lin et al. 2022a.

Analytical studies show that an optically thick, "warm" corona might not emit a fully—thermalised spectrum (e.g. Różańska et al. 2015). We can test the impact of the non-thermal Comptonisation effect on our $\{M_{\bullet}, a_{\bullet}\}$ constraints by replacing the thermal Comptonisation model thcomp with an empirical, very simple, Comptonisation model simpl (Steiner et al. 2009). The model simpl mimics the up-scattered continuum by a power-law without assuming a specific energy distribution of the electrons. In this manner, we can see how the $\{M_{\bullet}, a_{\bullet}\}$ constraints change if we do not assume a pure, thermal distribution of the coronal electrons. We find that, for this test scenario, the best-fit $\{M_{\bullet}, a_{\bullet}\}$ values are the same as those from the thermal scenario, with a best-fit C-stat/d.o.f. = 2020/2164 (Δ AIC = 4 compared to the thermal scenario). The $\{M_{\bullet}, a_{\bullet}\}$ constraints are not sensitive to whether the inverse-Comptonisation is done by electrons that have a thermal distribution (Fig. 2.H).

In addition to the Comptonisation scenarios, we test whether there could be any disc outflow emission/absorption that can explain the spectral shape observed at early epochs. A disc outflow is seen in simulations of sources at high/super–Eddington accretion rates (e.g., Ohsuga & Mineshige 2011; Takeuchi et al. 2013; Kitaki et al. 2021) and supported by observations (e.g., Middleton et al. 2013; Pinto et al. 2016; Kara et al. 2018; Pinto et al. 2021). However, there are no high-resolution spectral data of J150052 (e.g., from *XMM-Newton RGS*) with sufficient signal-to-noise ratio to confirm a disc outflow from emission and/or absorption lines. Furthermore, using the atomic library XSTAR in xspec (Kallman & Bautista 2001) to model the wind contribution (absorption/emission) to the continuum does not yield a good fit³.

It is still possible that an outflow is present in J150052 and that it might contribute to the aforementioned inverse–Comptonisation process. In this case, not detecting a direct outflow signature could either be due to the lack of high-resolution X-ray spectra or to observing the disc at a low inclination angle ($\theta \lesssim 30^{\circ}$). The low inclination angle could imply that not much of the wind outflow is along the line–of–sight (Pinto et al. 2017; Dai et al. 2018). Alternatively, the outflow velocity could be high, which, when combined with a low equivalent width of the line features, would lead to broadened lines that are difficult to detect. If such a wind were present, we can roughly estimate the associated mass loss. Based on the simulations of Takeuchi et al.

³The XSTAR model is constructed following Middleton et al. 2013. We assume a clump particle density of 10^{13} cm⁻³ and an input ionizing spectrum of a black body with a temperature kT of 0.28 keV and a luminosity of 1×10^{43} erg/s. We then construct an XSTAR grid, stepping between a $\log(\xi)$ of 3 and 5 in 10 linear steps and a column density of 1×10^{20} and 1×10^{23} in 20 logarithmic steps.

2.4 Discussion 31

(2013), we expect wind clump sizes of $\sim 10~R_g$. Using the τ and kT_e constrained by our thermal Comptonisation models, we estimate a yearly mass loss of $\sim 2 \times 10^{-3}~M_{\odot}$, assuming that the wind velocity equals the escape velocity at $10~R_g$.

2.4.3 Transition from super- to sub-Eddington accretion

Fig. 2.5 shows the change of the source luminosity and the slim disc accretion rate \dot{M} over time based on our best-fit slim disc+thermal Comptonisation model, assuming a distance of ~690 Mpc (Lin et al. 2017b). Note that the actual \dot{M} in kg s⁻¹ units is not identical to the \dot{m} parameter (in $\dot{m}_{\rm Edd}$ units) in the model, and needs to be calculated ($\dot{M} = \dot{m} \cdot \dot{m}_{\rm Edd}$; see Section 2.3.2). We use the upper–case \dot{M} to distinguish from the \dot{m} .

During the long-term decay of J150052, \dot{M} decreases from $\sim 10~\dot{M}_{\rm Edd}$ to $\lesssim 1~\dot{M}_{\rm Edd}$ (here $\dot{M}_{\rm Edd}=16L_{\rm Edd}/c^2$ for consistency with Sądowski et al. 2011; Abramowicz & Fragile 2013). The decrease in \dot{M} might lead to a decreased amount of the inverse–Comptonisation if fewer high-energy electrons are generated at lower mass accretion rates (e.g., if the wind becomes less powerful as the mass accretion rate decreases below the Eddington limit). Therefore, it is possible that, as \dot{M} decreases, the source spectrum can be well described by the slim disc model without the thermal Comptonisation component. The previous studies by Lin et al. (2017b, 2022a) already showed that the spectra at late epochs are different from the spectra preceding C9, and they proposed that the spectral evolution is caused by the transition from a super–Eddington to a sub–Eddington accretion rate. Our results are in agreement with this suggestion.

Spectral analyses of other TDEs indicate that TDEs might undergo a spectral transition during the decay (e.g., Bade et al. 1996; Komossa et al. 2004; Wevers et al. 2019a; Jonker et al. 2020; Wevers et al. 2021). Several TDEs appear to transition from a soft, disc-dominated state to a hard, non-thermal state, where the X-ray spectrum is characterised by a power-law. Interestingly, in J150052, we find evidence for a spectral state transition analogous to a transition from the ultra-luminous state of BH-XRBs (e.g., Gladstone et al. 2009; Motta et al. 2012; Sutton et al. 2013) to the soft state. If the mass accretion rate in J150052 continues to decrease, we predict that the spectrum will exhibit a Comptonised component again when the BH transitions from the soft to the hard state, in analogy to the soft-to-hard state transition in BH-XRBs.

2.4.4 Constraining ultralight boson masses

Following the procedure described in Wen et al. (2021), we derive constraints on the mass of hypothetical ultralight bosons based on our spin and mass measurements of J150052. As mentioned in §2.1, a BH will only spin down efficiently when bosons of mass m exist such that $\frac{GM_sm}{c\hbar} \sim 1$ (here \hbar is the reduced Planck constant; Bardeen et al. 1972; Press & Teukolsky 1972). For $\frac{GM_sm}{c\hbar}$ values away from 1, the timescale τ_I for growing the instability increases exponentially. We compute τ_I as a function of m to investigate the ultralight boson constraints that can be imposed from J150052.

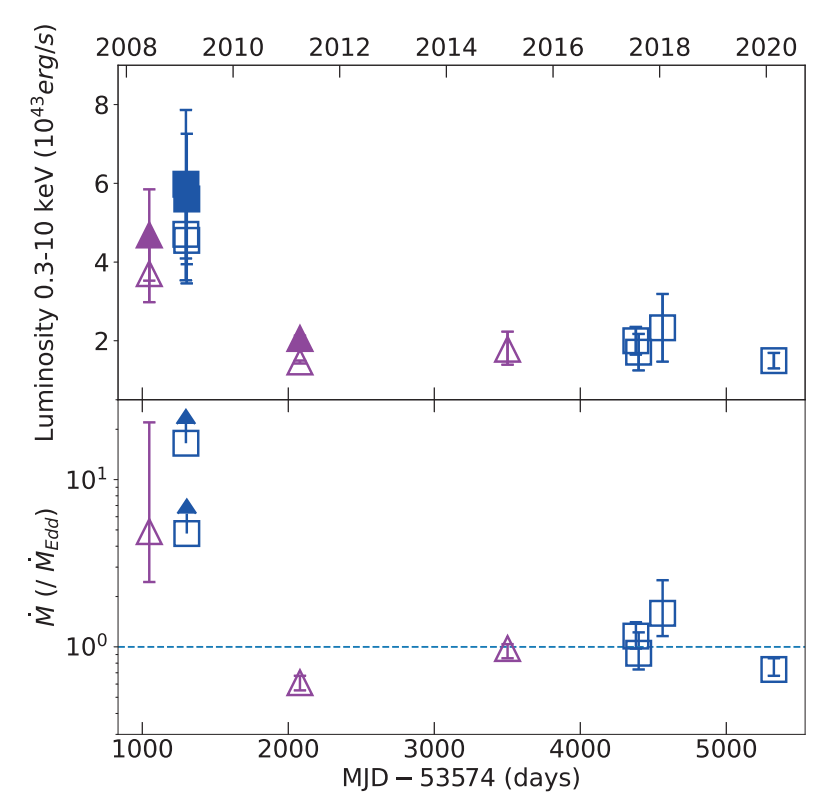


FIGURE 2.5: *Upper panel*: Lightcurve of J150052 starting from 2008, constructed from the joint-fits of the slim disc+thermal Comptonisation scenario. The format follows Fig. 2.2. The open symbols show the slim disc luminosity, and the filled symbols at early epochs show the total (slim disc+Comptonisation) luminosity. The lightcurve is corrected for both the effects of intrinsic and Galactic absorption. We show the statistical uncertainty on each luminosity at the 1σ (68%) confidence level. These uncertainties are calculated by varying the normalisation of the source fit function and are likely to underestimate those determined when all parameters are allowed to vary. However, the latter is computationally unfeasible in this case. *Bottom panels*: Accretion rate \dot{M} derived from the slim disc+thermal Comptonisation model, in units of the Eddington accretion rate $\dot{M}_{\rm Edd} = 16L_{\rm Edd}/c^2$ (for consistency with Sądowski et al. 2011; Abramowicz & Fragile 2013). Note that due to this different definition of the Eddington accretion rate from the $\dot{m}_{\rm Edd}$ in the slim disc model, the actual \dot{M} in $\dot{M}_{\rm Edd}$ units is not identical to the \dot{m} parameter (in $\dot{m}_{\rm Edd}$ units) in the model, and needs to be calculated (see section 2.3.2). We use the upper-case \dot{M} and lower-case \dot{m} to distinguish them. The Eddington rate $\dot{M} = \dot{M}_{\rm Edd}$ is shown by a dashed horizontal line.

2.5 Conclusions 33

Fig. 2.6 shows the excluded particle masses (green coloured regions) derived from our mass and spin measurements of J150052. The black hole instability time on the x-axis is calculated using eqs. 2.13 and 2.18 of Cardoso et al. 2018, taking our best-fit values for M_{\bullet} and a_{\bullet} . We also show the constraints derived from other accreting BHs with spin measurements: Cygnus X-1 ($M_{\bullet} = 21.2 \ M_{\odot}$, $a_{\bullet} = 0.998$; Miller-Jones et al. 2021, Zhao et al. 2021), NGC 4051 ($M_{\bullet} = 1.91 \times 10^6 \ M_{\odot}$, $a_{\bullet} = 0.99$; Denney et al. 2009, Patrick et al. 2012), and 3XMM J215022.4-055108 (J2150; $M_{\bullet} = 1.75^{+0.45}_{-0.05} \times 10^4 \ M_{\odot}$ and $a_{\bullet} = 0.80^{+0.12}_{-0.02}$; Wen et al. 2021).

The stellar-mass BH Cygnus X-1 (cyan regions) excludes massive vector (e.g., dark photons) and scalar fields (e.g., axion-like particles) with $m \sim 10^{-12}$ eV, whereas the supermassive BH NGC 4051 (yellow) excludes those particles at $m \sim 10^{-17}$ eV. Compared to J2150 (red), which excludes the $m \sim 10^{-15}$ eV region, J150052 excludes a new region, $m \sim 10^{-16}$ eV, for both kinds of particles. For each $\{M_{\bullet}, a_{\bullet}\}$ pair measurement, we are able to exclude roughly one to two orders of magnitude in ultralight boson mass across large $\tau_{\rm I}$ range.

As seen in Fig 2.6, the range of excluded ultralight boson masses increases with τ_1 . If we further assume Eddington–limited accretion for BHs, it is possible to use timescale arguments to restrict τ_1 to $\gtrsim 10^7$ yr, given the high spins of these BHs, and thereby focus on the wider particle mass exclusion ranges on the right in Fig. 2.6. The dashed vertical line in Fig. 2.6 shows the Salpeter timescale of $\sim 3 \times 10^7$ yr required to spin up a BH from $a_{\bullet} = 0$ to 1 (Salpeter 1964). As this is the timescale for a BH to gain an e-fold in mass growth when accreting at the Eddington–limit, it is the shortest timescale over which significant astrophysical spin–up will occur. If the instability timescale is shorter than this spin–up timescale, the BH will never reach a high spin. Therefore, J150052's high spin and those of the other plotted BHs rule out the short instability timescales to the left of the vertical line, unless super–Eddington accretion is dominating the mass growth.

2.5 Conclusions

In this paper, we present and analyse all the publicly available *XMM-Newton* and *Chandra* data of the tidal disruption event J150052 since 2008, obtained during its decade—long decay. We fit the X-ray spectra with the slim disc model (Wen et al. 2020, 2021), thereby constraining the black hole mass and spin to a higher precision than previously possible. We have examined the implications of these measurements for the existence of IMBHs and their growth, for the masses of hypothetical ultralight bosons, and for the origin of the observed coronal emission and its evolution. This analysis is only the second of its kind for an IMBH TDE candidate. Our conclusions are:

• The BH mass is $\approx 2 \times 10^5 \text{ M}_{\odot}$. More precisely, if the coronal emission at early epochs arises from thermal Comptonisation, we obtain $M_{\bullet} = 2.0^{+1.0}_{-0.3} \times 10^5 M_{\odot}$. Here the errors are at the 68% confidence level. The strong mass constraint demonstrates the potential of

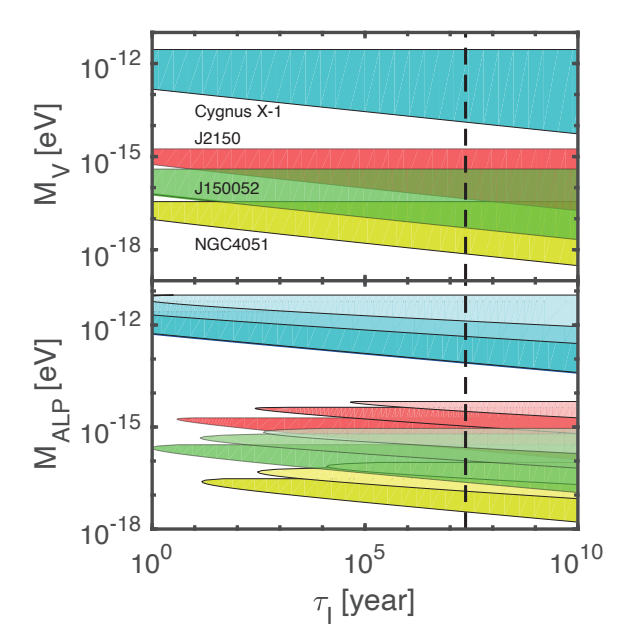


FIGURE 2.6: Exclusion ranges for the masses of hypothetical ultralight bosons, including both Proca vector bosons (mass M_V ; top panel) and scalar axion-like particles (mass M_{ALP} ; bottom panel), as a function of the BH instability timescale τ_I . The format follows Fig. 5 in Wen et al. (2021), who derive the exclusion regions from the BH mass and spin measurements of 3XMM J215022.4-055108 (J2150; red contours). We add the exclusion regions derived from our J150052 measurements (green). The contours denote the excluded masses for a given $\{M_{\bullet}, a_{\bullet}\}$ pair and τ_I (Wen et al. 2021). The cyan and yellow contours are the constraints from the stellar BH system Cygnus X-1 and the supermassive BH system NGC 4051, respectively. The dark, light, and lighter contours in the lower panel denote the cases of low-order instability modes (mode–number m = 1, 2 and 3, respectively). The dashed vertical line indicates the timescale ($\sim 3 \times 10^7 \text{ yr}$) for a BH with $a_{\bullet} = 0$ to undergo an Eddington-limited e-fold in mass growth, which is the shortest timescale over which significant astrophysical spin-up will occur under the Eddington-limit (the Salpeter timescale; Salpeter 1964). If the instability timescale is shorter than this spin-up timescale, the BH will never reach a high spin. Thus, unless super-Eddington accretion is dominating the mass growth, our discovery of J150052's rapid spin rules out the short instability timescales to the left side of the vertical line and allows the wider range of excluded particle masses to the right.

2.5 Conclusions 35

using X-ray TDEs to search for IMBHs and is consistent with the previous estimate of a few $\times 10^5 M_{\odot}$ based on the optxagnf model (Lin et al. 2022a).

- The lower limit on the BH spin is > 0.97 at the 1σ 84.1% single–sided confidence level for the slim disc+thermal Comptonisation models. Thus, J150052 is a fast spinning, perhaps near–extremal, IMBH. We discuss different IMBH formation channels; our mass and spin measurements imply that, if J150052 did not form near its current mass ($\sim 10^5~M_{\odot}$), then it must have accreted up to its current mass in episodes where the angular momentum vectors of the spin and accreted material were aligned.
- Our mass and spin measurements of J150052 rule out both vector bosons and axions of
 masses ~ 10⁻¹⁶ eV. Vector bosons and axion-like particles are of astrophysical interest as
 particle dark matter candidates. We show here that, for the mass and spin pair measurement
 of J150052, the masses of such ultralight bosons can be significantly constrained.
- Our spectral analyses suggest that J150052 undergoes a transition during its decay, quenching the corona while the mass accretion rate decreases from super–Eddington to \approx Eddington levels. The spectral changes are reminiscent of the state transitions in Galactic ultra–luminous X-ray sources. We discuss the origin of the corona. From the spectral constraints of the Compton component, we infer the corona of J150052 to be optically thick and warm $(kT_e = 2.3^{+2.7}_{-0.8} \text{ keV})$.

By constraining the mass and the spin of J150052, we have demonstrated the potential of using the X–ray spectra of TDEs to find IMBHs and measure their masses and spins. Similar analyses of large samples of TDEs with suitable early and/or multi–epoch X–ray observations will ultimately constrain the distributions of BH masses and spins, leading to a better understanding of the formation and evolution of both IMBHs and SMBHs. While such analyses are beyond the scope of this paper, we plan to carry them out in future work.

ACKNOWLEDGEMENTS

We thank the anonymous referee for insightful comments. AIZ and SW thank the UA Department of Astronomy and Steward Observatory for support. AIZ acknowledges additional funding from NASA ADAP grant #80NSSC21K0988. This work used the Dutch national e-infrastructure with the support of the SURF Cooperative using grant no. EINF-1077.

2.6 APPENDIX

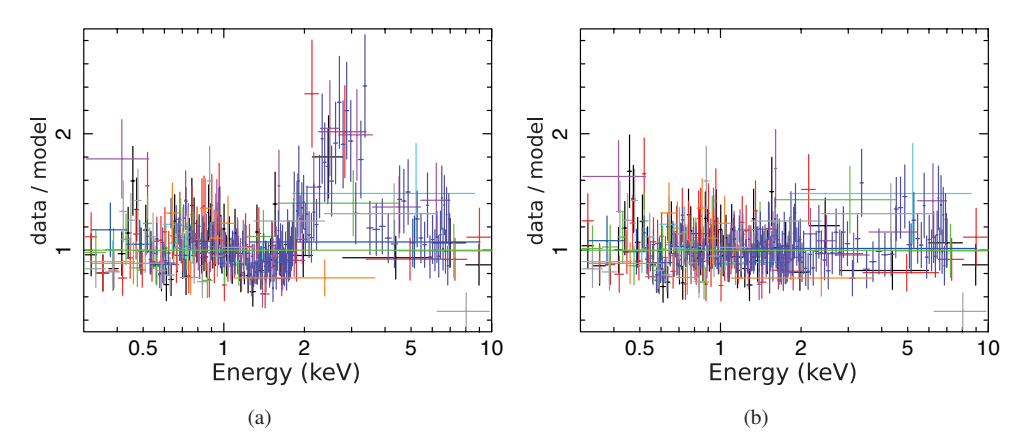


FIGURE 2.A: Data/model ratio for the spectral fits of each epochs. The source fit function is comprised of **a**) a single BB, or **b**) two BBs. The source+background data at C1, X1, X2, C2–C8, C9, X3, X4, X5, and X6 (in time sequence), are shown in magenta, black, red, purple, orange, green, blue, cyan, and grey, respectively. The background dominates above 3 keV in all epochs. We can see that a single–BB model does not describe the spectra well around 2 keV in several early epochs.

2.6 Appendix 37

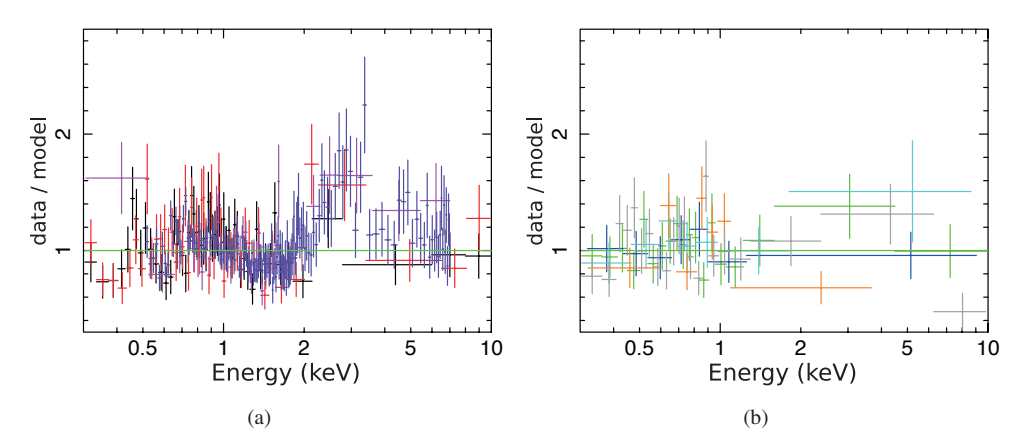


FIGURE 2.B: Data/model ratio of the joint-fit of J150052 spectra at $\bf a$) early epochs and $\bf b$) late epochs, using a fit function TBabs*s1imdisc to describe the source spectra. The colours represent the same as those in Fig. 2.A. During the fit, we let the spectral hardening factor f_c free to vary during the early epochs while we fix it to 2.2 during the late epochs. The best-fit f_c during the early epochs is found to be larger than 4.0, whereas in theory f_c should have a maximum value of around 2.4 in the super-Eddington regime (Davis et al. 2006). Still, strong residuals between 2–3 keV are present.

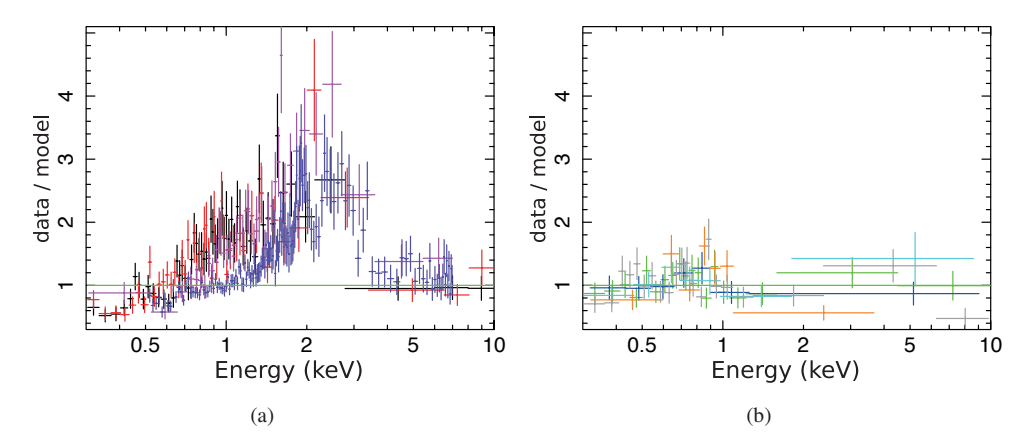


FIGURE 2.C: The same as Fig. 2.B but with the f_c parameter fixed to 2.4 for the early epochs and to 2.2 for the late epochs. The excess around 2 keV at early epochs is more prominent than the fit where f_c is left to float freely, showing that the slim disc model can not account for all the hard photons detected at early epochs.

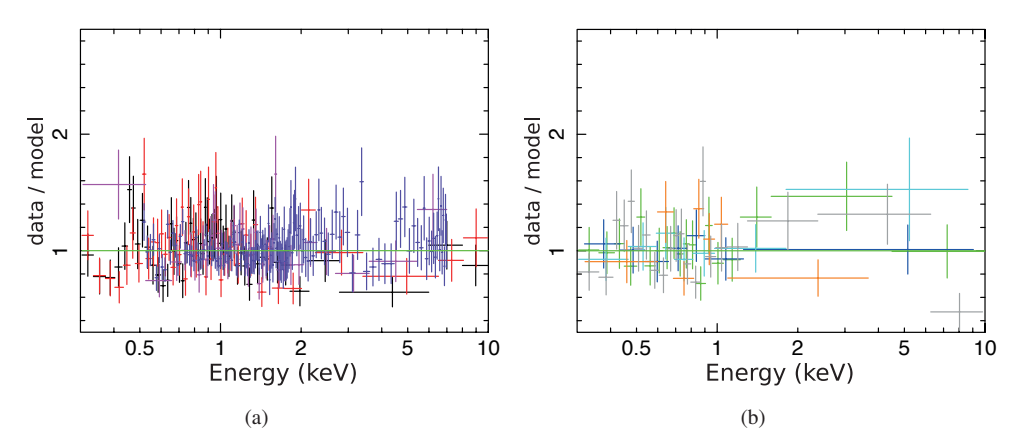


FIGURE 2.D: Data/model ratio for the joint-fit of the J150052 spectra for the thermal Comptonisation scenario, at **a**) early epochs and **b**) late epochs. The colour scheme follows that of Fig. 2.B. Compared to the slim-disc-alone scenario (Fig. 2.C), adding a Comptonisation component explains the excess flux present in the spectra, particularly around 2 keV at early epochs. During the joint fits we switch off the Comptonisation in the spectra at the late epochs, as those spectra are consistent with the slim disc spectra.

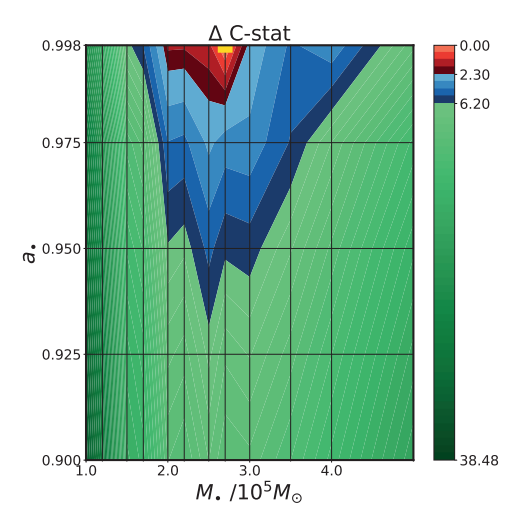


FIGURE 2.E: Same as Fig. 2.4 but with f_c parameter free-to-vary between 1 and 2.4 for late epoch spectra. The best-fit grid-point moves to a higher value of M_{\bullet} =2.7 × 10⁵ compared to Fig. 2.4 but the constrained 1 σ error range is not changed essentially for either M_{\bullet} or a_{\bullet} , and the Δ AIC=0 (C-stat/d.o.f. = 2023/2163). Choices of f_c for the late-epoch spectra do not influence the constraints on either M_{\bullet} or a_{\bullet} significantly.

2.6 Appendix 39

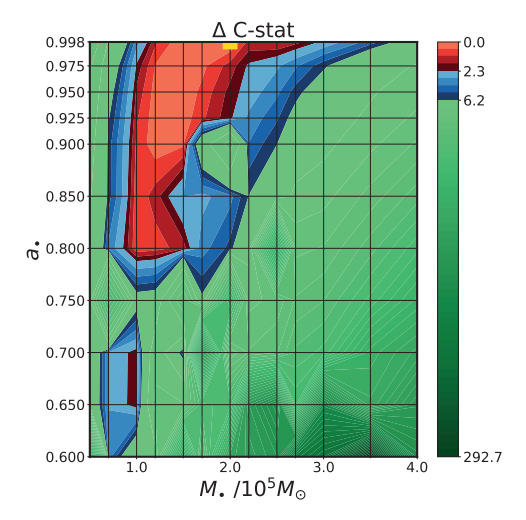


FIGURE 2.F: Same as Fig. 2.4 but here the joint-fit uses only the data from late epochs (C9, X3, X4, X5, X6) and a fit-function of TBabs*zTBabs*slimdisc. Note the range in the y-axis are different from Fig. 2.4. The best-fit C-stat/d.o.f. = 707/748. We find that the best-fit { M_{\bullet} , a_{\bullet} } values are the same as those derived considering both early— and late epoch spectra, although the uncertainties on the best-fit values increase.

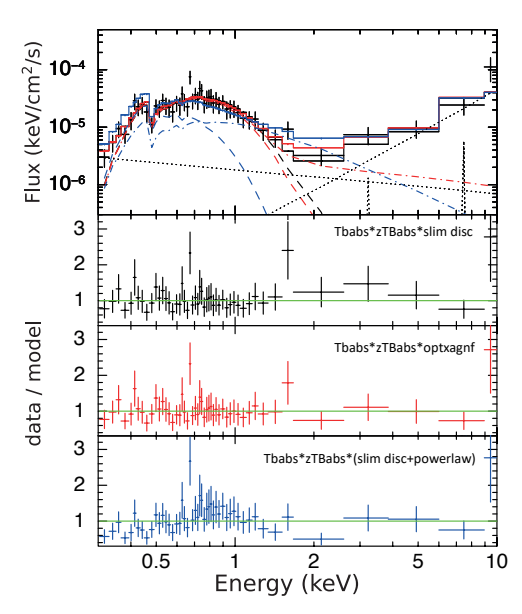


FIGURE 2.G: Comparison between our best–fit slim disc scenario (black) and optxagnf scenario (red) for the late–epoch spectra. For clarity we only show the X3 spectrum as an example. In optxagnf scenario, We set $N_{H,i} = 0.26 \times 10^{22} {\rm cm}^{-2}$, $M_{\bullet} = 7.6 \times 10^5 \ M_{\odot}$, and $a_{\bullet} = 0.998$, taken from Lin et al. 2022a. Top panel: the thermal disc emission (dashed lines) in optxagnf (red) and that in the slim disc model (black) are similar to each other. The red dot–dashed line represents the full optxagnf model (a thin disc+the non–thermal Comptonisation of a corona). We also include a scenario where the slim disc is forced to have $M_{\bullet} = 8 \times 10^5 \ M_{\odot}$, and $a_{\bullet} = 0.998$ (in blue color). In this case a powerlaw (blue dot–dashed line) is required to fit the data, resulting in C-stat/d.o.f. = 761/748. The same background models in all scenarios are represented by black dotted lines. The solid lines represent the total background+source model in each scenario. Rest panels: The data/model ratio for each scenario.

2.6 Appendix 41

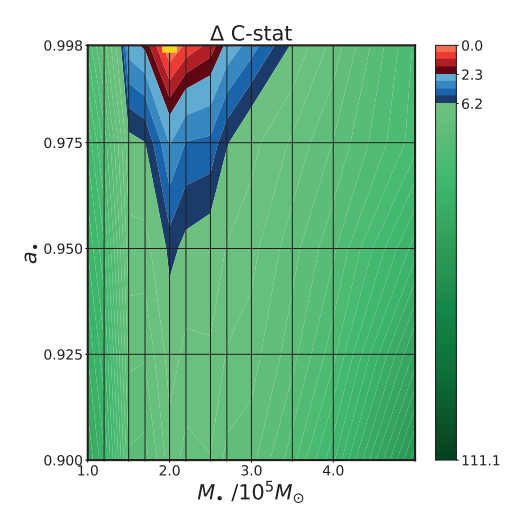


FIGURE 2.H: Same as Fig. 2.4 but with the model simpl replacing the model thcomp, describing the up–scattered continuum by a power-law instead of assuming any specific electron energy distribution. The best–fit grid–point is the same as that in Fig. 2.4. The constrained 1σ error range is similar to that derived from the physically self-consistent thermal Comptonisation model thcomp. The Δ AIC value is 4 (C-stat/d.o.f. = 2020/2164). We find the $\{M_{\bullet}, a_{\bullet}\}$ constraints are not sensitive to whether or not the inverse–Comptonisation is done by electrons that have a thermal distribution.

The intermediate—mass black hole 2XMM J123103.2+110648: A varying disc accretion rate during possible X–ray quasi–periodic eruptions?

Z. Cao, P.G. Jonker, S. Wen, N.C. Stone, A.I. Zabludoff Submitted to Astronomy & Astrophysics

Abstract

We fit the evolving X-ray spectra of the variable and fading source 2XMM J123103.2+110648 (J1231), which is an intermediate-mass black hole (IMBH) candidate. Recent X-ray timing studies have proposed that J1231's quasi-periodic oscillation (QPO) observed at the peak of its X-ray lightcurve is a variant of the quasi-periodic eruptions (QPEs) observed in other sources. Here, we fit X-ray spectra from XMM-Newton, Swift, and Chandra using a slim disc model for the black hole's accretion disc, obtaining a best-fit black hole mass of $(6 \pm 3) \times 10^4 M_{\odot}$ and spin of > 0.6 at 2σ confidence. This mass is consistent with past estimates, supporting the IMBH interpretation, and the spin measurement is new. Yet the nature of J1231 remains uncertain: its long-term variability (decade-long continuum evolution, which is explained by a varying disc accretion rate \dot{m} in our study) could signal a tidal disruption event or active galactic nuclear variability. Meanwhile, we find that during the short-term variability (the QPO with a ~ 3.8 hr period), the average mass accretion rate of the disc \dot{m} increases to ~Eddington levels, while each oscillation does not show the "hard-rise-soft-decay" typical of QPEs. We fit the average spectrum at the QPO lightcurve maxima and the average spectrum at its minima, finding that \dot{m} decreases from peaks to valleys. This result suggests that the short-term QPO behaviour might also be driven by a varying disc m.

Table 3.1: Journal listing properties of the archival observations of J1231 used in this work. Labels of observing epochs are given in brackets following the observation ID. *Swift* obtained 11 exposures between 2013 March and 2014 July. In our analysis, we average all those data and treat them as a single epoch (Epoch S1). For the *XMM-Newton* epochs, we give the exposure after filtering out periods of enhanced background radiation. This is done separately for each of the two instruments used, as specified in between brackets following the exposure time. For each spectrum, the energy band we use in our spectral analysis is also given, as we discard the data bins where the background count rate is larger than the source count rate. In the last column we estimate the net source counts in the given energy bands (the *XMM-Newton* pn and MOS counts are added).

Satellite	ObsID (Label)	Date	Exposure (ks)	Energy range (keV)	Est. # Source counts
XMM-Newton	0145800101 (X1)	2003/07/13	36.5 (pn) / 45.3 (MOS)	0.3-1.0	1026
	0306630101 (X2)	2005/12/13	52.9 (pn) / 65.0 (MOS)	0.3-2.0	3094
	0306630201 (X3)	2005/12/17	80.6 (pn) / 90.8 (MOS)	0.3-2.0	3459
Swift	00032732001-00032732011 (S1)	2013/03/08-2014/07/27	51.2 (XRT)	0.3-1.0	17
Chandra	17129 (C1)	2016/02/10	39.5 (ACIS)	0.3-7.0	9

3.1 Introduction

Intermediate—mass (10^2 - 10^6 M $_{\odot}$) black holes (IMBHs) are believed to play a vital role in the formation history of supermassive black holes (SMBHs; $\gtrsim 10^6$ M $_{\odot}$; e.g., Volonteri 2010; Kormendy & Ho 2013; Natarajan 2014; Shankar et al. 2016; Pacucci et al. 2018; Banados et al. 2018). Measuring the mass and spin distributions of IMBHs can help us understand the collective formation and evolutionary history of IMBHs and SMBHs (e.g., Greene et al. 2020; Inayoshi et al. 2020). 2XMM J123103.2+110648 (J1231; redshift z=0.11871; Ho et al. 2012) is an accreting IMBH candidate. It was serendipitously discovered in archival *XMM-Newton X*—ray data (Terashima et al. 2012; Lin et al. 2013b). The source X-ray flux decayed by ≈ 1 order of magnitude over the time period 2006 to 2016 (Lin et al. 2017a). Optical data indicate that the source could be an IMBH; the BH mass is derived using the observed line width extrapolating the empirical relation between the BH mass and the velocity dispersion of optical lines from the galaxy ($\sim 1 \times 10^5$ M $_{\odot}$; Ho et al. 2012).

The origin of the changes in J1231's X-ray emission is unclear. It has been proposed that J1231 is a tidal disruption event (TDE; Lin et al. 2013a, 2017a), i.e., a star that has approached and then been tidally disrupted by the black hole, leading to the formation of an accretion disc (e.g., Hills 1975; Rees 1988). The behaviour of J1231's X-ray emission supports this picture: both staying at high X-ray luminosity for years (> 10^{41} erg/s between 0.3–10 keV) (e.g., Rees 1988; Maksym et al. 2014; Lin et al. 2017a; Wen et al. 2020) and the very soft (most photons are ≤ 2 keV) X-ray spectra are in line with typical TDE lightcurves and spectra, which are dominated by disc emission (e.g., Ulmer 1999; Lodato & Rossi 2011; Lin et al. 2013a, 2017a; Guolo et al. 2024a).

It is also possible that J1231's long—term changing emission over the decade arises from active galactic nucleus (AGN) variability. Optical spectra from the host galaxy indicate the presence of a low—luminosity (*g*—band magnitude -17.9 mag), type—2 AGN (Ho et al. 2012; Lin et al. 2017a). As stressed by Lin et al. (2017a), the observed long—term variability may be due to an AGN disc

instability (as proposed for NGC 3599 and IC 3599; e.g., Saxton et al. 2015; Grupe et al. 2015; Inkenhaag et al. 2021).

Adding to the intrigue is J1231's X–ray quasi–periodic short-term variability, over a timescale of hours, that is observed during two of the three *XMM-Newton* epochs. *XMM-Newton* observed J1231 on 2003-07-13, 2005-12-13, and 2005-12-17¹. In this paper, we label these three epochs as X1, X2, and X3, respectively. Lin et al. (2013a) find X–ray quasi–periodic oscillations (QPOs) with a ~ 3.8 hr period at X2 and X3, but at X1 the QPO is not turned on yet. Observations ≈ 10 years later by *Chandra* and *Swift* do not show such short–term variability, suggesting that the QPO has either turned off or that it has become undetectable due to the diminished source flux (see Table 3.1 for the estimated flux at each observation epoch). It is possible that the J1231's QPO is related to the low–frequency QPOs (LFQPOs; e.g., Remillard & McClintock 2006) detected in X–ray binaries of stellar–mass BHs, but scaled–up to the IMBH mass regime (Lin et al. 2013a). LFQPOs in X-ray binaries are sometimes attributed to Lense-Thirring precession of a misaligned accretion disk, which would arise naturally in a TDE (Stone & Loeb 2012).

Recently, a new form of X–ray variability — quasi–periodic eruptions (QPEs)— has been discovered in several TDEs and AGNs (e.g, Miniutti et al. 2019; Giustini et al. 2020; Arcodia et al. 2021; Chakraborty et al. 2021; Evans et al. 2023; Quintin et al. 2023; Nicholl et al. 2024; Arcodia et al. 2024; Guolo et al. 2024b). While the physical origin of QPEs is actively debated, they are observed as rapid X–ray flares (~ks) separated by quiescent baselines, differentiated from the gentler, quasi–sinusoidal modulations of standard QPOs. Even though J1231's QPOs do not show a clear distinction between the flares and quiescence, the variability timescales are similar to QPEs, so it has been proposed that J1231 is a QPE variant (e.g., Webbe & Young 2023; King 2023). Investigating the physical origin of J1231's short–term variability could shed light on both mechanisms responsible for X–ray variability, and the possible link between J1231 and QPE sources.

In this paper, we fit a decade of evolving J1231 X–ray spectra to constrain the black hole mass and spin with our slim disc model of the accretion disc. As the X–ray timing analysis for X2 and X3 has been performed in previous work (Lin et al. 2013a; Webbe & Young 2023), we focus on spectral analysis here. This paper is structured as follows: In Section 2, we describe the data and data reduction methods. In Section 3, we present the results from our analysis. In Section 4, we discuss the implications of our results. In Section 5, we present our conclusions.

3.2 Observations and data reduction

J1231 has been observed in X–rays by several satellites since the outburst start in 2003. In our analysis, we use all the archival X–ray data of J1231 available by the end of 2024. A journal of the data used is given in Table 3.1.

¹ObsID: 0145800101, 0306630101, and 0306630201, respectively.

3.2.1 XMM-Newton observations

XMM-Newton observed J1231 over one epoch in 2003 and two in 2005. To perform the *XMM-Newton* data reduction and extract the scientific products, we use the HEASOFT (version 6.33.2) and SAS (version 21.0.0) software packages with the calibration files released on April 23, 2024 (CCF release: XMM-CCF-REL-411). The source is outside the field—of—view² in one of the Metal Oxide Semi-conductor (MOS) cameras, MOS1, at Epoch X2 and X3. Meanwhile, the signal—to—noise ratio in the Reflection Grating Spectrometer (RGS) detectors is too low to perform spectral analysis. For consistency, in this paper we use only data from the pn and the MOS2 cameras (both are European Photon Imaging Cameras; EPICs). Therefore, we refer to MOS2 as MOS hereafter.

We use the SAS command epproc and emproc to process the Science 0 data from the pn and the MOS camera, respectively. We exclude the data from periods with an enhanced background count rate, applying the standard filtering criteria³ to each camera. We require that the 10-12 keV detection rate of pattern 0 events is <0.4 counts s⁻¹ for the pn camera, and the >10 keV detection rate of pattern 0 events is <0.35 counts s⁻¹ for MOS. The first of the two X1 data segments (exposure ≤ 20 ks) is discarded due to the presence of strong background flares. We extract data of the source at RA=12h31m03.24s, Dec=+11°06′48.6″ using circular regions centred on the source of 30″ and 45″ radii, for the pn and MOS cameras, respectively. These regions are larger than the circular source region of 25″ used in Lin et al. 2013b, and they encircle the $\ge 90\%$ energy fraction at 1.0 keV for an off–axis (\sim 7′) point source. We check for the presence of photon pile–up using the SAS command epatplot, and find no evidence for pile–up at any one of the three epochs. The background spectra are extracted from circular apertures of ≥ 50 ″ radii that are free from sources. These circular regions used to measure the background spectrum lie close to the source and on the same detector as the source.

When performing spectral analysis for *XMM-Newton* data, we always jointly fit both the pn and the MOS spectra with the same fit function for the source spectra. To account for the instrument specific calibration differences, we use a constant component (constant in XSPEC) multiplying the source models. This constant serves as a re–normalisation factor between different instruments. Specifically, we fix the constant to be 1 for the pn spectra, and let the constant for MOS (C_{MOS}) free–to–vary in the fits for each epoch.

3.2.2 Swift observations

Swift performed 11 observations on the source J1231 between 2013 March and 2014 July. Following Lin et al. (2017a), we treat all *Swift* data as one epoch (Epoch S1). We combine the X–ray Telescope (*Swift*/XRT) data of all observations and extract the time–averaged, source+background

²http://www.cosmos.esa.int/web/xmm-newton/mos1-ccd6

³https://www.cosmos.esa.int/web/xmm-newton/sas-thread-epic-filterbackground

and the background X–ray spectra of J1231 using the online XRT pipeline⁴, applying the default reduction criteria (Evans et al. 2009).

3.2.3 Chandra observation

Chandra observed J1231 on 2016/02/10. We label the epoch as C1. We use CIAO (version 4.15) to perform the reduction of the data obtained by the Advanced CCD Imaging Spectrometer (ACIS) instrument onboard Chandra. We employ the CIAO command Chandra_Repro for the data filtering, and Specextract for extraction of the spectrum. The source counts are extracted from a circular source region of 1.6" radius centred on the source (this of course also contains a small background contribution). This region corresponds to an encircled energy fraction of 95% at 1 keV for an on–axis point source. The background spectrum is extracted from a circular region of ~ 20 " radius close to the source, on the same Chandra/ACIS chip, and free from sources.

3.2.4 FIT METHODS

We carry out spectral analysis using the XSPEC package (Arnaud 1996) version 12.14.0. For consistency, we create a logarithmic energy array of 1000 bins from 0.1 to 100.0 keV for model calculations in all analysis (energies command in XSPEC). When fitting models to data, we evaluate the goodness–of–fit using Poisson statistics (Cash 1979; C-STAT in XSPEC), due to the low photon counts (<100) in some of the spectra. To do so, we re–bin every background and source+background spectrum by the optimal–binning algorithm (Kaastra & Bleeker 2016; using the FTOOL ftgrouppha), while requiring the spectra to have a minimum of 1 count per bin (with parameter grouptype set to optmin in ftgrouppha). For each spectrum, we discard the data bins where the background count rate is higher than the source count rate. The energy range in each spectrum that remains after this filtering is listed in Table 3.1 for each observation. Unless mentioned otherwise, we quote all parameter errors at the 1σ (68%) confidence level, corresponding to Δ C-stat = 1.0 and Δ C-stat=2.3 for single– and two–parameter error estimates, respectively.

We first fit the background spectrum. The background fit function is phenomenological, and it consists of up to two Gaussian components and one to three power–law components (depending on the instrument). The full–width at half–maximum (FWHM) of each background Gaussian component is fixed to $\sigma_{\rm Gauss}=0.001$ keV, this is less than the spectral resolution of all instruments considered in this paper. This phenomenological background model accounts for both a background continuum and possible fluorescence lines (e.g., Katayama et al. 2004; Pagani et al. 2007; Harrison et al. 2010). Next, we add the best–fit background model to the fit function describing the source+background spectrum. The background–only spectrum. In this paper, when studying the source+background spectra, we refer to the part of the fit function that describes the source as *fit function*.

⁴https://www.swift.ac.uk/user_objects/

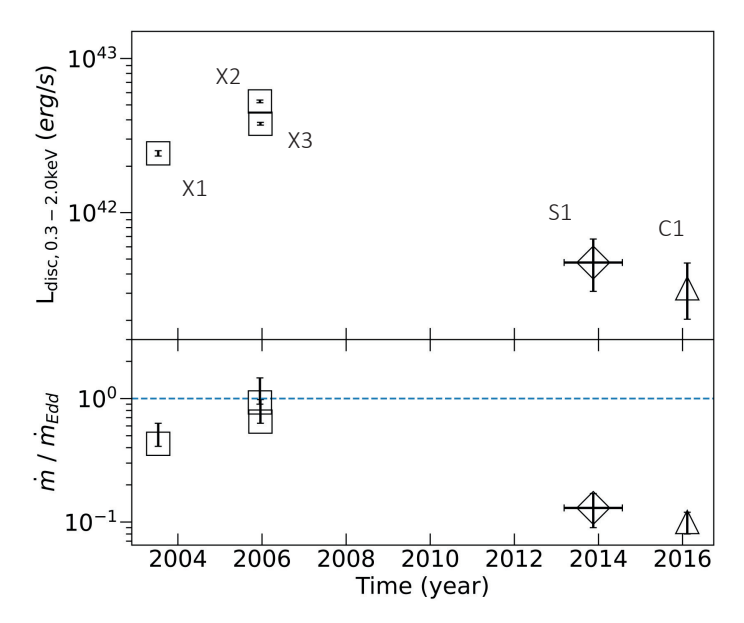


FIGURE 3.1: *Top panel*: We plot the disc luminosity in the 0.3–2.0 keV band versus time as derived from our spectral analysis (Table 3.2). The square, diamond, and triangle symbols represent the *XMM-Newton*, *Swift*, and *Chandra* observations, respectively. *Bottom panel*: the fitted disc mass accretion rate \dot{m} associated with each epoch, normalized by the Eddington-limited accretion rate (computed assuming a BH mass of $5.7 \times 10^4 \ M_{\odot}$). We indicate trans-Eddington accretion with a dashed line.

In the spectral analysis, we include the Galactic absorption in the fit function through the XSPEC model TBabs (Wilms et al. 2000). We fix the column density $N_{\rm H}$ of TBabs to $2.6 \times 10^{20} \, {\rm cm}^{-2}$, which is slightly larger than the $N_{\rm H}$ value used in previous studies ($\sim 2.3 \times 10^{20} \, {\rm cm}^{-2}$; e.g., Lin et al. 2017a; Webbe & Young 2023) derived from the density of the atomic hydrogen from 21 cm survey data (Kalberla et al. 2005). The new $N_{\rm H} = 2.6 \times 10^{20} \, {\rm cm}^{-2}$ is derived by mapping Galactic absorption using the X–ray afterglows of γ –ray bursts (Willingale et al. 2013), taking into account hydrogen in both atomic and molecular form⁵.

3.3 RESULTS

3.3.1 Low black hole mass and high spin from slim disc modelling

We use the slim disc model slimdz (Wen et al. 2020, 2022) to fit the accretion disc spectra of J1231, as its X-ray luminosity is close to Eddington. We note that slimdz was originally designed for TDE sources in that it assumes an outer disc radius $R_{\text{out}} \leq 600 R_{\text{g}}$ (Wen et al.

 $^{^{5}}$ In TBabs, the fraction of molecular hydrogen present as H_{2} is assumed to be 20% (Wilms et al. 2000), similar to the measured fraction along the line–of–sight towards J1231 (18.5%–20.3%; Willingale et al. 2013).

3.3 Results 49

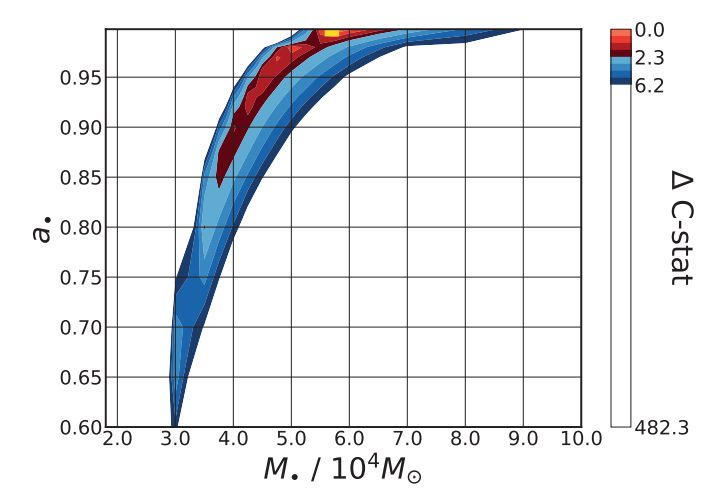


FIGURE 3.2: Constraints on M_{\bullet} and a_{\bullet} from the slim disc model-fit to the spectra obtained at all observing epochs. We calculate the ΔC -stat across the $\{M_{\bullet}, a_{\bullet}\}$ plane, with respect to the best-fit value from Table 3.2 (yellow marker). Areas within 1σ and 2σ confidence limits for two-parameter error estimates are filled by red and blue colours, respectively. At 1σ for the two-parameter fits, M_{\bullet} is constrained to be $(6 \pm 3) \times 10^4 \, \mathrm{M}_{\odot}$. The lower limit to the BH spin is constrained to be > 0.6 at the 2σ 97.8% single–sided confidence level.

2022). However, even if J1231 is a variable AGN and not a TDE, the disc region $\geq 600~R_g$ of a much larger (> $10^3~R_g$) AGN slim disc would contribute little to the X–ray spectrum ($\lesssim 1\%$; Wen et al. 2021) at $M_{\bullet} \sim 10^3 - 10^6~M_{\odot}$. Therefore, the spectral fits with slimdz are physically self–consistent irrespective of whether or not J1231 is a TDE. Further details of slimdz, including the assumption of a fixed viscosity $\alpha = 0.1$, are presented in Wen et al. 2022.

We fit all the epochs from X1 to C1 together using a fit function "constant*TBabs*slimdz". As we find no evidence for significant intrinsic absorption from our phenomenological fits (summarised in Appendix), we do not consider the intrinsic absorption in all of our analysis. We assume the black hole mass M_{\bullet} , spin a_{\bullet} , and inclination θ do not change over the ≈ 13 yr period during which the data was taken. For the joint fit (we simultaneously fit spectra from all epochs), we leave those parameters free to vary while forcing them to be constant between epochs. Due to the low number of photons detected at S1 and C1, we cannot constrain the re–normalisation factor between the EPIC/pn and the Swift/XRT (C_{XRT}), and the factor between the EPIC/pn and the Chandra/ACIS (C_{ACIS}), when \dot{m} in the slimdz model is left as a to-be-fit parameter at S1 and C1. Therefore, we leave the \dot{m} as a free parameter in the fit, while we fix both C_{XRT} and C_{ACIS} to unity during the joint–fit. Through this, we effectively assume the different instruments are perfectly cross–calibrated (while in reality the estimated uncertainties in C_{XRT} is $\lesssim 0.5\%$, and in C_{ACIS} is $\lesssim 10\%$; e.g., Plucinsky et al. 2017).

We present the best-joint-fit results in Table 3.2. The long-term X-ray evolution of J1231,

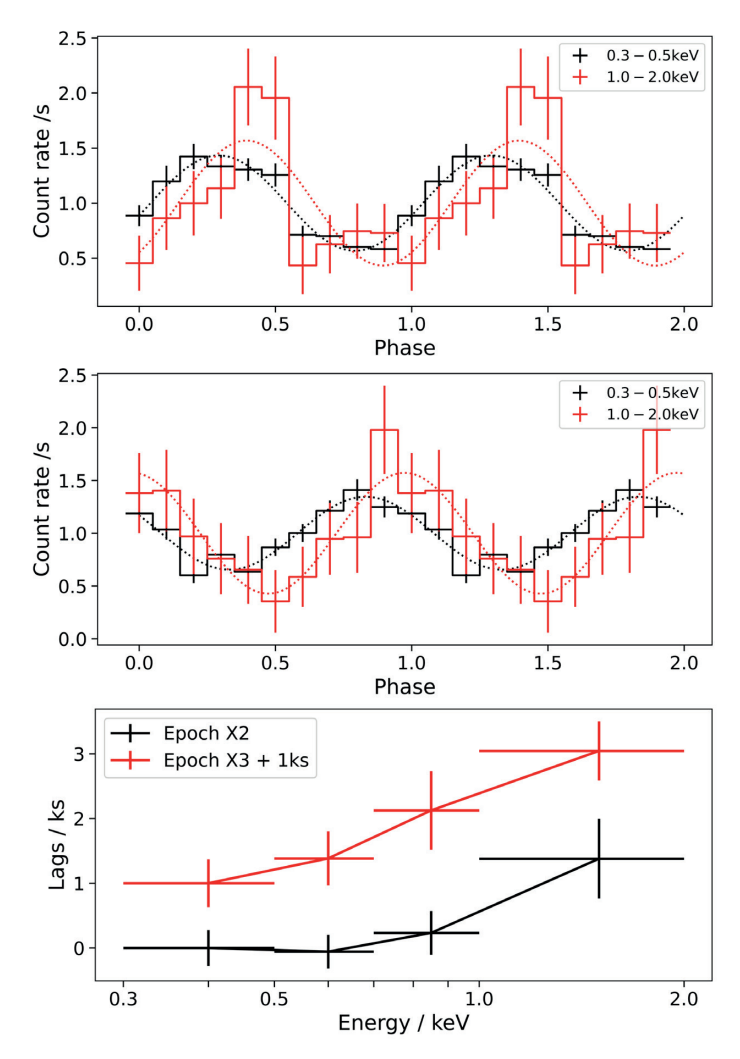


FIGURE 3.3: *Top panel*: Phase–folded lightcurves of epoch X2. We extract the lightcurves at different energy bands: 0.3–0.5 keV, 0.5–0.7 keV, 0.7–1.0 keV, and 1.0–2.0 keV. For clarity, we only plot the 0.3–0.5 keV and 1.0–2.0 keV lightcurves here. Dotted lines are the sinusoidal function fit best to the data (χ^2 /degree–of–freedom< 2 for data at each energy band). *Middle panel*: Phase–folded lightcurves of epoch X3. *Bottom panel*: Time lags of the lightcurves in different energy bands with respect to the reference band of 0.3–0.5 keV. A positive lag means that the band of our interest lags the reference band in X–ray signals. In the plot, the points of X3 are shifted by +1 ks in time difference for clarity. The J1231 data shows that the hard band (1.0–2.0 keV) lags the soft band (0.3–0.5 keV) in time (1.4 ± 0.9 ks at X2, and 2.0 ± 0.8 ks at X3). J1231 is thus unlike QPEs, which typically show a "hard–rise–soft–decay" mode, such that hard bands *lead* soft bands through each eruption.

3.3 Results 51

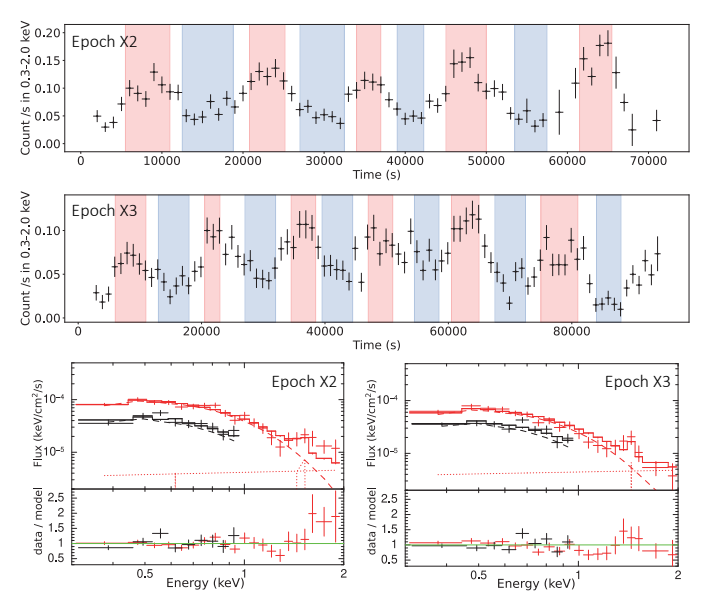


FIGURE 3.4: *Top two panels*: The 0.3–2.0 keV light–curves in the X2 (*top first*) and X3 (*top second*) epochs, re–binned to 1000 s per time bin. We mark the time intervals selected for generating the spectra by red (peaks; X2–p and X3–p) and blue (valleys; X2–v and X3–v) colour. We manually choose the time intervals to select peaks and valleys. For each set of data we average the spectra. The un–selected data in white are not considered. The exact time intervals are listed in the Appendix. *Bottom panels*: For each epoch, the black and red data are from the valley and the peak EPIC/pn, respectively. The EPIC/MOS data are not included for plotting purpose only. The solid, dashed, and dotted lines represent the total model, the slim disc, and the background components, respectively. Spectra at valleys have identical backgrounds as those at peaks. Therefore, the valley backgrounds are not shown. We freeze the best-fit slim disc model parameters (Table 3.2) allowing only the *m* to vary to fit the peak and valley spectra. This approach yields good fits to the peak and valley spectra, see Table 3.3 for the parameter constraints.

i.e., the decade-long decay, can be explained as due to variations in the mass accretion rate through the disc (\dot{m} , in units of Eddington accretion rate, $\dot{m}_{\rm Edd} = 1.37 \times 10^{21} \ {\rm kg \ s^{-1}} \times M_{\bullet}/10^6 M_{\odot}$; Wen et al. 2020). Specifically, the \dot{m} increases from $\sim 0.4 \ \dot{m}_{\rm Edd}$ at X1, to $\sim \dot{m}_{\rm Edd}$ at X2 and X3, before it decreases to $\sim 0.1 \ \dot{m}_{\rm Edd}$ at later epochs. Fig. 3.1 summarises the long-term evolution of the disc 0.3–2.0 keV luminosity, as well as the \dot{m} , based on our analysis results. Fig. 3.2 shows the ΔC -stat contours in $\{M_{\bullet}, a_{\bullet}\}$ space, where the BH mass is constrained to be $(6 \pm 3) \times 10^4 \ M_{\odot}$ and the spin to be > 0.6 at 2σ (97.8% single-sided) confidence. Note that the errors are for two-parameter error estimates counting for dependencies between the constraints of M_{\bullet} and a_{\bullet} , rather than the single-parameter error estimates in Table 3.2.

The spectra at S1 and C1 are likely disc spectra regardless of various scenarios explaining the source behaviour at earlier epochs (X1 to X3, see Discussion). We test the disc model derived

Table 3.2: Parameter constraints for the joint fit of the spectra at all the epochs. The fit function is "constant*TBabs*slimdz". Values held fixed during the fit are given in square brackets. During the fit, the M_{\bullet} , a_{\bullet} , and θ are free—to—vary but forced to be the same at each epoch. Due to low number of photons detected at S1 and C1, it is not possible to simultaneously constrain the re—normalisation factor (C_{XRT} and C_{ACIS}) and \dot{m} . Thus we fix C_{XRT} and C_{ACIS} to unity, assuming different instruments are well cross—calibrated. We find that the X—ray spectra of J1231 at all epochs can be well explained by a slim disc model varying only the mass accretion rate \dot{m} .

Model	Parameter	X1	X2	Х3	S1	C1
constant	constant C _{MOS}		0.93 ± 0.05	1.04 ± 0.05	-	-
	$C_{ m XRT}$ or $C_{ m ACIS}$	-	-	-	[1]	[1]
TBabs	$N_{\rm H}~(10^{20}~{\rm cm}^{-2})$			[2.6]		
slimdz	$\dot{m}~(\dot{m}_{ m Edd})$	$0.43^{+0.20}_{-0.02}$	$0.93^{+0.54}_{-0.03}$	$0.65^{+0.33}_{-0.02}$	0.13 ± 0.04	0.10 ± 0.02
	θ (°)			< 30		
$M_{ullet}\left(M_{\odot} ight)$				$(5.7^{+0.5}_{-0.8}) \times 10$)4	
a_{ullet}				> 0.96		
C-stat/d.o.f.			·	136.9/124	·	

from previous fits on these spectra by fitting each of them with the disc model and fixing the values of M_{\bullet} , a_{\bullet} , and θ to the best-fit values from Table 3.2. We then fit only \dot{m} for each of S1 and C1. We find the spectra at S1 and C1 are consistent with the disc derived from previous fits (Fig. 3.B and Table 3.C in the Appendix). In such a way, we also check that our choices of $C_{\text{XRT}} = 1$ and $C_{\text{ACIS}} = 1$ during the joint-fit (Tabel 3.2) do not result in BH mass and spin values that are unable to explain the spectra at S1 or C1.

3.3.2 An unusual short-term variability pattern for a QPE

It has been proposed that J1231's ~ 3.8 hr variability could be due to a QPE. A known QPE variability pattern is a "hard-rise-soft-decay" mode, which manifests itself as the hard X-ray flux peaks before the soft flux does through each eruption (e.g., Miniutti et al. 2019; Arcodia et al. 2024; Giustini et al. 2024). To check if J1231 behaves similarly to QPE sources with such spectral evolution, we examine the lightcurves at four energy bands: 0.3–0.5 keV, 0.5–0.7 keV, 0.7–1.0 keV, and 1.0–2.0 keV. We find no clear evidence for the peaks of hard bands (0.7–1.0 keV or 1.0–2.0 keV) leading those of the soft band (0.3–0.5 keV) in time. Fig. 3.3 shows the phase–folded EPIC/pn lightcurves at epoch X2 and X3. The periods for X2 and X3 are taken to be 13.52 ks and 14.35 ks, respectively (Webbe & Young 2023). When phase-folding the lightcurves of epoch X2 and X3, we set the start time (T=0) to be at 2.50856724E+08 s and at 2.51185225E+08 s, respectively. Here the start time is given in offsets in seconds from the *XMM-Newton* Mission Reference Time (MRT, 1997-12-31T23:58:56.816 UTC).

To quantify the time lags, we fit the phase–folded lightcurves with a sinusoidal fit function $CR_i = A_i \sin[2\pi(x - l_i)] + CR_{0,i}$, where CR_i is the count rate at energy band i, A_i is the amplitude,

3.3 Results 53

Table 3.3: Parameter constraints from fitting the time—resolved spectra at X2 and X3 with the slimdz model. The total fit function is "constant*TBabs*slimdz". Values held fixed during the fit are given in square brackets. Assuming the best—fit BH parameters $(M_{\bullet}, a_{\bullet}, \text{and } \theta)$ derived from Table 3.2, we test the disc explanation of the quasi—periodic variation observed at X2 and X3. At each epoch of X2 and X3, we jointly fit the average spectrum of the peaks (X2-p or X3-p) and that of the valleys (X2-v or X3-v). We find the difference between the source spectra at peaks and valleys can be explained by a varying \dot{m} . This \dot{m} conclusion holds qualitatively when we assume the case of the smallest spin value based on results in Fig. 3.2 $(M_{\bullet} = 3 \times 10^4 M_{\odot})$ and $a_{\bullet} = 0.6$.

	Model Parameter		Х2-р	X2-v	Х3-р	X3-v
-	constant C _{MOS}		0.94 ± 0.07	0.8 ± 0.1	0.97 ± 0.08	1.1 ± 0.1
	TBabs $N_{\rm H} (10^{20} {\rm cm}^{-2})$		[2	[2.6]		.6]
	slimdz $\dot{m} \left(\dot{m}_{\mathrm{Edd}} \right)$		1.71 ± 0.07	0.63 ± 0.03	1.05 ± 0.04	0.55 ± 0.02
		θ (°)	[10]		[10]	
		$M_{ullet}\left(M_{\odot}\right)$	[5.7]	< 10 ⁴]	$[5.7 \times 10^4]$	
	a_{ullet}		[0.99]		[0.99]	
	C-	stat/d.o.f.	75.1/64		74.7/64	
	Model Parameter		Х2-р	X2-v	Х3-р	X3-v
	constant	$C_{ m MOS}$	0.96 ± 0.07	7 0.8 ± 0.1	0.97 ± 0.08	1.1 ± 0.1
	TBabs $N_{\rm H} (10^{20} {\rm cm}^{-2})$		[2.6]		[2.6]	
	slimdz	$\dot{m}~(\dot{m}_{ m Edd})$	17 ± 2	2.5 ± 0.2	5.7 ± 0.4	2.1 ± 0.1
	θ (°)		[10]		[10]	
	$M_{ullet}\left(M_{\odot} ight)$		$[3 \times 10^4]$		$[3 \times 10^4]$	
	a_{ullet}		[0.6]		[0.6]	
		C-stat/d.o.f.	85	85.6/64		64

x is the phase value from the x-axis, l_i is the phase shift, and $CR_{0,i}$ is the count rate at phase $x = l_i$. The phase lag Δl is defined as the change in the l value between the energy band i of our interest and the reference band. We then infer the time lags between peaks at different energy bands by multiplying the phase lags and the periods. In this way, a positive time lag means that the band of our interest lags the reference band in X-ray signals. The time lag-energy plot (Fig. 3.3; reference band 0.3-0.5 keV) shows that, during the short-term variability in both epoch X2 and X3, the 1.0-2.0 keV band lags the 0.3-0.5 keV band in time, by 1.4 ± 0.9 ks at X2, and by 2.0 ± 0.8 ks at X3. This lag result is contrary to a "hard-rise-soft-decay" eruption (that the hard bands should lead the soft bands), suggesting that J1231's X-ray spectral variability is unlike that of typical QPEs during flares.

3.3.3 SHORT-TERM VARIABILITY FROM A CHANGING DISC MASS ACCRETION RATE?

We also fit the slim disc model to the time–resolved spectra within X2 and within X3, to test if the quasi–periodic variability at X2 or X3 introduces changes in the spectral shape within a single observation. Based on the *XMM-Newton*/EPIC-pn lightcurves, we select spectra according to the 0.3–2.0 keV count rate during local lightcurve maxima and minima, and then average those spectra to create a peak and a valley composite, respectively. Due to the lightcurve evolution between cycles, it is not possible to have strict count rate criteria for a peak and a valley across different cycles. Also, as the variability is not strictly periodic, we cannot separate the peaks and valleys based on the phase change of a fixed period to create the phase–resolved spectra. Therefore, we manually choose time intervals for peaks and valleys, and we discard the data in between. Next, we employ the SAS command GTIBUILD to combine the data of the selected time intervals and create the average peak and valley spectra from both pn and MOS for both epoch X2 and X3. We refer to the peak spectra as X2–p and X3–p, and to the valley spectra as X2–v and X3–v. Due to the decrease of source count rate below that of the background for energy bins > 1 keV, we only consider the energy range 0.3–1.0 keV for the X2–v and X3–v spectra in the analysis. Fig. 3.4 shows the time intervals selected during X2 and X3, which we also list in the Appendix.

At each epoch, we fit a composite spectrum made from averaging the spectra at the peaks of the short-term variability and a composite spectrum from averaging the valleys. We fix the values of M_{\bullet} , a_{\bullet} , and θ to the best–fit values from Table 3.2. Within both X2 and X3, the spectral difference between the peaks and valleys can be explained as due to a changing mass accretion rate (Fig. 3.4 and Table 3.3). This \dot{m} conclusion holds qualitatively when we assume the case of the smallest spin value based on results in Fig. 3.2 ($M_{\bullet} = 3 \times 10^4 M_{\odot}$ and $a_{\bullet} = 0.6$).

3.4 Discussion

J1231's five epochs of broad-band soft X-ray spectra are fit well by varying only the mass accretion rate in the slim disc model (Table 3.2). From data spanning more than a decade, we constrain the BH mass to be $(6 \pm 3) \times 10^4 \ M_{\odot}$, similar to the value estimated from extrapolating the scaling relation for BH mass and optically-derived host galaxy velocity dispersion: $\sim 10^5 \ M_{\odot}$ (Ho et al. 2012). Our study more strongly suggests that the central engine of J1231 is an IMBH.

Furthermore, our disc modelling indicates the BH has a high spin: $a_{\bullet} > 0.6$. A highly–spinning IMBH of $\lesssim 10^5~M_{\odot}$ could be formed via direct collapse of a gas cloud in the early Universe (e.g., Loeb & Rasio 1994; Bromm & Loeb 2003). Simulations have shown that $a_{\bullet} > 0.9$ can be produced if the collapsing cloud goes through a supermassive stellar (SMS) phase before collapsing into a BH (e.g., Reisswig et al. 2013; Inayoshi et al. 2014). Alternatively, if the BH was born at a much lower mass ($\lesssim 10^3~M_{\odot}$; e.g., via stellar remnants or gravitational runaway stellar collisions Madau & Rees 2001; Zwart & McMillan 2002; Devecchi & Volonteri 2009; Greif et al. 2011), then it must have gained its last *e*-fold in mass through subsequent accretion

3.4 Discussion 55

episodes. In such cases, reaching a high spin while avoiding being spun—down due to multiple accretion episodes (e.g., King et al. 2008; Metzger & Stone 2016) requires that the seed BH grew to its current mass in one or more accretion episodes where the angular momentum vector of the accreted material was aligned with that of the BH spin.

Fig 3.1 shows the long–term evolution of the J1231 disc luminosity in the 0.3–10 keV band, as well as the \dot{m} evolution as derived from our analysis of the X-ray spectra. We find that the \dot{m} of the disc increases to $\approx \dot{m}_{\rm Edd}$ at X2 and X3 compared to $\approx 0.4 \dot{m}_{\rm Edd}$ at X1 two years earlier, before it drops to ~ 0.1 $\dot{m}_{\rm Edd}$ at S1 and C1 several years later (Table 3.2). Assuming a linear interpolation between epochs in Fig 3.1, we roughly estimate the total mass accreted between 2004 and 2016 to be ~ 0.01 M_{\odot} . The small amount of total accreted mass suggests that, if J1231 is a bona–fide TDE (e.g., Rees 1988; Strubbe & Quataert 2009; Metzger & Stone 2016), it might be either a weak partial disruption that stripped off very little mass, or a full disruption of a subsolar object like a brown dwarf or large gas giant.

Several scenarios have been suggested by Lin et al. (2017a) to explain the luminosity increase from X1 to X2, for instance, the X1 epoch catching the initial fast rise of the TDE disc, or a slow disc circularisation in the TDE (e.g., Guillochon & Ramirez-Ruiz 2015; Hayasaki & Jonker 2021), or a prolonged disruption of an evolved star (MacLeod et al. 2012; though this TDE subclass is typically of low likelihood, see e.g., MacLeod et al. 2013; Kochanek 2016). In our study we find that the source spectrum is always consistent with a disc spectrum starting from X1, results in line with the scenarios except a slow disc circulariation process. Furthermore, Wen et al. (2020) find a TDE observed nearly edge-on would also result in a slow luminosity rise after the disruption, due to the process they called disc slimming. However, our results suggest a face-on viewing angle (Table 3.2), disfavouring the disc slimming scenario in J1231. A delayed X-ray luminosity increase with respect to the initial disruption can also be explained by a partial TDE where the star is not fully disrupted during its first passage through the pericenter, allowing subsequent disruptions and mass accretion (e.g., Wevers et al. 2023; Liu et al. 2023). Alternatively, J1231 might not be a TDE, but a variable AGN. However, in this case J1231 would be atypical for AGNs to have pure thermal X-ray spectra, while only 1.5% AGNs vary in X-rays by a factor of >10 (Lin et al. 2012, 2017a).

Regardless of whether J1231 is a TDE or solely due to an active nucleus, \dot{m} at all epochs lies in the range $\dot{m}_{\rm Edd} \gtrsim \dot{m} \gtrsim 0.1 \dot{m}_{\rm Edd}$ (Table 3.2). Classical disc theories predict that a disc radiation–pressure instability occurs in this \dot{m} range (e.g., Lightman & Eardley 1974; Shakura & Sunyaev 1976; Piran 1978; see Czerny 2019 for a review), preventing a steady \dot{m} in this instability range and forcing the disc to go through the so–called "limit cycle" (e.g., Lasota & Pelat 1991; Szuszkiewicz & Miller 1998; Xue et al. 2011). In such case the \dot{m} should avoid values in the instability range over a timescale larger than the thermal timescale at the outer edge of disc instability zone (~days in the J1231 case).

However, observational evidence from the XRB population indicate that a steady disc with \dot{m} in the $\dot{m}_{\rm Edd} \gtrsim \dot{m} \gtrsim 0.1 \dot{m}_{\rm Edd}$ instability range, remains likely. Except for two XRBs (GRS 1915+105 and IGR J17091-3624; e.g., Belloni et al. 1997; Janiuk et al. 2000, 2015; Altamirano et al. 2011),

most XRB discs in the range $\dot{m}_{\rm Edd} \gtrsim \dot{m} \gtrsim 0.1 \dot{m}_{\rm Edd}$ do not have signs of radiation–pressure instability (e.g., Gierliński & Done 2004; Czerny 2019). It is purposed that other factors such as magnetic fields may stabilise the accretion disc to prevent a limit cycle from occurring (e.g., Janiuk & Czerny 2011; Kaur et al. 2023). Strong outflows when the disc accretion is at high–Eddington/super–Eddington levels (e.g., Middleton et al. 2013; Pinto et al. 2016, 2021; Kara et al. 2018; Pasham et al. 2024a) will also help to stabilise the disc. These stabilising mechanisms could be important in J1231, as we find that the source spectrum is always consistent with a steady disc model of \dot{m} in the range $\dot{m}_{\rm Edd} \gtrsim \dot{m} \gtrsim 0.1 \dot{m}_{\rm Edd}$.

Besides the long–term spectral evolution over a decade, J1231 shows a short–term X–ray variability at X2 and X3, on the timescale of $\sim 3.8\,\mathrm{hr}$ ($\approx 0.07\,\mathrm{mHz}$). Lin et al. (2013a) first reported the variability, and they proposed it to be analogous to the low–frequency QPOs (LFQPO) detected in X–ray binaries (XRBs) which host a stellar–mass BH. Assuming a linear anti-correlation of the LFQPO frequency with BH mass, a 0.07 mHz QPO in an accretion disc around a $6\times 10^4\,M_\odot$ BH corresponds to $\sim 0.1\,\mathrm{Hz}$ for a 10 M_\odot BH, reminiscent of the lower–frequency end of LFQPOs in XRBs (0.1–30 Hz; Belloni et al. 2002; Remillard & McClintock 2006). Moreover, the disappearance of the QPO features in J1231 (when the X–ray luminosity decreases at later epochs) resembles the spectral state transition between the ultra-luminous state (ULS; also named as the steep powerlaw state) to the thermal state in XRBs (e.g., Remillard & McClintock 2006; Li et al. 2014). We note that factors other than the BH mass (e.g., disc accretion rate) might also impact the LFQPO frequency (e.g., McHardy et al. 2006; Li et al. 2014; van Doesburgh & van der Klis 2020).

Could Lense–Thirring precession, arising from a misalignment between the BH's equatorial spin plane and the disc plane shortly after the TDE (e.g., Stone & Loeb 2012), be responsible for J1231's short–term variability? Observational evidence supports such a scenario in two TDEs (ASASSN-14li; Pasham et al. 2019; AT2020ocn; Pasham et al. 2024b; Cao et al. 2024). In the case of J1231, if a solar–type star is disrupted, the predicted precession period for a < $10^5 \ M_{\odot}$ BH is > 1 day, irrespective of the value of the BH spin (e.g., Franchini et al. 2016; Teboul & Metzger 2023). As the precession period scales $\propto R_{\rm out}^3$ at first order (Pasham et al. 2024b), it is possible to have a Lense–Thirring precession period of hours if the outer disc radius is reduced by a factor of $\gtrsim 2$ compared to the typical disc outer radius, $R_{\rm out} = 2R_T$ (the tidal radius $R_T = R_*(M_{\bullet}/M_*)^{1/3}$ where R_* and M_* are the radius and mass of the disrupted star, respectively), which can be achieved if the disrupted star is less solar in mass and radius. However, it is difficult for a precession scenario to explain the X1 data, when the source shows a spectrum consistent with a steady disc.

It has also been proposed that J1231's short–term variability is a variant of the QPEs seen in some TDEs and AGN (e.g., Miniutti et al. 2019; Giustini et al. 2020; Arcodia et al. 2021; Chakraborty et al. 2021; Evans et al. 2023; Quintin et al. 2023; Webbe & Young 2023; Nicholl et al. 2024; Arcodia et al. 2024; Guolo et al. 2024b). Our tests on the peak and the valley spectra (Fig. 3.4) suggest that the spectral difference during one variability cycle can be explained by a difference in disc accretion rate. We now compare this result to possible QPE mechanisms.

3.5 Conclusions 57

The physical process driving the QPEs is under active debate. Possible mechanisms of QPEs include disc instability (e.g., Lightman & Eardley 1974; Shakura & Sunyaev 1976), repetitive partial TDEs (e.g., King 2020, 2023), and disc—star interactions (e.g., Suková et al. 2021; Linial & Metzger 2023b). In all of these proposed scenarios for QPEs, an increased disc accretion rate could be produced, either by a disc instability (e.g., Sniegowska et al. 2020; Kaur et al. 2023), or due to additional material supply from a partially disrupted star on a close orbit (e.g., King 2020, 2023), or due to the perturbation of the disc induced by the passage of a stellar object (e.g., Suková et al. 2021). Alternatively, the accretion disc might not be circularised or thermalised during a QPE (Krolik & Linial 2022; King 2023), so that the slimdz model is not applicable to X2 and X3 (though we find the source is consistent with a disc spectrum at the valleys and peaks).

If the quasi-periodic signal at X2 and X3 is indeed due to QPEs, our results provide evidence of an \dot{m} variation as the driver of the QPE phenomenon. However, we like to stress that the J1231 spectral variation at X2 and X3 differs from that observed in QPE sources. Contrary to the "hard-rise-soft-decay" eruptions in typical QPE sources (e.g., GSN 069; Miniutti et al. 2019), in the phase-folded lightcurves we find that the hard energy band (1.0–2.0 keV) lags the soft band (0.3–0.5 keV), resulting in a "soft-rise-hard-decay" mode (Fig. 3.3). One possibility to explain the hard lag is that the \dot{m} variation propagates from the outer disc, where most of the soft photons come from, to the innermost disc region, where most of the harder photons come from. This propagation takes time and thus leads to a delayed hard band variation. As the nature of QPEs is still under active debate, however, it remains unclear if J1231 is a variant of the QPE phenomenon or not.

3.5 Conclusions

We present our spectral analysis of J1231's evolving X–ray data, which are taken over more than a decade, from 2003 to 2016. Using a slim disc model for the accretion disc around the black hole, we find that the decade–long spectral evolution of J1231 can be explained with a varying mass accretion rate. The best slim disc fit simultaneously to all the spectra yields a BH mass of $(6\pm3)\times10^4~M_\odot$ at 2σ confidence, making J1231 one of only a handful of intermediate–mass black hole candidates in the range 10^2 – $10^6~M_\odot$. The black hole spin is > 0.6 at the 2σ 97.8% single–sided confidence level, a rapid spin. The source spectra $\gtrsim 10$ years after the first observation are consistent with the same BH mass and spin.

Previous studies have found a short–term QPO with a ~ 3.8 hr period in the X-ray light curve of J1231 when the source luminosity peaks, i.e., during the second and third of the five epochs observed. We separate the J1231 lightcurves into four different energy bands during the two QPO epochs. We find that the 1.0–2.0 keV hard band lags the 0.3–0.5 keV soft band by \sim kiloseconds, resulting in a "soft–rise–hard–decay" variation mode. This mode is in contrast to the typical QPE mode of "hard–rise–soft–decay", suggesting that J1231 is an atypical QPE candidate.

Furthermore, at those two epochs, the best-fit slim disc model shows that the average disc mass accretion rate increases to ~Eddington. For each of those two epochs, we produce a composite

spectrum of the QPO peaks and one of the valleys. Our analysis of the peak and valley composite spectra suggests that the QPO behaviour might as well be driven by a varying disc accretion rate. Such an accretion rate variation could be caused by any one of the mechanisms proposed also for QPEs. The hard—to—soft lag is explained by the inward propagation of the accretion rate variation on the disc.

ACKNOWLEDGEMENTS

This work made use of data supplied by the UK Swift Science Data Centre at the University of Leicester. This work used the Dutch national e-infrastructure with the support of the SURF Cooperative using grant no. EINF-6770. PGJ is supported by the European Union (ERC, StarStruck, 101095973). Views and opinions expressed are however those of the author(s) only and do not necessarily reflect those of the European Union or the European Research Council. AIZ acknowledges support in part from grant NASA ADAP #80NSSC21K0988.

3.6 Appendix 59

3.6 APPENDIX

3.6.1 Phenomenological characterisation of J1231 by blackbody models

We characterise the spectra of J1231 at different epochs using simple blackbody models (zbbody; spectral models are referred to in the XSPEC syntax hereafter). For Epochs X1, S1, and C1, the source spectrum is consistent with a blackbody model (the total fit function "constant*TBabs*zbbody"), while for X2 and X3 a second, hotter blackbody component is required to achieve a good–fit to the data (for these epochs the total fit function becomes "constant*TBabs*(zbbody+zbbody)"). The two–blackbody–like spectra with $\dot{m} \sim \dot{m}_{\rm Edd}$ at Epochs X2 and X3 resemble several TDE spectra when accreting at high–Eddington or super–Eddington levels (e.g., Kara et al. 2018; Cao et al. 2023). We summarise the best–fit parameters in Table 3.A. An example of the model fitted to the data at X2 is presented in Fig. 3.A. The temperature of the primary blackbody component is \sim 0.12 keV throughout the first four epochs before it drops to 0.07 ± 0.02 keV at the last epoch. For each epoch, we also test for the presence of intrinsic absorption (using the model zTBabs) and find that there is no evidence for significant intrinsic absorption in our analysis throughout the paper.

We also fit the time–resolved spectra produce in Section 3.3.3 using zbbody models. Best–fit parameters are summarised in Table 3.B. The primary blackbody component at either X2 or X3, which dominates the 0.3–1.0 keV range, is consistent in temperature for the peak and valley composite spectra within the 1σ uncertainty errors. However, it is not possible to constrain the second blackbody component of higher temperature in X2–v and X3–v due to the low number of spectral counts. Therefore, we cannot assess whether the variability introduces spectral shape changes above 1.0 keV.

3.6.2 GENERATING THE TIME-RESOLVED SPECTRA FOR X2 AND X3

Here we list the time intervals selected for stacking the spectra of the peaks (X2–p and X3–p) and the valleys (X2–v and X3–v), as presented in Fig. 3.4. The intervals are given in offsets in seconds from the *XMM-Newton* Mission Reference Time (MRT, 1997-12-31T23:58:56.816 UTC), minus

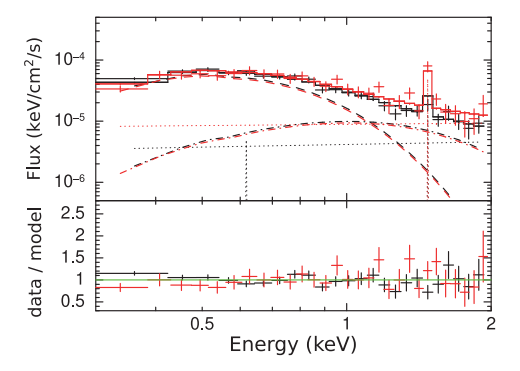


FIGURE 3.A: A phenomenological fit of two blackbodies (dashed and dot–dashed lines) to the *XMM-Newton*/EPIC–pn (black) and *XMM-Newton*/MOS (red) data from X2. The dotted lines represent the background spectra for each instrument. The bottom panel shows the ratio between the observed number of counts in each spectral bin (data; black and red points in the top panel) and the best–fit predicted number of counts in each spectral bin (model; solid lines in the top panel).

Table 3.A: Parameter constraints derived from fitting the spectrum at each epoch with one or two black bodies. The fit function is "constant*TBabs*(zbbody₁+zbbody₂)". Values held fixed during the fit are given in between square brackets. Parameter C_{MOS} is the re–normalisation factor between the EPIC/MOS and EPIC/pn on–board *XMM-Newton*. Statistically, only X2 and X3 require the second, hotter black body to achieve a good fit, and therefore the fit function used to fit the other epochs do not include a second black body.

Model	Parameter	X1	X2	X3	S1	C1
constant	$C_{ m MOS}$	0.9 ± 0.1	0.94 ± 0.05	1.04 ± 0.06	-	-
TBabs	$N_{ m H} (10^{20} \ { m cm}^{-2})$	[2.6]	[2.6]	[2.6]	[2.6]	[2.6]
zbbody1	kT_e (keV)	0.116 ± 0.004	0.13 ± 0.01	0.13 ± 0.01	0.14 ± 0.04	0.07 ± 0.02
	$Norm_{zbb1} (10^{37} (1+z)^{-2} erg/s/kpc^2)$	$(1.51 \pm 0.09) \times 10^{-6}$	$(2.3 \pm 0.2) \times 10^{-6}$	$(2.0 \pm 0.1) \times 10^{-6}$	$(2\pm1)\times10^{-7}$	$10^{+22}_{-6} \times 10^{-7}$
zbbody ₂	kT_e (keV)	-	$0.28^{+0.10}_{-0.05}$	$0.34^{+0.19}_{-0.09}$	-	-
	$Norm_{zbb2} (10^{37} (1+z)^{-2} erg/s/kpc^2)$	-	$(3^{+3}_{-2}) \times 10^{-7}$	$(1.1^{+0.7}_{-0.3}) \times 10^{-7}$	-	-
	C-stat/d.o.f.	10.4/18	41.3/46	46.0/46	1.8/6	4.3/4

Table 3.B: Same as Table 3.A, but here we fit the time–resolved spectra at the peaks (X2-p) and X3-p) and the valleys (X2-v) and X3-v). See Fig. 3.4 for the production of those spectra. Due to the decrease of the source flux below the background level, we only consider the energy range of 0.3–1.0 keV for the X2-v and X3-v spectra in the analysis. It is not possible to detect the second, hotter black body in X2-v and X3-v. We find the best–fit temperature of the primary black body to be consistent with being the same in the peak and valley spectra.

Model	Parameter	X2-p	X2-v	Х3-р	X3-v
constant	$C_{ m MOS}$	0.94 ± 0.07	0.8 ± 0.1	0.97 ± 0.08	1.1 ± 0.1
TBabs	$N_{ m H}~(10^{20}~{ m cm}^{-2})$	[2.6]	[2.6]	[2.6]	[2.6]
zbbody ₁	kT_e (keV)	0.14 ± 0.01	0.14 ± 0.01	0.11 ± 0.01	0.13 ± 0.01
	$Norm_{zbb1} (10^{37} (1 + z)^{-2} erg/s/kpc^2)$	$(3.6 \pm 0.3) \times 10^{-6}$	$(1.7\pm0.1)\times10^{-6}$	$(2.7 \pm 0.3) \times 10^{-6}$	$(1.4 \pm 0.1) \times 10^{-6}$
zbbody ₂	kT_e (keV)	0.3 ± 0.2	-	0.20 ± 0.04	-
	$Norm_{zbb2} (10^{37} (1 + z)^{-2} erg/s/kpc^2)$	$(4^{+6}_{-1}) \times 10^{-7}$	-	$(6^{+6}_{-3}) \times 10^{-7}$	-
	C-stat/d.o.f.	52.0/43	14.3/17	35.3/42	25.1/18

3.6 Appendix 61

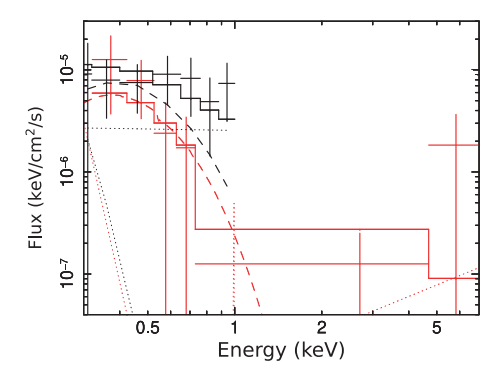


FIGURE 3.B: We fit the slim disc model to the spectra at S1 (black) and C1 (red). When fitting each spectrum, we assume the best–fit parameters derived from the joint–fit to the spectra of all epochs (Table 3.2), only allowing the \dot{m} to vary. The solid, dashed, and dotted lines represent the total model, the disc, and the background components, respectively. The spectra at S1 and C1 are consistent with the parameters derived from Table 3.2.

2.50860675e+08 s. Both the pn and the MOS data use the same time intervals to produce the stacked spectra.

For X2–p spectrum: from 0 to 5500; from 15300 to 19700; from 28500 to 31500; from 39500 to 44500; from 56000 to 60000.

For X2–v spectrum: from 7000 to 13300; from 21500 to 27000; from 33500 to 36800; from 48000 to 52000.

For X3–p spectrum: from 328151 to 333151; from 342651 to 345151; from 356651 to 360651; from 369151 to 373151; from 382651 to 387151; from 397151 to 403151.

For X3–v spectrum: from 335151 to 340151; from 349151 to 354151; from 361651 to 366651; from 376651 to 380651; from 389651 to 394651; from 406151 to 410151.

3.6.3 SLIM DISC FIT TO S1 AND C1 DATA

We fit the slim disc model to the spectra at S1 and C1. The total fit function is "constant*TBabs*slimdz". We fit each spectrum keeping the BH parameters M_{\bullet} , a_{\bullet} , and θ fixed at the values given in Table 3.2. We then fit only \dot{m} for each of S1 and C1. The results show that the spectra at S1 and C1 are consistent with the disc derived from previous fits (Fig. 3.B and Table 3.C)

Table 3.C: Parameter constraints from fitting the spectra at S1 and C1 with the slimdz model. The total fit function is "constant*TBabs*slimdz". Values held fixed during the fit are given in square brackets. We fit each spectrum keeping the BH parameters M_{\bullet} , a_{\bullet} , and θ fixed at the values given in Table 3.2. We confirm that the spectra at S1 and C1 are consistent with originating in a disc.

Model	Parameter	S1	C1
TBabs	$N_{\rm H} (10^{20} {\rm cm}^{-2})$	[2.6]	[2.6]
slimdz	$\dot{m}~(\dot{m}_{ m Edd})$	0.14 ± 0.04	0.11 ± 0.02
	θ (°)	[10]	[10]
	$M_{ullet}\left(M_{\odot}\right)$	$[5.7 \times 10^4]$	$[5.7 \times 10^4]$
	a_{ullet}	[0.99]	[0.99]
С	C-stat/d.o.f.	1.4/5	6.5/5

TIDAL DISRUPTION EVENT AT2020OCN: EARLY—TIME X—RAY FLARES CAUSED BY A POSSIBLE DISC ALIGNMENT PROCESS

Z. Cao, P.G. Jonker, D.R. Pasham, S. Wen, N.C. Stone, A.I. Zabludoff The Astrophysical Journal, Volume 970, Issue 1, July 2024

Abstract

A tidal disruption event (TDE) may occur when a star is torn apart by the tidal force of a black hole (BH). Eventually, an accretion disc is thought to form out of stellar debris falling back towards the BH. If the star's orbital angular momentum vector prior to disruption is not aligned with the BH spin angular momentum vector, the disc will be tilted with respect to the BH equatorial plane. The disc will eventually be drawn into the BH equatorial plane due to a combination of the Bardeen-Petterson effect and internal torques. Here, we analyse the X-ray and UV observations of the TDE AT2020ocn obtained by Swift, XMM-Newton, and NICER. The X-ray light curve shows strong flares during the first ≈ 100 days, while, over the same period, the UV emission decays gradually. We find that the X-ray flares can be explained by a model that also explains the spectral evolution. This model includes a slim disc viewed under a variable inclination plus an inverse-Comptonisation component processing the slim disc emission. A scenario where the ongoing Lense-Thirring precession during the disc alignment process is responsible for the observed inclination variations is consistent with the data. In later observations, we find that the X-ray spectrum of AT2020ocn becomes harder, while the mass accretion rate remains at super-Eddington levels, suggesting the formation of a corona in line with accretion onto other compact objects. We constrain the BH mass to be $(7^{+13}_{-3}) \times 10^5~{\rm M}_\odot$ at the 1σ (68%) confidence level.

4.1 Introduction

A star can be broken apart by tidal forces when approaching a black hole (BH), triggering a tidal disruption event (TDE; e.g., Hills 1975; Rees 1988). A part of the stellar debris from the disrupted star will fall back toward the BH. The orbit of this fallback material is expected to form an accretion disc (Rees 1988; Evans & Kochanek 1989; Ulmer 1999). Dozens of TDEs have been reported in the literature (Gezari 2021), and the number of candidates is increasing rapidly, thanks to large–scale sky surveys such as *Zwicky Transient Facility* (ZTF; Graham et al. 2019), *Asteroid Terrestrial-impact Last Alert System* (ATLAS; Tonry et al. 2018), and *All Sky Automated Survey for Supernovae* (ASAS–SN; Shappee et al. 2014).

The disruption often leads to processes that generate optical/UV and X-ray emission (e.g., Bade et al. 1996; Komossa et al. 2004; Gezari et al. 2006; van Velzen et al. 2011; Saxton et al. 2014; van Velzen et al. 2020; Saxton et al. 2020), which allows for the detection of massive BHs and the study of accretion processes. The thermal emission that is thought to originate in an accretion disc often dominates the TDE X-ray spectrum (e.g., Ulmer 1999; Lodato & Rossi 2011; Auchettl et al. 2017). In some cases, non-thermal power-law-like X-ray emission is also observed (e.g., Saxton et al. 2017; Lin et al. 2017b; Wevers et al. 2019b; Lin et al. 2020; Jonker et al. 2020). This non-thermal X-ray emission has been associated with the inverse-Comptonisation process where the thermal disc photons act as seed photons. While the late-time optical/UV emission (typically several hundreds of days after the initial disruption) is consistent with originating from the disc (e.g., Van Velzen et al. 2019; Mummery & Balbus 2020; Wen et al. 2023), the origin of the early time optical and UV emission is still a matter of debate (e.g., see Roth et al. 2020 for a review). One possibility is that UV photons are powered by the shocks (self-intersection shocks, or nozzle shocks) in the debris streams during the circularisation process, dissipating energy and angular momentum of the streams (e.g., Piran et al. 2015; Shiokawa et al. 2015; Ryu et al. 2020; Andalman et al. 2022; Steinberg & Stone 2024). Another possibility is that the UV emission comes from a "reprocessing layer" that captures the X-rays emitted by the inner disc and re-emits their energy in the UV (e.g., Loeb & Ulmer 1997; Metzger & Stone 2016; Roth & Kasen 2018; Dai et al. 2018; Wevers et al. 2019b; Bonnerot & Lu 2020).

When the orbital angular momentum vector of the star prior to disruption is not aligned with the BH spin angular momentum vector, the disc plane might well be misaligned with respect to the BH equatorial plane (e.g., Stone & Loeb 2012; Franchini et al. 2016). Due to a combination of the Bardeen–Petterson effect (Stone & Loeb 2012) and internal torques (Franchini et al. 2016), (the inner part of) this tilted disc will eventually be forced to align with the equatorial plane of a spinning BH. Predicted in theory and found in simulations, this disc alignment process manifests itself largely as Lense–Thirring precession, with the observed inclination angle of the disc varying during the process (e.g., Fragile & Anninos 2005; Franchini et al. 2016; Zanazzi & Lai 2019; White et al. 2019). A varying disc inclination likely affects the broadband appearance of the source (e.g., Dai et al. 2018). It has been proposed that the disc alignment is important in explaining the highly variable jet features observed in jetted TDEs (e.g., Swift J164449.3+573451;

4.1 Introduction 65

Tchekhovskoy et al. 2014; Liska et al. 2018; see also Teboul & Metzger 2023).

TDE studies can help test accretion theories in the super–Eddington regime. The mass accretion rate in the disc formed after the disruption can vary from highly super–Eddington to sub–Eddington levels (Strubbe & Quataert 2009; Lodato & Rossi 2011; Guillochon & Ramirez-Ruiz 2013; Metzger & Stone 2016). In the high–/super–Eddington regime, energy advection across the BH horizon can no longer be neglected, and the disc geometry is different from the standard Shakura–Sunyaev geometrically thin disc; instead, the disc is geometrically thick (Abramowicz et al. 1988). In such cases, a "slim" disc model (e.g., Abramowicz et al. 1988; Sądowski 2009; Sądowski et al. 2011) is more appropriate than the standard thin disc model (Shakura & Sunyaev 1973). Furthermore, TDEs are good laboratories for studying the spectral evolution associated with the transition from super– to sub– Eddington mass accretion rate. Many TDEs show spectral state transitions in the X–rays along their decay (e.g., Komossa et al. 2004; Jonker et al. 2020; Wevers et al. 2019b; Cao et al. 2023). Modelling the TDE X–ray spectrum allows to test whether such transitions appear under the same physical conditions as spectral state transitions observed in other super–Eddington accretors (e.g., ultraluminous X–ray sources, hereafter ULXs; Gladstone et al. 2009; Sutton et al. 2013; Kaaret et al. 2017).

The broadband source AT2020ocn (ZTF18aakelin) was first detected by ZTF in the optical on 2020-04-29 (Modified Julian Date, MJD 58968) and has been classified as a TDE candidate by Gezari et al. (2020). It is located at the centre of an otherwise quiescent, early type galaxy SDSS J135353.80+535949.7 at a redshift of z=0.0705. The $M-\sigma_*$ relation suggests a BH mass of $\sim 10^{6.4\pm0.6}$ solar mass (Pasham et al. 2024b). Subsequent observations by the *Neil Gehrels Swift* satellite revealed the source to be bright in the UV and the X–ray band (Gezari et al. 2020; Miller & Reynolds 2020). *Neutron star Interior Composition ExploreR (NICER)* started monitoring the source on 2020-07-11 (MJD 59041). Recently, Pasham et al. (2024b) discovered a ~ 17 day quasiperiodicity modulating the X–ray flux of AT2020ocn as observed by *NICER* over the first ~ 130 days. Various mechanisms can lead to this phenomenon, including a precessing accretion disc, as suggested by those authors. Therefore, a spectral analysis with physical models is needed to see which mechanisms are consistent with the data.

In this paper, we use a standard Λ CDM cosmology with $H_0 = 67.4 \,\mathrm{km \, s^{-1} \, Mpc^{-1}}$, $\Omega_m = 0.315$ and $\Omega_{\Lambda} = 1$ - $\Omega_m = 0.685$ (Aghanim et al. 2020) when converting the redshift to the luminosity distance. Throughout the paper, c is the speed of light, G is the gravitational constant, r is the radial coordinate measured from the BH centre, and R_g is the gravitational radius $\frac{GM_{\bullet}}{c^2}$ for a BH of mass M_{\bullet} . We use R_* and M_* , for the stellar radius and mass of the star prior to the disruption, respectively. R_t is the tidal radius of the TDE, defined as $R_t = R_*(M_{\bullet}/M_*)^{1/3}$.

Here we analyse the light curves in the UV and X–ray bands, and spectra of AT2020ocn obtained by *Swift*, *XMM-Newton*, and *NICER*. The paper is structured as follows: In Section 2, we describe our data reduction method. In Section 3, we present the results from our analyses. In Section 4 we discuss the physical scenarios implied by our modelling. In Section 5, we present our conclusions.

4.2 Data and data reduction

4.2.1 *NICER*

We started our *NICER* data analysis with the raw/level–1 files available on the HEASARC public archive¹. First, we reduced the data using the *nicerl2* task. Then, Good time intervals (GTIs) were produced with the default filters. We used the 3c50 background model (Remillard et al. 2022) to extract background spectra on a per GTI basis. Following the recommendations by Remillard et al. (2022) we excluded GTIs that do not pass the level-3 filtering. For more details of our procedure, please see Pasham et al. (2023, 2022). Both the background and the source+background spectra of *NICER* are rebinned by the optimal–binning algorithm (Kaastra & Bleeker 2016; ftool command ftgrouppha). Also, we ensure that both the background and the source+background spectra have a minimum of one count per bin (with parameter grouptype in ftgrouppha set to optmin).

Due to the super–soft X–ray nature of the source, *NICER* source counts are significantly below the background counts roughly above 1.1 keV for most of its observations. Therefore, we ignore *NICER* bands above 1.1 keV in this study. Meanwhile, to avoid spectra dominated by the noise in the background and uncertainties in estimating the background level, we exclude *NICER* observations where the source counts rate is lower than the background counts rate in 0.3-0.5 keV band. In this way, 1010 out of 1125 epochs of *NICER* observations remain.

When performing spectral analysis on *NICER* spectra, systematic errors of $1.5\%^2$ in the 0.3-1.1 keV band are added to the spectra using the "systematic" command in the XSPEC package (Arnaud 1996; version 12.13.0c). We adjust the fitting energy range of each *NICER* spectrum using the ignore command in XSPEC, to discard the energy bins of the hard spectral tail where the source flux is lower than the background flux. The number of the discarded energy bins differs from epoch to epoch. Meanwhile, to have sufficient bins to fit a two-parameter fit-function, we further require the spectrum to have a fitting energy range from 0.3 keV to at least 0.6 keV (>3 bins) to be considered for the fit procedure. In the analysis, data are considered to be consistent with the fit-function if C-stat/d.o.f. < 2.

4.2.2 XMM-*Newton*

AT2020ccn was observed by *XMM-Newton* on three occasions during the *NICER* monitoring. The observations are identified by their ID: 0863650101 (XMM#1), 0863650201 (XMM#2), and 0872392901 (XMM#3). For the *XMM-Newton* data reduction, we use HEASOFT (version 6.31.1) and SAS (version 20.0.0) with the calibration files renewed on October 25th, 2022 (CCF release: XMM-CCF-REL-391). During XMM#2, the observation of two MOS detectors was interrupted for calibration purposes. Therefore, for consistency, we do not use the MOS data. We also do not use the RGS data, because the signal—to—noise ratio in the RGS detectors is too low.

¹https://heasarc.gsfc.nasa.gov

²identical to the systematic errors applied by the NICER data reduction task niphasyserr. See https://heasarc.gsfc.nasa.gov/docs/nicer/analysis_threads/spectrum-systematic-error/

TABLE 4.1: *XMM-Newton* observations of AT2020ocn analysed in this work. The exposure time is the time remaining after filtering for epochs of enhanced background count rates. The average count rates of the source+background spectra are given in the energy ranges 0.3–1.1 keV for XMM#1 & 2, and in 0.3–10.0 keV for XMM#3. We also list in the last column the source counts calculated by subtracting the estimated number of background counts in the source extraction region.

Satellite	ObsID (Label)	Date	Exposure (ks)	Source region	Count rate (cts/s)	Est. Source counts (cts)
XMM-Newton	0863650101 (XMM#1)	2020-07-18	46	annulus (15"-30")	$(4.5 \pm 0.1) \times 10^{-2}$	1517
	0863650201 (XMM#2)	2020-07-21	47	annulus (15"-30")	$(6.3 \pm 0.1) \times 10^{-2}$	2833
	0872392901 (XMM#3)	2021-05-15	42	circular (30")	$(67.6 \pm 0.4) \times 10^{-2}$	27546

We use the SAS command EPPROC to process the Science 0 data from XMM-Newton/EPIC-pn. We employ the standard filtering criteria³ for EPIC-pn data, where we require that the 10–12 keV detection rate of pattern 0 events is < 0.4 counts s⁻¹. This way the data are cleared from periods with an enhanced background count rate. We use a circular source region of 30" radius centred on the source for the spectral counts extraction, corresponding to a ~90\% energy fraction encirclement for a point source. Using the SAS command EPATPLOT, we check for the presence of photon pile-up, and find that XMM#1 and XMM#2 are suffered by pile-up while XMM#3 does not. To clean the spectra from the pile-up effect, we use an annulus region of 15" inner radius and 30" outer radius for the source counts extraction of XMM#1 and XMM#2. We find no pile-up effect in the data when using such an annulus source region. In all three XMM-Newton observations, the background spectral counts are extracted from apertures close to the source on the same EPIC-pn detector and free from other bright sources. We use a circular region of 50" radius for the background extraction. Using the specgroup command in SAS, we rebin both the background and the source+background spectra of XMM-Newton/EPIC-pn to have a minimum of one count per bin, while the oversampling factor is 3. We summarise the XMM-Newton data used in this paper in Table 4.1.

In this study we focus on the 0.3-10.0 keV band for the *XMM-Newton*/EPIC-pn data. We find in XMM#1 and XMM#2 the background counts dominate the source+background spectrum $\gtrsim 1$ keV. Therefore, we discard data above 1.1 keV during the analysis of XMM#1 and XMM#2, which is consistent with our treatment to the *NICER* data.

4.2.3 *Swift*

We complement our study of the X-ray flares of AT2020ocn with the UV data from the UVOT instrument (Roming et al. 2005) on–board *Swift* satellite. We reduce the archived *Swift*/UVOT images of AT2020ocn obtained between 2020-06-25 (MJD 59025) and 2021-06-22 (MJD 59387) using the UVOTPRODUCT task. We use a circular source region centred on the coordinates of AT2020ocn provided in the SIMBAD astronomy database⁴, using a standard radius of 5 arcsec as suggested by the *Swift* team⁵. We use an annulus centred on the source as the background

³https://www.cosmos.esa.int/web/xmm-newton/sas-thread-epic-filterbackground

⁴http://simbad.u-strasbg.fr/simbad/

⁵https://www.swift.ac.uk/analysis/uvot/mag.php

region, with an inner radius of 10 arcsec and an outer radius of 25 arcsec. We also extract the soft X-ray light curve from the *Swift*/XRT instrument using the online XRT tool⁶ (Evans et al. 2009), to compare with the X-ray behaviour of AT2020ocn as seen by *NICER*.

Throughout this paper, we carry out the spectral analyses using the XSPEC package (Arnaud 1996; version 12.13.0c). We use Poisson statistics (Cash 1979; C-STAT in XSPEC). In this paper, we quote all the parameter errors at the 1σ (68%) confidence level, assuming Δ C-stat=1.0 and Δ C-stat=2.3 for single– and two–parameter error estimates, respectively. In the figures the spectra are re-binned for plotting purposes only. In all fits we perform in this paper, we include the Galactic absorption using the model TBabs (Wilms et al. 2000), and we fix the column density $N_{H,G}$ to its measured value at the host direction of $1 \times 10^{20} \text{cm}^{-2}$ (Schlafly & Finkbeiner 2011). No intrinsic absorption is found by any of our fits in this paper. With the energies command in XSPEC, in all analysis we take a logarithmic energy array of 1000 steps from 0.1 to 1000.0 keV for model calculations instead of energy arrays from the response file, to be self–consistent and to correctly calculate the Comptonisation model when needed (see Section 4.3.3). When needed, we use the Akaike information criteria (AIC; Akaike 1974) to investigate the significance of adding model components to the fit–function, which is calculated by Δ AIC= $-\Delta$ C + 2Δ k (C is the C-stat and k is the degree–of–freedom; Wen et al. 2018). The Δ AIC>5 and >10 cases are considered a strong and very strong improvement, respectively, over the alternative model.

For each spectrum of *XMM-Newton*/EPIC-pn or *NICER*, we first fit the background spectrum with a phenomenological model. When fitting the source+background spectrum, we then add the best–fit background model to the fit function, fixing the parameters of the background model to their best–fit values determined from the fit to the background–only spectrum. The best–fit background model for *XMM-Newton*/EPIC-pn data varies from epoch to epoch, consisting of 1 Gaussian components and 2 power–law components for XMM#1 and XMM#2, or 3 power–law and 1 Gaussian components for XMM#3 that detects photons of higher energies, accounting for the background continuum and background fluorescence lines (e.g. Katayama et al. 2004). Meanwhile, we find the background spectra of *NICER* data can be described by a model consisting of 2 Gaussian components and 2 power–law components. The full–width half–maximum or FWHM σ_{gauss} is set to 0.001 keV for all the Gaussian components with an FWHM lower than the spectral resolution of *XMM-Newton*/EPIC-pn or *NICER*. In the following, when studying the source+background data, we refer only to the part of the fit function that describes the source as *fit function*.

4.3 Results 69

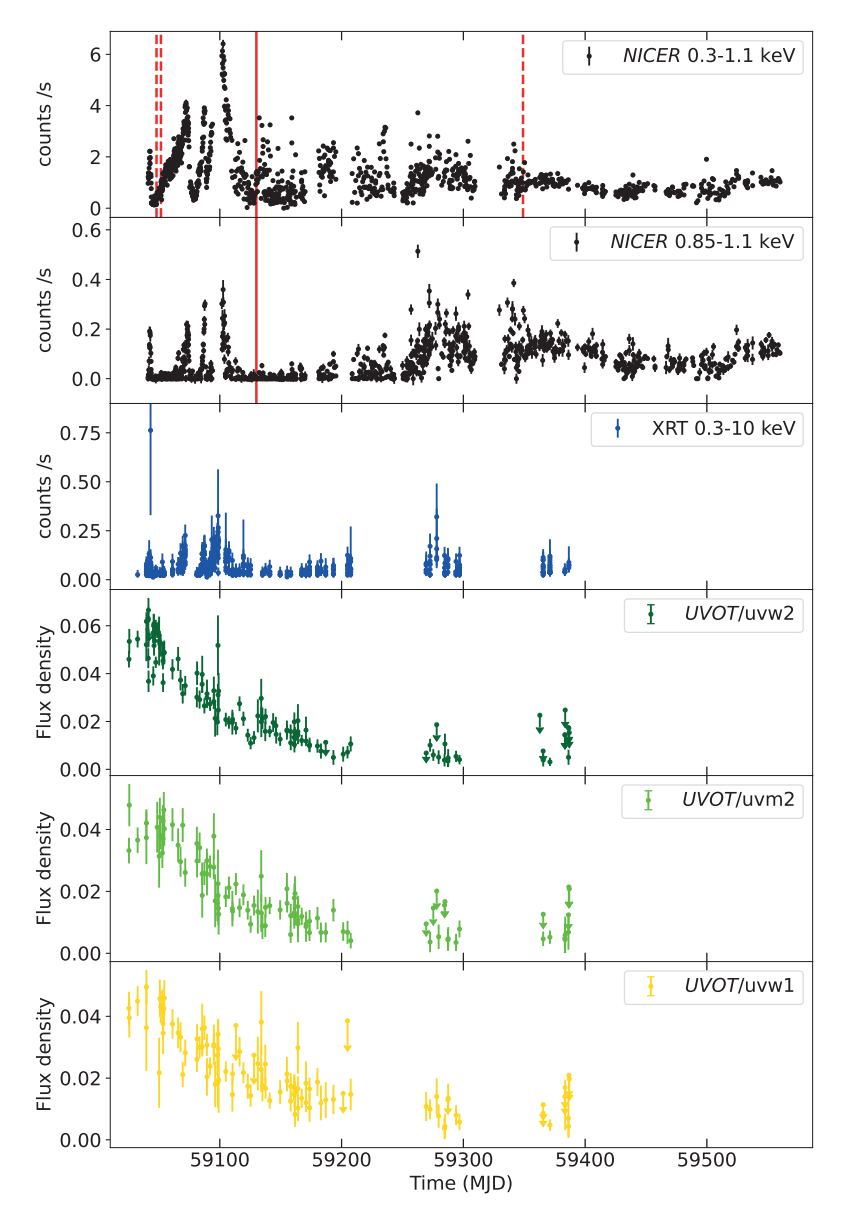


FIGURE 4.1: Long—term light curve of AT2020ocn as observed by *NICER* and *Swift*. From top to bottom: *NICER* count rate in the 0.3-1.1 keV band; *NICER* count rate in the 0.85-1.1 keV band; *Swift*/XRT count rate in the 0.3-10 keV band; the flux densities are in units of 10^{-26} erg/s/cm²/Hz for the *Swift*/UVOT light curves in the uvw1, uvm2, and uvw2 filters. The x-axis denotes Modified Julian Date (MJD). Dashed lines in the top panel mark the times of the *XMM-Newton* observations (in this paper we refer to these as XMM#1, XMM#2, and XMM#3 in chronological order). The solid line marks MJD 59130, the date we use in this paper to separate the so-called early and late periods.

4.3 RESULTS

4.3.1 Long-term light curve of AT2020ocn

We show the long–term UV and X–ray light curves of AT2020ccn in Fig. 4.1. Based on the *NICER* data, we find that the behaviour of the X–ray emission of AT2020ccn can be divided into two stages: an early period when strong X-ray flares are present (Modified Julian Date [MJD] ≤59130) and a late period of more gradual changes (MJD≥59130). There are 375 epochs for the early period, and 635 for the late period. The *NICER* hard X–ray (0.85-1.1 keV) count rate is low outside the flares in the early epoch data. The flares cannot be explained by background fluctuations (Fig. 4.A). In the late period, the light curve in the hard band shows a re–brightening around MJD 59300, with strong variations in the count rate. The X-ray light curve does not show a gradual decay in general. The *Swift*/XRT also detected the early X–ray flares. Meanwhile, the UV flux of AT2020ocn in all of the three UV bands of *Swift*/UVOT (uvw1, uvm2, and uvw2 band) decreases gradually with time, showing no evidence for flares such as those in the X-ray light curve. In other words, the X–ray and the UV light curves seem to be decoupled in the case of AT2020ocn.

4.3.2 Long-term spectral evolution of AT2020ocn

We study the spectral evolution of the source using the spectral hardness ratio in the *NICER* bands. We define the spectral hardness ratio as the ratio between the count rates in the 0.85-1.1 keV and the 0.3-0.5 keV bands. In an analogy with the hardness—intensity diagram used often in X—ray binary studies, we present the hardness ratios of the *NICER* data of AT2020ocn as a function of the broadband count rate (0.3-1.1 keV) in Fig. 4.2. We find that the evolution of the hardness ratio is different for the early and the late period. Generally, during the early period the source spectrum is softer and the observed flux is higher. The hardness evolution during the 4 flares traces out a different region of the hardness-intensity diagram, showing a harder—when—brighter pattern within each flare. During the late period, the source hardness ratio is higher while the observed flux is lower.

We here use phenomenological model fits to the *XMM-Newton/EPIC-*pn spectra to investigate the spectral changes between the early and late spectra in some detail. Of the three *XMM-Newton* observations obtained during the *NICER* monitoring period (marked by dashed lines in Fig. 4.1), the observation XMM#1 and XMM#2 are in the early period while XMM#3 falls in the late period. We find that the XMM#1 and the XMM#2 spectra can be fitted well together (C-stat/d.o.f. = 20.5/31) with a fit–function comprised of two blackbody models (Fig. 4.3, we used the blackbody model zbbody in XSPEC syntax). However, XMM#3 cannot be fitted well with such a fit function. Instead, it can be fitted with a power law with a photon index $\Gamma = 2.89 \pm 0.01$ (C-stat/d.o.f. = 316.5/166). Fig. 4.3 shows the different *XMM-Newton/EPIC-*pn spectra. The XMM#3 spectrum is much harder than the other two spectra. This spectral difference between

⁶https://www.swift.ac.uk/user_objects/

4.3 Results 71

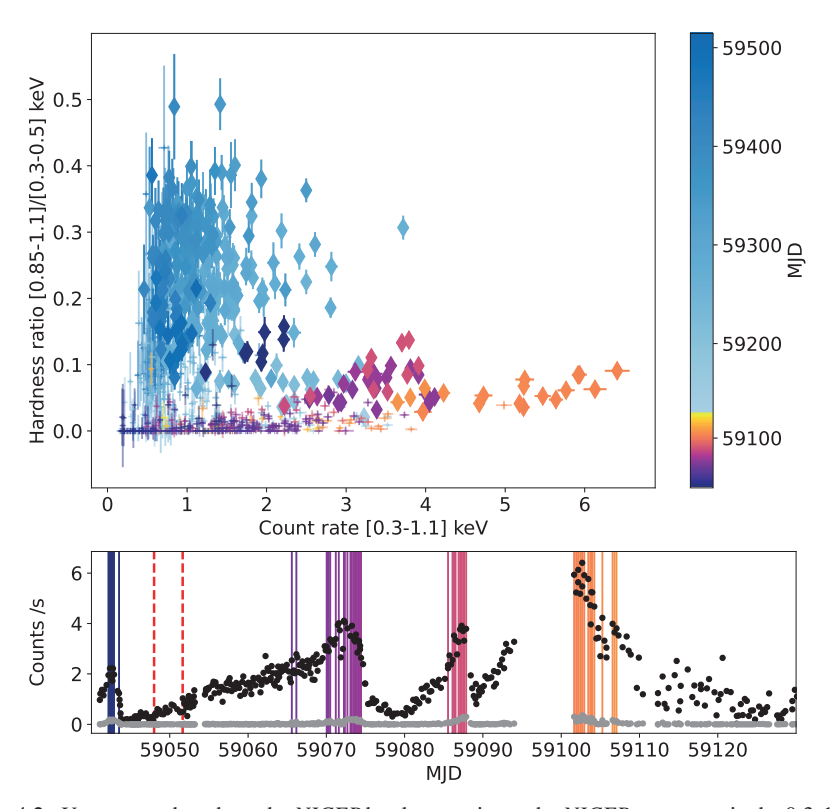


FIGURE 4.2: *Upper*: we show here the *NICER* hardness ratio vs. the *NICER* count rate in the 0.3-1.1 keV band. We define the spectral hardness ratio as the ratio between the count rate in the 0.85-1.1 keV band and that in the 0.3-0.5 keV band. The shown data are colour–coded by their observation time in MJD. We use different colours to show the hardness evolution during the early period (MJD<59130; from purple to yellow), and during the late period (MJD>59130; from light blue to dark blue). Epochs highlighted with diamond markers have the source count rate higher than the background count rate in the 0.85-1.1 keV band, so that their hardness ratios determined are least affected by the uncertainties in the *NICER* background estimation. *Bottom*: zoom-in of the *NICER* early–time light curve (i.e., data obtained before 59130 MJD) also shown in the *top* panel in Fig 4.1. The black and grey data show the source count rates in the 0.3-1.1 keV and 0.85-1.1 keV band, respectively. The solid coloured vertical lines mark the observation times of the corresponding data highlighted by diamond markers in the upper panel, following the same colour scheme. From left to right, the red dashed lines mark the observation time of XMM#1 and XMM#2, respectively.

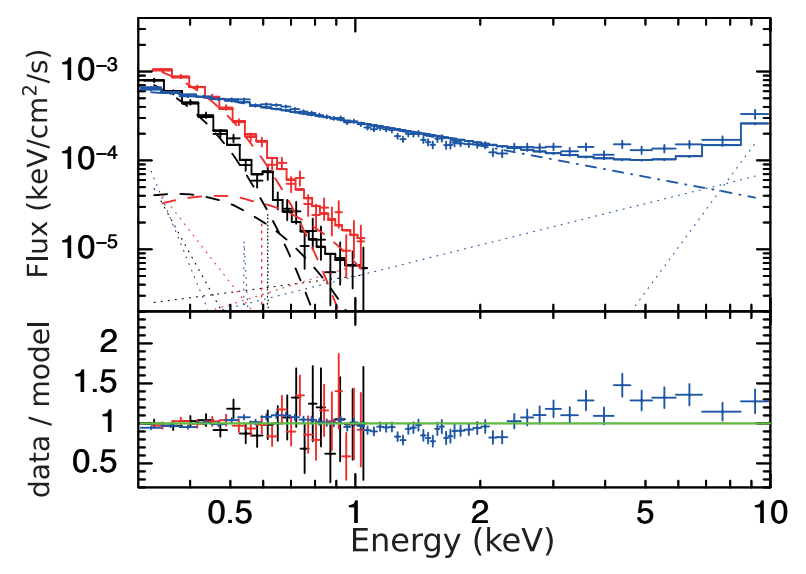


FIGURE 4.3: Top panel: We show the EPIC-pn source+background spectra of XMM#1 (*black*), XMM#2 (*red*), and XMM#3 (*blue*). The solid, dashed, dotted-dashed and dotted lines represent the best-fit total models using phenomenological source models, the blackbody models used for XMM#1 & 2, the power-law model used for XMM#3, and the contribution from the background as determined from fitting extracted spectra from background-only data separately, respectively. The best-fit background power-law indices and Gaussian parameters have been held constant during the fit to the source+background spectra. Bottom panel: The ratio between the observed number of counts in each spectral bin (data; black, red and blue points in the top panel) and the best-fit predicted number of counts in each spectral bin (model; solid lines in the top panel) is shown.

the early and late spectra observed by *XMM-Newton* is consistent with our findings based on the *NICER* data (Fig. 4.2).

4.3.3 Spectral analysis of X-ray data

4.3.3.1 XMM#1 AND XMM#2

To constrain parameters (such as the BH mass and spin, and the accretion rate) of AT2020ocn, we use the slim disc model slimdz (Wen et al. 2022) to simultaneously fit the two XMM#1 and XMM#2 spectra, allowing the mass accretion rate \dot{m} to vary between epochs. We find a good fit with the slim disc model (C-stat/d.o.f. = 26.4/34; XSPEC's syntax "TBabs*slimdz"). As stated in Section 4.2, we fix the column density of the Galactic absorption ($N_{H,G}$ in TBabs) to to its measured value in the host's direction $1 \times 10^{20} \text{cm}^{-2}$ (Schlafly & Finkbeiner 2011). We will keep using this $N_{H,G}$ value and fix it during the fits for all the following fit–functions considered in this paper. For a 1σ , single–parameter error estimate, the best–fit value for the BH mass M_{\bullet} is

4.3 Results 73

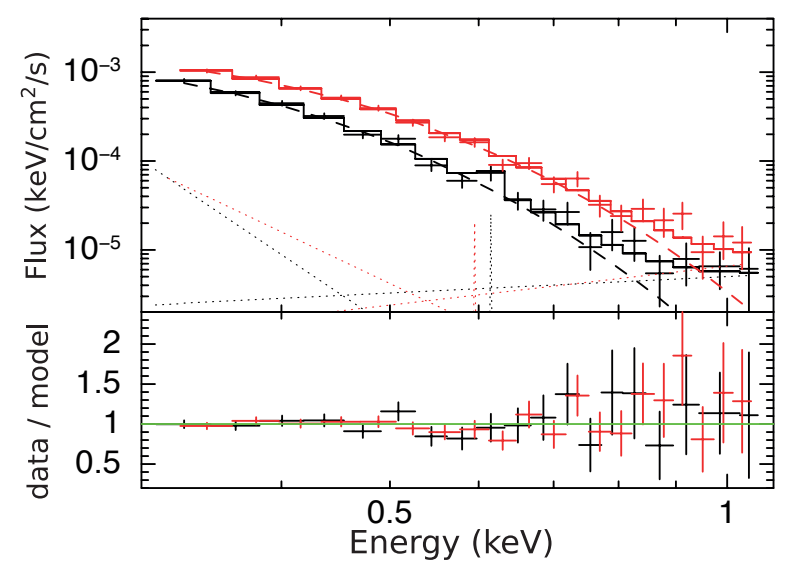


FIGURE 4.4: Top panel: the EPIC-pn XMM#1 (black) and XMM#2 (red) spectra of AT2020ocn fitted by a fit-function comprised of the following model components: TBabs*slimdz. The solid, dashed, and dotted lines represent the best-fit total model, the slim disc emission, and the contribution from the background as determined from fitting extracted spectra from background-only data separately, respectively. The best-fit background power-law indices and Gaussian parameters have been held constant during the fit to the source+background spectra. Bottom panel: We show the ratio between the observed number of counts (data; red and black points in the top panel) and the best-fit predicted number of counts in each spectral bin (model; red and black solid lines in the top panel).

 $(7\pm1)\times10^5~M_{\odot}$, and for the inclination it is 74^{+1}_{-11} degrees. The BH spin a_{\bullet} is constrained to have a lower limit of 0.25. We present the best–fit slim disc model in Fig. 4.4, and the parameter constraints in Table 4.2. The accretion rate \dot{m} at these two epochs do not differ from each other by more than 1σ error range. By investigating the Δ C-stat across the $\{M_{\bullet}, a_{\bullet}\}$ plane, we find a degeneracy between the BH mass and BH spin (Fig. 4.5): the lower limit on a_{\bullet} increases with increasing M_{\bullet} . In general, a_{\bullet} cannot be constrained. Specifically, the 1σ lower limit on a_{\bullet} for a two–parameter error estimate, at the best–fit BH mass value, is $a_{\bullet} > -0.1$. We also find an equivalently–good fit with not \dot{m} but θ varying between the two epochs (C-stat/d.o.f. = 26.1/34; Table 4.2). In this test case, the BH mass is $M_{\bullet} = (7\pm1)\times10^5~M_{\odot}$ and $a_{\bullet} > 0.41$; the inclination θ at these two epochs is consistent with being constant within 1σ (74^{+1}_{-9} degree for XMM#1, and 72^{+1}_{-9} degree for XMM#2).

4.3.3.2 NICER SPECTRA FROM THE EARLY FLARING PERIOD

Given the results of the spectral fits to the XMM#1 and XMM#2 data, we try to fit the individual *NICER* spectra of the early flaring period using the same fit–function (TBabs*slimdz). We aim

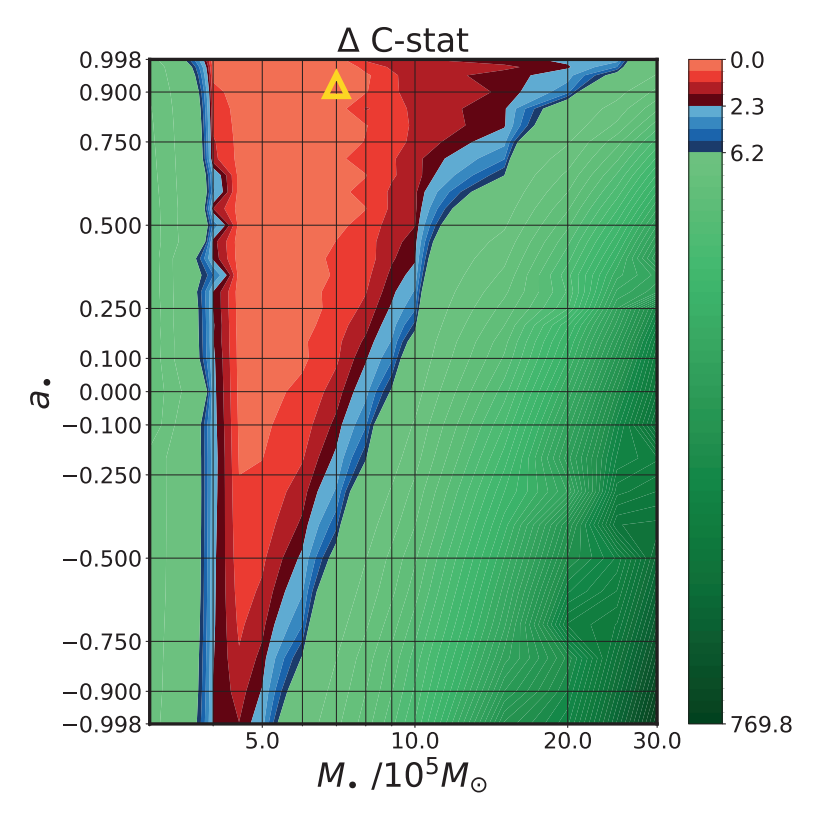


FIGURE 4.5: Constraints on M_{\bullet} and a_{\bullet} from the slim disc model-fit to the joint XMM#1 & 2 spectra. We calculate the ΔC -stat across the $\{M_{\bullet}, a_{\bullet}\}$ plane. The best–fit point with the lowest C-stat is marked by a yellow triangle. Areas within 1σ and 2σ for two–parameter error estimations are filled by red and blue colours, respectively. At 1σ for the two-parameter fits, M_{\bullet} is constrained to be $(7^{+13}_{-3}) \times 10^5 \, \mathrm{M}_{\odot}$.

to test whether allowing the values of one or more parameters of the slim accretion disc to vary can explain the spectral and flux variability observed by *NICER* over the early period. According to our selection criteria of *NICER* data as described in Section 4.2.1, a total of 206 epochs in the early period are considered for the spectral analysis. We list these epochs in Table 4.A.

For the slim disc fit function, we fix the BH mass M_{\bullet} to the best-fit value obtained from the joint XMM#1 and XMM#2 spectral fit using the same fit-function $(7 \times 10^5 M_{\odot})$, and we fix the BH spin $a_{\bullet} = 0.9$. This spin value corresponds to the best-fit slim disc model to the joint XMM#1 & 2 spectra given our choice of the BH mass value (Fig. 4.5).

We first test whether the spectral evolution of the early period *NICER* data can be explained by a slim disc varying its accretion rate \dot{m} as well as its inclination angle θ with respect to our line-of-sight. We find that for only 108 out of the 206 *NICER* early spectra this procedure gives a C-stat/d.o.f. < 2 (Fig. 4.B). The slim disc model fails to fit most of the spectra at the peak of each

4.3 Results 75

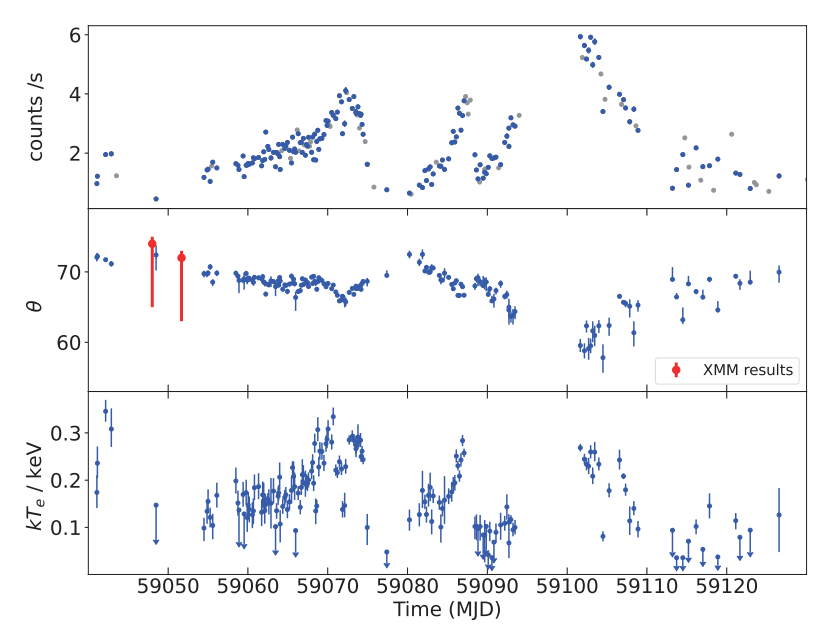


FIGURE 4.6: *Top panel*: The *NICER* 0.3-1.1 keV early–time source light curve. We only consider the epochs where the source flux stays above the background level from 0.3 keV to at least 0.6 keV (a total of 206 epochs in the early period). Spectra at epochs marked by blue dots are well–fit (C-stat/d.o.f. < 2) by the model in this analysis, while grey dots mark spectra that have C-stat/d.o.f. > 2. *Middle panel*: Inclination θ constraints derived from the *NICER* spectra obtained before MJD 59130. The fit–function is comprised of the following model components: TBabs*(thcomp*slimdz). We fit each of the 206 spectra individually allowing the inclination θ , and the temperature of the Comptonising medium kT_e to vary. We fix $M_{\bullet} = 7 \times 10^5 \ M_{\odot}$ and $a_{\bullet} = 0.9$ based on the results of the spectral fits to the *XMM-Newton* data (Fig. 4.5). The slim disc accretion rate \dot{m} and the optical depth of the Comptonising medium are held fixed at a value of $30 \ \dot{m}_{\rm Edd}$ and $\tau = 20$, respectively. We show the fit parameter values for the 165 out of the 206 spectra where the C-stat/d.o.f. < 2 (the results from the blue points in the top panel). The inclinations constrained from the joint–fit to the XMM#1 and XMM#2 X–ray spectra are marked with the red dots. *Bottom panel*: Constraints on the electron temperature kT_e derived from the same fitting procedure described above.

flare. Specifically, from the fit residuals we find the spectral hardening at the flare peaks makes the spectrum deviate from a slim disc model (e.g., Fig. 4.C). We conclude that the X-ray flares of AT2020cm in the early period can not be fully explained by only varying the disc accretion rate \dot{m} and the inclination angle θ .

A hard spectral component additional to a disc continuum in the X-ray spectra of BH accretion systems has been interpreted before to be due to inverse–Comptonisation (IC; e.g., Belloni 2009; Kubota & Done 2019; Mummery & Balbus 2021), where high–energy electrons scatter the soft disc photons to higher energies. This IC component is commonly used to explain the harder–than–disc BH spectra in many TDEs or ultra–luminous X-ray sources that have been proposed to be at near–/super– Eddington accretion rate (e.g., Magdziarz et al. 1998; Gladstone et al. 2009; Saxton et al. 2019; Wevers et al. 2021; Yao et al. 2022a). Therefore, we test if the spectra at the peak of the flares can be fit well when including an IC component with seed photons coming from the slim disc, using the model thcomp (Zdziarski et al. 2020; the thcomp model parameterises the up–scattered spectra through the Thomson optical depth τ and the electron temperature kT_e . The total fit function in XSPEC's syntax is "TBabs*thcomp*slimdz"). We fix the covering fraction of thcomp to unity, so that all seed photons go through the Comptonising medium. Given the data quality we find parameter degeneracies in most epochs between the IC electron temperature kT_e and the IC optical depth τ . The best–fit τ is typically \gtrsim 10. We therefore fix τ = 20 during the fit so that the IC component is parameterised by a single free parameter (kT_e).

We find that for 165 out of the 206 NICER early spectra the fit procedure gives a C-stat/d.o.f. < 2 by assuming a similar \dot{m} as determined in XMM#1 & 2 ($\dot{m}=30~\dot{m}_{\rm Edd}$). Each spectrum has at least 2 d.o.f. left to be fitted with a 2–parameter (θ and kT_e) fit function, and most of the not–well–fit spectra also give a C-stat/d.o.f. close to 2 (Fig. 4.D). We present the evolution of the parameter constraints produced from this fit procedure in Fig. 4.6. This slim disc+IC model can fit most of the spectra at flare peaks (e.g., Fig 4.E). We find that the Comptonising medium becomes hotter ($kT_e \sim 0.3~{\rm keV}$) during the flares, while the kT_e is lower ($kT_e \lesssim 0.3~{\rm keV}$) outside the flares. Meanwhile, no intrinsic absorption is needed to model any flares.

Next, we investigated if variations in \dot{m} and kT_e can explain the early X–ray flares instead of variations in θ and kT_e . When fitting individual spectra, we fix θ to the best–fit value determined from XMM#1 & 2 (74°) and let \dot{m} and kT_e free to vary. This fit procedure results in a much lower number of spectra to be well-fit by the slim disc+IC model (59 spectra fitted instead of 165 for the procedure where θ and kT_e are free to vary). Letting also τ free to vary does not improve the fits. We conclude that the variation in inclination are likely to be important during the early period, while the \dot{m} variation is not the leading factor causing the flares.

4.3.3.3 THE LATE-TIME SPECTRUM OBSERVED IN XMM#3

During the late–time period (MJD>59130) XMM-Newton observed AT2020ocn once (XMM#3). The spectrum of XMM#3 can be well-fit by a power law with index $\Gamma = 2.89 \pm 0.01$ (TBabs*powerlaw; C-stat/d.o.f. = 316.5/166). However, there are trends in the residuals for this fit showing the model under–predicting the data systematically above 2 keV (Fig. 4.7). The fit can be then significantly

4.3 Results 77

Table 4.2: Parameter constraints and the fit statistics from our joint–fits to the XMM#1 and XMM#2 spectra. Parameter values held fixed during the fit are given inside square brackets. In this table we quote the parameter errors derived using ΔC -stat=1.0 for single–parameter error estimates. The first joint–fit assumes a difference in the mass accretion rate \dot{m} between the two epochs, while the second joint–fit assumes a difference in the inclination θ .

Fit-function	Epoch	Tbabs	slimdz				
		$N_H/10^{20} \text{ cm}^{-2}$	$\dot{m}/\dot{m}_{ m Edd}$	$\theta/^{\circ}$	M_{ullet}/M_{\odot}	a_{\bullet}	
Tbabs*slimdz	Tbabs*slimdz XMM#1		> 17	74^{+1}_{-11}	$(7\pm1)\times10^5$	> 0.25	
	XMM#2	=XMM#1	$19^{+173}_{-6} = XMM#1 = XMM#1$			‡ 1	
	C-stat/d.o.f. = 26.4/34						
			slimdz				
Fit-function	Epoch	Tbabs		sli	imdz		
Fit-function	Epoch	Tbabs $N_H/10^{20}~\mathrm{cm}^{-2}$	$\dot{m}/\dot{m}_{ m Edd}$	$ heta/^\circ$	imdz M_{ullet}/M_{\odot}	a_{ullet}	
Fit-function Tbabs*slimdz	Epoch XMM#1		$\dot{m}/\dot{m}_{\rm Edd}$ 27^{+171}_{-4}			<i>a</i> • > 0.41	
		$N_H/10^{20}~{\rm cm}^{-2}$,	θ/°	M_{ullet}/M_{\odot}	> 0.41	

improved using a fit–function consisting of a power law and a black body (C-stat/d.o.f. = 193.1/164 and Δ AIC = 119.4; XSPEC's syntax "TBabs*(powerlaw+zbbody)"). The black body model with a temperature of ~0.12 keV accounts for part of the continuum at the soft end (<2.0 keV; Fig. 4.F).

Besides these phenomenological models, we use a fit-function to fit the spectrum of XMM#3 that contains TBabs*thcomp*slimdz. Like the case using a fit-function of only a power-law, this fit-function does not describe the XMM#3 data well and has similar residuals. Part of the coronal emission can be reflected off the accretion disk, this reflection spectrum is calculated using the relxillCp model (Dauser et al. 2014; García et al. 2014). In relxillCp, the disc is assumed to be a standard Shakura–Sunyaev thin disc (Shakura & Sunyaev 1973), and the incident coronal emission is modelled by nthcomp (the now depreciated, stand–alone version of thcomp; Zdziarski et al. 1996, 2020), that assumes a multi–temperature black body seed spectrum. There are currently no reflection models using a slim disc for the disc seed photons, and so we use relxillCp to approximate the reflected emission off a slim disc. For this reason, one should be cautious when interpreting the results.

Overall, the total fit-function in XSPEC's syntax is "TBabs*(thcomp*slimdz+relxillCp)". Given the mentioned inconsistency of disc assumptions between the two model components, we do not try to measure the M_{\bullet} and a_{\bullet} values by analysing XMM#3 using this fit-function. Instead, we fix the M_{\bullet} and a_{\bullet} to their best-fit values from the analysis of XMM#1 & 2 (Fig. 4.5). The inclination θ shared between the slimdz and relxillCp models is free to float in the fit but it is required to be the same between models. The kT_e shared between the thcomp and relxillCp models is also free to float in the fit but likewise it is required to be the same between models. We fix the Refl_{frac} parameter in relxillCp to be -1 so that the model only accounts for the reflected emission. Other parameters for relxillCp that we have held fixed are: the iron abundance $A_{\rm Fe} = 1$ (in units of the solar abundance), the redshift z = 0.0705, the disc inner radius which we

assumed to be at the innermost–stable–circular–orbit (ISCO; $R_{\rm in}=-1$ in relxillCp's syntax), the disc's particle density $\rho=10^{17}$ cm⁻³ from order–of–magnitude estimations (Stone 2015), and the disc outer radius $R_{\rm out}=100R_g$ since that is the typical scale of a TDE disc for a BH of $1\times 10^6~M_\odot$ (Franchini et al. 2016; Zanazzi & Lai 2019). Since the X–ray emission is generated primarily in the inner–most accretion region, the disc outer radius will have little effect on the fit results. Finally, the reflection emissivity is set to be r^{-q} within $15R_g$ and r^{-3} outside $15R_g$ with q as a free parameter).

We find that the spectrum XMM#3 can be well-fit by such a fit-function (C-stat/d.o.f. = 175.0/159; Fig. 4.7). This fit statistic is better (Δ AIC = 8.1) than that of the phenomenological fit with a power law and a black body. Adding relxillCp into the fit-function improves the fit significantly (Δ AIC = 96.8) compared to the fit-function without the relxillCp model component ("TBabs*(thcomp*slimdz)"; C-stat/d.o.f. = 279.8/163). We find that the corona is optically thick ($\tau \gtrsim 1$) and warm ($kT_e < 10 \text{ keV}$), and the covering fraction of the corona over the disc continuum needs to be less than unity so that ~20% of the disc photons are observed without being Comptonised. A full list of parameter constraints from the fit is presented in Table 4.3. Letting the disc's particle density be a free parameter does not improve the goodness-of-fit (Δ AIC = -0.1), and neither does letting the iron abundance be a free parameter (Δ AIC = -2).

4.3.4 Analysis of UV data using MOSFiT

We analyse *Swift/*UVOT photometry data for the observations listed in Table 4.B using the Modular Open Source Fitter for Transients (MOSFiT; Guillochon et al. 2018). The assumptions and details of its TDE module can be found in Mockler et al. (2019). In summary, the module simultaneously fits the UV light curves using a library for model light curves derived using hydrodynamical simulations of TDEs (Guillochon & Ramirez-Ruiz 2013). The fallback mass rate $\dot{M}_{\rm fb}(t)$ as a function of time is determined from the simulations by varying the M_{\bullet} , the stellar mass M_{*} , and the scaled impact parameter b^{7} . Then the $\dot{M}_{\rm fb}$ is transformed into a viscously–delayed accretion rate $\dot{M}_{\rm acc}$ using the viscous timescale $T_{\rm visc}$ (eq. 7 in Mockler et al. 2019). The module assumes a time–independent efficiency ϵ in the energy conversion from $\dot{M}_{\rm acc}c^{2}$ to a bolometric luminosity L so that $L = \epsilon \dot{M}_{\rm acc}c^{2}$. Then assuming thermal radiation, this radiation is emitted from a photosphere with an effective temperature $T_{\rm eff}(L,R_{\rm ph})$, where the photospheric radius $R_{\rm ph} = R_{\rm ph,0}a_{\rm p}(L/L_{\rm Edd})^{l_{\rm ph}}$. Here $R_{\rm ph,0}$ is a normalising factor, and $l_{\rm ph}$ is an exponential index (eq. 9& 10 in Mockler et al. 2019). The $a_{\rm p}$ can be regarded as the semimajor axis of the averaged bound orbit of material being accreted when the $\dot{M}_{\rm fb}$ is at its peak.

The fit parameters are M_{\bullet} , M_{*} , b, $T_{\rm visc}$, ϵ , $R_{\rm ph,0}$, $l_{\rm ph}$, the difference t_0 between the time at peak luminosity and the time of the first detection, and the host column density $N_{\rm H,host}$. Given no intrinsic absorption is found in the X–ray analysis, we fix the $N_{\rm H,host} = 1 \times 10^{19}$ cm⁻² an order–of–

⁷The impact parameter β can be calculated from b: if $0 \le b < 1$, $\beta = 0.6 + 1.25b$ when $\gamma = 4/3$, and $\beta = 0.5 + 0.4b$ when $\gamma = 5/3$; if $1 \le b \le 2$, $\beta = 1.85 + 2.15(b - 1)$ when $\gamma = 4/3$, and $\beta = 0.9 + 1.6(b - 1)$ when $\gamma = 5/3$. Here γ is the polytropic index of the disrupted star so that the equation–of–state of the star is $P \propto \rho^{\gamma}$ (P is the pressure and ρ is the density). See more in Guillochon & Ramirez-Ruiz 2013 and Mockler et al. 2019.

4.3 Results 79

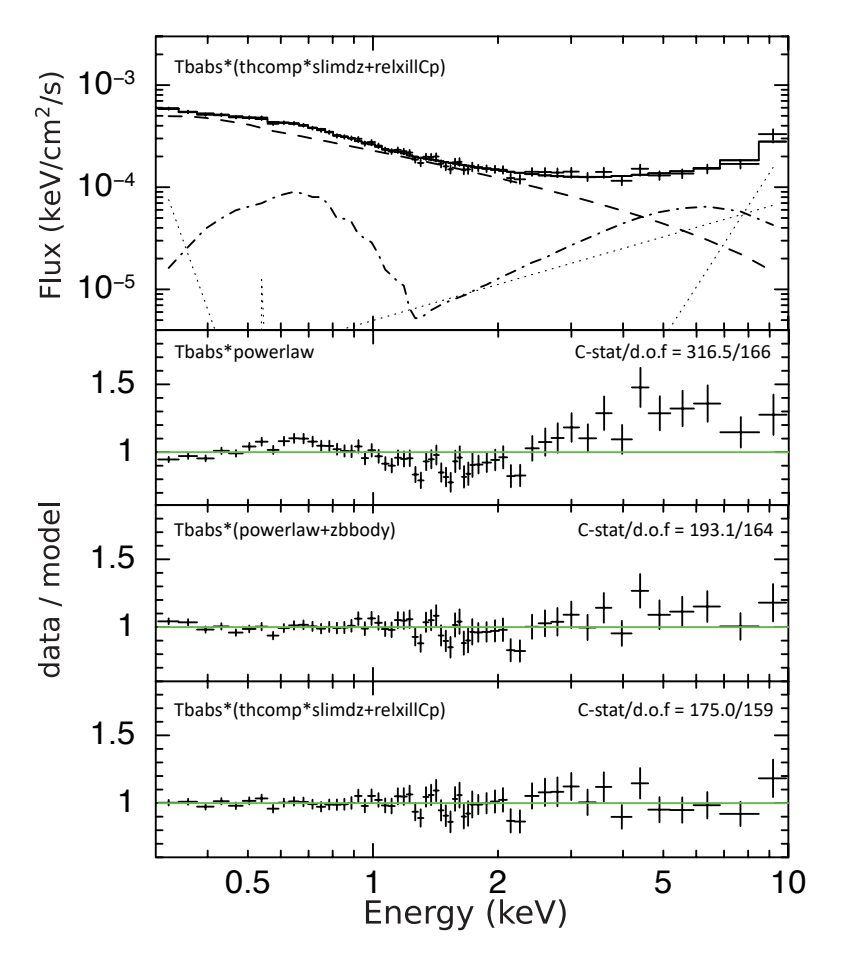


FIGURE 4.7: Top panel: The X-ray spectrum and the best-fit "TBabs*(thcomp*slimdz+relxillCp) model for the XMM#3 observation. The solid, dashed, and dot-dashed lines represent the best-fit total model, the coronal component thcomp*slimdz, and the corona reflection relxillCp, respectively. The dotted black lines show the contribution from the background as determined from fitting separately background—only spectra. The best-fit background power—law indices have been held constant during the fits to the source spectrum. Upper—middle panel: The ratio between the observed number of counts (data) and the best-fit predicted number of counts in each spectral bin (model), for a source fit—function of "TBabs*powerlaw" to describe the XMM#3 spectrum. Lower—middle panel: The ratio between the data and the model for a source fit—function of "TBabs*(powerlaw+zbbody)" to describe the XMM#3 spectrum. Bottom panel: The ratio between the data and the model for the source fit—function of "TBabs*(thcomp*slimdz+relxillCp)" shown in the top panel.

Table 4.3: Best-fit parameter values obtained using a fit-function of TBabs*(thcomp*slimdz+relxillCp) to describe XMM#3's spectrum. Parameters held fixed, and their values are given in between square brackets. Parameter f_c is the covering fraction of the Comptonising medium. The unit of the normalisation of the relxillCp model is that of flux in the 0.3-10 keV band.

Model	Parameter	Value	
TBabs	$N_H / 10^{20} \mathrm{cm}^{-2}$	[1.0]	
thcomp	τ	8 ± 3	
	kT_e / keV	$2.4^{+1.4}_{-0.7}$	
	f_c	0.8 ± 0.1	
slimdz	\dot{m} / $\dot{m}_{ m Edd}$	> 3.3	
	θ / °	81+4	
relxillCp	Γ	1.5 ± 0.2	
	q	1.6 ± 0.8	
	$\log(\xi)$	0.7 ± 0.3	
	$Refl_{frac}$	[-1]	
	$\log(\rho / \mathrm{cm}^{-3})$	[17]	
	norm / erg cm $^{-2}$ s $^{-1}$	$(1.3 \pm 0.3) \times 10^{-5}$	
C-stat/d.o.f.	175.0/159		

magnitude lower than the Galactic column density in the host direction. No other parameter values are fixed. We use the Markov–Chain–Monte–Carlo (MCMC) routine in MOSFiT to perform the fit. We set 20 walkers and run for 30,000 iterations. We then exclude the first 10,000 iterations as burn–in. In MOSFiT, the goodness–of–fit and the chain convergence are measured using the Watanabe–Akaike information criteria (WAIC; Watanabe & Opper 2010) and the potential scale reduction factor (PSRF; Gelman & Rubin 1992), where a fit with a PSRF≤ 1.2 is considered to have converged.

We find the MOSFiT produces a fit to the data with PSRF=1.167 and WAIC=207. A full list of the parameter values and their uncertainties is presented in Table 4.4. We find the M_{\bullet} is constrained to be between 5×10^5 and 5×10^6 M_{\odot} , which is in agreement with our black hole mass measurement using spectral fits to the X-ray data. The systematic errors for each fitting parameter estimated from Mockler et al. (2019) are also given in Table 4.4. We note for parameters other than M_{\bullet} , the systematic errors are large compared to the 1σ error range given by the fitting procedure. This conclusion also holds if we treat the M_{\bullet} as a known value taken from the analysis of X–ray data (Fig. 4.5) when performing the fit. We present the data as well as the best–fit MOSFiT model in Fig. 4.G.

4.4 Discussion 81

Table 4.4: Parameters and their constraints derived from modelling the *Swift*/UVOT light curves using MOSFiT. See the text for the meaning of each parameter. Systematic errors are taken from Mockler et al. (2019).

Parameter	Value	Systematic Error
$\log(M_{\bullet}/M_{\odot})$	6.2 ± 0.3	±0.2
$\log(M_*/M_\odot)$	-0.01 ± 0.09	±0.66
b	1.2 ± 0.2	±0.35
$\log(T_{\rm visc} / {\rm days})$	< 0.6	±0.1
$\log(\epsilon)$	-3.4 ± 0.1	±0.68
$\log(R_{\rm ph,0})$	-0.4 ± 0.3	±0.4
$l_{ m ph}$	0.05 ± 0.04	±0.2
t ₀ / days	-19 ± 6	±15

4.4 Discussion

In this paper we present XMM-Newton/EPIC-pn and NICER X-ray spectral analysis of AT2020ccn. The X-ray data can be divided into two periods: an early period with flares (MJD \leq 59130), and a late period without flares. Over the same period, the UV light curves observed by Swift show a gradual decay (Fig. 4.1). No evidence for UV flares is found.

We show that the spectra in the early period can be well-fit by a slim disc (Wen et al. 2020, 2022) plus an inverse–Comptonisation (IC) model (Zdziarski et al. 2020). Specifically, the spectral evolution along the flares can be explained by variations in the disc inclination and the electron temperature kT_e of the Comptonising medium. Using this fit-function, we constrain the BH mass to be $(7^{+13}_{-3}) \times 10^5 \ M_{\odot}$, while there is no constraint on the BH spin. The best–fit BH mass derived from analysing the UV data with the TDE module of MOSFiT is consistent with this result. Using the empirical $M - \sigma_*$ relation and a velocity dispersion of the stellar absorption lines $\sigma_* = 82 \pm 4$ km/s, Pasham et al. (2024b) estimate the BH mass to be $\sim 10^{6.4 \pm 0.6} \ M_{\odot}$. The consistency between different methods further prove that AT2020ocn can be explained as a tidal disruption of a star by a massive BH.

The observed inclination variation along the flares can be caused by Lense–Thirring precession during the disc alignment process (e.g., Stone & Loeb 2012; Franchini et al. 2016). Such inclination variations have been observed in simulations (e.g., Fragile & Anninos 2005; Zanazzi & Lai 2019; White et al. 2019), and they have been proposed to explain the highly-variable jet features in jetted TDEs (e.g., Swift J164449.3+573451; Tchekhovskoy et al. 2014; Liska et al. 2018; see also Teboul & Metzger 2023). For a fast–spinning BH of $M_{\bullet} = 10^6 M_{\odot}$, the

Lense-Thirring precession period during the disc alignment process is calculated to be ~ 10 days (Franchini et al. 2016; Zanazzi & Lai 2019), and the timescale for the whole alignment phase is $\lesssim 10^2$ days (Franchini et al. 2016). Such timescales for AT2020ocn are in agreement with the calculations (a duration of $\sim 1-10$ days for individual flares, and the source stops flaring ≤ 200 days after the first Swift detection of the event). Pasham et al. (2024b) discovered a $17.0^{+1.2}_{-2.4}$ day quasi-periodicity in *NICER* data in the early-time period, using an energy band of 0.3–1.0 keV that is slightly different from that in our study (0.3–1.1 keV). Without assuming their best-fit period, we fit the early-time NICER spectra and find an evolution of the θ and the IC strength. We investigated if the already-found periodicity in the light curve data (Pasham et al. 2024b) can also be found in a Lomb-Scargle periodogram (LSP; Lomb 1976; Scargle 1982) of our best-fit θ or kT_e parameter values as a function of time. An LSP is designed to search for (quasi-)periodic signals in unevenly-sampled time series. In the frequency domain, we find that LSPs of the count rate in 0.3–1.1 keV and the kT_e as a function of time show periodicity peaks that are consistent with those found in Pasham et al. (2024b), while the LSP of the θ as a function of time only shows peaks at $\leq 3\sigma$ significance level assuming a white–noise background (Fig. 4.H). It is possible that, as the IC component dominates the spectrum when the inclination decreases, most of the periodicity is imprinted in the IC component while the periodicity in θ is less pronounced. A thorough timing analysis of the NICER early-time data, where the impact of the background red-noise is included in estimating the detection significance, can be found in Pasham et al. (2024b).

The electron temperature kT_e of the IC component traces the spectral hardness ratio (*Left panel Fig.* 4.8): for all flares a higher kT_e is found when the spectrum becomes harder. This correlation is expected: the higher the temperature, the more energy a single photon is likely to get from the up–scattering events before escaping the Comptonising medium, thus the harder the emergent photon spectrum. A possible supply of high–energy electrons for the IC process comes from a disc outflow. For sources at high/super–Eddington accretion rates, a disc outflow is seen in both simulations (e.g., Ohsuga & Mineshige 2011; Takeuchi et al. 2013; Kitaki et al. 2021) and observations (e.g., Middleton et al. 2013; Pinto et al. 2016; Kara et al. 2018; Pinto et al. 2021). However, for AT2020ocn, the lack of high-resolution X-ray spectral data with a sufficient signal–to–noise ratio (e.g., from *XMM-Newton RGS*) precludes confirmation of the presence of a disc outflow.

In addition, we find an inverse correlation between θ and the count rate in 0.3–1.1 keV band (*Right panel* in Fig. 4.8). This behaviour can be understood as follows: as the inclination decreases, more photons from the inner disc region are observed. The slim disc model predicts a harder and brighter disc continuum the more the inner disc region is observable (e.g., Wen et al. 2020, 2022). As the source flux increases along each flare, we detect the IC component. Some disc photons with energies < 0.3 keV are up–scattered into the 0.3–1.1 keV band by the Comptonising medium, more than those being scattered out of this energy band, resulting in a higher count rate than that predicted by only a slim disc. We find that the inverse–Comptonisation starts to be detected at higher inclinations along the first flare compared to the subsequent flares,

4.4 Discussion 83

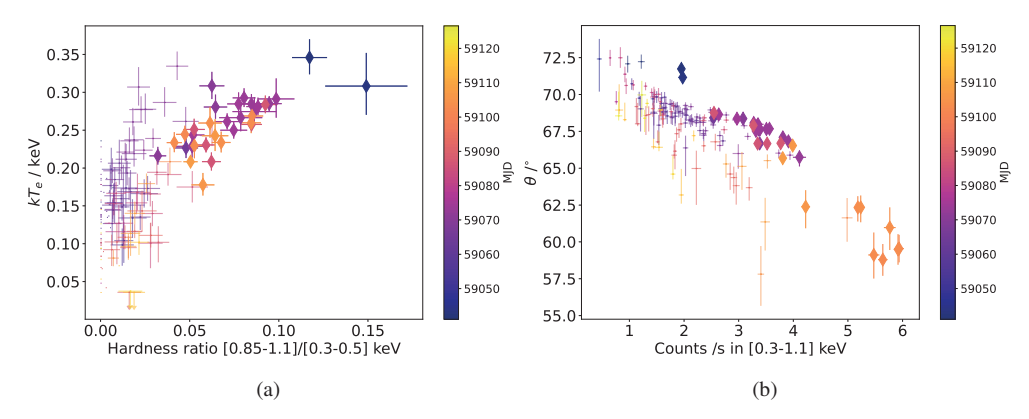


FIGURE 4.8: Left panel: The electron temperature kT_e vs. spectral hardness ratio, derived from the fit procedure producing Fig. 4.6. The epochs are colour–coded by their observation time in MJD. Epochs highlighted with diamond markers have a source count rate higher than the background count rate in the 0.85-1.1 keV energy band, so their hardness ratios are least affected by uncertainties in the NICER background estimation. The hardness ratio is traced by the temperature kT_e for all flares. Right panel: The disc inclination θ vs. the total count rate inn the 0.3-1.1 keV energy band. Generally, the lower the θ , the higher the count rate in the 0.3-1.1 keV band. The spectra at the X–ray flare peaks are hard, which can be explained by enhanced inverse–Comptonisation. Some disc photons with energies < 0.3 keV are up–scattered into the 0.3-1.1 keV band, more than those being scattered out, resulting in a higher count rate than that predicted by a model including only a slim disc.

distinguishing the first flare from the rest in both the hardness ratio vs. count rate diagram (Fig. 4.2 and Fig. 4.8).

A physical link between the strengthening/weakening of the IC component, and the inclination variation of the disc, is possible, as indicated by the analysis of the early–time *NICER* data. Simulations suggest that when a massive BH accretes at super–Eddington levels, in the scenario of a powerful disc outflow, the temperature of the inner accretion region reaches $\gtrsim 10^6$ K (corresponding to $\gtrsim 0.09$ keV; e.g., Jiang et al. 2019; Yang et al. 2023). Our results are consistent with the picture that, as the disc inclination decreases, more photons from the hotter accretion region at smaller radii are observed. Thus, we observe the temperature kT_e of electrons participating the IC process to increase during the X–ray flares, and its value (~ 0.3 keV) is similar to the value expected from simulations.

In our analysis, for the *NICER* spectra that are not well fit by the slim disc+IC model, residuals may be caused by any or several of the following reasons: 1) The background in the source+background spectrum deviates from the background spectrum generated from *NICER* prescriptions. 2) The source spectrum varies during the exposure of a single epoch (typically ~ks). The slim disc model assumes a steady state. Given a slim disc of $M_{\bullet} = 7 \times 10^5 M_{\odot}$, $a_{\bullet} = 0.9$, and $\dot{m} = 30 \dot{m}_{\rm Edd}$, the disc viscous timescale $t_{\rm vis} = \alpha^{-1} \Omega^{-1}(R) (H/R)^{-2}$ in the inner disc region (e.g., $\lesssim 10 R_{\rm g}$) is ~ ks. Here α is the Shakura–Sunyaev viscosity parameter (Shakura &

Sunyaev 1973), H(R) is the disc height, and $\Omega(R)$ is the orbital frequency; with such a high \dot{m} , the scaled disc height H/R reaches ~ 0.4 at $10~R_g$. The Photons from the inner disc region dominate the disc spectrum. Thus, on a timescale similar to the exposure time of individual *NICER* epochs, the steady–state approximation of the slim disc model may not be 100% valid. 3) Meanwhile, other physical mechanisms such as disc outflow (e.g., Middleton et al. 2013; Kara et al. 2018), or disc reflection (e.g., Masterson et al. 2022) could affect the observed TDE spectrum. With the current data, it is not possible to disentangle different origins of the residuals. Given that most of the early–time *NICER* spectra are describe well by our fit-function, we conclude that a slim disc+IC model describes the source X–ray spectrum well, and the observed long–term ($\gtrsim 10~{\rm days}$) variation of the disc inclination is not due to variations in the physics of the disc.

We test if the enhancement of the IC component during the flares can be explained by an increase in the covering fraction or the optical depth τ of the Comptonising medium, instead of an increase in kT_e . We find that a slim disc plus a Comptonising medium with a varying covering fraction (with fixed $kT_e = 0.3$ keV and $\tau = 20$) can describe 140 out of 206 early-time NICER spectra (C-stat/d.o.f. < 2). The value of the covering fraction in a black hole accretion system has sometimes been found to be ≤ 0.5 (e.g., Done & Kubota 2006; Wilkins & Gallo 2015; Chen et al. 2022; Dai et al. 2023), while in other cases it is consistent with the maximum value of 1 (e.g., Tripathi & Dewangan 2022; Liu et al. 2023; Cao et al. 2023). We re-run the fitting procedure as used for Fig. 4.6 but fixing the covering fraction to 0.5 instead of 1. In this case, we find that 152 out of 206 spectra are well-fit (Fig. 4.I), and both the θ and kT_e behaviour is similar to Fig. 4.6. Similarly, a slim disc plus a Comptonising medium with a varying optical depth (with fixed $kT_e = 0.3$ keV and a covering fraction of unity) can describe 153 spectra. It is possible that during each flare multiple parameters of the Comptonising medium are varying as the disc inclination changes. However, with the current data, it is not possible to disentangle the effects of different IC parameters. Nonetheless, in all the tests, the IC becomes prominent at different θ values between the first and the subsequent flares (e.g., Fig. 4.8). Our tests on the IC parameters suggest that the physical properties of the Comptonising medium vary between flares.

Given the large uncertainties in constraining the BH spin from the XMM-Newton data (Fig. 4.5), we test if our findings about the θ and kT_e behaviour are sensitive to the choice of a_{\bullet} . We perform the fit procedure described in Section 4.3.3.2, but with fixed $M_{\bullet} = 5 \times 10^5 \ M_{\odot}$ and $a_{\bullet} = 0.2$. We find that 160 spectra are well-fit (Fig. 4.J). The variation behaviour of both θ and kT_e is qualitatively similar to that in Fig. 4.6, but the range over which the inclination varies is much larger for the $a_{\bullet} = 0.2$ case (the smallest inclination value within the concerned period from $\sim 57^{\circ}$ to near-zero). This enlarged variation is to be expected: for $a_{\bullet} = 0.2$ the inner edge of the disc is further away from the BH yielding a lower temperature and subsequently, a softer spectrum, as the innermost-stable-circular-orbit (ISCO) lies further away from the BH event horizon (the inner edge of the disc is set to the ISCO in the slimdz). As the inclination decreases, more hard (> 1keV) photons from the inner disc are observed, explaining the flares. Therefore, to get the same increase in flux of hard X-ray photons, the inclination must reach a value closer to zero for $a_{\bullet} = 0.2$, compared to the situation for $a_{\bullet} = 0.9$. Meanwhile, the peak features in $\theta(t)$ with

4.4 Discussion 85

Table 4.5: Different fit functions used in this paper to fit the *NICER* data in the early–time period. In total, there are 206 spectra to be fit. kT_{zbb} and norm_{zbb} are the temperature and the normalisation of a black body model, respectively. See the text for more details. Histograms of the C-stat/d.o.f. from each test are presented in Fig. 4.L

No.	Model	Free parameter	Fixed parameter	Number of good-fits (C-stat/d.o.f. < 2)
1	TBabs*slimdz	\dot{m} , θ	$N_{H,G} = 1 \times 10^{20} \text{cm}^{-2}, M_{\bullet} = 7 \times 10^5 M_{\odot}, a_{\bullet} = 0.9$	108
2	TBabs*thcomp*slimdz	\dot{m}, kT_e	$N_{H,G}=1\times10^{20} {\rm cm^{-2}}, M_{\bullet}=7\times10^5~M_{\odot}, a_{\bullet}=0.9, f_c=1, \tau=20, \theta=74^{\circ}$	59
3		θ, kT_e	$N_{H,G}=1\times10^{20} {\rm cm^{-2}}, M_{\bullet}=7\times10^5~M_{\odot}, a_{\bullet}=0.9, f_c=1, \tau=20, m=30~m_{\rm Edd}$	165
4		θ, au	$N_{H,G}=1\times10^{20}{\rm cm^{-2}}, M_{\bullet}=7\times10^5M_{\odot}, a_{\bullet}=0.9, f_c=1, kT_e=0.3$ keV, $m=30m_{\rm Edd}$	153
5		θ, kT_e	$N_{H,G}=1\times10^{20}\rm cm^{-2},M_{\bullet}=7\times10^5~M_{\odot},a_{\bullet}=0.9,f_{C}=0.5,\tau=20,m=30~m_{\rm Edd}$	152
6		θ, f_c	$N_{H,G}=1\times10^{20}{\rm cm^{-2}}, M_{\bullet}=7\times10^5M_{\odot}, a_{\bullet}=0.9, \tau=20, kT_e=0.3$ keV, $m=30m_{\rm Edd}$	140
7		θ, kT_e	$N_{H,G}=1\times10^{20}\rm{cm^{-2}},M_{\bullet}=5\times10^5~M_{\odot},a_{\bullet}=0.2,f_c=1,\tau=20,\dot{m}=30~\dot{m}_{\rm Edd}$	160
8	TBabs*(slimdz+zbbody)	θ , kT_{zbb} , $\mathrm{norm}_{\mathrm{zbb}}$	$M_{\bullet} = 7 \times 10^5 \ M_{\odot}, a_{\bullet} = 0.9, \dot{m} = 30 \ \dot{m}_{\rm Edd}$	115

respect to time t occur at similar t for both cases. We conclude that, qualitatively, our findings about the θ and kT_e behaviour with respect to time are not sensitive to the choice of BH spin during the *NICER* fitting procedure.

We also test if the early–time AT2020ocn data can be equally–well described by a slim disc plus a blackbody component instead of an IC component. We perform the fitting procedure similar to that producing Fig. 4.6, but replacing the IC model thcomp by a black–body model zbbody. The XSPEC's syntax for the test fit–function is then TBabs*(zbbody+slimdz). We find a large fraction of the *NICER* spectra cannot be well–fitted with a varying black body of $kT_e \sim 0.3$ keV (Fig.4.K; only 71 out of 206 have a C-stat/d.o.f. < 2). Allowing the black body temperature to be free–to–vary during the fitting procedure increases the number of good fits to 115 out of 206 but this is still less than in the number of good fits when using the slim disk plus IC component (see Fig. 4.6; 165 out of 206 fits are good, with one more d.o.f. than the case of zbbody in each individual fit). Therefore, we conclude that a variable IC component provides a better description of the data compared to a varying black body component. To summarise the different fits and tests we perform for the early–time *NICER* data, we list them in Table 4.5. For reference, we also show the histograms of C-stat/d.o.f. for each fit in Fig. 4.L.

We note there are several limitations to our modelling. One key assumption in the slimdz model is that the disc is aligned with the BH equatorial plane. In this paper we find that the early-time X-ray flares are well-explained by a variable inclination, and we interpret it as results from the disc alignment process. We are not modelling the dynamic solutions of a precessing disc, and there are currently no analytic solutions of a tilted slim disc (i.e., with the disc outside the equatorial plane). Changing θ in the model is really changing the observer's direction, which is not identical to a precessing disc while the observer is on a fixed position regarding the Kerr metric. Therefore, it is important that we try to estimate the deviations of a disc described by the slimdz model from a tilted disc. From Fig. 4.6 we find the amplitude of the inclination

variation to be $\lesssim 10^\circ$. In such a case, we estimate a change of $1-\sin^2(90^\circ-10^\circ)\approx 3\%$ in the tilted disk metric from the approximate equatorial metric of a Kerr black hole, corresponding to a change of 3% in the estimation of accretion rate (Page & Thorne 1974). Furthermore, using general relativistic magnetohydrodynamic simulations, Fragile et al. (2007) find that the tilt will change the inner radius of the disc, consequently impacting the efficiency of disk radiation. By studying the disc properties, they conclude that effectively, a tilted disc acts like an untilted disc with a lower black hole spin. In this sense, we estimate the tilt-induced X-ray flux change by comparing two slim discs with the same accretion rate but different spin values. Assuming $M_{\bullet} = 7 \times 10^5 \ M_{\odot}$, $\dot{m} = 30 \ \dot{m}_{\rm Edd}$, and $\theta = 60$, we estimate the flux difference between an un-tilted slim disc with $a_{\bullet} = 0.998$, and a 10-degree-tilted disc approximated by a disc with $a_{\bullet} = 0.998 \sin(90^\circ - 10^\circ) = 0.983$, to be $\sim 10\%$ (from $\sim 5.13 \times 10^{-12}$ erg cm⁻² s⁻¹ to $\sim 4.67 \times 10^{-12}$ erg cm⁻² s⁻¹) in the energy range 0.3-1.5 keV. The full impact of tilt on the disc physics necessitates further investigation, which is beyond the scope of this paper.

Meanwhile, parameter constraints (M_{\bullet} , a_{\bullet} , etc.) from the slimdz might be impacted by this tilt nature of the disc. We estimate the parameter deviations by comparing the results from the early-time spectra with those from the late-time spectra. XMM#3 is taken after the flaring period, likely when the disc has settled in the equatorial plane. We re-fit the XMM#3 spectrum with the model in Table 4.3 but let also M_{\bullet} and a_{\bullet} free-to-vary (though note the consistency issue between thcomp and relxillCp). In this test we find a C-stat/d.o.f. of 174.4/157 (Δ AIC=-3.4, meaning the improvement of including an additional free parameter is not significant). The BH mass is constrained to be $(1.8^{+1.0}_{-0.5}) \times 10^6 M_{\odot}$, and the spin is constrained to be between -0.62 and 0.97; the inclination is constrained to be > 78°. We conclude that the results from our modelling of the early-time XMM#1, XMM#2, and NICER data are consistent with those from the late period, and therefore, that the assumption in the slimdz model that the disc lies in the equatorial plane of the BH spin is not the dominant factor in the uncertainty in the parameter estimation.

Furthermore, when using the slimdz model to describe the spectrum emitted by a mis-aligned disc during the alignment process, the best-fit spin value derived from modelling could deviate from the true BH spin, and vary between epochs. We test and find that, due to the data quality, it is not possible to constrain the spin value using the slimdz for individual epochs when we treat the spin as a free parameter in our fits of the early-time *NICER* data. Together with the above tests, and the consistent mass constraint from the $M - \sigma_*$ relation, we conclude that the uncertainties in parameter constraints in our study are dominated by the statistical uncertainty of the data instead of our model assumptions on the early-time spectra with slimdz.

Moreover, we do not consider the possibility of a warped disc in our study. Such a warp could happen during the disc alignment phase (e.g., Franchini et al. 2016; White et al. 2019), although it is important to realise that the TDE discs are much smaller than AGN and X-ray binary discs (when expressed in Schwarzschild radii). As suggested by pioneering numerical simulations on accretion discs (e.g., White et al. 2019; Liska et al. 2023), the disc warp and the disc twist make it possible that, when the inner part of the disc precesses to the phase of minimum inclination (i.e., the inner disc region is face—on), the outer part of the disc is at a different phase so that it intersects

4.4 Discussion 87

our line of sight to the inner disc region and obscures radiations coming from that region. In this sense, the non-planarity of the disc introduces a temporary disc self-obscuration of the inner disc region that will reduce the peak X-ray flux. In such a case, using a planar disc model to fit a warp disc will result in an under-estimation of the amplitude of the inclination variation. However, quantifying the impact of warp on the disc spectrum and the black hole measurements require further studies that incorporate the slim disc and the ray-tracing effects, which we defer to future studies.

From our spectral fits to the X-ray data obtained in the "late period," we find an accretion rate $\dot{m} > 3.3 \, \dot{m}_{\rm Edd}$ (Table 4.3), indicating that the source remains at super–Eddington levels throughout the first several hundred days after its detection. This behaviour is consistent with our BH mass constraint of $M_{\bullet} \sim 10^6 \, M_{\odot}$. Theory predicts that TDEs arising from such a BH tend to stay at super–Eddington levels for more than hundreds of days (Stone & Metzger 2016; Wen et al. 2020).

An IC component from a corona describes the spectrum well during the late period (Table 4.3). This corona is not necessarily the same as the Comptonising medium detected in the early period. We do not refer to the one detected in the early period as a "corona" to mark the potential difference. In the late period, the source develops a corona characterised by an optical depth $\tau = 8 \pm 3$ and a $kT_e = 2.4^{+1.4}_{-0.7}$ keV. The appearance of a coronal component when the disc accretion rate remains above the Eddington mass accretion rate has also been found in the TDE 3XMM J150052.0+015452 (J150052; Cao et al. 2023). The coronal temperature in AT2020ocn $(2.4^{+1.4}_{-0.7} \text{ keV})$ is consistent with that in J150052 $(2.3^{+2.7}_{-0.8} \text{ keV})$. The magnetic field in the disc might be critical to power such a corona (e.g., Ghisellini et al. 1988; Merloni & Fabian 2001; Veledina et al. 2011; Beloborodov 2017). It is possible that the electron temperature of the Comptonising medium in the late period is order-of-magnitude larger than that in the early period. As mentioned earlier, the dominant mechanism powering the Comptonising medium might be different between the early and the late period, since the physical properties of the accretion system (e.g., magnetic field) can be much changed as the disc stops precessing and the accretion rate decreases. In the late period, the disc luminosity decreases as the accretion rate decreases, leading to less cooling of the corona through inverse-Comptonisation, that might also contribute to a hotter corona.

The development of a corona also leads to its emission being reflected from the disc, which is taken into account in our fit in an approximate way by using the relxillCp model. The emissivity index q is constrained to be shallow (<3), which might indicate an extended geometry of the corona or a thick disc (e.g., Mundo et al. 2020). Ezhikode et al. (2020) have found that many AGN in Seyfert I galaxies also have a shallow emissivity (fig. 5 in their paper). Therefore, a shallow emissivity index in AT2020ocn in the late period is not without precedent. The fit also suggest a high inclination of the system (81^{+4}_{-7} degree) during the XMM#3 epoch. This inclination value is consistent with the highest value ($\sim 74^{\circ}$) found during the disc alignment phase, within 2σ error range (and marginally at 1σ error range). After the disc alignment is completed, the disc rests at the high inclination.

As a comparison, the IC process contributes < 34 % of the source flux in the 0.3–1.1 keV band at early epochs, while, at XMM#3, the photons directly from the corona and from the reflection

component contribute 64 % of the flux in the 0.3–1.1 keV band. Together with the evidence of the hardness ratio (Fig. 4.2), we conclude that during the first 500 days after its detection, AT2020ocn transits from a soft, disc-dominated spectral state to a hard, corona-dominated spectral state. Spectral state transitions involving a varying coronal component are also observed in other TDEs (e.g., Bade et al. 1996; Komossa et al. 2004; Wevers et al. 2019a; Jonker et al. 2020; Wevers et al. 2021; Cao et al. 2023). Similarly, many ULXs are believed to be powered by high/super-Eddington accretion onto stellar-mass BHs in X-ray binaries (e.g., Gladstone et al. 2009; Motta et al. 2012; Sutton et al. 2013). The strengthening/weakening of a coronal component, when the source accretes at about or at super-Eddington rates, is critical to explain spectral state transitions in ULXs (e.g., Sutton et al. 2013; Feng et al. 2016; Kaaret et al. 2017; Barra et al. 2022). Our findings in AT2020ocn provide further evidence that a varying coronal component might be common in systems accreting at about or at super-Eddington rates.

The UV light curves of AT2020ocn show no flares but instead only a gradual decay (Fig. 4.1). This is similar to the UV light curve behaviour observed in other TDEs (e.g., van Velzen et al. 2020). Assuming a slim disc as observed by XMM-Newton (Table 4.2), we estimate the UV flux of the disc to be an order-of-magnitude lower ($\lesssim 10^{-29}$ erg/s/cm²/Hz with a disc outer radius of $2R_t \approx 117R_g$) than what is observed by Swift/UVOT during the X-ray early period (Fig. 4.1). Similarly, the observed early-time (within several hundred of days after the initial disruption) UV flux in several other TDEs is higher than the expected disc UV flux (e.g., Mummery & Balbus 2020; Mummery et al. 2023; Wen et al. 2023). The decoupling of X-rays and UV (flaring and non-flaring) is also seen in other TDEs (e.g., Pasham et al. 2022; Evans et al. 2023; Guolo et al. 2024b). It is not possible to distinguish different UV emission mechanisms (e.g., self-intersection shocks in debris streams or a layer reprocessing the X-rays from the inner accretion region) in MOSFiT, which is agnostic about the emission mechanism and only assumes an efficiency ϵ for the fraction of accretion energy converted to the bolometric luminosity $L = \epsilon \dot{M}_{\rm acc} c^2 (\dot{M}_{\rm acc}(t))$ is the accretion rate from viscously delayed fall–back mass accretion $\dot{M}_{\rm fb}(t)$, see also Section 4.3.4). The ϵ is treated as a time-independent, free parameter in our UV modelling and is found to be $\sim 10^{-3}$ (Table 4.4). The energy emitted by the UV photons is similar to our estimate of the energy dissipated in the circularisation process⁸ ($\gtrsim 0.007 \dot{M}_{\rm fb} c^2$). It is possible that the circularisation process plays an important role in powering the early–time UV emission.

Overall, our analysis combining the UV and X-ray data is consistent with the picture where the X-ray flares arise from the inner accretion disc, whose inclination varies during the disc alignment process, while the UV emission comes from another mechanism. Recently, Mummery et al. (2024b) developed a method using the late-time UV data to constrain the BH mass in a TDE. For this method to be applicable, it is important that the source has reached a "plateau phase" in UV in the late time of the TDE (e.g., Inkenhaag et al. 2023; Mummery et al. 2024b), and that the disc emission dominates the detected UV emission. Even though the current UV

⁸A lower limit on the dissipated energy in the circularisation process is estimated, in an order–of–magnitude way, by comparing the orbital energy of the fallback orbit of the most tightly bound debris (major axis $\sim 10^3~R_g$; Rees 1988) to the orbital energy of a circularised orbit of radius $2R_t \approx 117R_g$ at the disc outer edge (Franchini et al. 2016).

4.5 Conclusions 89

data is not sufficient to tell if this state is achieved before the end of the observed period, it would be interesting to see if the UV scaling method can provide a mass estimation for the AT2020ocn similar to our result or the $M - \sigma_*$ result using future deep UV observations.

4.5 Conclusions

In this paper, we present our analysis of the X-ray and UV data of TDE AT2020ocn observed by *NICER*, *XMM-Newton*, and *Swift*. The X-ray lightcurve shows strong flares in the first ≈ 100 days, while, over the same period, the UV emission decays gradually. From our X-ray spectral fits using a slim disc model, we constrain the BH mass to be $(7^{+13}_{-3}) \times 10^5$ M_{\odot} at the 1σ (68%) confidence level. This mass is consistent with that derived from the analysis of the UV light curve, $\log(M_{\bullet}/M_{\odot}) \sim 6.2 \pm 0.3$, and with that derived from the $M - \sigma_*$ relation, $\log(M_{\bullet}/M_{\odot}) \sim 6.4 \pm 0.6$.

We find that the disc alignment process might well be responsible for the qualitatively different behaviour of the X-ray and UV light curves with X-ray flares while the UV emission decays gradually. In particular:

- The early *XMM-Newton*/EPIC-pn spectra can be well-fit by the slim disc emission. The X-ray flares observed by *NICER* can arise from a combination of a varying disc inclination and a varying inverse–Comptonisation component.
- We explain the inclination variation in this TDE by proposing that the disc alignment is
 ongoing, which requires that the orbital angular momentum vector of the star prior to
 disruption is misaligned from the BH spin angular momentum vector. The inner part of
 the tilted disc is drawn into the BH equatorial plane due to a combination of the Bardeen–
 Petterson effect and internal torques. This alignment process causes the inner disc to
 temporarily precess, explaining the observed inclination variations.
- The observed spectral variations during the X-ray flares can be explained by the slim
 disk model convolved with the effect of inverse-Comptonisation. The contribution of the
 inverse-Comptonisation process to the observed spectrum increases with increasing X-ray
 photon count rate, consistent with observing more up-scattered photons from the inner
 accretion region as the inclination decreases.
- The UV light curves for AT2020ocn show no evidence for flares but instead only a gradual
 decay similar to the UV light curves of other TDEs. Most of the UV light likely originates
 from somewhere other than the accretion disk. The amount of energy emitted in the UV
 bands is similar to the estimate of that dissipated in the circularisation process.
- After the period of X–ray flares, the source spectrum becomes much harder. While the mass accretion rate remains at super–Eddington levels, a corona with an optical depth $\tau = 8 \pm 3$ and an electron temperature $2.4^{+1.4}_{-0.7}$ keV forms after ~300 days. We interpret the late–time *XMM-Newton/EPIC*-pn spectrum as a combination of disc emission, coronal

emission, and emission reflected off the disc. Our findings in AT2020ocn provide further evidence that a varying coronal component might be common in systems accreting at about or at super–Eddington rates.

ACKNOWLEDGEMENTS

We thank the anonymous referee for insightful comments. This work used the Dutch national e-infrastructure with the support of the SURF Cooperative using grant no. EINF-3954. This work made use of data supplied by the UK Swift Science Data Centre at the University of Leicester. AIZ acknowledges support from NASA ADAP grant #80NSSC21K0988.

4.6 Supplementary materials

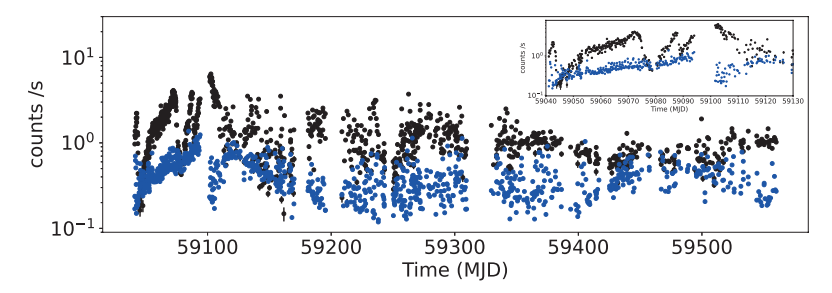


FIGURE 4.A: The *NICER* light curve of the 0.3-1.1 keV band (black) and the background light curve of the 0.3-1.1 keV band (blue). The insert shows the zoomed–in view of the early flares (MJD< 59130).

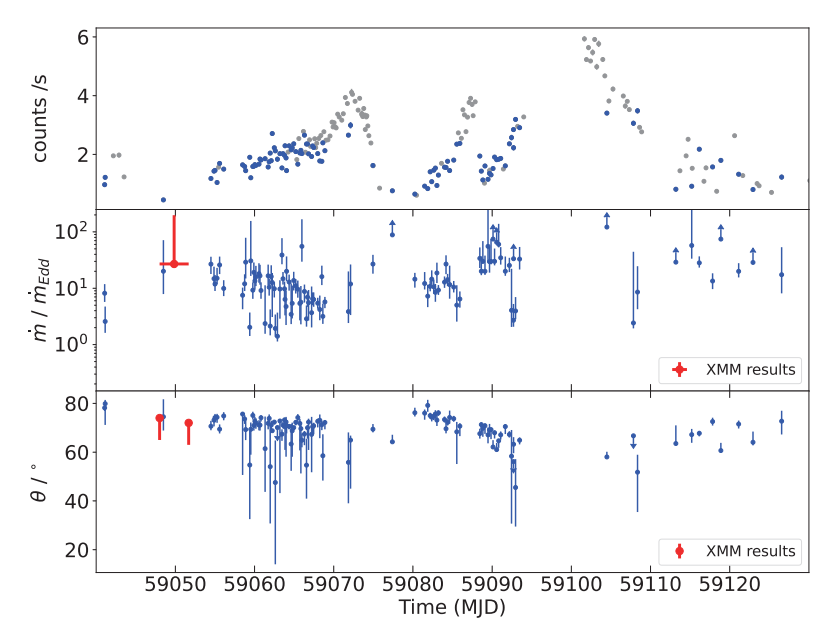


FIGURE 4.B: *Top panel*: The *NICER* 0.3-1.1 keV early–time source light curve. We only consider the epochs where the source flux stays above the background level from 0.3 keV to at least 0.6 keV (a total of 206 epochs in the early period). Spectra in epochs marked by blue dots are well–fit (C-stat/d.o.f. < 2; 108 in total) by the model in this analysis, while grey dots mark spectra that have C-stat/d.o.f. > 2. The fit–function here is different from Fig. 4.6: TBabs*slimdz. *Middle panel*: Constraints on the disc mass accretion rate \dot{m} derived from the *NICER* spectra obtained before MJD 59130. We fit each of the 206 spectra individually allowing the accretion rate \dot{m} and the inclination θ to vary. We use $N_H = 1 \times 10^{20}$ cm⁻² for all spectral fits in this paper. We fix $M_{\bullet} = 7 \times 10^5 M_{\odot}$ and $a_{\bullet} = 0.9$ based on the results of the spectral fits to the *XMM-Newton* data (Fig. 4.5). We show the fitted parameter values for the 108 out of the 206 spectra where the C-stat/d.o.f. < 2 (the results from the blue points in the top panel). The accretion rate constrained from the joint–fit to the XMM#1 and XMM#2 X–ray spectra is marked with the red dots. *Bottom panel*: Constraints on the inclination θ derived from the same fitting procedure described above. We conclude that the slim disc alone cannot explain the early–time *NICER* data well, especially the hard spectra at the peak of the flares are not well fit.

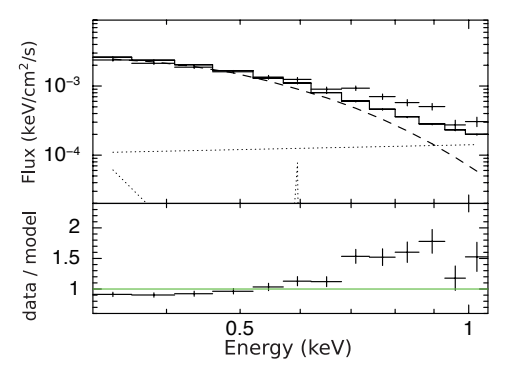


FIGURE 4.C: Top panel: An example of the hard *NICER* spectra at flare peaks, taken on MJD 59074.4. The fit-function is comprised of the following model components: TBabs*slimdz. The fit procedure is described in Section 4.3.3.2 and Fig. 4.B. The solid, dashed, and dotted lines represent the total model, the slim disc emission, and the contribution from the background as determined from fitting the estimated background—only spectrum separately, respectively. The best–fit background power–law indices and Gaussian parameters have been held constant during the fit to the source+background spectra. Bottom panel: We show the ratio between the observed number of counts (data) and the predicted number of counts in each bin (model). The spectra at flare peaks are much harder than a continuum described by a slim disc.

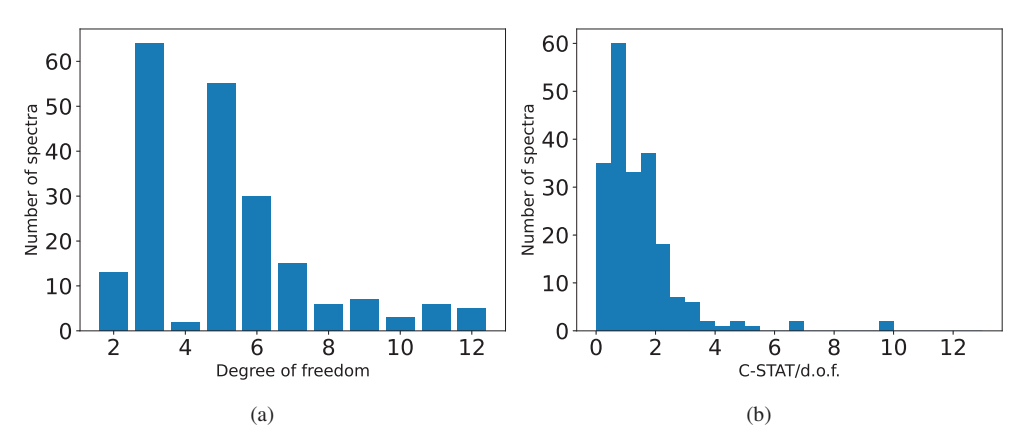


FIGURE 4.D: *Left*: Histogram of the degree–of–freedom (d.o.f) in each fit produced by the fit procedure described in Section 4.3.3.2 and of which the results are shown in Fig. 4.6. Each spectrum has at least 2 d.o.f. left to be fitted with the 2–parameter (θ and kT_e) fit function. *Right*: Histogram of the C-stat/d.o.f. produced by the same fit procedure.

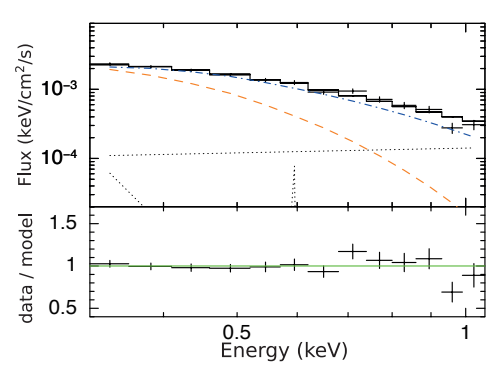


FIGURE 4.E: Same as Fig 4.C but with a fit—function comprising of the following model components: TBabs*thcomp*slimdz. Moreover, the orange dashed line represents the slim disc emission before the inverse—Comptonisation, and the blue dash—dotted line represents the slim disc emission after the inverse—Comptonisation. The C-stat/d.o.f. = 13.9/11.

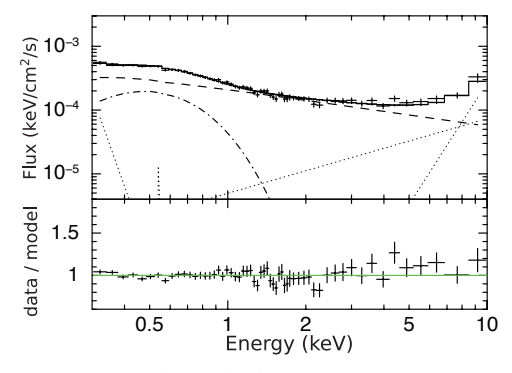


FIGURE 4.F: Top panel: phenomenologically fitting the XMM#3 spectrum with a fit function comprised of a power-law and a black body. In XSPEC's syntax, the fit function is "TBabs*(powerlaw+zbbody)". The sold, dashed, dot-dashed, and dot lines represent the best-fit total model, the power-law, the black body emission, and the contribution from the background as determined from fitting extracted spectra from background-only data separately, respectively. Bottom panel: The ratio between the observed number of counts (data) and the best-fit predicted number of counts in each spectral bin (model).

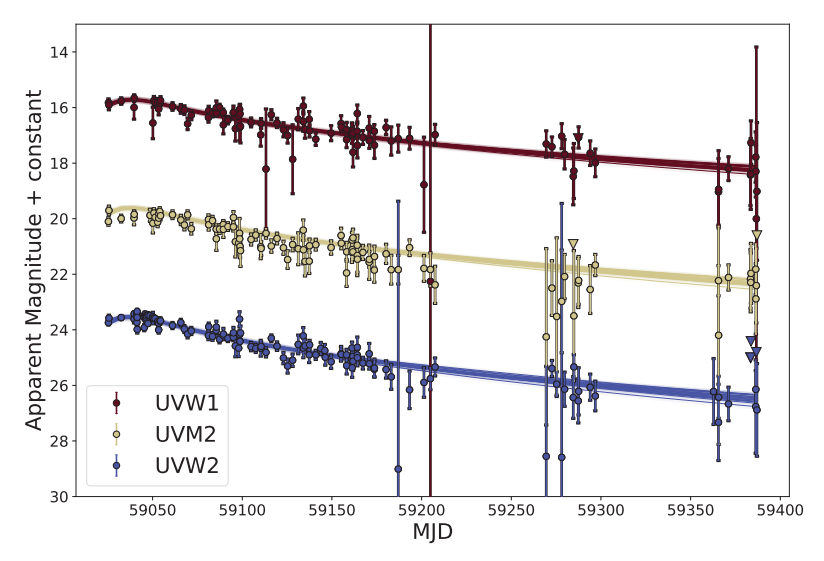


FIGURE 4.G: *Swift/UVOT* data fitted using the MOSFiT, as described in Section 4.3.4. We shift the y-axis of UVW1 and UVW2 bands by a constant (-4 for UVW1 and +4 for UVW2) for plot clarity.

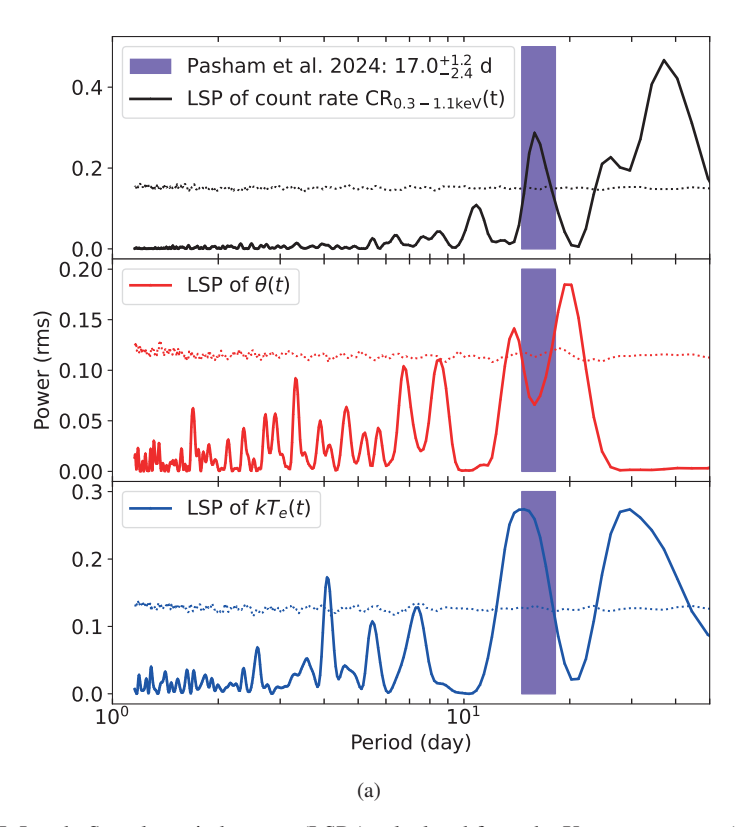


FIGURE 4.H: Lomb-Scargle periodograms (LSPs) calculated from the X-ray count rate (CR) in 0.3-1.1 keV (solid black), the measured inclination θ (solid red) and electron temperature kT_e (solid blue), from the results in Fig. 4.6. The x-axis is the period, and the y-axis is the LSP power for a given periodic mode. All three parameters are derived or measured over the period MJD 59041-59130. Dotted lines are the 3σ detection thresholds, which is roughly estimated by a bootstrapping approach similar to that in Evans et al. 2023: for each time series (the count rate, θ , or kT_e), we redistribute the value of the parameter under consideration randomly among the same set of time bins as the original, simulating a new time series. We perform 10000 such simulations and then calculate the Lomb-Scargle periodogram of each simulation. The 99.7 percentile of power at each frequency is then calculated. We note a better treatment of the significance estimation should include modelling the red noise in the lightcurves, which is beyond the purpose of this paper and can be found in Pasham et al. 2024b. The periodicity peaks in the count rate and kT_e are consistent with a period of $17^{+1.2}_{-2.4}$ days (purple) found by Pasham et al. 2024b, while the LSP of θ only shows two weak peaks around 17 days. As the IC component dominates the spectrum during the flares, it is possible that most of the periodicity is imprinted in the IC component, while the periodicity in θ is less observed. A double–period peak can be found in the LSPs of the count rate, and the kT_e . Meanwhile, the LSP of kT_e also shows a 4-day peak that barely reaches the 3σ level, which corresponds to no signals in the data (the LSP of the 0.3-1.1 keV count rate lightcurve) and is likely a noise component.

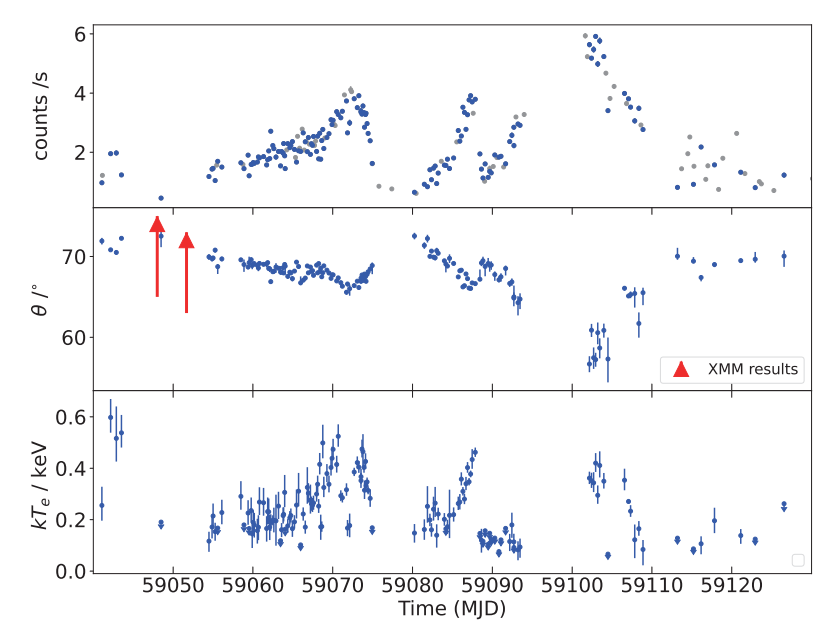


FIGURE 4.I: Same as Fig. 4.6, but in deriving these panels, we fixed the covering fraction of the IC component to 0.5 instead of unity when fitting the *NICER* spectra. In total, 152 out of 206 spectra are fitted with C-stat/d.o.f. < 2 (blue data points).

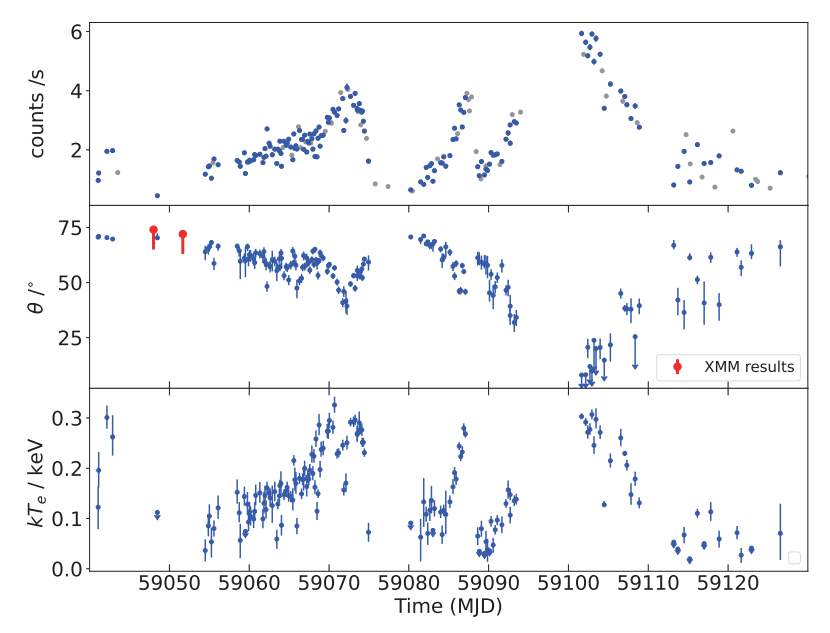


FIGURE 4.J: Same as Fig. 4.6, but we fix M_{\bullet} to 5×10^5 M_{\odot} and a_{\bullet} to 0.2 when fitting the *NICER* spectra. In total, 160 out of 206 spectra are fitted with C-stat/d.o.f. < 2.

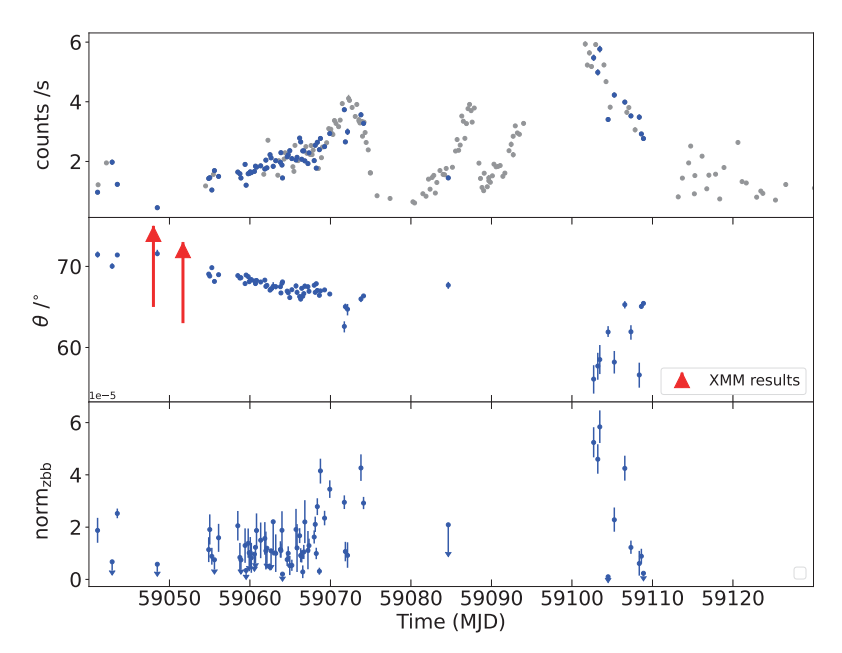


FIGURE 4.K: Same as Fig. 4.6, but to derive these panels we used a fit-function of TBabs*(slimdz+zbbody) when fitting the *NICER* spectra. The black body temperature is fixed to 0.3 keV during the fit. In total, 71 out of 206 spectra are fitted with C-stat/d.o.f. < 2 (blue data points in the *top* panel). Allowing the black body temperature to be free—to—vary during the fit would increase the number of good—fits to 115 out of 206 but still far less than Fig. 4.6 (165 out of 206).

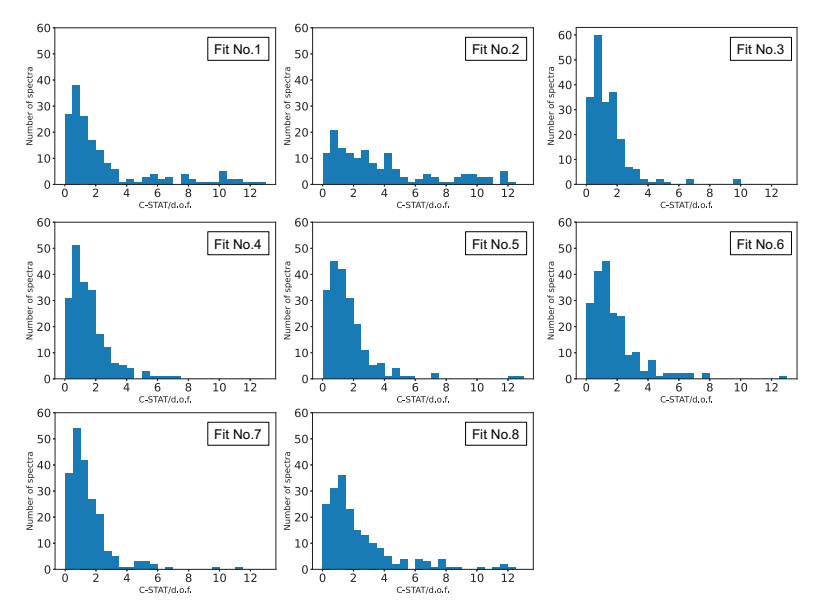


FIGURE 4.L: Histograms of the C-stat/d.o.f. produced by the fits performed in this paper. Labels show from which fit each histogram is derived, and details of each fit are listed in Table 4.5. The third figure is identical to Fig. 4.D(b), and other histograms are comparable to it.

TABLE 4.A: List of per–GTI–based *NICER* spectra used for the spectral analysis in Section 4.3.3.2.

Observation ID	Date	GTI duration (s)	Estimated Source Count Rate (count /s)
3201670101	2020-07-11 01:44:46	483.0	0.97 ± 0.05
3201670101	2020-07-11 03:17:28	373.0	1.22 ± 0.06
3201670102	2020-07-12 04:03:47	1717.0	1.95 ± 0.04
3201670102	2020-07-12 21:11:06	332.0	1.98 ± 0.08
3201670103	2020-07-13 12:34:07	1216.0	1.23 ± 0.03
3201670108	2020-07-18 11:46:49	342.0	0.45 ± 0.05
3201670114	2020-07-24 11:47:06	1665.0	1.18 ± 0.03
3201670114	2020-07-24 21:04:25	1196.0	1.43 ± 0.04
3201670115	2020-07-25 00:10:25	1276.0	1.46 ± 0.04
3201670115	2020-07-25 06:22:05	1857.0	1.04 ± 0.03
3201670115	2020-07-25 11:00:50	1089.0	1.56 ± 0.04
3201670115	2020-07-25 14:06:29	1524.0	1.69 ± 0.04
3201670116	2020-07-26 02:29:45	1064.0	1.50 ± 0.04
3201670118	2020-07-28 11:47:45	1075.0	1.64 ± 0.04
3201670118	2020-07-28 17:59:20	1080.0	1.59 ± 0.04
3201670118	2020-07-28 21:04:55	526.0	1.45 ± 0.06
3201670119	2020-07-29 09:28:03	1097.0	1.90 ± 0.05
3201670119	2020-07-29 12:34:37	507.0	1.20 ± 0.06
3201670119	2020-07-29 18:45:43	1077.0	1.59 ± 0.04
3201670119	2020-07-29 21:51:45	1075.0	1.60 ± 0.04
3201670120	2020-07-30 00:57:23	1077.0	1.65 ± 0.04
3201670120	2020-07-30 04:03:28	1072.0	1.63 ± 0.04
3201670120	2020-07-30 13:21:03	1077.0	1.67 ± 0.04
3201670120	2020-07-30 16:27:03	1057.0	1.84 ± 0.05
3201670120	2020-07-30 19:32:43	1077.0	1.81 ± 0.05
3201670121	2020-07-31 07:56:45	1035.0	1.85 ± 0.05
3201670121	2020-07-31 17:14:26	1034.0	1.57 ± 0.04
3201670121	2020-07-31 20:20:26	1033.0	1.75 ± 0.05
3201670121	2020-07-31 23:26:07	1045.0	2.04 ± 0.05
3201670122	2020-08-01 02:32:07	1033.0	1.79 ± 0.05
3201670122	2020-08-01 05:38:07	1029.0	2.71 ± 0.06
3201670122	2020-08-01 11:49:49	1031.0	2.23 ± 0.05
3201670122	2020-08-01 14:55:43	1031.0	2.12 ± 0.05
3201670122	2020-08-01 21:18:12	387.4	1.84 ± 0.08
3201670123	2020-08-02 04:52:09	1025.0	2.02 ± 0.05
3201670123 3201670123	2020-08-02 11:03:48 2020-08-02 14:09:47	1030.0	1.54 ± 0.04 2.02 ± 0.05
3201670123	2020-08-02 14:09:47	1024.0 1040.0	2.02 ± 0.03 1.97 ± 0.05
3201670123	2020-08-02 18:48:03	1030.0	1.97 ± 0.03 2.29 ± 0.05
3201670123			1.88 ± 0.05
3201670123	2020-08-02 23:27:27 2020-08-03 01:00:26	1016.0 397.0	1.88 ± 0.03 1.45 ± 0.07
3201670124	2020-08-03 01:00:20	1027.0	2.08 ± 0.07
3201670124	2020-08-03 08:45:05	1027.0	2.08 ± 0.03 2.29 ± 0.05
3201670124	2020-08-03 14:56:48	1024.0	2.29 ± 0.03 2.16 ± 0.05
3201670124	2020-08-03 14:30:48	1017.0	2.10 ± 0.05 2.22 ± 0.05
3201670124	2020-08-03 18:02:40	1033.0	2.36 ± 0.05
32010/012 1	2020 00 03 22.41.27	1055.0	2.50 ± 0.05

1	Con	tini	nation	of Tak	10	1 A

		Con	tilluation of Table 4.A	
	3201670125	2020-08-04 04:53:28	1012.0	2.10 ± 0.05
	3201670125	2020-08-04 07:59:08	1032.0	1.82 ± 0.05
	3201670125	2020-08-04 11:05:06	1006.0	1.67 ± 0.05
	3201670125	2020-08-04 14:11:04	1023.0	2.54 ± 0.05
	3201670125	2020-08-04 17:16:47	988.0	2.05 ± 0.05
	3201670125	2020-08-04 20:22:47	1028.0	2.14 ± 0.05
	3201670125	2020-08-04 23:28:26	1043.0	2.03 ± 0.05
	3201670126	2020-08-05 04:07:26	1033.0	2.78 ± 0.06
	3201670126	2020-08-05 07:13:26	1027.0	2.66 ± 0.06
	3201670126	2020-08-05 10:19:06	1034.0	2.07 ± 0.05
	3201670126	2020-08-05 13:25:07	1033.0	2.35 ± 0.05
	3201670126	2020-08-05 16:31:06	1033.0	2.35 ± 0.05 2.36 ± 0.05
	3201670126	2020-08-05 19:36:47	1042.0	2.02 ± 0.05
	3201670126	2020-08-05 22:42:46	1034.0	2.50 ± 0.06
	3201670127	2020-08-06 01:48:47	1030.0	2.27 ± 0.05
	3201670127	2020-08-06 04:54:27	1045.0	1.93 ± 0.05
	3201670127	2020-08-06 08:00:26	1034.0	2.29 ± 0.05
	3201670127	2020-08-06 11:06:20	1040.0	2.24 ± 0.05
	3201670127	2020-08-06 14:12:06	1048.0	2.53 ± 0.05
	3201670127	2020-08-06 17:18:08	1041.0	2.23 ± 0.05
	3201670127	2020-08-06 20:24:01	1038.0	2.38 ± 0.05
	3201670127	2020-08-06 23:29:47	1051.0	2.03 ± 0.05
	3201670128	2020-08-07 02:35:51	1042.0	2.54 ± 0.05
	3201670128	2020-08-07 05:41:27	1036.0	1.78 ± 0.05
	3201670128	2020-08-07 08:49:41	919.0	2.64 ± 0.06
	3201670128	2020-08-07 11:53:28	1048.0	1.76 ± 0.05
	3201670128	2020-08-07 14:59:05	1068.0	2.39 ± 0.05
	3201670128	2020-08-07 18:05:07	1053.0	2.77 ± 0.06
	3201670128	2020-08-07 21:10:45	1075.0	2.13 ± 0.05
	3201670129	2020-08-08 00:16:45	1073.0	2.48 ± 0.05
	3201670129	2020-08-08 06:28:28	1072.0	2.50 ± 0.05
	3201670129	2020-08-08 12:40:24	1076.0	2.63 ± 0.05
	3201670129	2020-08-08 18:52:08	1086.0	3.10 ± 0.06
	3201670129	2020-08-08 21:57:49	1091.0	2.93 ± 0.06
	3201670130	2020-08-09 01:03:45	1095.0	3.08 ± 0.06
	3201670130	2020-08-09 04:09:46	1094.0	2.94 ± 0.06
	3201670130	2020-08-09 07:16:44	1036.0	2.90 ± 0.06
	3201670130	2020-08-09 11:54:24	1116.0	3.37 ± 0.06
	3201670130	2020-08-09 16:33:08	1132.0	3.27 ± 0.06
	3201670131	2020-08-10 00:17:47	1136.0	3.17 ± 0.06
	3201670131	2020-08-10 04:56:45	1155.0	3.39 ± 0.06
	3201670131	2020-08-10 11:08:27	1123.0	3.94 ± 0.06
	3201670131	2020-08-10 17:20:06	1189.0	3.73 ± 0.06
	3201670131	2020-08-10 20:26:06	1198.0	2.66 ± 0.05
	3201670132	2020-08-11 02:53:42	328.0	2.99 ± 0.10
	3201670132	2020-08-11 05:59:23	320.0	4.11 ± 0.12
	3201670132	2020-08-11 08:49:27	1234.0	4.05 ± 0.06
_				

	Con	tinuation of Table 4	↓.A
3201670132	2020-08-11 16:34:06	1294.0	3.81 ± 0.06
3201670133	2020-08-12 01:51:47	1286.0	3.51 ± 0.06
3201670133	2020-08-12 06:30:28	1124.0	3.91 ± 0.06
3201670133	2020-08-12 12:56:02	365.0	3.39 ± 0.10
3201670133	2020-08-12 13:02:30	363.0	3.35 ± 0.10
3201670133	2020-08-12 16:02:01	1317.0	3.29 ± 0.05
3201670133	2020-08-12 18:54:07	773.0	3.56 ± 0.08
3201670133	2020-08-12 21:59:48	1585.0	3.34 ± 0.05
3201670133	2020-08-12 23:32:45	1308.0	2.85 ± 0.05
3201670134	2020-08-13 02:38:45	1359.0	3.28 ± 0.05
3201670134	2020-08-13 04:11:45	918.0	3.32 ± 0.07
3201670134	2020-08-13 07:17:27	1203.0	2.97 ± 0.05
3201670134	2020-08-13 10:23:26	1257.0	2.64 ± 0.05
3201670134	2020-08-13 16:35:05	1277.0	2.39 ± 0.05
3201670134	2020-08-13 22:46:47	1170.0	1.62 ± 0.04
3201670134	2020-08-13 23:06:44	496.0	1.61 ± 0.07
3201670135	2020-08-14 18:54:44	1436.0	0.85 ± 0.03
3201670137	2020-08-16 09:38:08	1375.0	0.76 ± 0.03
3201670140	2020-08-19 05:46:48	2083.0	0.65 ± 0.02
3201670140	2020-08-19 10:49:10	682.0	0.61 ± 0.04
3201670141	2020-08-20 11:28:57	1302.6	0.92 ± 0.03
3201670141	2020-08-20 20:49:25	828.0	0.83 ± 0.04
3201670142	2020-08-21 04:14:11	1722.0	1.41 ± 0.03
3201670142	2020-08-21 08:55:29	1584.0	1.07 ± 0.03
3201670142	2020-08-21 15:04:50	1584.0	1.46 ± 0.04
3201670142	2020-08-21 20:01:55	842.0	1.53 ± 0.05
3201670143	2020-08-22 00:37:08	1372.0	0.94 ± 0.03
3201670143	2020-08-22 05:08:36	1804.0	1.30 ± 0.03
3201670143	2020-08-22 14:25:35	858.0	1.70 ± 0.05
3201670144	2020-08-22 23:42:54	1826.0	1.57 ± 0.04
3201670144	2020-08-23 04:14:46	1307.0	1.56 ± 0.04
3201670144	2020-08-23 08:59:32	1408.0	1.77 ± 0.04
3201670144	2020-08-23 15:11:55	685.0	1.45 ± 0.07
3201670145	2020-08-24 03:35:12	1426.0	1.81 ± 0.04
3201670145	2020-08-24 12:52:09	772.0	2.35 ± 0.06
3201670145	2020-08-24 17:30:54	999.0	2.73 ± 0.06
3201670145	2020-08-24 22:10:32	1549.1	2.37 ± 0.05
3201670146	2020-08-25 02:42:49	1517.4	2.55 ± 0.05
3201670146	2020-08-25 07:27:32	1491.0	3.52 ± 0.05
3201670146	2020-08-25 12:06:08	1502.0	3.35 ± 0.05
3201670146	2020-08-25 16:44:07	1460.0	2.77 ± 0.05
3201670146	2020-08-25 21:22:49	1589.0	3.27 ± 0.05
3201670147	2020-08-26 02:01:48	1465.0	3.77 ± 0.06
3201670147	2020-08-26 06:41:29	1638.5	3.91 ± 0.05
3201670147	2020-08-26 11:19:46	872.0	3.70 ± 0.07
3201670147	2020-08-26 14:26:03	1481.0	3.32 ± 0.05
3201670147	2020-08-26 20:39:25	1455.0	3.79 ± 0.06

Continuation of	f Table 4.A
-----------------	-------------

		Coi	itiliuation of Table 4.A	
	3201670148	2020-08-27 10:38:43	1117.0	1.94 ± 0.05
	3201670148	2020-08-27 15:11:24	1747.0	1.43 ± 0.04
	3201670148	2020-08-27 19:50:26	1735.3	1.13 ± 0.03
	3201670149	2020-08-28 00:46:51	679.6	1.02 ± 0.05
	3201670149	2020-08-28 02:18:03	754.4	1.61 ± 0.06
	3201670149	2020-08-28 11:29:08	731.9	1.15 ± 0.05
	3201670149	2020-08-28 15:57:20	260.8	1.45 ± 0.10
	3201670149	2020-08-28 16:03:23	952.6	1.35 ± 0.05
	3201670149	2020-08-28 10:03:23	1231.0	1.30 ± 0.03 1.30 ± 0.04
	3201670149	2020-08-29 02:42:46		
			1608.0	1.52 ± 0.04
	3201670150	2020-08-29 07:22:25	1569.0	1.91 ± 0.04
	3201670150	2020-08-29 13:41:27	1096.2	1.82 ± 0.05
	3201670150	2020-08-29 19:45:21	2035.0	1.83 ± 0.04
	3201670151	2020-08-30 01:56:06	1688.0	1.86 ± 0.04
	3201670151	2020-08-30 09:58:40	1004.0	1.50 ± 0.05
	3201670151	2020-08-30 15:56:11	1527.0	1.61 ± 0.04
	3201670152	2020-08-31 04:15:17	1777.0	2.36 ± 0.04
	3201670152	2020-08-31 10:43:41	390.0	2.57 ± 0.09
	3201670152	2020-08-31 16:39:00	901.0	2.84 ± 0.06
	3201670152	2020-08-31 16:55:57	404.0	2.23 ± 0.09
	3201670152	2020-08-31 22:58:00	1069.0	3.19 ± 0.06
	3201670153	2020-09-01 05:09:58	944.0	2.96 ± 0.06
	3201670153	2020-09-01 11:15:06	1317.0	2.91 ± 0.06
	3201670154	2020-09-01 23:43:31	974.0	3.28 ± 0.07
	3201670155	2020-09-09 15:35:28	772.0	5.94 ± 0.09
	3201670155	2020-09-09 21:47:27	953.0	5.23 ± 0.08
	3201670156	2020-09-10 03:57:28	777.0	5.64 ± 0.09
	3201670156	2020-09-10 10:12:10	1149.0	5.18 ± 0.07
	3201670156	2020-09-10 16:36:04	576.0	5.47 ± 0.10
	3201670156	2020-09-10 22:39:37	1023.0	5.92 ± 0.08
	3201670157	2020-09-11 04:56:23	577.0	4.98 ± 0.10
	3201670157	2020-09-11 10:54:43	517.0	5.77 ± 0.11
	3201670157	2020-09-11 23:18:17	983.0	5.23 ± 0.07
	3201670158	2020-09-12 05:30:23	957.0	4.67 ± 0.07
	3201670158	2020-09-12 11:41:35	1025.0	3.41 ± 0.06
	3201670158	2020-09-12 17:51:33	715.0	3.82 ± 0.08
	3201670159	2020-09-13 06:11:07	713.0	4.23 ± 0.08
	3201670160	2020-09-14 13:28:31	869.0	3.99 ± 0.07
	3201670160			
		2020-09-14 19:28:45	518.0	3.65 ± 0.09
	3201670161	2020-09-15 01:31:07	2153.0	3.81 ± 0.04
	3201670161	2020-09-15 07:43:54	856.0	3.53 ± 0.07
	3201670161	2020-09-15 20:10:18	515.0	3.06 ± 0.08
	3201670162	2020-09-16 08:36:46	532.0	3.48 ± 0.09
	3201670162	2020-09-16 14:50:07	1576.0	2.92 ± 0.05
	3201670162	2020-09-16 21:05:09	934.0	2.77 ± 0.06
	3201670167	2020-09-21 04:44:27	271.0	0.81 ± 0.07
_	3201670167	2020-09-21 17:06:48	1013.0	1.44 ± 0.05

3201670179

3201670180

3201670184

2020-10-03 06:37:27

2020-10-04 13:19:08

2020-10-08 02:45:23

	Cont	tinuation of Table	4.A
3201670168	2020-09-22 11:51:05	1098.0	1.95 ± 0.05
3201670168	2020-09-22 17:51:57	856.0	2.52 ± 0.06
3201670169	2020-09-23 04:48:04	1333.0	0.92 ± 0.03
3201670169	2020-09-23 06:20:43	1440.0	1.53 ± 0.04
3201670170	2020-09-24 03:47:48	2315.0	2.18 ± 0.04
3201670170	2020-09-24 17:51:47	1876.0	1.08 ± 0.03
3201670171	2020-09-25 00:08:10	427.0	1.54 ± 0.07
3201670171	2020-09-25 20:04:12	1103.0	1.57 ± 0.05
3201670172	2020-09-26 08:27:44	1140.0	0.74 ± 0.04
3201670172	2020-09-26 21:09:11	1249.0	1.80 ± 0.05
3201670174	2020-09-28 14:45:24	1024.0	2.64 ± 0.06
3201670175	2020-09-29 03:03:50	2083.0	1.32 ± 0.03
3201670175	2020-09-29 15:33:30	2154.0	1.28 ± 0.03
3201670176	2020-09-30 22:31:45	334.0	0.80 ± 0.07
3201670177	2020-10-01 10:55:46	1453.0	1.01 ± 0.04
3201670177	2020-10-01 17:01:30	1599.0	0.93 ± 0.03

1117.0 End of Table

354.4

303.9

 0.71 ± 0.06

 1.23 ± 0.08

 1.11 ± 0.04

Table 4.B: Swift observations used for the MOSFiT analysis of the UV data in Section 4.3.4.

Observation ID	Date	XRT exposure (s)	UVOT exposure (s)
00013592001	2020-06-25	2200	2167
00013592002	2020-07-02	1612	1595
00013592003	2020-07-09	1885	1824
00013608001	2020-07-11	4958	4948
00013608002	2020-07-11	3977	3916
00013608003	2020-07-13	4983	4920
00013608005	2020-07-15	4701	4693
00013592004	2020-07-16	568	567
00013608006	2020-07-16	4483	4477
00013608007	2020-07-17	4603	4601
00013608008	2020-07-18	995	987
00013608009	2020-07-19	241	240
00013608010	2020-07-20	933	911
00013592005	2020-07-21	1402	1383
00013608011	2020-07-22	943	929
00013592006	2020-07-23	2208	2175
00013608012	2020-07-23	1003	990
00013608013	2020-07-24	835	823
00013608014	2020-07-31	963	952
00013608016	2020-08-04	827	816
00013608017	2020-08-06	905	895
00013608018	2020-08-08	938	924
00013608019	2020-08-10	1058	1047
00013608020	2020-08-20	1665	1640
00013608021	2020-08-22	1138	1127
00013608022	2020-08-24	1803	1779
00013608023 00013608024	2020-08-26 2020-08-28	1316 1729	1304 1706
00013608024	2020-08-28	1637	1624
00013608025	2020-08-30	1597	0
00013608020	2020-09-01	2088	2054
00013608027	2020-09-05	2055	2003
00013608028	2020-09-12	1443	1432
00013608029	2020-09-15	915	910
00013608031	2020-09-18	1672	1649
00013608031	2020-09-21	998	986
00013608033	2020-09-24	1382	1370
00013608034	2020-09-27	1363	1351
00013608035	2020-09-30	1413	1400
00013608036	2020-10-03	1387	1375
00013608037	2020-10-06	1038	1025
00013608038	2020-10-09	313	303
00013608039	2020-10-11	1401	1368
00013608040	2020-10-15	1850	1827
00013608041	2020-10-18	1680	1668
00013608042	2020-10-21	268	267

	Continuation of Table 4.B						
00013608043	2020-10-23	346	482				
00013608044	2020-10-27	1256	1243				
00013608046	2020-11-02	2174	2152				
00013608047	2020-11-05	1951	1885				
00013608048	2020-11-08	2136	2102				
00013608049	2020-11-08	1988	1967				
00013608050	2020-11-11	1842	1807				
00013608051	2020-11-14	1434	1423				
00013608052	2020-11-17	2023	2002				
00013608053	2020-11-20	1908	1886				
00013608054	2020-11-27	868	856				
00013608055	2020-11-30	835	823				
00013608056	2020-12-03	955	943				
00013608057	2020-12-10	873	860				
00013608059	2020-12-18	880	868				
00013608060	2020-12-21	653	643				
00013608061	2020-12-24	980	969				
00013608062	2021-02-24	707	696				
00013608063	2021-02-27	940	930				
00013608064	2021-03-02	537	531				
00013608065	2021-03-05	955	933				
00013608066	2021-03-11	903	880				
00013608067	2021-03-14	1063	1040				
00013608068	2021-03-20	855	843				
00013608069	2021-03-23	1068	1056				
00013608070	2021-05-28	68	67				
00013608071	2021-05-31	1738	1715				
00013608072	2021-06-06	1695	1683				
00013608073	2021-06-18	1259	1225				
00013608074	2021-06-21	1786	1744				

End of Table

SLIM-DISK MODELING REVEALS AN ACCRETING INTERMEDIATE-MASS BLACK HOLE IN THE LUMINOUS FAST BLUE OPTICAL TRANSIENT AT2018cow

Z. Cao, P.G. Jonker, D.R. Pasham, S. Wen, A.I. Zabludoff Astronomy & Astrophysics, Volume 691, November 2024

Abstract

The origin of the most luminous subclass of the fast blue optical transients (LFBOTs) is still unknown. We present an X-ray spectral analysis of AT2018cow — the LFBOT archetype — using *NuSTAR*, *Swift*, and *XMM-Newton* data. The source spectrum can be explained by the presence of a slim accretion disk, and we find that the mass accretion rate decreases to sub-Eddington levels ≥ 200 days after the source's discovery. Applying our slim-disk model to data obtained at multiple observational epochs, we constrain the mass of the central compact object in AT2018cow to be $\log(M_{\bullet}/M_{\odot})=2.4^{+0.6}_{-0.1}$ at the 68% confidence level. Our mass measurement is independent from, but consistent with, the results from previously employed methods. The mass constraint is consistent with both the tidal disruption and the black hole—star merger scenarios, if the latter model can be extrapolated to the measured black hole mass. Our work provides evidence for an accreting intermediate—mass black hole $(10^2-10^6~M_{\odot})$ as the central engine in AT2018cow, and, by extension, in LFBOT sources similar to AT2018cow.

5.1 Introduction

Fast blue X-ray transients (FBOTs; e.g., Drout et al. 2014; Arcavi et al. 2016; Tanaka et al. 2016; Pursiainen et al. 2018; Tampo et al. 2020; Ho et al. 2022a, 2023) have attracted significant attention in recent years as their physical nature is not yet known. Those at the most luminous end ($\gtrsim 10^{44} \ erg \ s^{-1}$) of the FBOT population are often referred to as luminous FBOTs (LFBOTs).

LFBOTs are characterized by a rapid optical rise and high peak luminosity (reaching peak luminosity on a timescale of days; e.g., Drout et al. 2014; Pursiainen et al. 2018; Rest et al. 2018; Ho et al. 2023).

The archetype of LFBOTs is AT2018cow, which was discovered on June 16, 2018, or modified Julian date (MJD) 58285, by the ATLAS survey (Smartt et al. 2018). The host galaxy CGCG137-068 has a luminosity distance of \sim 60 Mpc (redshift z=0.01404; Adelman-McCarthy et al. 2008). AT2018cow is the nearest LFBOT to Earth and has been observed across a broad energy range. Multi-wavelength observations show that the source emission extends from radio to gamma rays (e.g., Prentice et al. 2018; Rivera Sandoval et al. 2018; Kuin et al. 2019; Margutti et al. 2019; Perley et al. 2019; Ho et al. 2019; Nayana & Chandra 2021). In particular, X–ray emission was observed immediately after the source's discovery (Rivera Sandoval et al. 2018; Kuin et al. 2019). Analysis of the X–ray spectrum shows that the earliest deep X–ray observation of *NuSTAR* could be described well by reflection off an accretion disk (Margutti et al. 2019).

Different models have been proposed to explain the multi–wavelength behavior of AT2018cow, or AT2018cow–like LFBOTs (e.g., AT2020xnd/ZTF20acigmel, Perley et al. 2021; AT2020rmf, Yao et al. 2022b). One class of scenarios involves an accreting compact object, either a neutron star or a black hole (BH), as the "central engine" for the highly variable, nonthermal X–ray emission. Examples in this class of models include i) a tidal disruption event (TDE) involving an intermediate–mass black hole (IMBH; BH mass, M_{\bullet} , between 10^2 and 10^6 M_{\odot} ; Kuin et al. 2019; Perley et al. 2019); ii) a core–collapse event such as a supernova giving birth to the central compact object, which then accretes fall-back progenitor material (e.g., Prentice et al. 2018; Margutti et al. 2019; Perley et al. 2019; Mohan et al. 2020; Gottlieb et al. 2022); and iii) a binary merger of a BH and its massive stellar companion (Metzger 2022).

Meanwhile, there is another class of models that relies exclusively on shock interactions in the circumstellar material (CSM; e.g., Rivera Sandoval et al. 2018; Fox & Smith 2019; Leung et al. 2021; Pellegrino et al. 2022). However, these models cannot explain the observed early–time X–ray/γ–ray behavior without also invoking an accreting compact object (see, e.g., Margutti et al. 2019; Coppejans et al. 2020; Pasham et al. 2022; Yao et al. 2022b; Metzger 2022; Migliori et al. 2023). Furthermore, late–time (≥ 200 days since MJD 59295) observations of AT2018cow reveal a soft X–ray source spectrum (Migliori et al. 2023). Moreover, the source enters a long–lasting "plateau" phase in the UV light curves (e.g., Inkenhaag et al. 2023), resembling a BH evolving from a high to a low mass accretion rate, which can last months to years (e.g., similar to what has been seen in many TDEs; van Velzen et al. 2019; Mummery & Balbus 2020; Wen et al. 2023; Cao et al. 2023; Mummery et al. 2024b).

The mass of the central compact object is of key importance in unveiling the nature of AT2018cow-like LFBOTs. To that end, it is essential to compare different mass measurements to verify the different measurement methods. Several studies have reported (limits on) the compact object mass in AT2018cow. From an X-ray timing analysis, Pasham et al. (2022) find an upper limit on the central object mass of $\lesssim 850\,M_\odot$, assuming the quasiperiodic oscillations in the arrival times of X-ray photons are due to particular orbital frequencies in an accretion disk (but see Zhang

et al. 2022). Migliori et al. (2023) constrain the compact object mass to be $\approx 10-10^4~M_{\odot}$ based on energetic arguments, while Inkenhaag et al. (2023) find the mass to be $10^{3.2\pm0.8}~M_{\odot}$ based on modeling of the late–time UV emission as coming from a TDE–like accretion disk. In this paper, we use X–ray spectral analysis to provide a mass measurement of the central compact object.

The paper is structured as follows: In Sect. 2 we describe the data and the data reduction method. In Sect. 3 we describe the slim-disk model. In Sect. 4 we present the results from our analysis. In Sect. 5 we discuss the results and present our conclusions.

5.2 Methods and data reduction

In this study, we used Poisson statistics (Cash 1979; C-STAT in XSPEC). We quote all parameter errors at the 1σ (68%) confidence level, assuming Δ C-stat = 1.0 and Δ C-stat=2.3 for single—and two–parameter error estimates, respectively. When needed, we used the Akaike information criterion (AIC; Akaike 1974) to investigate the significance of adding model components to the fit function, which is calculated as Δ AIC= $-\Delta$ C + 2Δ k (C is the C-stat and k is the degree of freedom; Wen et al. 2018). The Δ AIC > 5 and > 10 cases are considered a strong and a very strong improvement, respectively, over the alternative model. For all the fits we performed in this study, we included Galactic absorption using the model TBabs (Wilms et al. 2000). We fixed the column density, $N_{\rm H}$, to $5 \times 10^{20} {\rm cm}^{-2}$ without considering any intrinsic absorption, consistent with the work by (Margutti et al. 2019; Migliori et al. 2023).

5.2.1 NuSTAR observations

AT2018cow has been observed by NuSTAR on five occasions since June 23, 2018 (MJD 58292). Due to the X–ray flux decreasing above 3 keV, AT2018cow was not detected in the last NuSTAR observation (ObsID: 80502407002), and a count–rate upper limit of 1.1×10^{-4} counts s⁻¹ has been inferred (Migliori et al. 2023). To perform spectral analysis, in this study we only considered the first four NuSTAR observations, which were all taken within 37 days of the discovery of the source. A list of the NuSTAR observations analyzed in this paper is presented in Table 5.A. We performed the NuSTAR data reduction using NuSTARDAS version 1.9.7 with calibration files updated on October 17, 2023 (version 20231017). We used the pipeline tool Nuprpeline to extract the level–2 science data, and the tool Nuproduct to produce the source+background and background spectra from the level–2 data. For both the focal plane detector modules (FPMA and FPMB) on board NuSTAR, the source+background spectra are extracted from a circular source region of 30" radius, centered on the source. The background spectra are extracted from circular apertures of > 50" radii close to the source on the same detector, free from other bright sources.

5.2.2 XMM-Newton observations

AT2018cow was observed by *XMM-Newton* on three occasions within 300 days of its discovery, and another three occasions in the year 2022. Because the source becomes so faint that the back-

ground flux dominates over the source+background flux, we discarded the last three *XMM-Newton* observations (ObsID: 0843550401, 0843550501, 0843550601) in our subsequent analysis. We list the *XMM-Newton* observations used for the analysis presented in this paper in Table 5.A. We reduced the *XMM-Newton* data using HEASOFT version 6.32.1 and SAS version 21.0.0 with calibration files renewed on October 5, 2023 (CCF release: XMM-CCF-REL-402). During one of the observations (ObsID: 0822580501), one of the two MOS detectors onboard *XMM-Newton* was used for calibration, and no scientific data was obtained. Meanwhile, the signal—to—noise ratio in the RGS detectors is too low to perform spectral analysis. Therefore, for consistency, we only used the data from the EPIC-pn detector.

We used the SAS task epproc to process the data. We employed the standard filtering criteria to exclude periods with an enhanced background count rate, requiring that the 10-12 keV detection rate of pattern 0 events is < 0.4 counts $\rm s^{-1}$. We used a circular source region of 25'' radius centered on the source for the source+background spectral extraction. This extraction region is somewhat smaller than what we would normally have used because it is designed to avoid contamination from nearby soft–X-ray sources and the detector edges. Using the SAS command EPATPLOT, we checked for the presence of photon pileup and find no evidence for effects caused by pileup. The background spectra are extracted from circular apertures of $\gtrsim 40''$ radii close to the source on the same detector, free from other bright sources.

5.2.3 *Swift* **observations**

In this paper we also include the X–ray data from the *Swift*/XRT instrument. *Swift* monitored AT2018cow in the first 100 days after its discovery. We extracted the X–ray light curve from *Swift*/XRT using the online data reduction pipeline¹(Evans et al. 2009), applying the default reduction criteria. Using the same tool, we also extracted the *Swift*/XRT source+background spectra and the background spectra (see Evans et al. 2009 for more details). Furthermore, for each of the *NuSTAR* epochs, we combined the extracted *Swift*/XRT spectra that were taken on the same date. In this way, we prepared the quasi–simultaneous *Swift*/XRT observations for joint spectral analysis with the *NuSTAR* observations. We present the information from these periods for the spectral count extraction in Table 5.A.

Throughout this study, we carried out spectral analysis using the XSPEC package (Arnaud 1996; version 12.13.1). With the energies command in XSPEC, we created a logarithmic energy array of 1000 bins from 0.1 to 1000.0 keV for model calculations in all analyses for the sake of consistency. Using the FTOOL ftgrouppha for spectral analysis, we re-binned every background and source+background spectrum using the optimal-binning algorithm (Kaastra & Bleeker 2016), while requiring the spectra to have a minimum of one count per bin (with parameter grouptype in ftgrouppha set to optimin). For every spectrum, we discarded the data bins where the background flux dominates over the source+background flux. The remaining energy bands in each spectrum for our spectral analysis are given in Table 5.A.

¹https://www.swift.ac.uk/user objects/

For every remaining observation, we first fit the background spectrum using a phenomenological model. When fitting the source+background spectrum, we added the best–fit background model to the fit function describing the source+background spectrum, with the background model parameters all fixed to their best–fit values as determined from the fit to the background–only spectrum. The best–fit background model varies from instrument to instrument, and from epoch to epoch. For the *XMM-Newton*EPIC-pn data, the best–fit phenomenological background model consists of between two and three power–law components and two to three Gaussian components; for *NuSTAR*, it consists of two power–law and three Gaussian components; for *Swift*, it consists of two power–law components. The full width at half maximum of every background Gaussian component was fixed to $\sigma_{\text{Gauss}} = 0.001 \text{ keV}$, which is less than the spectral resolution of *XMM-Newton*/EPIC-pn, *NuSTAR*, or *Swift*. Such phenomenological models account for both the background continuum and the fluorescence lines (e.g., Katayama et al. 2004; Pagani et al. 2007; Harrison et al. 2010). In this paper, when studying the source+background spectra, we refer only to the part of the fit function that describes the source as the fit function.

We grouped all the data mentioned above into six epochs by time of observation. A list of the epochs and the associated observations can be found in Table 5.A. When performing spectral analysis, we always jointly fit the spectra within the same epoch using the same fit function for the source spectra. To account for the mission-specific calibration differences, we used a constant component (constant in XSPEC) to multiply the source models. This constant serves as a re–normalization factor between different instruments. Specifically, we fixed the constant to 1 for *NuSTAR*/FPMA spectra and left the constant for other instruments free to vary in the fits for each epoch.

5.3 Extending slim disk model slimdz to lower M_{\bullet}

The very luminous X-ray emissions from AT2018cow (peak luminosity $L_x \gtrsim 10^{44} \, {\rm erg \ s^{-1}}$) imply the source is in the super-Eddington regime, at least for the early days when its X-rays are near their peak, if powered by accretion onto a BH of $10^1 - 10^3 \, M_\odot$. When the mass accretion rate is at near- or super-Eddington levels, the accretion disk can no longer be adequately described by a standard thin-disk model (Shakura & Sunyaev 1973), as the inward advection of the liberated energy is no longer negligible (e.g., Abramowicz et al. 1988). Therefore, we chose to use a slim-disk model, slimdz (Wen et al. 2022), to model the disk thermal emission from AT2018cow in our spectral analysis.

In its original form in Wen et al. 2022, the slim-disk model slimdz does not allow for XSPEC fitting of BH masses, M_{\bullet} , lower than $1000~M_{\odot}$, because the precalculated library of disk spectra only extends to that BH mass limit. To model the high-Eddington or super-Eddington disk of a BH on $10^1-10^3~M_{\odot}$ mass scales, we modified slimdz by expanding the precalculated library down to $10~M_{\odot}$. We followed the same procedures as in Wen et al. 2022 to calculate and ray-trace the disk spectrum given M_{\bullet} .

To make the new spectral library consistent with the original library, we sampled the 10^1 –

 $10^3~M_{\odot}$ mass range in the same way as the original $10^3-10^5~M_{\odot}$ mass range, simply scaling down all sampled values by two orders of magnitude. Then, for each sampled M_{\bullet} , we calculated the disk spectra for various mass accretion rates, \dot{m} , inclinations, θ , and BH spins, a_{\bullet} . We used the same sampled values of \dot{m} , θ , and a_{\bullet} used to construct the original library in Wen et al. 2022.

Notably, when the disk is nearly face—on ($\theta < 3^{\circ}$), the ray—tracing does not behave well, as described in Psaltis & Johannsen 2011. Thus, to avoid errors and to keep the model self—consistent across different mass scales, we set the lower boundary of θ allowed in the modified slimdz to 3° . This is slightly larger than the limit of 2° in the original slimdz model for more massive BHs. The reason is that, for the lower-mass BH range we considered here, the curvature is larger, aggravating the problems with near–face—on ray—tracing.

We note that in the slimdz model, the viscosity parameter, α (Shakura & Sunyaev 1973) is fixed to 0.1. Numerical simulations of super–Eddington accretion flows have shown that $\alpha \sim 0.1$ for a BH of 10 M_{\odot} and various \dot{m} (Sądowski et al. 2015). Furthermore, calculations indicate that the impact of α (0.01–0.1) on the emergent spectrum is small compared to that of other model parameters like M_{\bullet} or a_{\bullet} across different M_{\bullet} scales (from 10 to $10^6~M_{\odot}$; e.g.,Dotan & Shaviv 2011; Wen et al. 2020).

Meanwhile, although the disk radiative efficiency, η , was fixed to 0.1 in the slimdz model, this was only done to determine the unit of the mass accretion rate: $\dot{m}_{\rm Edd} = 1.37 \times 10^{21} \, {\rm kg \, s^{-1}} (0.1/\eta) (M_{\bullet}/10^6 M_{\odot})$. The actual disk radiative efficiency can be determined from the physical value of \dot{m} after constraining the mass M_{\bullet} , and the efficiency can vary between epochs (as expected in the slim-disk scenario when the \dot{m} changes; e.g., Abramowicz & Fragile 2013).

Moreover, Wen et al. 2022 ray-traced the accretion disk only up to $\leq 600 \ R_g$ (here $R_g = GM_{\bullet}/c^2$ is the gravitational radius of the BH), as regions with $R > 600 \ R_g$ are expected to contribute little to the X-ray flux of TDEs due to the significant temperature decrease as a function of radius. Wen et al. (2021) find that an error of $\leq 1\%$ in flux is introduced by this choice of outer disk radius for the ray-tracing. However, TDEs with lower-mass BHs are likely to have larger disks ($\geq 2 \times 10^5 \ R_g$ for a $10 \ M_{\odot}$ BH disrupting a solar-type star), and such disks are quantitatively different from those with $\geq 10^4 \ M_{\odot}$ BHs. We tested and find that, to keep the flux error $\leq 1\%$ for most prograde spinning BHs, we have to extend the ray-tracing to at least $800 \ R_g$ (Fig. 5.A(a)). In the appendix, we show the comparison between the disk spectra with different choices of outer radii for the ray-tracing. Therefore, in our model calculations, the disk is ray-traced up to $800 \ R_g$. We note that, in extreme cases of retrograde spinning BHs (e.g., $M_{\bullet} = 10 \ M_{\odot}$, $a_{\bullet} = -0.998$, and $\dot{m} = 100 \ \dot{m}_{\rm Edd}$), the flux errors introduced by this choice for the ray-tracing radius could be as large as $\sim 50\% < 1 \ {\rm keV}$ (Fig. 5.A(b)). We are therefore cautious when interpreting the results in those cases.

Recently, by combining thin–disk results at the innermost stable circular orbit (ISCO) with numerical simulations, Mummery et al. 2024a find that in some cases the plunging region inside the ISCO also contributes a significant part to the BH X–ray spectrum, associated with a finite stress at the ISCO due to a magnetic field and an extremely high spectral hardening factor of $f_c \sim 100$. In our case, the slim-disk solution (e.g., temperature, T, and surface density, Σ , as a

5.4 Results 115

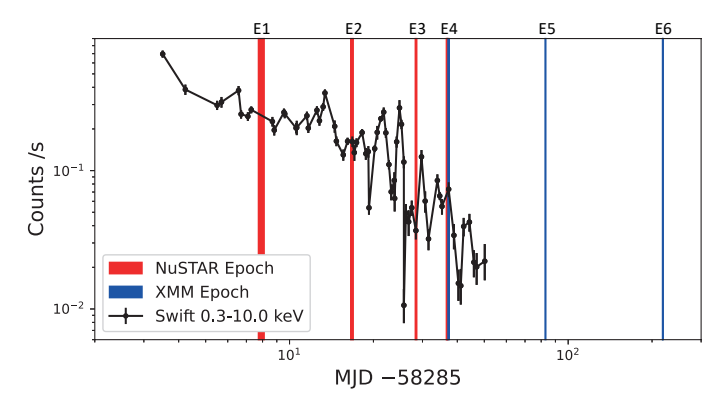


FIGURE 5.1: *Swift* 0.3–10.0 keV light curve of AT2018cow. The times of the *NuSTAR* and *XMM-Newton* observations are highlighted with red and blue vertical lines, respectively. The six epochs we use to group the observations and the joint analysis in this paper are marked at the top of the figure. See Table 5.A for details of the observations in each epoch. We note that, at E4, the *NuSTAR* and *XMM-Newton* observations do not overlap in time.

function of the disk radius, r) describes the disk self—consistently from the event horizon to the outer disk edge (Sądowski et al. 2011; Wen et al. 2020). When constructing the slimdz spectra library, we employed an inner boundary at the ISCO for ray—tracing purposes only. Wen et al. 2021 find that the flux difference in the 0.2-10 keV energy band between ray—tracing down to the horizon and down to the ISCO is nearly always $\lesssim 2\%$. Therefore, we conclude that the spectral impact of the disk-plunging region is not significant in the slim-disk cases of interest to us, and for consistency we employed the ISCO as the inner boundary of the ray—tracing process in this study as well.

5.4 RESULTS

Fig. 5.1 shows the *Swift* 0.3-10.0 keV light curve as well as the epochs of *NuSTAR* and *XMM-Newton* observations. We first explored the spectral characteristics by fitting the data with a fit function comprised of a power law modified by the effects of Galactic extinction (the fit function in XSPEC's syntax is "constant*TBabs*powerlaw"). Results show that, except for Epoch 1, spectra from the other epochs can be fitted well by a power law (C-stat/d.o.f.<2; Table 5.B). From Epoch 2 to 6, the source becomes increasingly softer in X–rays, with the power–law index changing from $\Gamma = 1.38 \pm 0.02$ (Epoch 2) to 2.8 ± 0.6 (Epoch 6). The soft source spectrum at the latter epoch might indicate the appearance of a soft disk component in the energy range 0.3-1.5 keV.

From the fit residuals for Epoch 1 (Fig. 5.2), we confirm the X–ray features of \sim 6.4 keV and \gtrsim 10 keV found previously (Margutti et al. 2019). These features cause the source spectrum to be

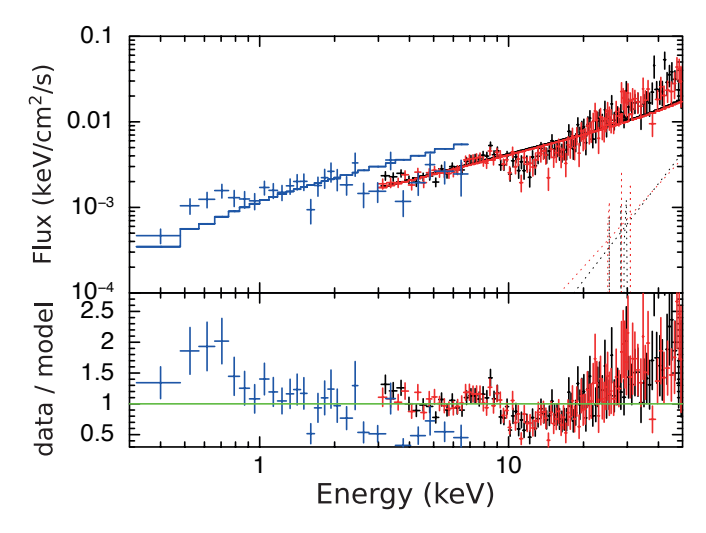


FIGURE 5.2: X–ray spectra from Epoch 1 fitted by a power–law model. In the upper panel we present the data, the power–law model (solid lines), and the background models (dotted lines). The blue, black, and red data are from *Swift*/XRT, *NuSTAR*/FPMA, and *NuSTAR*/FPMB, respectively. In the lower panel, we show the ratio between the observed number of counts (data) and the predicted number of counts in each spectral bin (model). Similarly to what previous studies find, we observe X–ray features around ~6.4 keV and above 10 keV that are likely due to reflection.

inconsistent with a single power–law fit function at Epoch 1, and they have been proposed to be due to the reflection of the primary power–law emission (possibly caused by a BH corona or a jet base) off an accretion disk.

We then used the model relxillCp (Dauser et al. 2014; García et al. 2014; see also the References for a detailed description of each model parameter) to account for the disk reflection in the fit function. We note, in relxillCp, that the disk is assumed to be a standard Shakura–Sunyaev thin disk (Shakura & Sunyaev 1973), and the incident power–law emission is modeled by nthcomp (Zdziarski et al. 1996), which assumes a multi–temperature black body seed spectrum modified by a Comptonizing medium. Currently, there are no reflection models that use a slim disk for the disk seed photons or calculating the relativistic effect, and so we used relxillCp to approximate the reflected emission off a slim disk (the total fit function in XSPEC's syntax is "constant*TBabs*relxillCp"). Therefore, we exercise caution when interpreting the results from our fits with relxillCp. At Epoch 1, we find the source emission is consistent with relxillCp, that is, an incident power–law–like emission plus a disk reflection (Table 5.C). The Comptonizing medium is constrained, so it emits a hard power law ($\Gamma = 1.22 \pm 0.02$), and its electron temperature is constrained to be 28 ± 8 keV. The inclination constraint is $74^{\circ} \pm 2$, and the BH spin constraint is 0.98 ± 0.01 .

We then tested for the presence of a spectral component originating from an accretion disk in the other epochs of AT2018cow, using slimdz. The results are summarized in Table 5.C. For

5.4 Results 117

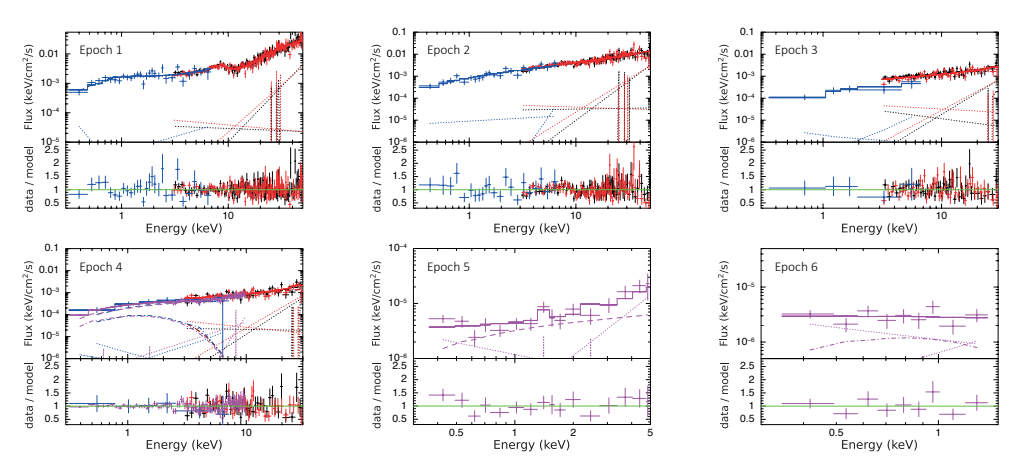


FIGURE 5.3: Best–fit results based on the spectral analysis presented in Table 5.C. For each figure, in the upper panel we present the spectrum and the best–fit models, and in the lower panel we present the ratio between the observed number of counts (data) and the best–fit predicted number of counts in each spectral bin (model). In all figures, the solid, dashed, dot–dashed, and dotted lines represent the best–fit source+background model, the power–law spectral component, the slim-disk component, and the background models, respectively; the blue, black, red, and magenta data are from *Swift*/XRT, *NuSTAR*/FPMA, *NuSTAR*/FPMB, and *XMM-Newton*/EPIC-pn, respectively. The y–axes in the upper panels have different scales in each figure.

Epochs 2 to 6, we find that it is only for Epoch 4 that the fit to the data is significantly improved by adding a disk component to the fit function (the total fit function in XSPEC's syntax is "constant*TBabs*(powerlaw+slimdz)"; Δ AIC=12.8; as a comparison, the power-law-only case exceeds the very strong improvement threshold of 10; Akaike 1974); statistically, Epochs 2, 3, 5, and 6 require no disk components besides a simple power law to attain a good fit to the data. Meanwhile, for Epochs 2, 3, and 5, a slim disk alone ("constant*TBabs*slimdz" in XSPEC's syntax) cannot describe the data well. However, as the source becomes much softer at Epoch 6, we tested and find that the source spectrum at this epoch is consistent with the slim-disk model, yielding a BH mass $\log(M_{\bullet}/M_{\odot})=2.3\pm0.9$, while due to data quality, other disk parameters are not well constrained $(\dot{m}, \theta, a_{\bullet})$. The constraints on the BH mass derived from the spectra at both Epoch 4 and Epoch 6 are consistent with $\log(M_{\bullet}/M_{\odot})\approx 2.4$.

Physically, it is likely that the accretion disk is present around the BH not only at Epochs 1, 4, and 6, but also throughout the period (weeks) after the first detection (Epoch 1). At Epochs 2 and 3, the soft X–ray band (0.3–3.0 keV) can only be investigated through the *Swift*/XRT data. As the slim disk primarily emits soft X–rays, a lack of higher-quality data in the soft band, together with the presence of a strong power–law emission component, make it impossible to constrain the disk emission at Epochs 2 and 3. At Epoch 4, however, the high-quality 0.3–3.0 keV *XMM-Newton* data allow significant measurements of this soft disk component to be made. At Epoch 5, the general decrease in the source luminosity makes it impossible to detect the disk in the

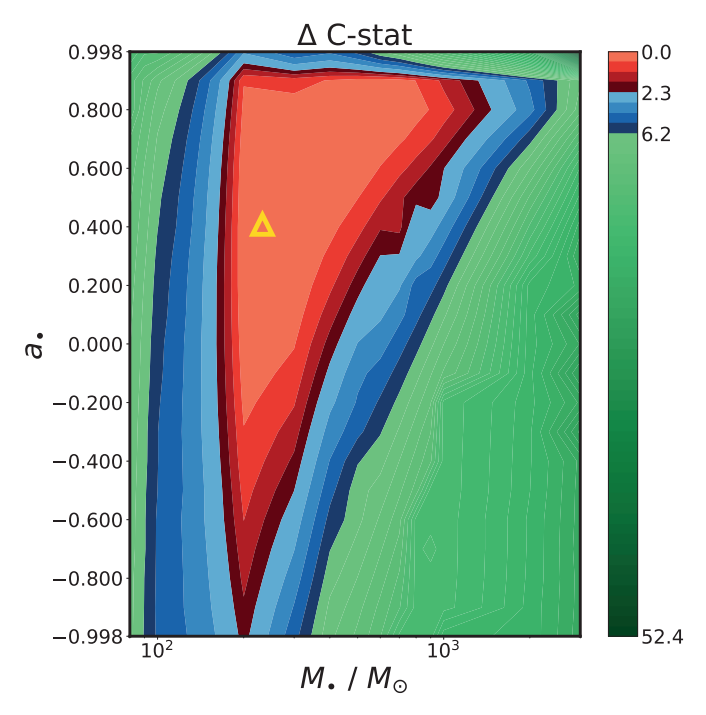


FIGURE 5.4: Constraints on M_{\bullet} and a_{\bullet} based on a joint fit of the X-ray spectra from Epochs 2 to 6 with the slim-disk model (Table 5.D). We calculate the ΔC -stat across the $\{M_{\bullet}, a_{\bullet}\}$ plane. The best-fit point with the lowest C-stat is marked by the yellow triangle. Areas within 1σ and 2σ confidence levels are in red and blue, respectively. At 1σ for the two-parameter fits, M_{\bullet} is constrained to be $\log(M_{\bullet}/M_{\odot}) = 2.4^{+0.6}_{-0.1}$, while a_{\bullet} is virtually unconstrained.

XMM-Newton observation, especially as the source spectrum remains dominated by a power law. At Epoch 6, although the luminosity keeps decreasing, we find the source spectrum has become much softer (Table 5.B). It is likely that at this epoch the luminosity of the nonthermal component has diminished and the spectrum can be explained solely by the disk emission. The disk model fits the data well without the need for nonthermal components (Fig. 5.3).

Therefore, based on the results above, we assumed the disk is present at all epochs and performed joint fits combining the data from Epochs 2 to 6. The total fit function in XSPEC's syntax is "constant*TBabs*(powerlaw+slimdz)." We forced the disk parameters θ , M_{\bullet} , and a_{\bullet} to be the same across epochs and fit their values, while we allowed \dot{m} to vary between epochs and treated each \dot{m} as an individual fit parameter for each epoch. The power-law emission was also allowed to vary between epochs in our joint fit. By jointly fitting Epochs 2 to 6, we find the BH mass to be $\log(M_{\bullet}/M_{\odot}) = 2.4^{+0.6}_{-0.1}$, an upper limit to the inclination $\theta < 76^{\circ}$, and a broadly constrained BH spin $a_{\bullet} = 0.4^{+0.5}_{-0.9}$. We present the full list of parameter constraints from the joint fit in Table 5.D, and the Δ C-stat contour in $\{M_{\bullet}, a_{\bullet}\}$ space in Fig. 5.4.

5.5 Discussion 119

The data at Epochs 4 and 6 play a vital role in constraining the value of the BH mass. Nonetheless, it is important that we also consider the data at other epochs, because they will help us constrain parameters that might vary over the event and can help us exclude models that are not consistent with the data (e.g., upper limits on the disk luminosity can be derived). Notably, the inclination constraint derived from the thin–disk reflection model at Epoch 1 does not deviate from the slim-disk results based on this joint fit, while the thin–disk reflection model suggests a higher BH spin than the slim-disk results. The *m* constraints are consistent with a scenario in which the accretion rate decreases from super–Eddington to sub–Eddington levels.

In all the fits above, we notice that the re–normalization constant for the *Swift* spectrum at Epoch 3 is constrained to be \sim 0.5, which stands out from the re–normalization of *Swift* observations at other epochs. We manually checked the CCD image for this particular *Swift* observation and find a stripe of dead pixels in the source extraction region. We also checked the other *Swift* data and find this row of dead pixels to be outside the source extraction region. This defect on the CCD leads to a loss in the effective instrumental area and thus results in a decrease in the number of counts in this particular spectrum, which explains the lower constant in the joint fit of the *Swift* spectra with those of the other satellite data.

5.5 Discussion

By analyzing AT2018cow data from Swift, NuSTAR, and XMM-Newton, we find that starting from Epoch 2 the source's X-ray spectrum can be interpreted as originating from a slim disk plus a nonthermal spectral component modeled by a power law. For the X-ray spectral fits, we extended the BH mass range available for the slim-disk model slimdz (Wen et al. 2022) from $10^3-10^6~M_{\odot}$ to the BH mass range $10^1-10^6~M_{\odot}$. This extension to the model slimdz is now publicly available² for use in XSPEC. We confirm that AT2018cow's X-ray spectrum during Epoch 1 can be described well by a disk reflection model, as was reported before (Margutti et al. 2019). When the source becomes softer in X-rays after ≥ 200 days, the source spectrum becomes consistent with the emission from a slim disk. From slim-disk modeling, an IMBH of mass $\log(M_{\bullet}/M_{\odot}) = 2.4^{+0.6}_{-0.1}$ (at the 68% confidence level) is derived for the mass of the central compact object, while the disk inclination ($\theta < 76^{\circ}$) and the BH spin ($a_{\bullet} = 0.4^{+0.5}_{-0.9}$) are less strongly constrained (see Table 5.D for all the parameter constraints). All the parameter constraints are derived under the assumption that the disk viscosity parameter $\alpha = 0.1$. Our spectral modeling shows that the X-ray spectrum becomes softer at late times due to the disappearance of the nonthermal spectral component together with a decrease in the mass accretion rate, \dot{m} . The \dot{m} values derived from our spectral fit are consistent with a decrease from super- to sub-Eddington levels at late times.

Our independent mass measurement of AT2018cow is consistent with several mass constraints available in the literature based on energetic arguments, late-time UV data modeling, and X-

²10.5281/zenodo.11110331

ray timing assumptions (Pasham et al. 2022; Migliori et al. 2023; Inkenhaag et al. 2023). The mass constraint $\log(M_{\bullet}/M_{\odot}) = 2.4^{+0.6}_{-0.1}$ confirms the presence of an accreting IMBH as the central compact object. Such an IMBH can be formed through the accretion of gas onto a seed stellarmass BH (which can take cosmic timescales; e.g., Madau & Rees 2001; Greif et al. 2011), through the direct collapse of pristine gas clouds in the early Universe (e.g., Loeb & Rasio 1994; Bromm & Loeb 2003; Lodato & Natarajan 2006), or through BH merger events (e.g., Abbott et al. 2016b). The direct mass measurement from slim-disk modeling demonstrates a possible new way to study other AT2018cow–like LFBOTs that are also accompanied by variable X–ray emission (e.g., AT2020xnd/ZTF20acigmel, Ho et al. 2022b; Bright et al. 2022; AT2020rmf, Yao et al. 2022b).

An IMBH nature for AT2018cow is in line with scenarios that involve an accreting central compact object (e.g., TDE; Kuin et al. 2019; Perley et al. 2019; BH–star binary merger; Metzger 2022). In particular, for the IMBH–TDE scenario, we estimate the late–time disk outer radius to be $\approx 13~R_{\odot}$ given an IMBH of mass $10^{2.4} \approx 250~M_{\odot}$ disrupting a solar–mass star³. Thus, the predicted radius from the IMBH–TDE scenario is similar to that from the binary merger scenario (15–40 R_{\odot} ; Migliori et al. 2023) and has the same order of magnitude as values derived from the late–time UV observations ($\approx 40~R_{\odot}$; Inkenhaag et al. 2023; Migliori et al. 2023). Meanwhile, in the core–collapse scenario, the fall–back stellar ejecta typically form a much smaller disk, and this generally leads to an outer disk radius of $\sim 10^{-3}~R_{\odot}$ at late times (Migliori et al. 2023). Besides the outer disk radius, other parameters might also differ between scenarios, for example the peak \dot{m} . We refer to previous studies for a quantitative discussion of how those parameters depend on the BH mass in different scenarios (e.g., Metzger 2022; Migliori et al. 2023).

In our study, the nonthermal spectral component is modeled by a power-law component. Possible origins of the power-law component include a Comptonizing medium (BH corona) upscattering the disk photons, similar to that found in other BH accretion systems like X-ray binaries or active galactic nuclei (e.g., Esin et al. 1997; Nowak et al. 2011). It is also possible that some of the nonthermal emission is generated by shock interactions with the CSM (e.g., Rivera Sandoval et al. 2018; Margutti et al. 2019; Fox & Smith 2019; Leung et al. 2020. Interestingly, when the accretion rate becomes sub–Eddington at late times, we find that the nonthermal emission diminishes and the X-ray spectrum can be fit well by a slim-disk model. Spectral state transitions involving a varying nonthermal spectral component have also been observed in several TDE systems (e.g., Bade et al. 1996; Komossa et al. 2004; Wevers et al. 2019a; Jonker et al. 2020; Wevers et al. 2021; Cao et al. 2023).

In AT2018cow, there is evidence for a dense CSM (Ho et al. 2019). Theoretical work shows that a dense CSM can be present in both a TDE scenario (Linial & Quataert 2024), where the dense CSM is produced by the outflows from the BH–star mass transfer prior to full stellar disruption,

³While the slimdz model limits the disk outer radius to ≤ 800 R_g (for ray-tracing purposes; see Sect. 5.3), in the case of AT2018cow, we estimate an error on the flux of ≤ 0.5% introduced to the model below 1 keV by this choice of disk radius (Fig. 5.A(c)). Meanwhile, the actual disk radius is estimated by assuming a typical TDE disk, whose outer radius is about twice the tidal radius: $R_{\text{out}} \approx 2R_t = 2R_{\text{star}}(M_{\bullet}/M_{\text{star}})^{1/3}$ (e.g., Rees 1988; Kochanek 1994). See also the appendix.

5.5 Discussion 121

and in a binary merger scenario, where the dense CSM is produced in the common envelope phase between a stellar–mass BH (1–20 M_{\odot}) and its massive stellar companion (Metzger 2022). At present, it is unclear if this latter model can be extrapolated to accommodate a BH of $\approx 250~M_{\odot}$, the value suggested by our work. If that extrapolation is plausible, our BH mass determination of AT2018cow is consistent with both the TDE and BH–star merger scenarios.

Since no reflection models for the reflected emission from a slim disk are available, in our analysis, the reflection features (i.e., the broadened iron $K\alpha$ line ~6.4 keV and the Compton hump >10 keV) dominating the first NuSTAR epoch (and not detected in any later epochs) were modeled by disk reflection relxillCp (Dauser et al. 2014; García et al. 2014). The model relxillCp assumes that a standard thin disk reflects the emission from a Comptonizing medium with an incident power–law spectral shape. Given the same Comptonizing medium, the geometrical differences between the thin and the slim disks will result in differences in the emissivity profile of the reflected emission. This inconsistency between the likely super–Eddington accretion and the thin–disk assumption at Epoch 1 might contribute to the different spin constraints derived from the thin–disk $(a_{\bullet} = 0.98 \pm 0.01)$ and the slim–disk $(a_{\bullet} = 0.4^{+0.5}_{-0.9})$ results. Despite that, we notice that the inclination constraint from relxillCp $(\theta = 74^{\circ} \pm 2)$ is in general agreement with the value derived from the slim-disk modeling using data from all later epochs (< 76°). The material that is responsible for the reflected emission can involve the rapidly expanding outflow. Its density will decrease with time, which leads to the diminishing of reflection features in later epochs (e.g., Margutti et al. 2019).

While we extended the precalculated library of the disk spectra in slimdz to model the disk of $M_{\bullet} < 1000~M_{\odot}$, there exists a slim-disk model slimbh (Sądowski et al. 2011; Straub et al. 2011) that is available for the disk luminosity $L_{\rm disk} \leq 1.25~L_{\rm Edd}$ (with $L_{\rm disk}$ as one of the fit parameters in slimbh, and $L_{\rm Edd} \equiv 1.26 \times 10^{38} (M/M_{\odot})~{\rm erg/s})^4$. Physically, compared to slimbh, the slimdz model includes the loss of angular momentum due to radiation at each disk annulus. This adjustment alters the predicted effective temperature of the inner disk region, especially for high-spin, low-accretion disks (Wen et al. 2021). Moreover, a different estimate of the disk spectral hardening factor, f_c (Davis & El-Abd 2019) is employed by slimdz compared with slimbh.

We compared the results derived using slimdz with those obtained using slimbh by jointly fitting Epochs 2 to 6 with the fit function "constant*TBabs*(powerlaw+slimbh)," and comparing the results (presented in Table 5.E) to the those obtained with slimdz (Table 5.D). Both disk models provide a good fit to the combined data from Epochs 2 to 6. The mass constraint derived from slimbh is slightly higher ($\log(M_{\bullet}/M_{\odot})=3.2\pm0.2$) though marginally consistent with that in the slimdz case ($\log(M_{\bullet}/M_{\odot})=2.4^{+0.6}_{-0.1}$). Besides the physical differences between the disk models, it is possible that when fitting the super–Eddington spectra at Epoch 4, the upper parameter range of $L_{\rm disk}/L_{\rm Edd} \leq 1.25$ in slimbh limits the lower boundary of the mass constraint (since for a given observed luminosity, $L_{\rm disk}/L_{\rm Edd} \propto 1/M_{\bullet}$). In this sense, as $L_{\rm disk}/L_{\rm Edd}$ at Epoch

⁴Note in slimdz, instead of $L_{\rm disk}$, \dot{m} (in units of $\dot{M}_{\rm Edd} \equiv 1.37 \times 10^{15} (M/M_{\odot})$ kg/s) is used to solve the disk equations, which parameter determines the disk luminosity in erg/s.

4 is constrained to be >1.0 and is limited by the parameter range of \leq 1.25, the lower boundary of the mass constraint derived from slimbh is underestimated, causing the mass constraints between the two disk models to be only marginally consistent in Tables 5.D and 5.E. Indeed, the mass constraints derived from the two disk models are consistent when jointly fitting Epochs 5 and 6 (Table 5.F), the disk likely being at sub-Eddington accretion levels at these two epochs. We also tested the $\alpha=0.01$ cases in the slimbh model. The fit results with $\alpha=0.01$ do not differ from those with $\alpha=0.1$ shown in Table 5.E and Table 5.F (for slimbh cases). This test suggests that the choice of $\alpha=0.1$ does not significantly affect the slim-disk spectrum or the BH mass constraint, though the spectral library for slimdz does not currently extend to lower α values. For the above reason concerning the upper limit of $L_{\rm disk}/L_{\rm Edd}$, and due to the improved treatment of the angular momentum transport by radiation with slimdz mentioned above, we prefer the results derived from slimdz (Table 5.D).

5.6 Conclusions

We performed X-ray spectral analysis on *NuSTAR*, *Swift*, and *XMM-Newton* data for the LFBOT AT2018cow and find evidence for an accretion disk soon after the source's discovery. Based on slim-disk modeling, we constrain the mass of the central compact object to be $\log(M_{\bullet}/M_{\odot})$ = $2.4^{+0.6}_{-0.1}$ at the 68% confidence level. Our mass measurement is independent from, but consistent with, the results from previously employed methods. Therefore, we provide further evidence for an accreting IMBH (10^2 — $10^6~M_{\odot}$) as the central compact object residing in AT2018cow, and by extension in similar LFBOT sources. The mass constraint is consistent with both the tidal disruption and the BH–star merger scenarios, if the latter model can be extrapolated to the measured BH mass.

Our results are consistent with the scenario in which the source accretion rate decreases from super–Eddington to sub–Eddington levels ~200 days after its discovery. We find the late–time spectrum to be softer than the early–time spectra, which is consistent with emission from a slim disk at sub–Eddington accretion levels. In our analysis, a modified version of the existing slim-disk model slimdz is used to model the high–Eddington or super–Eddington disk of a BH at mass scales of 10 to 1000 M_{\odot} . Through this work, we demonstrate a possible new way of studying LFBOT sources that have X–ray emissions similar to AT2018cow.

ACKNOWLEDGEMENTS

We thank the referee for comments that helped to improve this manuscript. This work used the Dutch national e-infrastructure with the support of the SURF Cooperative using grant no. EINF-3954. This work made use of data supplied by the UK Swift Science Data Centre at the University of Leicester. P.G.J. has received funding from the European Research Council (ERC) under the European Union's Horizon 2020 research and innovation programme (Grant agreement

5.6 Conclusions 123

No. 101095973). AIZ acknowledges support in part from grant NASA ADAP #80NSSC21K0988 and grant NSF PHY-2309135 to the Kavli Institute for Theoretical Physics (KITP).

5.7 APPENDIX

5.7.1 THE EFFECT OF THE CHOICE OF OUTER DISK RADIUS IN Slimdz

For a $10~M_{\odot}$ BH disrupting a solar–type star, the TDE disk radius could be well above $1\times10^5~R_g$. However, the regions $\geq 10^3~R_g$ contribute little to the X–ray flux, since the disk temperature decreases with radius. It is orders of magnitude lower for $\geq 10^3~R_g$ compared to the innermost disk region (e.g., Straub et al. 2011; Sądowski et al. 2011). As it is too expensive computationally to ray–trace the whole disk, when constructing the spectral library for slimdz, we set a fixed value of the outer disk radius, $R_{\rm out}$, and did not ray–trace the disk region farther than $R_{\rm out}$. Wen et al. 2021 estimate a flux error of $\leq 1\%$ when choosing $R_{\rm out} = 600~R_g$ for a $10^4~M_{\odot}$ BH. Here we tested different choices of $R_{\rm out}$ when ray–tracing the slim disk around a $10~M_{\odot}$ BH.

We considered a $10~M_{\odot}$ non-spinning BH with $\dot{m}=\dot{m}_{\rm Edd}$, observed at an inclination of 45°. Figure 5.A(a) shows the relative flux differences between different $R_{\rm out}$ choices. The relative flux error is $\lesssim 1\%$ when $R_{\rm out} > 800~R_g$. For higher M_{\bullet} , higher a_{\bullet} , and lower \dot{m} , the flux difference would be smaller, as the innermost disk region becomes more dominant than the outer disk region. Therefore, in the main text, we produce the spectral library of slimdz with $R_{\rm out} = 800~R_g$, accelerating the calculation while the flux error is minimal.

We note that a choice of $R_{\rm out} = 800~R_g$ could introduce larger flux errors for a lower a_{\bullet} or for a higher \dot{m} . In extreme cases, for example $M_{\bullet} = 10~M_{\odot}$, $a_{\bullet} = -0.998$, and $\dot{m} = 100~\dot{m}_{\rm Edd}$, the flux error could be as large as $\sim 50\%$ (Fig. 5.A(b)). Therefore, one should be cautious when modeling a retrograde stellar–mass BH and a disk of large \dot{m} with the currently available slimdz model.

Lastly, we estimated the flux error imposed by the choice of $R_{\rm out} = 800~R_g$ in the particular case of AT2018cow. We considered the case of $M_{\bullet} = 250~M_{\odot}$, $a_{\bullet} = 0.4$, $\dot{m} = 5~\dot{m}_{\rm Edd}$, and $\theta = 74^{\circ}$ (as derived from the slimdz disk modeling in Table 5.D). We find a relative flux error of $\lesssim 0.5\%$ with $R_{\rm out} = 800~R_g$ (Fig. 5.A(c)).

5.7 Appendix 125

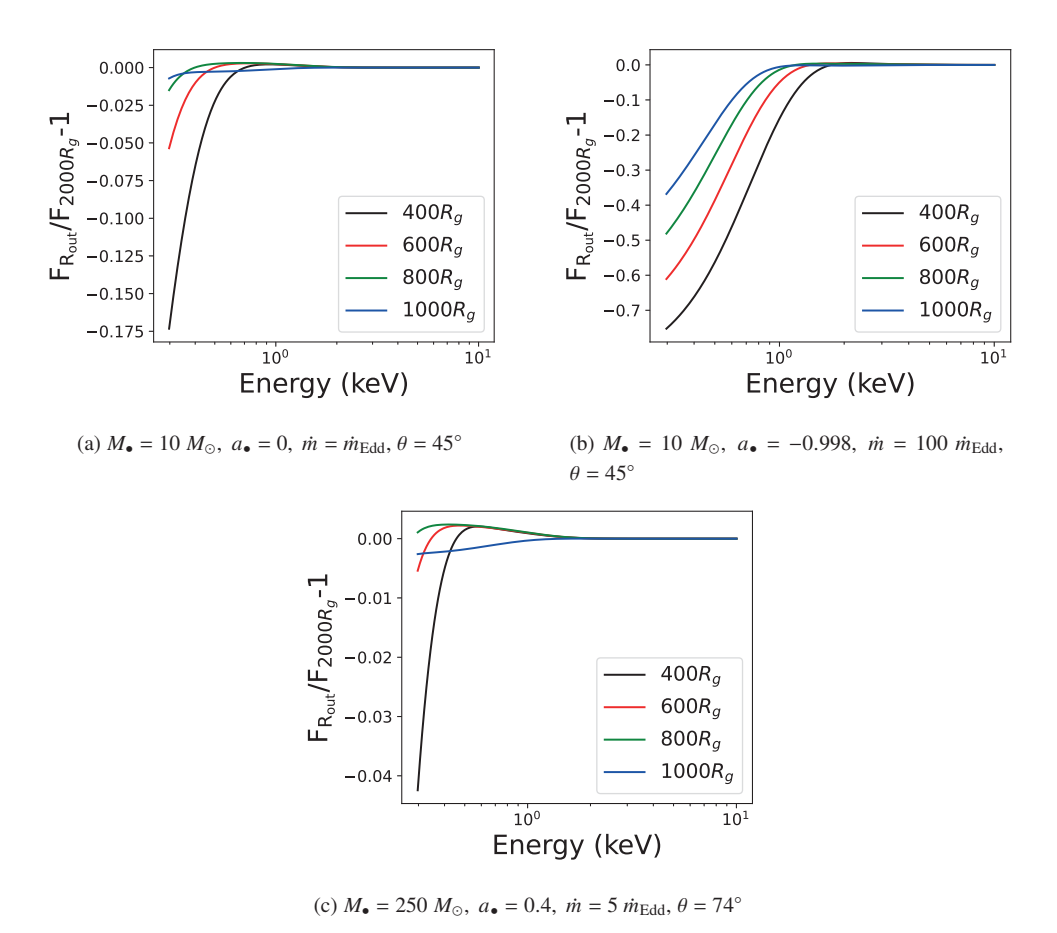


FIGURE 5.A: Effects of different choices of outer disk radius, $R_{\rm out}$, for the ray-tracing on the emergent disk spectrum. The relative error is calculated as $\frac{F_{R_{\rm out}} - F_{2000R_g}}{F_{2000R_g}}$. F_r denotes the X-ray flux calculated with $R_{\rm out} = r$. We use F_{2000R_g} as the reference spectrum, as regions beyond 2000 R_g do not produce significant X-ray emissions due to the disk temperature decreasing as a function of radius. In the last test (bottom-middle), the values of the disk parameters are similar to our best-fit results for AT2018cow (Table 5.D).

5.7.2 TABLES

TABLE 5.A: Journal listing properties of the observations analyzed in this paper.

Satellite	ObsID(Label)	Date	Exposure (ks)	R _{circ} (")	Energy band (keV)
NuSTAR	90401327002	2018-06-23	32.4	30	3.0-50.0 keV
Swift	00010724012	2018-06-23	2.5	59	0.3-7.0
	00010724013	2018-06-23			
	00010724010	2018-06-23			
NuSTAR	90401327004	2018-07-02	30.0	30	3.0-50.0
Swift	00010724046	2018-07-02	2.5	59	0.3-7.0
	00010724047	2018-07-02			
	00010724048	2018-07-02			
	00010724049	2018-07-02			
NuSTAR	90401327006	2018-07-14	31.2	30	3.0-30.0
Swift	00088782001	2018-07-14	2.2	35.4	0.3-7.0
NuSTAR	90401327008	2018-07-22	32.9	30"	3.0-30.0
Swift	00010724087	2018-07-21	1.6	35.4	0.3-7.0
XMM-Newton	0822580401	2018-07-23	33.0	25	0.3-10.0
XMM-Newton	0822580501	2018-09-06	45.0	25	0.3-5.0
XMM-Newton	0822580601	2019-01-20	56.4	25	0.3-1.5
	NuSTAR Swift NuSTAR Swift NuSTAR Swift NuSTAR Swift NuSTAR Swift XMM-Newton XMM-Newton	NuSTAR 90401327002 Swift 00010724012 00010724013 00010724010 NuSTAR 90401327004 Swift 00010724047 00010724047 00010724048 00010724049 00010724049 NuSTAR 90401327006 Swift 00088782001 NuSTAR 90401327008 Swift 00010724087 XMM-Newton 0822580401 XMM-Newton 0822580501	NuSTAR 90401327002 2018-06-23 Swift 00010724012 2018-06-23 00010724013 2018-06-23 00010724010 2018-06-23 NuSTAR 90401327004 2018-07-02 Swift 00010724046 2018-07-02 00010724047 2018-07-02 00010724048 2018-07-02 00010724049 2018-07-02 NuSTAR 90401327006 2018-07-14 Swift 00088782001 2018-07-12 NuSTAR 90401327008 2018-07-22 Swift 00010724087 2018-07-21 XMM-Newton 0822580401 2018-07-23 XMM-Newton 0822580501 2018-09-06	NuSTAR 90401327002 2018-06-23 32.4 Swift 00010724012 2018-06-23 2.5 00010724013 2018-06-23 2.5 00010724010 2018-06-23 2.5 NuSTAR 90401327004 2018-07-02 30.0 Swift 00010724046 2018-07-02 2.5 00010724047 2018-07-02 2.5 00010724048 2018-07-02 2.5 NuSTAR 90401327006 2018-07-14 31.2 Swift 00088782001 2018-07-14 2.2 NuSTAR 90401327008 2018-07-22 32.9 Swift 00010724087 2018-07-21 1.6 XMM-Newton 0822580401 2018-07-23 33.0 XMM-Newton 0822580501 2018-09-06 45.0	NuSTAR 90401327002 2018-06-23 32.4 30 Swift 00010724012 2018-06-23 2.5 59 00010724013 2018-06-23 2.5 59 00010724010 2018-06-23 2.5 59 NuSTAR 90401327004 2018-07-02 30.0 30 Swift 00010724046 2018-07-02 2.5 59 00010724047 2018-07-02 2.5 59 00010724048 2018-07-02 2.5 59 NuSTAR 90401327006 2018-07-02 31.2 30 Swift 00088782001 2018-07-14 31.2 30 Swift 00010724087 2018-07-14 2.2 35.4 NuSTAR 90401327008 2018-07-12 32.9 30" Swift 00010724087 2018-07-21 1.6 35.4 XMM-Newton 0822580401 2018-07-23 33.0 25 XMM-Newton 0822580501 2018-07-20 45.0 25

Notes: We group all observations by time into six epochs and fit the data in each epoch simultaneously. Swift observations within the same epoch are combined and treated as a single observation. We also give the radius of the circular region that we use for the source+background spectral extraction in each observation (R_{circ}). We followed Evans et al. (2009) in determining the radius of this source+background region to extract for Swift observations. In our spectral analysis, the energy band we use is given in the last column.

5.7 Appendix 127

Table 5.B: Parameter constraints from fitting the data within each epoch with a power-law model.

Model	Parameter	Epoch 1	Epoch 2	Epoch 3	Epoch 4	Epoch 5	Epoch 6
Constant	C_{FPMA}				[1.0]		
	C_{FPMB}	-	1.01 ± 0.03	0.92 ± 0.04	1.00 ± 0.06	-	-
	C_{Swift}	-	0.95 ± 0.07	0.47 ± 0.08	0.9 ± 0.1	-	-
	$C_{\text{XMM-Newton}}$	-	-	-	0.78 ± 0.04	-	-
TBabs	$N_{ m H}~(10^{20}~{ m cm}^{-2})$				[5.0]		
powerlaw	Γ	-	1.38 ± 0.02	1.52 ± 0.05	1.68 ± 0.01	1.7 ± 0.2	2.4 ± 0.7
	$\mathrm{norm}(\mathrm{keV}^{-1}\mathrm{cm}^{-2}\mathrm{s}^{-1})$	-	$(10.0\pm0.5)\times10^{-4}$	$(4.2 \pm 0.4) \times 10^{-4}$	$(3.9 \pm 0.2) \times 10^{-4}$	$(3.7 \pm 0.4) \times 10^{-6}$	$(1.2 \pm 0.4) \times 10^{-6}$
	C-stat/d.o.f.	-	256.8/267	174.0/158	221.0/231	47.0/33	12.0/9

Notes: We use a constant model to account for differences in normalization between each instrument and fix the constant for NuSTAR/PFMA spectra $C_{FPMA}=1$ in each epoch. The total fit function is thus "constant*TBabs*powerlaw." Parameter values held fixed during the fit are given inside square brackets. No parameter constraints are given for Epoch 1, because at this epoch the source X—rays are dominated by reflection. With time the source spectrum seems to become softer.

Table 5.C: Parameter constraints from our spectral analysis, with fit function of "constant*TBabs*relxillCp" for **Epoch** 1, and a fit function "constant*TBabs*(powerlaw+slimdz)" for Epochs 2 to 6.

Model	Parameter	Epoch 1	Epoch 2	Epoch 3	Epoch 4	Epoch 5	Epoch 6
Constant	C_{FPMB}	0.96 ± 0.02	1.01 ± 0.03	0.92 ± 0.04	1.00 ± 0.06	-	-
	C_{Swift}	1.00 ± 0.06	0.95 ± 0.07	0.47 ± 0.08	0.9 ± 0.1	-	-
	$C_{\text{XMM-Newton}}$	-	-	-	0.79 ± 0.04	-	-
TBabs	$N_{\rm H}~(10^{20}~{\rm cm}^{-2})$	[5.0]					
powerlaw	Γ	-	1.38 ± 0.02	1.52 ± 0.05	1.52 ± 0.05	1.7 ± 0.2	-
	$\mathrm{norm}\;(\mathrm{keV}^{-1}\mathrm{cm}^{-2}\mathrm{s}^{-1})$	-	$(10.0\pm0.5)\times10^{-4}$	$(4.2 \pm 0.4) \times 10^{-4}$	$(2.8 \pm 0.4) \times 10^{-4}$	$(3.7 \pm 0.4) \times 10^{-6}$	-
slimdz	$\dot{m} (\dot{m}_{ m Edd})$	-	-	-	>0.5	-	<4.0
	θ (°)	-	-	-	<81	-	NC
	$\log(M_{\bullet}/M_{\odot})$	-	-	-	$2.4^{+0.8}_{-0.2}$	-	2.3 ± 0.9
	a_{\bullet}	-	-	-	>-0.6	-	NC
relxillCp	θ (°)	74 ± 2	-	-	-	-	-
	a_{ullet}	0.98 ± 0.01	-	-	-	-	-
	kT_e (keV)	28 ± 8	-	-	-	-	-
	Γ	1.22 ± 0.02	-	-	-	-	-
	q	4 ± 2	-	-	-	-	-
	$\log(\xi)$	3.45 ± 0.06	-	-	-	-	-
	A_{Fe}	>8.0	-	-	-	-	-
	Refl _{frac}	11+21	-	-	-	-	-
	$\log(\rho/\text{cm}^{-3})$	<15.2	-	-	-	-	-
	$\mathrm{norm}\;(\mathrm{erg}\;\mathrm{cm}^{-2}\mathrm{s}^{-1})$	$(3 \pm 2) \times 10^{-5}$	-	-	-	-	-
	C-stat/d.o.f.		256.8/267	174.0/158	200.2/227	47.0/33	12.2/7

Notes: Parameter values held fixed during the fit are given inside square brackets. We use a constant model to account for differences in normalization between each instrument and fix the constant for NuSTAR/PFMA spectra $C_{FPMA}=1$ in each epoch. For the models slimdz and relxillCp, the redshift of AT2018cow (z=0.01404) is taken. We find that it is only for Epoch 4 that adding a slimdisk component significantly improves the fit compared to only using a power–law model (Table 5.B). Nonetheless, we also test a model of a slim disk alone ("constant*TBabs*slimdz") for Epoch 6, as the source becomes much softer at this epoch compared to previous epochs. The symbol "NC" means the parameter cannot be constrained within the allowed range of values (for θ this is $3^{\circ} \le \theta \le 90^{\circ}$ and for a_{\bullet} this is $-0.998 \le a_{\bullet} \le 0.998$). See Dauser et al. 2014 and García et al. 2014 for detailed descriptions of relxillCp parameters.

5.7 Appendix 129

TABLE 5.D: Same as Table 5.C, but here we jointly fit all data from Epochs 2 to 6.

Model	Parameter	Epoch 1	Epoch 2	Epoch 3	Epoch 4	Epoch 5	Epoch 6
Constant	C_{FPMB}	0.96 ± 0.02	1.01 ± 0.03	0.92 ± 0.04	1.00 ± 0.06	-	-
	C_{Swift}	1.00 ± 0.05	0.95 ± 0.07	0.46 ± 0.08	0.9 ± 0.1	-	-
	$C_{\text{XMM-Newton}}$	-	-	-	0.79 ± 0.04	-	-
TBabs	$N_{\rm H} (10^{20} {\rm cm}^{-2})$			[5.0]			
powerlaw	Γ	-	1.38 ± 0.02	1.52 ± 0.05	1.51 ± 0.05	0.9+0.6	-
	$\mathrm{norm}\;(\mathrm{keV}^{-1}\mathrm{cm}^{-2}\mathrm{s}^{-1})$	-	$(10.0\pm0.5)\times10^{-4}$	$(4.2 \pm 0.4) \times 10^{-4}$	$(2.7 \pm 0.3) \times 10^{-4}$	$(2.1 \pm 1.5) \times 10^{-6}$	-
slimdz	$\dot{m} (\dot{m}_{ m Edd})$	-	<4.9	<18	>4.8	< 0.23	< 0.17
	θ (°)	-			<76		
	$\log(M_{\bullet}/M_{\odot})$	-			$2.4^{+0.6}_{-0.1}$		
	a_{ullet}	-			0.4+0.5		
relxillCp	θ (°)	74 ± 2	-	-	-	-	-
	a_{\bullet}	0.98 ± 0.01	-	-	-	-	-
	kT_e (keV)	28 ± 8	-	-	-	-	
	Γ	1.22 ± 0.02	-	-	-	-	
	q	4 ± 2	-	-	-	-	-
	$\log(\xi)$	3.45 ± 0.06	-	-	-	-	-
	A_{Fe}	>8.0	-	-	-	-	-
	Reflfrac	11+21	-	-	-	-	-
	$\log(\rho/\text{cm}^{-3})$	<15.2	-	-	-	-	-
	$norm (erg \ cm^{-2} s^{-1})$	$(3 \pm 2) \times 10^{-5}$	-	-	-	-	-
	C-stat/d.o.f.	279.5/275			688.5/691		

Notes: We force the slim-disk component in each epoch to have the same inclination, θ , BH mass, M_{\bullet} , and BH spin, a_{\bullet} . Since statistically the slim-disk component is not needed for Epochs 2, 3, and 5, only an upper limit on the disk accretion rate was obtained for these epochs.

TABLE 5.E: Same as Table 5.C, but here we jointly fit all data from Epochs 2 to 6, and we replace slimdz with slimbh.

Model	Parameter	Epoch 1	Epoch 2	Epoch 3	Epoch 4	Epoch 5	Epoch 6
Constant	C_{FPMB}	0.96 ± 0.02	1.01 ± 0.03	0.92 ± 0.05	1.00 ± 0.06	-	-
	$C_{ m Swift}$	1.00 ± 0.05	0.94 ± 0.07	0.47 ± 0.09	0.9 ± 0.1	-	-
	$C_{ ext{XMM-Newton}}$	-	-	-	0.79 ± 0.04	-	-
TBabs	$N_{\rm H} (10^{20} {\rm cm}^{-2})$			[5.0]			
powerlaw	Γ	-	1.38 ± 0.02	1.52 ± 0.05	1.57 ± 0.04	1.1 ± 0.3	-
	$\mathrm{norm}\ (\mathrm{keV}^{-1}\mathrm{cm}^{-2}\mathrm{s}^{-1})$	-	$(10.0\pm0.5)\times10^{-4}$	$(4.2 \pm 0.4) \times 10^{-4}$	$(3.1 \pm 0.2) \times 10^{-4}$	$(2.5^{+0.4}_{-0.7}) \times 10^{-6}$	-
slimbh	$L_{ m disk} (L_{ m Edd})$	-	<1.2	NC	>1.0	< 0.07	< 0.06
	θ (°)	-			75 ± 8		
	$\log(M_{\bullet}/M_{\odot})$	-			3.2 ± 0.2		
	a_{ullet}	-			< 0.5		
relxillCp	θ (°)	74 ± 2	-	-	-	-	-
	a_{ullet}	0.98 ± 0.01	-	-	-	-	-
	kT_e (keV)	28 ± 8	-	-	-	-	-
	Γ	1.22 ± 0.02	-	-	-	-	-
	q	4 ± 2	-	-	-	-	-
	$\log(\xi)$	3.45 ± 0.06	-	-	-	-	-
	A_{Fe}	>8.0	-	-	-	-	-
	Reflfrac	11 ⁺²¹	-	-	-	-	-
	$\log(\rho/\text{cm}^{-3})$	<15.2	-	-	-	-	-
	$\mathrm{norm}\;(\mathrm{erg}\;\mathrm{cm}^{-2}\mathrm{s}^{-1})$	$(3 \pm 2) \times 10^{-5}$	-	-	-	-	-
	C-stat/d.o.f.	279.5/275			691.8/691		

Notes: We force the slim-disk component in each epoch to have the same inclination, θ , BH mass, M_{\bullet} , and BH spin, a_{\bullet} . Furthermore, we replace slimdz with the preexisting slim-disk model slimbh. The total fit function for the joint fit is then "constant*Tbabse*(powerlaw+slimbh)." See the main text for the physical differences between the models. In slimbh, $0.05 < L_{\rm disk}/L_{\rm Edd} < 1.25$ with $L_{\rm Edd} \equiv 1.26 \times 10^{38} (M/M_{\odot})$ erg/s, and only the prograde spin is considered ($a_{\bullet} > 0$). Both limb-darkening and surface profile are switched on in slimbh during the fit (model switch vflag= 1 and lflag= 1), and the disk viscosity parameter $\alpha = 0.1$.

5.7 Appendix 131

TABLE 5.F: Joint fits of XMM-Newton/EPIC-pn spectra from Epochs 5 and 6.

Model	Parameter	Epoch 5	Epoch 6	Model	Parameter	Epoch 5	Epoch 6
TBabs	$N_{\rm H} (10^{20} \ {\rm cm}^{-2})$	[5.0]		TBabs	$N_{\rm H}~(10^{20}~{\rm cm}^{-2})$	[5.0]	
powerlaw	Γ	0.9+0.8	-	powerlaw	Γ	0.7+0.8	-
	$norm\ (keV^{-1}cm^{-2}s^{-1})$	$(190^{+171}_{-188}) \times 10^{-8}$	-		$norm\ (keV^{-1}cm^{-2}s^{-1})$	$(151^{+181}_{-149}) \times 10^{-8}$	-
slimdz	$\dot{m}~(\dot{m}_{ m Edd})$	<4.6	<3.6	slimbh	$L_{ m disk} \; (L_{ m Edd})$	< 0.60	< 0.17
	θ (°)	NC {3° ≤ θ ≤	90°}		θ (°)	NC $\{0^{\circ} \leq \theta \leq$	85°}
	$\log(M_{\bullet}/M_{\odot})$	$2.5^{+1.4}_{-0.9}$			$\log(M_{\bullet}/M_{\odot})$	$2.2^{+1.0}_{-0.2}$	
	a_{ullet}	$NC \{-0.998 \le a_{\bullet}\}$	≤ 0.998}		a_{ullet}	NC $\{0 < a_{\bullet} < 0\}$	0.999}
	C-stat/d.o.f.	57.7/39			C-stat/d.o.f.	57.3/39	

Notes: At these two epochs, the disk is likely to be at sub-Eddington mass accretion rates. We compare the results using the slimdz model with those using the slimbh model, employing a fit function of "constant*TBabs*(powerlaw+slimdz)" and a fit function of "constant*TBabs*(powerlaw+slimbh)," respectively. The symbol "NC" means the parameter cannot be constrained within the range of values allowed by the models (listed in curly brackets).

SUMMARY

Due to the limited detections, the IMBH population is barely constrained, yet they are expected to play a crucial role in forming the SMBHs found at the centres of massive galaxies. Finding more IMBHs helps us to better understand their formation mechanisms. In addition, studying IMBH accretion helps us to understand how IMBHs grow, and how SMBHs are produced through seed IMBHs.

In theory, compared to SMBHs, IMBHs are able to disrupt more kinds of stars. The theoretical expectation is that the TDE rate is dominated by IMBH-TDEs, if IMBHs with masses down to $\sim 10^4~M_{\odot}$, like the one recently found in ω Centauri, are abundant. Therefore, TDEs provide a powerful tool to search for IMBHs. Meanwhile, the high peak mass accretion rate, often seen in TDEs and especially those with a mass in the IMBH range, also provides us with unique opportunities to study accretion physics under extreme conditions.

This thesis uses individual (candidate) TDEs to find more IMBHs. Through X-ray data analysis and especially, modelling of the TDE X-ray spectra and their evolution as a function of time using a slim disc model, the work in this thesis draws novel, strong constraints on the mass and in some cases also the spin of the black hole studied, contributing to a better understanding of the IMBH mass distribution. When possible, we compare the results with the mass constraints from other methods such as M_{\bullet} – σ relation, and we find no tensions. This thesis also provide insights about individual sources concerning their emission mechanisms and their formation channels.

In Chapter 2 & 3, we study two TDEs that both show a decade–long decay. In each case, we perform multi–epoch data analysis utilising the data from the *XMM-Newton*, *Chandra*, and *Swift* X-ray satellites. In theory, an IMBH–TDE is likely to emit more of its bolometric luminosity in the X–ray band than an SMBH–TDE. The X–ray luminosity also correlates strongly with the black hole spin. The theoretical expectation is that, an IMBH accretes at super–Eddington levels for a longer period than an SMBH disrupting a similar star, and the faster the black hole spin, the higher the X–ray luminosity. Indeed, both black holes considered in Chapter 2 & 3 are constrained to be fast–spinning IMBHs: $M_{\bullet} = (2.0^{+1.0}_{-0.3}) \times 10^5 M_{\odot}$ and $a_{\bullet} > 0.97$ for J150052, and $M_{\bullet} = (6 \pm 2) \times 10^4 M_{\odot}$ and $a_{\bullet} > 0.85$ for J1231 at 1σ confidence in both cases. It is possible to form a fast–spinning IMBH of $\sim 10^4 - 10^5 M_{\odot}$ via direct collapse of a gas cloud. If a black hole is formed at a mass an order–of–magnitude lower than this and if it obtains its last e–fold

134 Summary

increase in mass via an accretion episode, then it will obtain a high spin (>0.9). Otherwise if the imparted angular momentum has random directions, such as when the IMBH obtains the last e-fold increase in mass through multiple accretion episodes from randomly distributed directions, the black hole is expected to have a low spin (~ 0.2).

In J150052, we find that the source transits from a spectral state that can be well explained as a superposition of a disc and a corona spectral component, to a state of a pure disc spectrum. This transition happens when the mass accretion rate through the disc decreases from a super-Eddington to an ~Eddington level. This spectral change, where the power-law-shaped, corona component to the X-ray spectrum, diminishes is analogous to the transition from the ultraluminous state to the soft state in BH-XRBs. This similarity shows that there are connections between the accretion behaviours observed for different black hole masses. For J1231, we confirm the presences of a transient quasi-periodic variation in the arrival time of the X-ray photons with a period of roughly ~ 3.8 hr. The spectral behaviour during that variability is consistent with a slim disc of varying mass accretion rate. Mechanisms such as disc instability, repetitive partial TDEs, or disc-star interactions possibly cause these accretion rate variations. Some previous studies have also proposed a quasi-periodic eruption (QPE) explanation for the variability. We find that, J1231's quasi-periodic variability does not show the typical, "hard-rise-soft-decay", QPE behaviour. This would make J1231 to be an atypical QPE candidate. In general, these two chapters demonstrate the importance of multi-epoch observations and analysis in the disc modelling for constraining the black hole mass and spin. As the TDE accretion evolves constantly after the disruption, multi-epoch analysis helps us to distinguish the influence of parameters that remain constant such as the black hole mass and spin, and those that are likely to vary, such as for instance the mass accretion rate through the disc. Disentangling their contributions is nearly impossible in single epoch data.

In Chapter 4 we present another TDE, named AT2020ocn, where we derive the black hole mass to be $(7^{+13}_{-3}) \times 10^5 M_{\odot}$ at 1σ confidence. The black hole spin could not be constrained. We explain the source spectrum with a slim disc model, convolved with the effect of inverse-Comptonisation that is likely to take place due to the presence of a corona of hot electrons. Furthermore, we study the early-time X-ray flares of AT2020ccn, occurring within 200 days after its detection, using the data from XMM-Newton, Swift, and NICER. The spectral evolution during the flares can be explained by a slim disc varying its inclination. A slim disc in the process of aligning its angular momentum vector with the black hole spin angular momentum would explain this inclination variation. Meanwhile, the UV emission of AT2020ocn, during the X-ray flares, is decoupled from the changes in the X-ray emission. The UV light curves show no distinct flares. The decoupling of the UV and X-ray emission variations, which is also seen in other TDEs, supports the hypothesis that the UV and X-rays do not share the same origin at least within the first few hundred of days after the tidal disruption of the star. The X-rays are emitted by the inner regions of the accretion disc, while the UV photons are produced at a different location. Possible origins of the UV photons include the reprocessing of X-rays from the disc in an outer envelope, self-interaction shocks in the debris stream, and a so-called nozzle shock in the debris stream.

Summary 135

In Chapter 5, we study the archetype of the relatively newly discovered class of Luminous Fast Blue Optical Transients (LFBOTs), AT2018cow. We analyse the *NuSTAR*, *Swift*, and *XMM-Newton* data. The UV and X–ray behaviour of AT2018cow resembles that of an IMBH–TDE. Despite the unknown nature of AT2018cow, data shows that its X–ray emission is likely to come from an accretion disc. Therefore, we focus on the disc modelling and derive a novel, strong mass constraint of $\log(M_{\bullet}/M_{\odot}) = 2.4^{+0.6}_{-0.1}$. In our analysis, we extend the slim–disc model solutions to the mass range of 10— $1000~M_{\odot}$ by calculating the disc spectra from this mass range and adding them to the model spectral library. Originally only solutions for $10^8 M_{\odot} \ge M_{\bullet} \ge 1000 M_{\odot}$ black holes had been calculated. A central IMBH is consistent with both the tidal disruption scenario and the BH–star merger scenario for AT2018cow, assuming the latter model can indeed be extrapolated to the measured black hole mass. We provide observational evidence of an accreting IMBH as the central compact object residing in AT2018cow, and demonstrate a new way to study LFBOTs that have the X–ray emissions similar to AT2018cow.

The future in the field of IMBH studies will be enhanced by the next–generation surveys. Surveys such as those from *Einstein Probe* and the *Vera C. Rubin Observatory*, are expected to greatly increase the number of IMBH–TDE detections. Then, with the fast–responding follow–up observations from, e.g., *Einstein Probe* (in particular the Fast X–ray Telescope) and *NICER*, we will have more high quality X-ray spectral TDE data especially in the early stages right after the disruption, gaining better knowledge about the super–Eddington accretion of IMBHs, and the early–time TDE behaviour.

SAMENVATTING

Vanwege het beperkte aantal waarnemingen is de populatie van middelgrote zwarte gaten (IMBHs) nauwelijks begrensd. Toch wordt verwacht dat ze een cruciale rol spelen bij de vorming van de superzware zwarte gaten (SMBHs) die in de kernen van massieve sterrenstelsels worden aangetroffen. Het vinden van meer IMBHs helpt ons hun vormingsmechanismen beter te begrijpen. Bovendien helpt het bestuderen van IMBH-accretie ons te begrijpen hoe IMBHs groeien en hoe SMBHs worden gevormd via zaad-IMBHs.

Theoretisch gezien kunnen IMBHs, in vergelijking met SMBHs, meer soorten sterren verstoren. De theoretische verwachting is dat de TDE-ratio wordt gedomineerd door IMBH-TDEs, als IMBHs met massa's tot $\sim 10^4~M_{\odot}$, zoals degene die recentelijk is gevonden in ω Centauri, overvloedig aanwezig zijn. Daarom bieden TDEs een krachtig hulpmiddel om naar IMBHs te zoeken. Ondertussen biedt het hoge piekmassaccretiepercentage, dat vaak wordt gezien in TDEs, en vooral in die met een massa in het IMBH-bereik, ons ook unieke mogelijkheden om de fysica van accretie onder extreme omstandigheden te bestuderen.

Dit proefschrift maakt gebruik van individuele (kandidaat-)TDEs om meer IMBHs te identificeren. Door middel van röntgengegevensanalyse, en in het bijzonder het modelleren van de TDE-röntgenspectra en hun evolutie in de tijd met behulp van een slank-schijfmodel, legt het werk in dit proefschrift nieuwe, sterke beperkingen op aan de massa en in sommige gevallen ook de spin van de bestudeerde zwarte gaten. Dit draagt bij aan een beter begrip van de massaverdeling van IMBHs. Waar mogelijk vergelijken we de resultaten met massa-beperkingen van andere methoden, zoals de M_{\bullet} - σ -relatie, en constateren we geen tegenstrijdigheden. Dit proefschrift biedt tevens inzichten in individuele bronnen met betrekking tot hun emissiemechanismen en vormingskanalen.

In Hoofdstuk 2 en 3 bestuderen we twee TDEs die beide een afname vertonen over een periode van een decennium. In elk geval voeren we multi-epoch gegevensanalyse uit met behulp van de data van de *XMM-Newton*, *Chandra* en *Swift* röntgensatellieten. Theoretisch gezien zal een IMBH–TDE waarschijnlijk meer van zijn bolometrische luminositeit in het röntgenbereik uitzenden dan een SMBH–TDE. De röntgenluminositeit correleert ook sterk met de spin van het zwarte gat. De theoretische verwachting is dat een IMBH gedurende een langere periode accreteert op super-Eddington niveaus dan een SMBH die een vergelijkbare ster verstoort, en hoe

138 Samenvatting

sneller de spin van het zwarte gat, hoe hoger de röntgenluminositeit. Inderdaad, beide zwarte gaten die in Hoofdstuk2 en 3 worden beschouwd, worden beperkt tot snel draaiende IMBHs: $M_{\bullet} = (2.0^{+1.0}_{-0.3}) \times 10^5 M_{\odot}$ en $a_{\bullet} > 0.97$ voor J150052, en $M_{\bullet} = (6 \pm 2) \times 10^4 M_{\odot}$ en $a_{\bullet} > 0.85$ voor J1231 met 1σ -betrouwbaarheid in beide gevallen. Het is mogelijk om een snel draaiend IMBH van $\sim 10^4 - 10^5 M_{\odot}$ te vormen via de directe instorting van een gaswolk. Als een zwart gat wordt gevormd bij een massa die een orde van grootte lager is dan dit en het zijn laatste e-vouwtoename in massa verkrijgt via een accretieepisode, dan zal het een hoge spin verkrijgen (>0.9). Als de overgedragen hoekimpuls echter willekeurige richtingen heeft, zoals wanneer het IMBH zijn laatste e-vouwtoename in massa verkrijgt door meerdere accretieepisodes uit willekeurig verdeelde richtingen, wordt verwacht dat het zwarte gat een lage spin heeft (~ 0.2).

In J150052 vinden we dat de bron overgaat van een spectrale toestand die goed verklaard kan worden als een superpositie van een schijf- en een corona spectraalcomponent, naar een toestand van een puur schijfspectrum. Deze overgang vindt plaats wanneer de massa-accretiesnelheid door de schijf afneemt van een super-Eddington naar een ~Eddington-niveau. Deze spectrale verandering, waarbij de power-law-vormige corona-component in het röntgenspectrum afneemt, is analoog aan de overgang van de ultra-lumineuze toestand naar de zachte toestand in BH-XRBs. Deze overeenkomst toont aan dat er verbanden bestaan tussen de waargenomen accretiegedragingen voor verschillende zwarte gatenmassa's. Voor J1231 bevestigen we de aanwezigheid van een tijdelijke quasi-periodieke variatie in de aankomsttijd van de röntgenfotons met een periode van ongeveer ~ 3.8 uur. Het spectrale gedrag tijdens die variabiliteit is consistent met een slanke schijf met variërende massa-accretiesnelheid. Mechanismen zoals schijfinstabiliteit, repetitieve gedeeltelijke TDEs, of schijf-sterinteracties kunnen mogelijk deze accretiesnelheidsvariaties veroorzaken. Sommige eerdere studies hebben ook een quasi-periodieke uitbarsting (OPE) verklaring voor de variabiliteit voorgesteld. We vinden dat de quasi-periodieke variabiliteit van J1231 niet het typische "harde-stijging-zachte-afname" QPE-gedrag vertoont. Dit zou J1231 tot een atypische QPE-kandidaat maken. In het algemeen tonen deze twee hoofdstukken het belang aan van multi-epoch waarnemingen en analyse in het schijfmodellering voor het beperken van de zwarte gatenmassa en spin. Aangezien de TDE-accretie voortdurend evolueert na de verstoring, helpt multi-epoch analyse ons het onderscheid te maken tussen de invloed van parameters die constant blijven, zoals de zwarte gatenmassa en spin, en diegene die waarschijnlijk variëren, zoals bijvoorbeeld de massa-accretiesnelheid door de schijf. Het ontrafelen van hun bijdragen is vrijwel onmogelijk met enkel gegevens uit één epoch.

In Hoofdstuk 4 presenteren we een andere TDE, genaamd AT2020ocn, waarvoor we de massa van het zwarte gat afleiden als zijnde $(7^{+13}_{-3}) \times 10^5~M_{\odot}$ met 1σ betrouwbaarheidsniveau. De spin van het zwarte gat kon niet worden beperkt. We verklaren het spectra van de bron met een slanke schijfmodel, convoluut met het effect van inverse Comptonisatie die waarschijnlijk plaatsvindt door de aanwezigheid van een corona van hete elektronen. Verder bestuderen we de vroege röntgenflare van AT2020ocn, die binnen 200 dagen na zijn detectie plaatsvond, met behulp van gegevens van de *XMM-Newton*, *Swift*, en *NICER* satellieten. De spectrale evolutie tijdens de flares kan worden verklaard door een slanke schijf die zijn inclinatie varieert. Een slanke schijf in het

Samenvatting 139

proces van het uitlijnen van zijn hoekmomentumvector met het hoekmomentum van het zwarte gat zou deze variatie in inclinatie verklaren. Ondertussen is de UV-straling van AT2020ocn tijdens de röntgenflaren losgekoppeld van de veranderingen in de röntgenstraling. De UV-lichtcurves vertonen geen duidelijke flares. De loskoppeling van de UV- en röntgenstralingsvariaties, die ook wordt waargenomen in andere TDE's, ondersteunt de hypothese dat de UV- en röntgenstraling niet dezelfde oorsprong hebben, althans niet binnen de eerste paar honderd dagen na de getijdenverstoring van de ster. De röntgenstralen worden uitgezonden door de binnenste regio's van de accretieschijf, terwijl de UV-fotonen op een andere locatie worden geproduceerd. Mogelijke oorsprongen van de UV-fotonen zijn de herverwerking van röntgenstralen van de schijf in een buitenste envelop, zelf-interactie schokken in de puinstroom, en een zogenaamde nozzle-shock in de puinstroom.

In Hoofdstuk 5 bestuderen we het archetype van de relatief nieuw ontdekte klasse van Lumineuze Snelle Blauwe Optische Transiënten (LFBOTs), AT2018cow. We analyseren de *NuSTAR*, *Swift*, en *XMM-Newton* gegevens. Het UV- en röntgengedrag van AT2018cow lijkt op dat van een IMBH-TDE. Ondanks de onbekende aard van AT2018cow, tonen de gegevens aan dat de röntgenstraling waarschijnlijk afkomstig is van een accretieschijf. Daarom richten we ons op het schijfmodel en bepalen we een nieuw, sterk massa-beperking van $\log(M_{\bullet}/M_{\odot}) = 2.4^{+0.6}-0.1$. In onze analyse breiden we de oplossingen van het slanke-schijfmodel uit naar het massa-bereik van $10-1000~M_{\odot}$ door de schijfspectra voor dit massa-bereik te berekenen en toe te voegen aan de model-spectrumbibliotheek. Oorspronkelijk waren alleen oplossingen voor zwarte gaten in het bereik van $10^8 M_{\odot} \ge M_{\bullet} \ge 1000 M_{\odot}$ berekend. Een centraal IMBH is consistent met zowel het scenario van getijdenverstoring als het BH-ster-samensmelting scenario voor AT2018cow, ervan uitgaande dat het laatste model inderdaad kan worden geëxtrapoleerd naar de gemeten massa van het zwarte gat. We leveren observationeel bewijs voor een accreterende IMBH als het centrale compacte object dat zich bevindt in AT2018cow, en demonstreren een nieuwe manier om LFBOTs te bestuderen die de röntgenstraling vertonen die vergelijkbaar is met die van AT2018cow.

De toekomst van IMBH-onderzoek zal worden versterkt door de volgende generatie surveys. Surveys zoals die van *Einstein Probe* en de *Vera C.RubinObservatory* worden verwacht het aantal IMBH-TDE detecties aanzienlijk te verhogen. Vervolgens zullen, met de snel reagerende follow-up waarnemingen van bijvoorbeeld *Einstein Probe* (in het bijzonder de Fast X-ray Telescope) en *NICER*, meer gegevens van hoge kwaliteit over de X-ray spectrale TDE's beschikbaar komen, vooral in de vroege fasen direct na de verstoring, wat ons in staat zal stellen om meer te leren over de super-Eddington accretie van IMBH's en het gedrag van TDE's in de vroege tijdsperiode.

BIBLIOGRAFIE

Abbott, B. P., Abbott, R., Abbott, T., et al. 2016a, PRL, 116, 131103

—. 2016b, PRL, 116, 241102

Abbott, R., Abbott, T., Abraham, S., et al. 2020, PRL, 125, 101102

Abbott, R., Abbott, T., Acernese, F., et al. 2023, PRX, 13, 041039

Abramowicz, M., Czerny, B., Lasota, J., & Szuszkiewicz, E. 1988, ApJ, 332, 646

Abramowicz, M. A., & Fragile, P. C. 2013, Living Reviews in Relativity, 16, 1

Abramowicz, M. A., & Kluźniak, W. 2001, A&A, 374, L19

Adelman-McCarthy, J. K., Agüeros, M. A., Allam, S. S., et al. 2008, ApJ Suppl, 175, 297

Aghanim, N., Akrami, Y., Ashdown, M., et al. 2020, A&A, 641, A6

Akaike, H. 1974, IEEE transactions on automatic control, 19, 716

Akiyama, K., Alberdi, A., Alef, W., et al. 2019, ApJL, 875, L6

—. 2022, ApJL, 930, L15

Alexander, K. D., van Velzen, S., Horesh, A., & Zauderer, B. A. 2020, Space Science Reviews, 216, 81

Altamirano, D., Belloni, T., Linares, M., et al. 2011, ApJL, 742, L17

Amaro-Seoane, P., Gair, J. R., Pound, A., Hughes, S. A., & Sopuerta, C. F. 2015, Journal of Physics: Conference Series, 610, 012002

Andalman, Z. L., Liska, M. T., Tchekhovskoy, A., Coughlin, E. R., & Stone, N. 2022, MNRAS, 510, 1627

Arcavi, I., Wolf, W. M., Howell, D. A., et al. 2016, ApJ, 819, 35

Arcodia, R., Merloni, A., Nandra, K., et al. 2021, Nature, 592, 704

Arcodia, R., Liu, Z., Merloni, A., et al. 2024, A&A, 684, A64

Arias, P., Cadamuro, D., Goodsell, M., et al. 2012, JCAP, 2012, 013

Arnaud, K. 1996, in Astronomical Data Analysis Software and Systems V, Vol. 101, 17

Arvanitaki, A., Dimopoulos, S., Dubovsky, S., Kaloper, N., & March-Russell, J. 2010, PRD, 81, 123530

Auchettl, K., Guillochon, J., & Ramirez-Ruiz, E. 2017, ApJ, 838, 149

Bade, N., Komossa, S., & Dahlem, M. 1996, A&A, 309, L35

Baldassare, V. F., Reines, A. E., Gallo, E., & Greene, J. E. 2015, ApJL, 809, L14

Banados, E., Venemans, B. P., Mazzucchelli, C., et al. 2018, Nature, 553, 473

Bardeen, J. M., Press, W. H., & Teukolsky, S. A. 1972, ApJ, 178, 347

Barra, F., Pinto, C., Walton, D., et al. 2022, MNRAS, 516, 3972

Barth, A. J., Greene, J. E., & Ho, L. C. 2008, ApJ, 136, 1179

Begelman, M. C., & Rees, M. J. 1978, MNRAS, 185, 847

Begelman, M. C., Volonteri, M., & Rees, M. J. 2006, MNRAS, 370, 289

Bellm, E. C., Kulkarni, S. R., Graham, M. J., et al. 2018, Publications of the Astronomical Society of the Pacific, 131, 018002

Belloni, T., Mendez, M., King, A., van der Klis, M., & Van Paradijs, J. 1997, ApJ, 488, L109

Belloni, T., Psaltis, D., & van der Klis, M. 2002, ApJ, 572, 392

Belloni, T. M. 2009, in The Jet Paradigm: From Microquasars to Quasars (Springer), 53–84

—. 2010, in The Jet Paradigm (Springer), 53–84

Bellovary, J. M., Cleary, C. E., Munshi, F., et al. 2019, MNRAS, 482, 2913

Beloborodov, A. M. 2017, ApJ, 850, 141

Berti, E., & Volonteri, M. 2008, ApJ, 684, 822

Blandford, R., & McKee, C. F. 1982, ApJ, 255, 419

Bogdán, Á., Goulding, A. D., Natarajan, P., et al. 2024, Nature Astronomy, 8, 126

Bolton, C. T. 1972, Nature, 235, 271

Bonnerot, C., & Lu, W. 2020, MNRAS, 495, 1374

Bonnerot, C., & Stone, N. 2021, Space Science Reviews, 217, 1

Brenneman, L. W., & Reynolds, C. S. 2006, ApJ, 652, 1028

Bricman, K., & Gomboc, A. 2020, The Astrophysical Journal, 890, 73

Bright, J. S., Margutti, R., Matthews, D., et al. 2022, ApJ, 926, 112

Brightman, M., Harrison, F. A., Barret, D., et al. 2016, ApJ, 829, 28

Brito, R., Cardoso, V., Pani, P., et al. 2020, Superradiance New Frontiers in Black Hole Physics (Springer)

Bromm, V., & Larson, R. B. 2004, Annu. Rev. Astron. Astrophys., 42, 79

Bromm, V., & Loeb, A. 2003, ApJ, 596, 34

Brown, J., Holoien, T.-S., Auchettl, K., et al. 2017, MNRAS, 466, 4904

Calderone, G., Ghisellini, G., Colpi, M., & Dotti, M. 2013, MNRAS, 431, 210

Campitiello, S., Celotti, A., Ghisellini, G., & Sbarrato, T. 2020, A&A, 640, A39

Cao, Z., Jonker, P., Pasham, D., et al. 2024, ApJ, 970, 89

Cao, Z., Jonker, P., Wen, S., Stone, N., & Zabludoff, A. 2023, MNRAS, 519, 2375

Cardoso, V., Dias, Ó. J., Hartnett, G. S., et al. 2018, JCAP, 2018, 043

Casares, J., & Jonker, P. G. 2014, Space Science Reviews, 183, 223

Cash, W. 1979, ApJ, 228, 939

Chakraborty, J., Kara, E., Masterson, M., et al. 2021, ApJL, 921, L40

Chen, Y.-P., Zhang, S., Ji, L., et al. 2022, ApJ, 936, 46

Collin, S., & Kawaguchi, T. 2004, A&A, 426, 797

Coppejans, D. L., Margutti, R., Terreran, G., et al. 2020, ApJL, 895, L23

Czerny, B. 2019, Universe, 5, 131

Dai, L., McKinney, J. C., Roth, N., Ramirez-Ruiz, E., & Miller, M. C. 2018, ApJL, 859, L20

Dai, X., Kong, L., Bu, Q., et al. 2023, MNRAS, 521, 2692

Daly, R. A. 2011, MNRAS, 414, 1253

Dauser, T., García, J., Parker, M., Fabian, A., & Wilms, J. 2014, MNRASL, 444, L100

Davis, S. W., Done, C., & Blaes, O. M. 2006, ApJ, 647, 525

Davis, S. W., & El-Abd, S. 2019, ApJ, 874, 23

Davis, S. W., & Laor, A. 2011, The Astrophysical Journal, 728, 98

Denney, K., Watson, L., Peterson, B. M., et al. 2009, ApJ, 702, 1353

Devecchi, B., & Volonteri, M. 2009, ApJ, 694, 302

Dine, M., & Fischler, W. 1983, PLB, 120, 137

Done, C., Davis, S., Jin, C., Blaes, O., & Ward, M. 2012, MNRAS, 420, 1848

Done, C., & Kubota, A. 2006, MNRAS, 371, 1216

Dotan, C., & Shaviv, N. J. 2011, MNRAS, 413, 1623

Drout, M. R., Chornock, R., Soderberg, A. M., et al. 2014, ApJ, 794, 23

Dubus, G., Hameury, J.-M., & Lasota, J.-P. 2001, A&A, 373, 251

Earnshaw, H. P., Roberts, T. P., Middleton, M. J., Walton, D. J., & Mateos, S. 2019, MNRAS, 483, 5554

Eckart, A., Genzel, R., Ott, T., & Schödel, R. 2002, MNRAS, 331, 917

Eilers, A.-C., Mackenzie, R., Pizzati, E., et al. 2024, ApJ Accepted

Esin, A. A., McClintock, J. E., & Narayan, R. 1997, ApJ, 489, 865

Esquej, P., Saxton, R., Freyberg, M., et al. 2007, Astronomy & Astrophysics, 462, L49

Evans, C. R., & Kochanek, C. S. 1989, ApJ, 346, L13

Evans, P., Beardmore, A., Page, K., et al. 2009, MNRAS, 397, 1177

Evans, P., Nixon, C., Campana, S., et al. 2023, Nature Astronomy, 7, 1368

Ezhikode, S. H., Dewangan, G. C., Misra, R., & Philip, N. S. 2020, MNRAS, 495, 3373

Fabian, A., Rees, M., Stella, L., & White, N. E. 1989, MNRAS, 238, 729

Fender, R., & Belloni, T. 2012, Science, 337, 540

Feng, H., & Kaaret, P. 2009, ApJ, 696, 1712

Feng, H., Tao, L., Kaaret, P., & Grisé, F. 2016, ApJ, 831, 117

Fox, O. D., & Smith, N. 2019, MNRAS, 488, 3772

Fragile, P. C., & Anninos, P. 2005, ApJ, 623, 347

Fragile, P. C., Blaes, O. M., Anninos, P., & Salmonson, J. D. 2007, ApJ, 668, 417

Franchini, A., Lodato, G., & Facchini, S. 2016, MNRAS, 455, 1946

Frank, J., King, A. R., & Raine, D. 2002, Accretion power in astrophysics (Cambridge university press)

García, J., Dauser, T., Lohfink, A., et al. 2014, ApJ, 782, 76

Gelman, A., & Rubin, D. B. 1992, Statistical science, 7, 457

Genzel, R., Eisenhauer, F., & Gillessen, S. 2010, Reviews of modern physics, 82, 3121

Gezari, S. 2021, ARA&A, 59, 21

Gezari, S., Velzen, S. v., Stern, D., et al. 2020, ATel, 13859, 1

Gezari, S., Martin, D., Milliard, B., et al. 2006, ApJ, 653, L25

Gezari, S., Chornock, R., Rest, A., et al. 2012, Nature, 485, 217

Ghez, A. M., Salim, S., Weinberg, N., et al. 2008, ApJ, 689, 1044

Ghisellini, G., Guilbert, P. W., & Svensson, R. 1988, ApJ, 334, L5

Ghisellini, G., Ceca, R. D., Volonteri, M., et al. 2010, MNRAS, 405, 387

Gierliński, M., & Done, C. 2004, MNRAS, 347, 885

Giustini, M., Miniutti, G., & Saxton, R. D. 2020, A&A, 636, L2

Giustini, M., Miniutti, G., Arcodia, R., et al. 2024, A&A, 692, A15

Gladstone, J. C., Roberts, T. P., & Done, C. 2009, MNRAS, 397, 1836

Gottlieb, O., Tchekhovskov, A., & Margutti, R. 2022, MNRAS, 513, 3810

Graham, A. W., & Scott, N. 2013, ApJ, 764, 151

Graham, M. J., Kulkarni, S., Bellm, E. C., et al. 2019, PASP, 131, 078001

Graham, P. W., Mardon, J., & Rajendran, S. 2016, PRD, 93, 103520

Greene, J. E., Strader, J., & Ho, L. C. 2020, Annual Review of Astronomy and Astrophysics, 58, 257

Greif, T. H., Springel, V., White, S. D., et al. 2011, ApJ, 737, 75

Grupe, D., Komossa, S., & Saxton, R. 2015, ApJL, 803, L28

Guillochon, J., Nicholl, M., Villar, V. A., et al. 2018, ApJS, 236, 6

Guillochon, J., & Ramirez-Ruiz, E. 2013, ApJ, 767, 25

—. 2015, ApJ, 809, 166

Gültekin, K., Richstone, D. O., Gebhardt, K., et al. 2009, ApJ, 698, 198

Guolo, M., Gezari, S., Yao, Y., et al. 2024a, ApJ, 966, 160

Guolo, M., Pasham, D. R., Zajaček, M., et al. 2024b, Nature Astronomy, 8, 347

Häberle, M., Neumayer, N., Seth, A., et al. 2024, Nature, 631, 285

Häring, N., & Rix, H.-W. 2004, ApJ, 604, L89

Harrison, F. A., Boggs, S., Christensen, F., et al. 2010, in Space Telescopes and Instrumentation 2010: Ultraviolet to Gamma Ray, Vol. 7732, SPIE, 189–196

Hayasaki, K., & Jonker, P. G. 2021, ApJ, 921, 20

Hayasaki, K., Stone, N., & Loeb, A. 2016, MNRAS, 461, 3760

Hills, J. G. 1975, Nature, 254, 295

Ho, A. Y., Phinney, E. S., Ravi, V., et al. 2019, ApJ, 871, 73

Ho, A. Y., Perley, D. A., Yao, Y., et al. 2022a, ApJ, 938, 85

Ho, A. Y., Margalit, B., Bremer, M., et al. 2022b, ApJ, 932, 116

Ho, A. Y., Perley, D. A., Gal-Yam, A., et al. 2023, ApJ, 949, 120

Ho, L. C., Kim, M., & Terashima, Y. 2012, ApJL, 759, L16

Holoien, T.-S., Kochanek, C., Prieto, J., et al. 2016, MNRAS, 463, 3813

Hughes, S. A., & Blandford, R. D. 2003, ApJ, 585, L101

Inayoshi, K., Omukai, K., & Tasker, E. 2014, MNRAS: Letters, 445, L109

Inayoshi, K., Visbal, E., & Haiman, Z. 2020, Annual Review of Astronomy and Astrophysics, 58, 27

Inkenhaag, A., Jonker, P. G., Cannizzaro, G., Mata Sánchez, D., & Saxton, R. D. 2021, MNRAS, 507, 6196

Inkenhaag, A., Jonker, P. G., Levan, A. J., et al. 2023, MNRAS, 525, 4042

Janiuk, A., & Czerny, B. 2011, MNRAS, 414, 2186

Janiuk, A., Czerny, B., & Siemiginowska, A. 2000, ApJ, 542, L33

Janiuk, A., Grzedzielski, M., Capitanio, F., & Bianchi, S. 2015, A&A, 574, A92

Jiang, Y.-F., Stone, J. M., & Davis, S. W. 2019, ApJ, 880, 67

Jonker, P., Stone, N., Generozov, A., van Velzen, S., & Metzger, B. 2020, ApJ, 889, 166

Kaaret, P., Feng, H., & Roberts, T. P. 2017, ARA&A, 55, 303

Kaastra, J., & Bleeker, J. 2016, A&A, 587, A151

Kalberla, P. M., Burton, W., Hartmann, D., et al. 2005, A&A, 440, 775

Kallman, T., & Bautista, M. 2001, ApJS, 133, 221

Kara, E., Dai, L., Reynolds, C., & Kallman, T. 2018, MNRAS, 474, 3593

Karlsson, T., Bromm, V., & Bland-Hawthorn, J. 2013, Reviews of Modern Physics, 85, 809

Katayama, H., Takahashi, I., Ikebe, Y., Matsushita, K., & Freyberg, M. 2004, A&A, 414, 767

Kaur, K., Stone, N. C., & Gilbaum, S. 2023, MNRAS, 524, 1269

Kesden, M. 2012, PRD, 85, 024037

Khabibullin, I., Sazonov, S., & Sunyaev, R. 2014, Monthly Notices of the Royal Astronomical Society, 437, 327

King, A. 2020, MNRAS: Letters, 493, L120

—. 2023, MNRAS: Letters, 523, L26

King, A., Pringle, J., & Hofmann, J. 2008, MNRAS, 385, 1621

King, A. R., Davies, M. B., Ward, M., Fabbiano, G., & Elvis, M. 2001, ApJ, 552, L109

Kitaki, T., Mineshige, S., Ohsuga, K., & Kawashima, T. 2021, PASJ, 73, 450

Kochanek, C. 2016, MNRAS, 461, 371

Kochanek, C., Shappee, B., Stanek, K., et al. 2017, Publications of the Astronomical Society of the Pacific, 129, 104502

Kochanek, C. S. 1994, Astrophysical Journal, Part 1 (ISSN 0004-637X), vol. 422, no. 2, p. 508-520, 422, 508

Komossa, S., Halpern, J., Schartel, N., et al. 2004, ApJL, 603, L17

Kormendy, J., & Ho, L. C. 2013, ARA&A, 51, 511

Kormendy, J., & Richstone, D. 1995, Annual Review of Astronomy and Astrophysics, 33, 581

Krolik, J. H., & Linial, I. 2022, ApJ, 941, 24

Kubota, A., & Done, C. 2019, MNRAS, 489, 524

Kuin, N. P. M., Wu, K., Oates, S., et al. 2019, MNRAS, 487, 2505

Laor, A. 1990, MNRAS, 246, 369

Lasota, J., & Pelat, D. 1991, A&A, 249, 574

Leung, S.-C., Blinnikov, S., Nomoto, K., et al. 2020, ApJ, 903, 66

Leung, S.-C., Fuller, J., & Nomoto, K. 2021, ApJ, 915, 80

Li, L.-X., Zimmerman, E. R., Narayan, R., & McClintock, J. E. 2005, ApJS, 157, 335

Li, Z., Gao, H., Zhang, Z., et al. 2014, MNRAS, 440, 143

Lightman, A. P., & Eardley, D. M. 1974, ApJ, 187, L1

Lin, D., Godet, O., Ho, L. C., et al. 2017a, MNRAS, 468, 783

Lin, D., Irwin, J. A., Godet, O., Webb, N. A., & Barret, D. 2013a, ApJL, 776, L10

Lin, D., Webb, N. A., & Barret, D. 2012, ApJ, 756, 27

—. 2013b, ApJ, 780, 39

Lin, D., Guillochon, J., Komossa, S., et al. 2017b, Nature Astronomy, 1, 1

Lin, D., Strader, J., Carrasco, E. R., et al. 2018, Nature Astronomy, 2, 656

Lin, D., Strader, J., Romanowsky, A. J., et al. 2020, ApJL, 892, L25

Lin, D., Godet, O., Webb, N. A., et al. 2022a, ApJL, 924, L35

Lin, Z., Jiang, N., Kong, X., et al. 2022b, ApJL, 939, L33

Linial, I., & Metzger, B. D. 2023a, The Astrophysical Journal, 957, 34

—. 2023b, ApJ, 957, 34

Linial, I., & Quataert, E. 2024, The Astrophysical Journal, 974, 67

Liska, M., Hesp, C., Tchekhovskoy, A., et al. 2018, MNRASL, 474, L81

Liska, M., Kaaz, N., Musoke, G., Tchekhovskoy, A., & Porth, O. 2023, ApJL, 944, L48

Liu, J., McClintock, J. E., Narayan, R., Davis, S. W., & Orosz, J. A. 2008, ApJ, 679, L37

Liu, Z., Malyali, A., Krumpe, M., et al. 2023, A&A, 669, A75

Lodato, G., & Natarajan, P. 2006, MNRAS, 371, 1813

Lodato, G., & Rossi, E. M. 2011, MNRAS, 410, 359

Loeb, A., & Rasio, F. A. 1994, ApJ, 432, 52

Loeb, A., & Ulmer, A. 1997, ApJ, 489, 573

Lomb, N. R. 1976, Ap&SS, 39, 447

Luo, Y., Shlosman, I., Nagamine, K., & Fang, T. 2020, MNRAS, 492, 4917

Lützgendorf, N., Gebhardt, K., Baumgardt, H., et al. 2015, A&A, 581, A1

MacLeod, M., Guillochon, J., & Ramirez-Ruiz, E. 2012, ApJ, 757, 134

MacLeod, M., Ramirez-Ruiz, E., Grady, S., & Guillochon, J. 2013, ApJ, 777, 133

Madau, P., & Rees, M. J. 2001, ApJ, 551, L27

Magdziarz, P., Blaes, O. M., Zdziarski, A. A., Johnson, W. N., & Smith, D. A. 1998, MNRAS, 301, 179

Maksym, W. P., Lin, D., & Irwin, J. A. 2014, ApJL, 792, L29

Mapelli, M. 2020, Handbook of gravitational wave astronomy, 1

Margutti, R., Metzger, B., Chornock, R., et al. 2019, ApJ, 872, 18

Markevitch, M., Bautz, M., Biller, B., et al. 2003, ApJ, 583, 70

Masterson, M., Kara, E., Ricci, C., et al. 2022, ApJ, 934, 35

McClintock, J. E., Narayan, R., & Steiner, J. F. 2015, The Physics of Accretion onto Black Holes, 295

McClintock, J. E., Shafee, R., Narayan, R., et al. 2006, ApJ, 652, 518

McHardy, I. M., Koerding, E., Knigge, C., Uttley, P., & Fender, R. 2006, Nat, 444, 730

Mediavilla, E., Jiménez-Vicente, J., Fian, C., et al. 2018, ApJ, 862, 104

Merloni, A., & Fabian, A. 2001, MNRAS, 321, 549

Merritt, D., & Ferrarese, L. 2001, ApJ, 547, 140

Metzger, B. D. 2022, ApJ, 932, 84

Metzger, B. D., & Stone, N. C. 2016, MNRAS, 461, 948

Mezcua, M., Kim, M., Ho, L., & Lonsdale, C. 2018, MNRAS: Letters, 480, L74

Middleton, M. J., Walton, D. J., Roberts, T. P., & Heil, L. 2013, MNRASL, 438, L51

Migliori, G., Margutti, R., Metzger, B., et al. 2023, ApJL accepted; arXiv preprint ar-Xiv:2309.15678

Miller, B. P., Gallo, E., Greene, J. E., et al. 2015, ApJ, 799, 98

Miller, J., Reynolds, C., Fabian, A., Miniutti, G., & Gallo, L. 2009, ApJ, 697, 900

Miller, J., & Reynolds, M. 2020, ATel, 13863, 1

Miller-Jones, J. C., Bahramian, A., Orosz, J. A., et al. 2021, Science, 371, 1046

Miniutti, G., Saxton, R., Giustini, M., et al. 2019, Nat, 573, 381

Mockler, B., Guillochon, J., & Ramirez-Ruiz, E. 2019, ApJ, 872, 151

Mohan, P., An, T., & Yang, J. 2020, ApJL, 888, L24

Moran, E. C., Shahinyan, K., Sugarman, H. R., Vélez, D. O., & Eracleous, M. 2014, AJ, 148, 136

Motta, S., Homan, J., Munoz-Darias, T., et al. 2012, MNRAS, 427, 595

Mummery, A. 2021, MNRAS, 504, 5144

Mummery, A., & Balbus, S. A. 2020, MNRAS, 492, 5655

—. 2021, MNRAS, 504, 4730

Mummery, A., Ingram, A., Davis, S., & Fabian, A. 2024a, MNRAS, 531, 366

Mummery, A., van Velzen, S., Nathan, E., et al. 2024b, MNRAS, 527, 2452

Mummery, A., Wevers, T., Saxton, R., & Pasham, D. 2023, MNRAS, 519, 5828

Mundo, S. A., Kara, E., Cackett, E. M., et al. 2020, MNRAS, 496, 2922

Murase, K., Kimura, S. S., Zhang, B. T., Oikonomou, F., & Petropoulou, M. 2020, ApJ, 902, 108

Narayan, R., & McClintock, J. E. 2012, MNRAS: Letters, 419, L69

Natarajan, P. 2014, GReGr, 46, 1

Natarajan, P., Pacucci, F., Ricarte, A., et al. 2023, ApJL, 960, L1

Nayana, A., & Chandra, P. 2021, ApJL, 912, L9

Nelson, A. E., & Scholtz, J. 2011, PRD, 84, 103501

Nguyen, D. D., Seth, A. C., Neumayer, N., et al. 2019, ApJ, 872, 104

Nicholl, M., Pasham, D., Mummery, A., et al. 2024, Nature, 1

Nowak, M. A., Hanke, M., Trowbridge, S. N., et al. 2011, ApJ, 728, 13

Noyola, E., Gebhardt, K., Kissler-Patig, M., et al. 2010, ApJL, 719, L60

Ohsuga, K., & Mineshige, S. 2011, ApJ, 736, 2

Pacucci, F., Loeb, A., Mezcua, M., & Martín-Navarro, I. 2018, ApJL, 864, L6

Pagani, C., Morris, D., Racusin, J., et al. 2007, in UV, X-Ray, and Gamma-Ray Space Instrumentation for Astronomy XV, Vol. 6686, SPIE, 80–88

Page, D. N., & Thorne, K. S. 1974, ApJ, 191, 499

Pasham, D. R., Remillard, R. A., Fragile, P. C., et al. 2019, Sci, 363, 531

Pasham, D. R., Ho, W. C., Alston, W., et al. 2022, Nature Astronomy, 6, 249

Pasham, D. R., Lucchini, M., Laskar, T., et al. 2023, Nature Astronomy, 7, 88

Pasham, D. R., Tombesi, F., Suková, P., et al. 2024a, Sci. Adv., 10, eadj8898

Pasham, D. R., Zajaček, M., Nixon, C., et al. 2024b, Nature, 1

Patrick, A., Reeves, J., Porquet, D., et al. 2012, MNRAS, 426, 2522

Paturel, G., Dubois, P., Petit, C., & Woelfel, F. 2002, LEDA, 0

Peccei, R. D., & Quinn, H. R. 1977, PRL, 38, 1440

Pellegrino, C., Howell, D., Vinkó, J., et al. 2022, ApJ, 926, 125

Perley, D. A., Mazzali, P. A., Yan, L., et al. 2019, MNRAS, 484, 1031

Perley, D. A., Ho, A. Y., Yao, Y., et al. 2021, MNRAS, 508, 5138

Peterson, B. M., Ferrarese, L., Gilbert, K., et al. 2004, ApJ, 613, 682

Pinto, C., Middleton, M. J., & Fabian, A. C. 2016, Nature, 533, 64

Pinto, C., Alston, W., Soria, R., et al. 2017, MNRAS, 468, 2865

Pinto, C., Soria, R., Walton, D., et al. 2021, MNRAS, 505, 5058

Piran, T. 1978, ApJ, 221, 652

Piran, T., Svirski, G., Krolik, J., Cheng, R. M., & Shiokawa, H. 2015, ApJ, 806, 164

Plucinsky, P. P., Beardmore, A. P., Foster, A., et al. 2017, A&A, 597, A35

Prentice, S., Maguire, K., Smartt, S., et al. 2018, ApJL, 865, L3

Preskill, J., Wise, M. B., & Wilczek, F. 1983, PLB, 120, 127

Press, W. H., & Teukolsky, S. A. 1972, Nature, 238, 211

Psaltis, D., & Johannsen, T. 2011, ApJ, 745, 1

Pursiainen, M., Childress, M., Smith, M., et al. 2018, MNRAS, 481, 894

Quintin, E., Webb, N., Guillot, S., et al. 2023, A&A, 675, A152

Rees, M. J. 1988, Nature, 333, 523

Reisswig, C., Ott, C. D., Abdikamalov, E., et al. 2013, Physical Review Letters, 111, 151101

Remillard, R. A., & McClintock, J. E. 2006, Annu. Rev. Astron. Astrophys., 44, 49

Remillard, R. A., Loewenstein, M., Steiner, J. F., et al. 2022, ApJ, 163, 130

Rest, A., Garnavich, P. M., Khatami, D., et al. 2018, Nature Astronomy, 2, 307

Reynolds, C. S. 2021, Annual Review of Astronomy and Astrophysics, 59, 117

Ricarte, A., & Natarajan, P. 2018, MNRAS, 481, 3278

Richstone, D., Ajhar, E., Bender, R., et al. 1998, Nature, 395, A14

Rivera Sandoval, L., Maccarone, T., Corsi, A., et al. 2018, MNRAS Letters, 480, L146

Rizzuto, F. P., Naab, T., Spurzem, R., et al. 2021, MNRAS, 501, 5257

Roberts, T. P. 2007, Ap&SS, 311, 203

Roming, P. W., Kennedy, T. E., Mason, K. O., et al. 2005, Space Science Reviews, 120, 95

Ross, R., Fabian, A., & Mineshige, S. 1992, MNRAS, 258, 189

Roth, N., & Kasen, D. 2018, ApJ, 855, 54

Roth, N., Rossi, E. M., Krolik, J., et al. 2020, Space Science Reviews, 216, 1

Różańska, A., Malzac, J., Belmont, R., Czerny, B., & Petrucci, P.-O. 2015, A&A, 580, A77

Ryu, T., Krolik, J., & Piran, T. 2020, ApJ, 904, 73

Ryu, T., Tanaka, T. L., Perna, R., & Haiman, Z. 2016, MNRAS, 460, 4122

Sądowski, A. 2009, ApJS, 183, 171

Sądowski, A., Abramowicz, M., Bursa, M., et al. 2011, A&A, 527, A17

Sądowski, A., Narayan, R., Tchekhovskoy, A., et al. 2015, MNRAS, 447, 49

Sagiv, I., Gal-Yam, A., Ofek, E., et al. 2014, ApJ, 147, 79

Salpeter, E. 1964, ApJ, 140, 796

Savonije, G. 1978, A&A, 62, 317

Saxton, R., Komossa, S., Auchettl, K., & Jonker, P. 2020, Space Science Reviews, 216, 1

Saxton, R., Read, A., Esquej, P., et al. 2012, A&A, 541, A106

Saxton, R., Read, A. M., Komossa, S., et al. 2017, A&A, 598, A29

Saxton, R., Read, A., Komossa, S., et al. 2014, A&A, 572, A1

—. 2019, A&A, 630, A98

Saxton, R. D., Motta, S. E., Komossa, S., & Read, A. M. 2015, MNRAS, 454, 2798

Scargle, J. D. 1982, ApJ, 263, 835

Schlafly, E. F., & Finkbeiner, D. P. 2011, ApJ, 737, 103

Shafee, R., McClintock, J. E., Narayan, R., et al. 2005, ApJ, 636, L113

Shakura, N., & Sunyaev, R. 1976, MNRAS, 175, 613

Shakura, N. I., & Sunyaev, R. A. 1973, A&A, 24, 337

Shankar, F., Bernardi, M., Sheth, R. K., et al. 2016, MNRAS, 460, 3119

Shappee, B. J., Prieto, J., Grupe, D., et al. 2014, ApJ, 788, 48

She, R., Ho, L. C., & Feng, H. 2017, ApJ, 842, 131

Shibata, M., & Shapiro, S. L. 2002, ApJL, 572, L39

Shimura, T., & Takahara, F. 1993, ApJ, 419, 78

—. 1995, ApJ, 445, 780

Shiokawa, H., Krolik, J. H., Cheng, R. M., Piran, T., & Noble, S. C. 2015, ApJ, 804, 85

Smartt, S., Clark, P., Smith, K., et al. 2018, ATel, 11727, 1

Sniegowska, M., Czerny, B., Bon, E., & Bon, N. 2020, A&A, 641, A167

Steinberg, E., & Stone, N. C. 2024, Nature, 625, 463

Steiner, J. F., McClintock, J. E., Orosz, J. A., et al. 2014, ApJL, 793, L29

Steiner, J. F., Narayan, R., McClintock, J. E., & Ebisawa, K. 2009, PASP, 121, 1279

Stone, N., & Loeb, A. 2012, PRL, 108, 061302

Stone, N. C. 2015, The Tidal Disruption of Stars by Supermassive Black Holes: An Analytic Approach (Springer), doi: 10.1007/978-3-319-12676-0

Stone, N. C., Küpper, A. H., & Ostriker, J. P. 2017, MNRAS, 467, 4180

Stone, N. C., & Metzger, B. D. 2016, MNRAS, 455, 859

Stone, N. C., Vasiliev, E., Kesden, M., et al. 2020, Space Science Reviews, 216, 1

Straub, O., Godet, O., Webb, N., Servillat, M., & Barret, D. 2014, A&A, 569, A116

Straub, O., Bursa, M., Sa, A., et al. 2011, A&A, 533, A67

Strubbe, L. E., & Quataert, E. 2009, MNRAS, 400, 2070

Suková, P., Zajaček, M., Witzany, V., & Karas, V. 2021, ApJ, 917, 43

Sutton, A. D., Roberts, T. P., & Middleton, M. J. 2013, MNRAS, 435, 1758

Szuszkiewicz, E., & Miller, J. C. 1998, MNRAS, 298, 888

Takeuchi, S., Ohsuga, K., & Mineshige, S. 2013, PASJ, 65, 88

Tampo, Y., Tanaka, M., Maeda, K., et al. 2020, ApJ, 894, 27

Tanaka, M., Tominaga, N., Morokuma, T., et al. 2016, ApJ, 819, 5

Tchekhovskoy, A., Metzger, B. D., Giannios, D., & Kelley, L. Z. 2014, MNRAS, 437, 2744

Teboul, O., & Metzger, B. D. 2023, ApJL, 957, L9

Terashima, Y., Kamizasa, N., Awaki, H., Kubota, A., & Ueda, Y. 2012, ApJ, 752, 154

Thorne, K. S. 1974, ApJ, 191, 507

Tonry, J., Denneau, L., Heinze, A., et al. 2018, PASP, 130, 064505

Tremou, E., Strader, J., Chomiuk, L., et al. 2018, ApJ, 862, 16

Tripathi, P., & Dewangan, G. C. 2022, ApJ, 930, 117

Ulmer, A. 1999, ApJ, 514, 180

van Doesburgh, M., & van der Klis, M. 2020, MNRAS, 496, 5262

van Velzen, S., Holoien, T. W.-S., Onori, F., Hung, T., & Arcavi, I. 2020, Space science reviews, 216, 1

van Velzen, S., Stone, N. C., Metzger, B. D., et al. 2019, ApJ, 878, 82

van Velzen, S., Farrar, G. R., Gezari, S., et al. 2011, ApJ, 741, 73

Van Velzen, S., Gezari, S., Cenko, S. B., et al. 2019, ApJ, 872, 198

Van Velzen, S., Gezari, S., Hammerstein, E., et al. 2021, ApJ, 908, 4

Veledina, A., Vurm, I., & Poutanen, J. 2011, MNRAS, 414, 3330

Volonteri, M. 2010, A&AR, 18, 279

Volonteri, M., Habouzit, M., & Colpi, M. 2021, Nature Reviews Physics, 3, 732

Volonteri, M., Sikora, M., & Lasota, J.-P. 2007, ApJ, 667, 704

Walsh, J. L., Barth, A. J., Ho, L. C., & Sarzi, M. 2013, ApJ, 770, 86

Wandel, A., & Petrosian, V. 1988, ApJ, 329, L11

Wang, J., & Merritt, D. 2004, ApJ, 600, 149

Warner, C., Hamann, F., & Dietrich, M. 2004, ApJ, 608, 136

Watanabe, S., & Opper, M. 2010, Journal of machine learning research, 11

Webbe, R., & Young, A. 2023, MNRAS, 518, 3428

Wen, S., Jonker, P. G., Stone, N. C., Van Velzen, S., & Zabludoff, A. I. 2023, MNRAS, 522, 1155

Wen, S., Jonker, P. G., Stone, N. C., & Zabludoff, A. I. 2021, ApJ, 918, 46

Wen, S., Jonker, P. G., Stone, N. C., Zabludoff, A. I., & Cao, Z. 2022, ApJ, 933, 31

Wen, S., Jonker, P. G., Stone, N. C., Zabludoff, A. I., & Psaltis, D. 2020, ApJ, 897, 80

Wen, S., Wang, S., & Luo, X. 2018, JCAP, 2018, 011

Wevers, T., Stone, N. C., van Velzen, S., et al. 2019a, MNRAS, 487, 4136

Wevers, T., Pasham, D., van Velzen, S., et al. 2019b, MNRAS, 488, 4816

Wevers, T., Pasham, D. R., van Velzen, S., et al. 2021, ApJ, 912, 151

Wevers, T., Coughlin, E., Pasham, D., et al. 2023, ApJL, 942, L33

White, C. J., Quataert, E., & Blaes, O. 2019, ApJ, 878, 51

Wilkins, D., & Gallo, L. C. 2015, MNRAS, 448, 703

Willingale, R., Starling, R., Beardmore, A. P., Tanvir, N. R., & O'Brien, P. T. 2013, MNRAS, 431, 394

Wilms, J., Allen, A., & McCray, R. 2000, ApJ, 542, 914

Wu, H., Yuan, H., Wang, Y., Niu, Z., & Zhang, H. 2024, The Astronomical Journal, 167, 277

Xue, L., Sądowski, A., Abramowicz, M. A., & Lu, J.-F. 2011, ApJS, 195, 7

Yang, H., Yuan, F., Kwan, T., & Dai, L. 2023, MNRAS, 523, 208

Yao, Y., Lu, W., Guolo, M., et al. 2022a, ApJ, 937, 8

Yao, Y., Ho, A. Y., Medvedev, P., et al. 2022b, ApJ, 934, 104

Yuan, W., Zhang, C., Ling, Z., et al. 2018, in Society of Photo-Optical Instrumentation Engineers (SPIE) Conference Series, Vol. 10699, Space Telescopes and Instrumentation 2018: Ultraviolet to Gamma Ray, ed. J.-W. A. den Herder, S. Nikzad, & K. Nakazawa, 1069925

Zanazzi, J., & Lai, D. 2019, MNRAS, 487, 4965

Zdziarski, A. A., Johnson, W. N., & Magdziarz, P. 1996, MNRAS, 283, 193

Zdziarski, A. A., Szanecki, M., Poutanen, J., Gierliński, M., & Biernacki, P. 2020, MNRAS, 492, 5234

Zhang, W., Shu, X., Chen, J.-H., et al. 2022, Research in Astronomy and Astrophysics, 22, 125016

Zhao, X., Gou, L., Dong, Y., et al. 2021, ApJ, 908, 117

Zhuang, M.-Y., & Ho, L. C. 2023, Nature Astronomy, 7, 1376

Zwart, S. F. P., & McMillan, S. L. 2002, ApJ, 576, 899

Życki, P. T., Done, C., & Smith, D. A. 1999, MNRAS, 309, 561

RESEARCH DATA MANAGEMENT

This thesis research has been carried out under the institute research data management policy of the *Institute for Mathematics Astrophysics and Particle Physics* (IMAPP), Radboud University Nijmegen.

- All the data used in Chapter 2 are publicly available from the data archive of HEASARC (https://heasarc.gsfc.nasa.gov/). A reproduction package is available at DOI: 10.5281/zenodo.6621932.
- All the data used in Chapter 3 are publicly available from the data archive of HEASARC (https://heasarc.gsfc.nasa.gov/). A reproduction package will be available in Zenodo.
- All the data in Chapter 4 are publicly available from the HEASARC data archive (https://heasarc.gsfc.nasa.gov/). A reproduction package is available at DOI: 10.5281/zen-odo.11162299.
- All the data in Chapter 5 are publicly available from the HEASARC data archive
 (https://heasarc.gsfc.nasa.gov/). A reproduction package is available at DOI 10.5281/ze nodo.11110331. The extension to the slimdz model used in this Chapter is available at
 10.5281/zenodo.11110331.

ABOUT THE AUTHOR

I was born on February 1, 1995 in Chengdu, China. I was raised in Shanghai and graduated from Qibao High School there. Then I went to Fudan University to pursue my Bachelor's degree in Physics, with a scholarship for outstanding entrants from the university. During my Bachelor's, I had the opportunity to take internships in various research fields in physics, and ended up working with Prof. Dr. Bambi who introduced me to the exciting field of black hole study. In 2016, I was awarded professional scholarship for undergraduates from Fudan. In 2018, after graduating with my Bachelor's degree, I joined the API (Anton Pannekoek Institute for Astronomy, University of Amsterdam) to pursue a Master's degree in astronomy and astrophysics. During my Master's thesis, I worked with Prof. Dr. Markoff and Dr. Lucchini on multi–wavelength studies of black hole X–ray binaries. I also took part of an internship in La Palma to perform ground–based optical observations using the telescope on the mountain.

In 2020, I joined SRON (Netherlands Institute for Space Research) to start my PhD under the supervision of Prof. Dr. Jonker. This happened to be in the middle of the COVID–19 pandemic. From 2020 to 2025, I worked as a PhD student at SRON and Radboud University Nijmegen. My PhD thesis focuses on using tidal disruption events to find intermediate—mass black holes, which mainly consists of analysing the X–ray data from space observatories like *XMM—Newton* and *Swift*. Twice (in 2023 and 2024), I was granted the Leids Kerkhoven—Bosscha Fonds research subsidies to attend international conferences. During my PhD, I had the opportunity to present my research in contributed talks at several conferences across Europe.

ACKNOWLEDGMENTS

Starting in the middle of the lockdown with everyone working remotely due to the pandemic, this PhD has become a unique life experience for me. Along the journey, I consider myself incredibly lucky to have the help of many talented and friendly people. Undoubtedly, it is impossible to mention all the names of those people that supported me. My apologies for an incomplete list here.

First, I would like to express my deepest gratitude to my PhD supervisor, Peter. I keep benefiting from your professional mentorship, rigorous scholarship, encouragement, humour, and patience. You help me to keep improving myself, and constantly support me when I take the slowest steps to progress my research. Not every PhD student has the same luxury. I particularly enjoy our meetings when we discuss physics and interesting ideas. Thank you also for giving me the opportunity to present my work and to visit different places that have broadened my horizon.

Thank you, Wen, for your generous and timely guidance, without which I would never be able to overcome so many scientific obstacles. I am very grateful for your support and your sharing of your passion for research. Thank you, Ann and Nick, for all the scientific discussions and constructive criticism. Your comments always keep me thinking about the physics and the logic of my research. Discussing physics with you in detail is one of the reasons I love being a PhD.

I would like to thank Sera, for your guidance and friendship that continue to support me from my Master's to my PhD. Your professionalism and kindness inspired me to pursue a PhD in this field. Thank you, Matteo, for your tutoring and encouragement. You are an example of an excellent PhD and a friendly researcher, whom I keep trying to follow. Thank you, Jan–Willem, for your guidance and encouragement that help me develop my career as a researcher, and thank you for your captivating lectures on space instruments. My special thanks to Cosimo, who introduced me to the exciting field of astrophysics, and made all the subsequent journey possible. You provided invaluable opportunities and all the support I needed to taste the joy in research and discover my potential. You inspired me to go abroad and seek opportunities to do research.

I would like to say thank you again to all my academic mentors. From you, I see what kind of researcher I want to become, and this whole journey is all about my attempts to imitate you.

Thank you, Deepak, for your friendliness that helped me to have a great start to the PhD even though it was during the pandemic. Sumedha, thank you for the spontaneous talks and the

162 Acknowledgments

encouragement. We shared many struggles as we started the PhD at the same time. I am thankful to all the members of the transient research group in Nijmegen, for the creative and enjoyable group meetings and friendly discussions. My thanks to all the people in the astrophysics department at Radboud. Although my time in this office was limited, I have enjoyed each time being here and talking to you. I want to thank SRON and Radboud for making me feel warm and welcomed when everyone had to work remotely at home during the pandemic.

Looking back on my PhD, I am glad to conclude that I like it as it is, and I have enjoyed it since its beginning. This conclusion has been made possible by three reasons: the tremendous academic help I have received, my constant failure to memorise all the struggles and depressive moments, and the daily support I have received from my family and friends. Zhong, Shuoying, Yufei, Kexin, Woud, Kinga, Menglei, I am grateful for the time we spent together in sharing lives and cheerful moments. Xinran, I want to express my special thanks to you. Through laughs and tears, joys and sorrows, you always stood beside me along this journey. You have such magic that I gain enormous energy from your love to overcome obstacles. I am the luckiest to share my life with you.

Finally, I would like to express my gratitude to my family. I owe an immeasurable debt of thanks to my parents, grandparents, and my sister for the unwavering love and support. It is my greatest joy to share this milestone with you. While I keep my eyes on the stars and black holes, my heart is always with you.

